USC-SIPI REPORT #427

Correction, Coregistration and Connectivity Analysis of Multi-Contrast Brain MRI

by

Chitresh Bhushan

May 2016

Signal and Image Processing Institute
UNIVERSITY OF SOUTHERN CALIFORNIA
Viterbi School of Engineering
Department of Electrical Engineering-Systems
3740 McClintock Avenue, Suite 400
Los Angeles, CA 90089-2564 U.S.A.

CORRECTION, COREGISTRATION AND CONNECTIVITY ANALYSIS OF MULTI-CONTRAST BRAIN MRI

by

Chitresh Bhushan

A Dissertation Presented to the
FACULTY OF THE USC GRADUATE SCHOOL
UNIVERSITY OF SOUTHERN CALIFORNIA
In Partial Fulfillment of the
Requirements for the Degree
DOCTOR OF PHILOSOPHY
(ELECTRICAL ENGINEERING)

May 2016

Abstract

Magnetic Resonance Imaging (MRI) is a versatile imaging technique that allows probing of the various properties of the soft-tissue within the body of living organisms and has been widely used for diagnostic as well as research purposes. MRI has been very useful for studying the brain as it provides an exceptional ability to study structural, functional and dynamic properties in a non-invasive fashion. For example, diffusion MRI allows imaging of the microstructural details of soft-tissue by probing the diffusion of water in tissue, while functional MRI allows the study of neuronal activity by probing blood oxygenation levels as the subject performs a task or function. The availability of diverse *in vivo* image contrasts facilitates the study of the brain by fusing information across multiple MRI images with different contrast mechanisms. However, analysis with multi-contrast MRI poses image and signal processing challenges. Different MRI sequences are required to obtain images with different tissue contrasts, which unfortunately also results in artifacts that are unique to the MRI sequence used. A reliable analysis of multi-contrast images requires the correction of image artifacts, co-registration of the images to establish a one-to-one mapping between voxels, use of appropriate models, filtering, and normalization techniques to extract meaningful parameters from these data. In this dissertation, we present and validate novel approaches and methods to address some of the challenges associated with multi-contrast MRI image analysis.

Diffusion MRI frequently makes use of echo planar imaging (EPI) for fast acquisition. EPI is very sensitive to inhomogeneity in the main magnetic field. These inhomogeneities are particularly pronounced at air-tissue interfaces where there are large changes in magnetic susceptibility and can cause severe local geometric distortion in the reconstructed EPI images. We present a new method for the distortion correction which uses an interlaced phase encoding scheme that exploits the dependency of distortion on phase encoding direction to obtain diffusion weighted images with differing distortion patterns but without repetitive acquisition of the same diffusion weighted images, as done in the state-of-the-art reversed-gradient method. The distorted diffusion-weighted images are corrected in a novel constrained joint reconstruction formulation which leverages the prior knowledge about the smoothness of diffusion processes and spatial smoothness of the images. Our approach demonstrates high-quality correction of susceptibility-induced geometric distortion artifacts in diffusion MRI images and requires half the scan

time in comparison to the reversed-gradient method.

We also developed a robust image co-registration technique for T_1- and T_2-weighted brain images which exploits the known inverted contrast relationships between these images to normalize the contrast differences. This effectively transforms the *inter*-modal image registration problem to an *intra*-modal problem which can leverage well-behaved similarity measures such as the sum of squared differences and are substantially easier to solve. We use the contrast normalization technique for rigid alignment of T_1-weighted anatomical and diffusion images as well as for distortion correction of the diffusion images in the absence of a field inhomogeneity map by formulating a non-rigid image registration problem with physics-based constraints. Our contrast normalization approach demonstrates superior performance and lower computation time as compared to mutual information based methods and other software tools.

Functional MRI (fMRI) is very useful in gaining insight into neuronal activity in the brain, however, data are usually corrupted by noise and unwanted physiological signals. Analysis of such data typically requires smoothing for improved sensitivity and visualization of the functional activity. We present a new filtering approach for fMRI that is based on the concept of non-local means filtering and leverages the temporal similarity in the functional data to adaptively weight the smoothing kernel. This reduces the local intensity fluctuations by averaging across points which have similar time course without the spatial blurring that occurs with linear filtering methods and enables direct visualization of the dynamic brain activity. Our filtering approach also shows significant improvement in the accuracy of function-based cortical sub-division from resting fMRI when compared to task-activated regions obtained with independent task fMRI.

We also developed another approach for brain sub-division based on microstructural differences, which complements the functional subdivision. We propose to fuse information across multi-contrast MRI images with appropriate normalization of vector-valued diffusion information to extract features which can be indicative of microstructural difference and could be used with modern machine learning approaches such as unsupervised clustering to identify cyto- or myelo-architectural subdivisions of the cerebral cortex. The preliminary application of our approach suggests a close correspondence with sub-divisions found in several histological studies.

Dedicated to my parents

Acknowledgment

I am thankful to a large number of people around me who helped, directly and indirectly, complete this dissertation. I could not have reached this point in my life without their generous support and would like to express my deepest gratitude to those wonderful people.

I would like to express my deepest respect and gratitude for my advisor and mentor Professor Richard M. Leahy. He not only helped me explore and define research directions but also provided me with opportunities for professional, scientific as well as personal development. I am thankful for his invaluable mentorship, encouragement, guidance and support throughout my graduate studies.

I am also thankful to Professor Justin P. Haldar for serving on my doctoral committee and co-advising me. He has been immensely helpful and provided opportunities for insightful discussion on various topics. He has been a source of inspiration and contributed greatly to my invaluable learning experience at the University of Southern California (USC).

I would also like to thank Professor Hanna Damasio for serving on my doctoral committee and providing valuable input on various projects I explored during my graduate studies. Her feedback has been instrumental in guiding the direction of my research and development.

I am also very grateful to Professor Krishna S. Nayak for serving on my doctoral committee and for his continuous support, advisement and encouragement throughout my stay at USC. He is a passionate teacher, and I owe him for formally introducing me to the exciting world of magnetic resonance imaging.

I am also indebted to Professor Anand A. Joshi, who got me started with hands-on research and provided an avenue for interesting technical discussions as well as advised me on several topics, curricular and extracurricular. I would also like to thank Professor David W. Shattuck, University of California, Los Angeles for his continued support and guidance in transforming bulk of my doctoral research into scientific software tools, which enabled a larger outreach of my methods to real-world applications.

I am also privileged to be part of the friendly and lively research group at BIG lab. I am very thankful to all current and past members of the group – especially Divya Varadarajan, Soyoung Choi, Sergül Aydöre, Jian Li, Daeun Kim, Yu-Teng Chang and Syed Ashrafulla – for their continued help and support. My special thanks also go to friends outside the lab – K. Naveen Kumar, Asif Zubair, Niharika Gajawelli, Vinod Vishwakarma, Prabhat Shankar and Arpit N. Garg – who helped me keep my spirits up

through the tough times.

I would also like to acknowledge the generous financial support for my graduate studies from USC Annenberg Graduate Fellowship Program and Signal and Image Processing Institute, USC.

Most importantly, I am grateful to my parents and my sister for their support, unfailing love, unlimited patience and endless sacrifices they made to help me realize my dreams.

Contents

List of Publications

Journal Articles

C. Bhushan, J. P. Haldar, S. Choi, A. A. Joshi, D. W. Shattuck, and R. M. Leahy. Co-registration and distortion correction of diffusion and anatomical images based on inverse contrast normalization. *NeuroImage*, 115:269 – 280, 2015. ISSN 1053-8119. doi:10.1016/j.neuroimage.2015.03.050.

C. Bhushan, M. Chong, S. Choi, A. A. Joshi, J. P. Haldar, H. Damasio, and R. M. Leahy. Non-local means filtering reveals real-time whole-brain cortical interactions in resting fMRI. *USC-SIPI Technical Report*, page 423, 2015. URL http://sipi.usc.edu/reports/abstracts.php?rid=sipi-423.

A. J. Degnan, J. L. Wisnowski, S. Choi, R. Ceschin, C. Bhushan, R. M. Leahy, P. Corby, V. J. Schmithorst, and A. Panigrahy. Alterations of resting state networks and structural connectivity in relation to the prefrontal and anterior cingulate cortices in late prematurity. *NeuroReport*, 26(1):22–26, 2015. doi:10.1097/WNR.0000000000000296.

A. J. Degnan, J. L. Wisnowski, S. Choi, R. Ceschin, C. Bhushan, R. M. Leahy, P. Corby, V. J. Schmithorst, and A. Panigrahy. Altered structural and functional connectivity in late preterm preadolescence: An anatomic seed-based study of resting state networks related to the posteromedial and lateral parietal cortex. *PLoS ONE*, 10(6):e0130686, 06 2015. doi:10.1371/journal.pone.0130686.

C. Bhushan, A. A. Joshi, R. M. Leahy, and J. P. Haldar. Improved B_0-distortion correction in diffusion MRI using interlaced q-space sampling and constrained reconstruction. *Magnetic Resonance in Medicine*, 72(5):1218–1232, 2014. ISSN 1522-2594. doi:10.1002/mrm.25026.

M. Bhagat, C. Bhushan, G. Saha, S. Shimjo, K. Watanabe, and J. Bhattacharya. Investigating neuromagnetic brain responses against chromatic flickering stimuli by wavelet entropies. *PLoS ONE*, 4(9): e7173, 09 2009. doi:10.1371/journal.pone.0007173.

Conference Proceedings

C. Bhushan, M. Chong, S. Choi, A. A. Joshi, J. P. Haldar, H. Damasio, and R. M. Leahy. Non-local means filtering for cortical parcellation of resting fMRI. In *22nd Annual Meeting of the Organization for Human Brain Mapping, Geneva, Switzerland*, page 2294, 2016.

M. Chong, C. Bhushan, A. A. Joshi, J. P. Haldar, R. N. Spreng, and R. M. Leahy. Individual performance of resting fMRI parcellation with group connectivity priors. In *22nd Annual Meeting of the Organization for Human Brain Mapping, Geneva, Switzerland*, page 4440, 2016.

A. A. Joshi, R. Salloum, C. Bhushan, and R. M. Leahy. Measuring asymmetric interactions in resting state brain networks. In S. Ourselin, D. C. Alexander, C.-F. Westin, and M. J. Cardoso, editors, *Information Processing in Medical Imaging*, volume 9123 of *Lecture Notes in Computer Science*, pages 399–410. Springer International Publishing, 2015. ISBN 978-3-319-19991-7. doi:10.1007/978-3-319-19992-4_31.

M. C. Chambers, C. Bhushan, J. P. Haldar, R. M. Leahy, and D. W. Shattuck. Correcting inhomogeneity-induced distortion in fMRI using non-rigid registration. In *IEEE International Symposium on Biomedical Imaging, New York City, USA*, pages 1364–1367, April 2015. doi:10.1109/ISBI.2015.7164129.

A. A. Joshi, R. Salloum, C. Bhushan, and R. M. Leahy. Measuring asymmetric connectivity in the default mode network. In *Annual meeting of the Organization for Human Brain Mapping (OHBM), Honolulu, Hawaii*, page 3815, 2015.

C. Bhushan, J. P. Haldar, A. A. Joshi, D. W. Shattuck, and R. M. Leahy. INVERSION: A robust method for co-registration of MPRAGE and diffusion MRI images. In *Joint Annual Meeting ISMRM-ESMRMB, Milan, Italy*, page 2583, 2014.

A. A. Joshi, C. Bhushan, R. Salloum, D. W. Shattuck, and R. M. Leahy. Estimation of cortical thickness from T1-weighted MRI images using tissue fractions. In *20th Annual Meeting of the Organization for Human Brain Mapping (OHBM), Hamburg*, page 1859, 2014.

M. C. Chambers, C. Bhushan, T. Pirnia, K. Narr, J. P. Haldar, R. M. Leahy, and D. W. Shattuck. Registration-based distortion and intensity correction in fMRI. In *20th Annual Meeting of the Organization for Human Brain Mapping (OHBM), Hamburg*, 2014.

C. Bhushan, A. A. Joshi, R. M. Leahy, and J. P. Haldar. Accelerating data acquisition for reversed-gradient distortion correction in diffusion MRI: A constrained reconstruction approach. In *21st Scientific Meeting of International Society for Magnetic Resonance in Medicine (ISMRM), Salt Lake City, Utah*, page 55, 2013.

S. Choi, C. Bhushan, A. A. Joshi, K. Raphel, D. Tranel, D. W. Shattuck, J. P. Haldar, R. M. Leahy, H. Damasio, and J. L. Wisnowski. Altered orbitofrontal tissue microstructure in patients with chronic anterior temporal lobe lesions. In *19th Annual Meeting of the Organization for Human Brain Mapping (OHBM), Seattle*, page 3781, 2013.

D. W. Shattuck, A. A. Joshi, J. P. Haldar, C. Bhushan, S. Choi, A. Krause, J. L. Wisnowski, H. Damasio, A. W. Toga, and R. M. Leahy. New BrainSuite13 tools for image segmentation, registration, connectivity analysis and visualization. In *19th Annual Meeting of the Organization for Human Brain Mapping (OHBM), Seattle*, 2013.

D. W. Shattuck, A. A. Joshi, J. P. Haldar, C. Bhushan, S. Choi, A. C. Krause, J. L. Wisnowski, A. W. Toga, and R. M. Leahy. Software tools for anatomical ROI-based connectivity analysis. In *21st Scientific Meeting of International Society for Magnetic Resonance in Medicine (ISMRM), Salt Lake City, Utah*, page 2691, 2013.

S. Choi, A. A. Joshi, C. Bhushan, D. W. Shattuck, R. M. Leahy, H. Damasio, A. Panigrahy, and J. L. Wisnowski. A multimodal investigation of neuronal/axonal integrity using structural T1-weighted imaging, diffusion tensor imaging, and H1 MR spectroscopy. In *21st Scientific Meeting of International Society for Magnetic Resonance in Medicine (ISMRM), Salt Lake City, Utah*, 2013.

D. Beroukhim, M. Konersman, M. Chong, A. A. Joshi, C. Bhushan, D. W. Shattuck, J. P. Haldar, R. M. Leahy, and C. J. Winstein. Effects of rehabilitation post-stroke: DTI analysis of corticospinal tract characteristics using BrainSuite13. In *Annual meeting of Society for Neuroscience (SfN)*, page 338.11/V3, 2013.

C. Bhushan, J. P. Haldar, A. A. Joshi, and R. M. Leahy. Correcting susceptibility-induced distortion in diffusion-weighted MRI using constrained nonrigid registration. In *Asia-Pacific Signal Information Processing Association Annual Summit and Conference (APSIPA ASC), Hollywood, CA*, pages 1–9, 2012. URL http://ieeexplore.ieee.org/xpls/abs_all.jsp?arnumber=6412009.

G. Antonelli, F. Arrichiello, C. Bhushan, S. Chiaverini, and S. Purkayasth. ROBBIT: An open source simulator for education in robotics. In *6th Vienna International Conference on Mathematical Modelling. Vienna, Austria*, 2009.

This page intentionally left blank.

Chapter 1

Introduction

This dissertation describes the work I have done over the past six years to fulfill the requirements for the Ph.D. degree. The content of each chapter is summarized as follows:

Chapter 2 and 3 provides the background material and review which is helpful in understanding and following the approaches described in later chapters. Chapter 2 provides a high level overview of image reconstruction with MRI and echo planar imaging (EPI) and describes the geometric distortion artifacts related to EPI and diffusion MRI. This chapter also briefly describes prior approaches for distortion correction and how they relate to the approaches presented in this dissertation. Chapter 3 provides a review of methods for the parcellation of the cortex based on microstructural differences using histological as well as *in vivo* MRI approaches and forms the motivation of fusion of information across multi-contrast MRI.

Chapter 4: Diffusion MRI provides quantitative information about microstructural properties which can be useful in neuroimaging studies of the human brain. EPI sequences, which are frequently used for acquisition of diffusion images, are sensitive to inhomogeneities in the primary magnetic (B_0) field that cause localized distortions in the reconstructed images. We describe and evaluate a new method for correction of susceptibility-induced distortion in diffusion images in the absence of an accurate B_0 fieldmap. In our method, the distortion field is estimated using a constrained non-rigid registration between an undistorted T_1-weighted anatomical image and one of the distorted EPI images from diffusion acquisition. Our registration framework is based on a new approach, INVERSION (Inverse contrast Normalization for VERy Simple registratION), which exploits the inverted contrast relationship between T_1- and T_2-weighted brain images to define a simple and robust similarity measure. We also describe how INVERSION can be used for rigid alignment of diffusion images and T_1-weighted anatomical images. Our approach is evaluated with multiple *in vivo* datasets acquired with different acquisition parameters. Compared to other methods, IN-

VERSION shows a robust and consistent performance in rigid registration and shows improved alignment of diffusion and anatomical images relative to normalized mutual information for non-rigid distortion correction. Related publications include [Bhushan et al., 2015b, 2014a, 2012].

Chapter 5 presents a new approach to enable high-quality correction of susceptibility-induced geometric distortion artifacts in diffusion MRI images without increasing scan time. Our distortion correction approach is based on subsampling a generalized version of the state-of-the-art reversed-gradient distortion correction method. Rather than acquire each q-space sample multiple times with different distortions (as in the conventional reversed-gradient method), we sample each q-space point once with an interlaced sampling scheme that measures different distortions at different q-space locations. Distortion correction is achieved using a novel constrained reconstruction formulation that leverages the smoothness of diffusion data in q-space. The effectiveness of our method is demonstrated with simulated and *in vivo* diffusion MRI data. The presented method is substantially faster than the reversed-gradient method, and can also provide smaller intensity errors in the corrected images and smaller errors in derived quantitative diffusion parameters. Our approach enables state-of-the-art distortion correction performance without increasing data acquisition time. Related publications include [Bhushan et al., 2014b, 2013].

Chapter 6: Intensity variations over time in resting BOLD fMRI exhibit spatial correlation patterns consistent with a set of large scale cortical networks. However, visualizations of this data on the brain surface, even after extensive preprocessing, are dominated by local intensity fluctuations that obscure larger scale behavior. Our novel adaptation of non-local means (NLM) filtering, which we refer to as temporal NLM or tNLM, reduces these local fluctuations without the spatial blurring that occurs when using standard linear filtering methods. We show examples of tNLM filtering that allow direct visualization of spatio-temporal behavior on the cortical surface. These results reveal patterns of activity consistent with known networks as well as more complex dynamic changes within and between these networks. This ability to directly visualize brain activity may facilitate the development of new insights into spontaneous brain dynamics. Further, temporal NLM can also be used as a preprocessor for resting fMRI for exploration of dynamic brain networks. We demonstrate its utility through application to graph-based functional parcellation, showing significant improvements in quantitative agreement with regions identified independently using task-based experiments and with probabilistic Brodmann areas as well as in test-retest evaluations with *in vivo* data. Simulations with known ground truth functional regions demonstrate that tNLM filtering based parcellation obtain a meaningful subdivision of the functional regions when number of desired parcels is larger than number of the ground truth regions. Related publications include [Bhushan et al., 2016, 2015a].

Chapter 7 proposes a new framework for *in vivo* microstructural sub-division of the brain by fusing information from multi-contrast MRI images and using machine learning based clustering methods. In the context of fusing information, we describe a normalization approach for orientation dependent diffusion data that appropriately reorients the diffusion data to match the local cortical geometry and allows direct comparison of the diffusion information. The preliminary use of this approach for the subdivision of brain is demonstrated in our results.

Chapter 8 concludes the dissertation with a brief discussion of the main results of the dissertation and ideas for future work that could build on these results.

Software implementation: We have implemented the methods presented in this thesis (as well as few other methods used for evaluation) in MATLAB (The MathWorks, Inc., USA) and have made the source code available to other investigators under GNU General Public License, version 2.0 from http://neuroimage.usc.edu/. The distortion correction methods are also a part of the BrainSuite software and are available as pre-compiled executable for Windows, Linux and Mac platforms from http://brainsuite.org/. Publications related to the implemented methods include [Bhushan et al., 2012, Shattuck et al., 2013a,b].

Chapter 2

Background

This chapter describes the background information that is helpful in understanding and following the approaches discussed in upcoming chapters. Sec. 2.1 briefly review the MRI signal model, which is followed by a brief description of the basic echo planar imaging (EPI) technique and intuitive explanation of different types of artifacts that occur with EPI in Sec. 2.2. Sec. 2.3 presents an in-depth understanding of the susceptibility-induced geometric distortion artifact in EPI images, which is the primary focus of chapter 4 and 5. We briefly survey different approaches for distortion correction in Sec. 2.4 in the context of neuroimaging application with particular emphasis on diffusion imaging and finish with mentioning some other artifacts in diffusion MRI in Sec. 2.5.

2.1 MRI signal model

This section presents basic details of the signal model in MRI that is required to understand the MRI artifacts discussed later. More rigorous details about MRI acquisition and reconstruction are available in Brown et al. [2014c], Liang and Lauterbur [2000], and Bernstein et al. [2004]. In conventional MRI, the acquired data is generally expressed as samples from the Fourier domain, commonly referred to as "k-space", of the object being imaged. So, the basic imaging equation for two-dimensional (2D) MRI is expressed as a 2D Fourier transform [Liang and Lauterbur, 2000]:

$$S(K_x, K_y) = \iint I(x, y)\; e^{-i2\pi(K_x x + K_y y)}\, \mathrm{d}x\, \mathrm{d}y, \tag{2.1}$$

where I is the 2D image of the object being imaged and S is the corresponding Fourier domain or k-space representation. In 2D MRI acquisition a finite number of samples are observed in the k-space of the image, *i.e.* observed data is the set of k-space samples $\{S(K_x, K_y)\}$ corresponding to a finite number of k-space locations (K_x, K_y). The most common strategy for acquiring the data in MRI is to sample the k-space locations lying on a Cartesian grid, *i.e.* $(K_x, K_y) \in \{\cdots, -\Delta K_x, 0, \Delta K_x, 2\Delta K_x, \cdots\} \times$

$\{\cdots, -\Delta K_y, 0, \Delta K_y, 2\Delta K_y, \cdots\}$, where ΔK_x and ΔK_y are the sample spacing along two k-space dimensions and $\times$ represents the Cartesian product of the two sets. Further, it also common to acquire the k-space samples in a sequential line-by-line fashion, *i.e.* first all k-space samples are acquired corresponding to a fixed K_y starting from minimum value to maximum value of K_x, which is repeated by incrementing K_y by ΔK_y and so on. The set of k-space sample acquired for a fixed value of K_y is referred to as *a line of k-space samples*. Conventionally, the direction along which the lines of k-space are acquired is referred to as the *readout* direction (here along the dimension of K_x of the Cartesian grid). Similarly, the direction orthogonal to the readout direction (along the dimension of K_y of the Cartesian grid) is referred to as the *phase encoding* direction (PED).

In MRI, the process of acquiring k-space samples at known k-space locations is achieved through use of spatially linear magnetic gradient fields $G_x(t)x$ and $G_y(t)y$ along the two dimensions of the Cartesian grid, such that the sample at the desired location (K_x, K_y) at time t is represented by

$$K_x = \frac{\gamma}{2\pi} \int_0^t G_x(t')\mathrm{d}t' \tag{2.2}$$

$$K_y = \frac{\gamma}{2\pi} \int_0^t G_y(t')\mathrm{d}t' \tag{2.3}$$

where, γ is the gyromagnetic ratio for hydrogen proton in units of radians per Tesla. In Cartesian sampling, the acquisition of one line of k-space along the readout direction is typically achieved by turning on the x-gradient while keeping the y-gradient off until the maximum value of K_x is achieved. According to above equations, the x-gradient (G_x) achieves acquisition along readout direction and, so, it is referred to as the *readout gradient*. Similarly, the y-gradient (G_y) controls the acquisition along phase encoding direction and is referred to as the *phase encoding gradient*.

As the data samples are sequentially recorded, the k-space samples are commonly represented as a function of the acquisition time t by substituting the above equations in Eq. (2.1) as [Liang and Lauterbur, 2000, Haacke et al., 1999]

$$S(t) \propto \iint I(x,y)\, e^{-i\gamma\left(x\int_0^t G_x(t')\mathrm{d}t' + y\int_0^t G_y(t')\mathrm{d}t'\right)} \mathrm{d}x\, \mathrm{d}y. \tag{2.4}$$

The desired image (I) is reconstructed from the acquired k-space samples $S(t)$ by first filling out the sampled k-space matrix $S(K_x, K_y)$ using the knowledge of eq. (2.2) and (2.3), which is followed by an inverse Fourier transform to obtain $I(x, y)$ according to eq. (2.1). Eq. (2.4) provides a very simplified model of the data acquisition with MRI and does not describe or model several other effects in main magnetic field (B_0), radiofrequency (RF) pulse (also referred to as B_1 field), gradient performance, relaxation, receiver arrays, etc. – all of which are also important for MR image generation [Bernstein et al., 2004, Haacke et al., 1999]. The simplified expression in eq. (2.4) allows easier explanations of different features of EPI, but it may not be the best data model for modern scanners.

2.2 Echo-planar imaging sequence and artifacts

Echo-planar imaging (EPI) was invented by Nobel Laureate Sir Peter Mansfield in 1977 and has been one of the most popular fast imaging technique since then [Mansfield, 1977, Stehling et al., 1991, Mansfield, 2003, Ordidge, 1999, Schmitt, 2015]. The convention MR imaging acquires each line of k-space in a separate RF excitation, which results in long scan-times [Bernstein et al., 2004]. EPI provides the capability to acquire all the lines of k-space in a single RF excitation (*i.e.* single shot), which makes it several folds faster than the conventional MR imaging[1]. EPI enables construction of a 2D image in about 60-100ms, which would have required few minutes with convention MR imaging [Stehling et al., 1991]. Mansfield's group presented the first *in vivo* human and animal EPI images in 1981 [Ordidge et al., 1981], which was closely followed by the first *in vivo* dynamic movie, using EPI, of a rabbit heart in 1982 [Ordidge et al., 1982]. EPI was first utilized for clinical application in 1983 to study high respiratory and heart rates of three children in the age range of 3-14 months [Rzedzian et al., 1983]. The interesting history of the evolution of EPI from its conception to widespread commercial use can be found in Schmitt et al. [1998, chapter 1], Cohen and Schmitt [2012] and Schmitt [2015].

The rapid collection of data by EPI sequence is particularly useful for clinical and research applications where several observations or experiments are required in a single imaging session [Stehling et al., 1991, Schmitt et al., 1998]. EPI's fast acquisition of individual MR slices also naturally allows robustness to subject motion and, at the same time, also enables the ability to observe dynamic characteristics *in vivo* [Stehling et al., 1991]. That is the reason why EPI became the imaging sequence of choice for functional, perfusion and diffusion imaging [Kwong et al., 1992, Stehling et al., 1991, Richard and Rzedzian, 1987, Schmitt, 2015, Schmitt et al., 1998, Poustchi-Amin et al., 2001]. EPI sequences have been widely used in the study of temporal neuronal activity by blood-oxygen level dependent (BOLD) contrast, also popularly referred to as functional MRI (fMRI) [Kwong et al., 1992, Stehling et al., 1991, Kwong, 1996]. Diffusion experiments also require observing several diffusion-weighted images (DWIs) sensitive along different directions, which makes EPI a natural choice for diffusion imaging [Turner et al., 1991, Stehling et al., 1991, Skare and Bammer, 2010].

EPI achieves substantial reduction in scan time, often by a factor of 10-20 times, as compared to conventional acquisition but it is more prone to artifacts than the conventional acquisition [Fischer and Ladebeck, 1998, Bernstein et al., 2004, Haacke et al., 1999, Brown et al., 2014a]. In this section, we briefly describe the basic EPI pulse sequence and different types of artifacts in EPI. We start with a short description of the rectilinear single-shot EPI (SSEPI) pulse sequence, which is sometimes also

[1] EPI has also been used for multi-shot acquisition of the k-space data, which also benefits from faster acquisition as compared to conventional acquisition [Schmitt and Wielopolski, 1998, Wielopolski et al., 1998, Andersson and Skare, 2011, Skare and Bammer, 2010, Pipe, 2014].

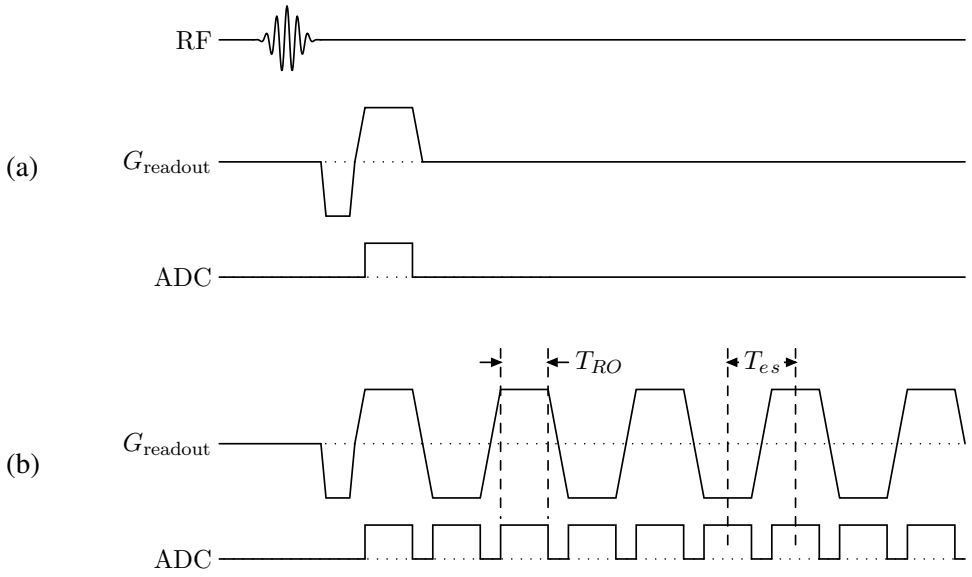

Figure 2.1: A comparison of conventional and basic EPI readout sequences. (a) shows an RF excitation pulse with conventional readout gradient. (b) Shows a simple EPI readout gradient. For both the methods, ADC shows the duration during which the data is acquired.

referred to as 'blipped EPI'. This is followed by an intuitive explanation of few artifacts in EPI including geometric distortion artifact. In addition to artifacts discussed in this chapter, EPI images are also likely to be affected by several other artifacts including low signal-to-noise ratio and spike-artifact [Macovski, 1996, Smith and Nayak, 2010, Josephs et al., 2007, spi, 2012, Haldar, 2011, Pierpaoli, 2010, Fischer and Ladebeck, 1998]. However, the methods presented in this thesis primarily focus on improving the quality of geometric distortion correction in diffusion MRI images. So, we largely assume in the remainder of the thesis that other major EPI and diffusion MRI artifacts have been reasonably addressed using state-of-the-art techniques. Further, discussions in this thesis are limited to rectilinear single-shot EPI images as it has been, and still is, the most widely used sequence for diffusion MRI [Pipe, 2014, Miller, 2014, Skare and Bammer, 2010].

2.2.1 Blipped single-shot EPI sequence

The main difference between SSEPI and conventional acquisition is that SSEPI acquires all the lines of k-space after a single RF excitation, whereas conventional acquisition requires several repeated RF excitations to acquire all the lines of the k-space [Mansfield, 1977, Stehling et al., 1991, Mansfield, 2003, Schmitt, 2015]. Figure 2.1 shows the difference between readout sequences of conventional and EPI acquisition after the RF excitation. In conventional sequence, there is just one block of analog to digital conversion (ADC) corresponding to one gradient echo, which acquires one line of k-space. In

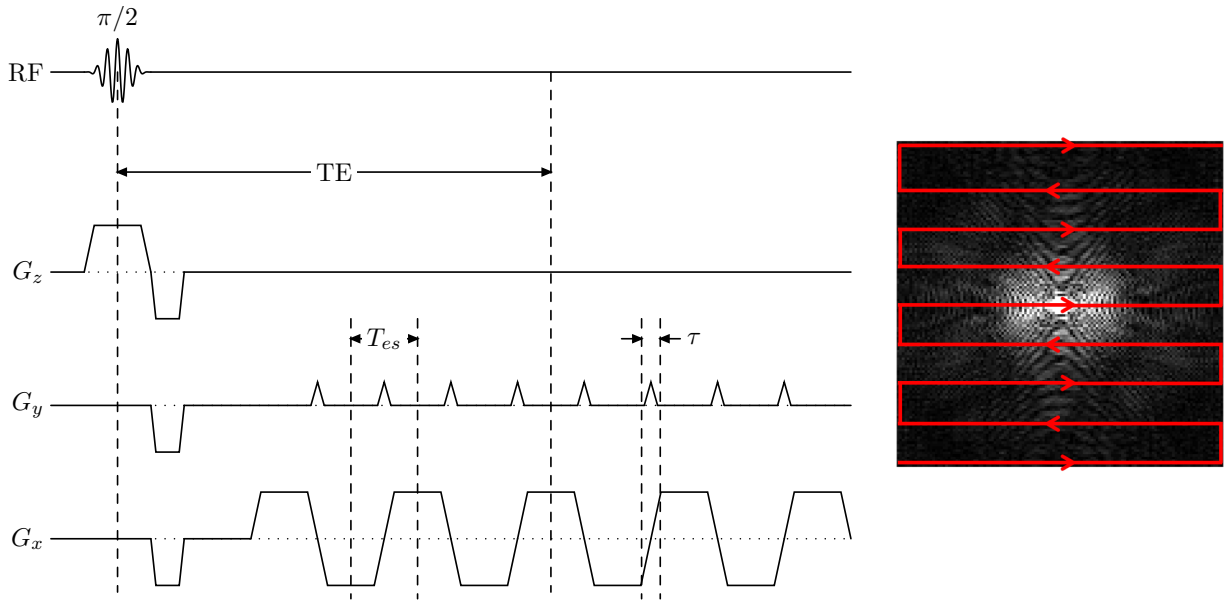

Figure 2.2: Pulse sequence for 2D blipped single-shot EPI sequence. The corresponding k-space traversal is shown on the right. Refer to text for more detailed explanation.

comparison, EPI makes use of an oscillating bipolar readout gradient with several ADC blocks, which allows multiple echos after a single RF excitation [Bernstein et al., 2004, Schmitt et al., 1998]. There are two important features that differentiate EPI readout from the conventional readout. First, the combined duration of all ADC blocks in EPI is an order of magnitudes longer than that in conventional acquisition (see Fig. 2.1), which means that data is acquired for much longer duration after each RF excitation, resulting in acquisition of much more data (or several lines of k-space) as compared to the conventional acquisition. This makes EPI substantially efficient in terms of numbers of k-space samples acquired per RF excitation, making EPI substantially faster. Second, the order of sampling of k-space data in adjacent ADC blocks is opposite due to the bipolar nature of the EPI readout gradient. In comparison, the conventional approach generally acquires all k-space sample with the same polarity of the readout gradient. These two features of EPI are the prime factors that contribute to the sensitivity of EPI images to several image artifacts.

Figure 2.2 shows the complete diagram of the 'blipped' SSEPI pulse sequence. The in-plane spatial encoding for each 2D image is achieved by use of a readout (G_x) and a phase (G_y) gradients. As described earlier, EPI uses a bipolar readout gradient to acquire the k-space lines *i.e.* the sign of G_x changes from +ve to -ve in successive lines. The location of successive k-space line is adjusted by application of a very short duration (τ) phase encoding gradient G_y. As the phase-encoding gradient turns on only for a fraction of a second, it is commonly represented by a sharp triangular shaped 'blip' in

the pulse sequence diagrams (G_y in Fig. 2.2). The k-space traversal diagram for blipped SSEPI sequence is shown in right side of the Fig. 2.2. If we ignore the ramps in the gradients switching, the k-space is traversed in a rectilinear fashion, and that is why sometimes this sequence is also referred to as 'rectilinear SSEPI'. EPI acquires several lines of k-space in a single shot and the time taken between the acquisition of successive k-space lines is called *echo spacing* (T_{es}), which is usually less than 1 ms. The bipolar gradients G_x and blipped gradient G_y are applied such that the center of the 2D k-space is sampled at the desired echo-time (TE). The total number of echos obtained after an RF excitation is called the *echo train length* and is generally equal to the number of k-space lines in the simplest SSEPI. EPI sequences are most widely used for 2D imaging [Bernstein et al., 2004, Schmitt and Wielopolski, 1998, Haacke et al., 1999, Brown et al., 2014c]. So, in general, a 3D volume is constructed by acquiring several 2D slices sequentially with SSEPI, where each of the slices is selectively excited by applying a z-gradient (G_z) of appropriate magnitude.

2.2.2 N/2 Ghost artifact

The k-space trajectory of SSEPI, shown in Fig. 2.2, shows that the adjacent k-space lines are acquired in opposite direction, which implies that the acquired k-space lines have to be time-reversed before the standard Fourier-based reconstruction. In non-ideal situations, as in the presence of eddy currents, inhomogeneous field and small timing errors in engaging the ADC, the acquired k-space lines could offset slightly from their intended true k-space location. The exact offset in the k-space locations depends on several practical factors including the polarity of the readout gradient G_x [Fischer and Ladebeck, 1998, Bernstein et al., 2004, Schmitt and Wielopolski, 1998, Brown et al., 2014a, Skare and Bammer, 2010]. As EPI acquires adjacent k-space lines with opposite gradient polarity these inconsistencies in k-space sampling location are very pronounced across adjacent k-space lines in EPI images. Such offset in k-space lines leads to phase inconsistencies in the acquired data, and when such corrupted data is reconstructed using Fourier transform, a 'ghost' image appears in the image domain that is displaced by halfway across the image. These ghost images are frequently referred to as 'Nyquist ghost' or 'N/2 ghost'. The presence of N/2 ghost can severely mislead the interpretation of the images and several approaches including phase calibration, modified sampling, interlaced reconstruction and image processing techniques have been developed to reduce the ghosting artifacts in the reconstructed EPI images [Schmitt and Wielopolski, 1998, Buonocore and Gao, 1997, Fischer and Ladebeck, 1998, Buonocore and Zhu, 2001, Bernstein et al., 2004, Skare and Bammer, 2010, Lee et al., 2016].

2.2.3 T_2^* effects

As seen in Fig. 2.1, SSEPI acquires all lines of k-space in a single shot which results in substantially longer readout time after each RF excitation as compared to conventional acquisition[2]. Acquisition of the data over a longer interval causes significant signal decay of k-space samples due to T_2^* relaxation effect [Fischer and Ladebeck, 1998]. The effect of this T_2^* relaxation is also different along the readout direction (x) and phase encoding direction (PED; y), which can be intuitively understood by observing the time intervals between sampling of the extremum k-space samples along both directions. From Fig. 2.1 we can see that the time interval between sampling extremum k-space points along the readout direction is T_{RO}. In comparison, this time interval along PED is $(N_y - 1)\, T_{es}$ (see Fig. 2.2; N_y is the total number of k-space lines), which is longer than T_{RO} by approximately a factor of N_y, as $T_{es} \approx T_{RO} + \tau$ (see Figs. 2.1 and 2.2). The T_2^* relaxation effect causes exponential decay in the signal intensity with respect to time and results into a k-space-position dependent signal demodulation. This signal demodulation can be expressed as a multiplication of the true k-space data by a window whose magnitude tapers exponentially along both readout and PED, which, however is much more severe along PED because of the longer T_2^* relaxation. Such demodulation of the k-space data results in the blurring of the reconstructed EPI image. The T_2^* blurring effect can be reduced by shortening the total acquisition time $T_{\text{Acq}} = N_y T_{es}$ (which is also roughly similar to the interval between sampling of extremum samples along PED). T_{Acq} can be shortened by shortening the T_{RO}, T_{es}, and τ as much as possible and generally would require better hardware or modified pulse sequence[3].

The T_2^* effect also causes intra-voxel dephasing of the MR signal, which could affect EPI, especially in the presence of inhomogeneous field and thick slices. The presence of local field inhomogeneity can exacerbate the intra-voxel dephasing by lowering the T_2^* relaxation time, which may cause substantial decay in the MR signal at TE resulting in very small detectable signal and is also referred to as 'signal dropout'. Signal dropout can be commonly seen around interfaces between different tissue types and can be partially addressed by using thinner slices, which could require better hardware (stronger gradients and a narrow RF bandwidth) [Fischer and Ladebeck, 1998, Bernstein et al., 2004]. Acquisition of the data with smaller TE can help in increasing the intensity of the detectable MR signal, but is not always feasible as TE also controls the desired image contrast. The pulse sequence shown in Fig. 2.2 is sensitive

[2] EPI has longer readout after each RF excitation but the total acquisition time is still substantially shorter than conventional acquisition. The primary reason is that SSEPI sequences require only one RF excitation, while conventional acquisition can require tens, or even hundreds, of RF excitations [Wielopolski et al., 1998, Bernstein et al., 2004]. The total repetition time (TR) over several excitation (which are typically in order of seconds for each excitation) is order of magnitudes longer than the increase in readout time in EPI.

[3] Multi-shot segmented EPI can also be used to shorten the echo train length (and effective T_{Acq}), but it requires more complex image reconstruction scheme and overall longer scan time (see sec. 2.4.5) [Schmitt and Wielopolski, 1998, Wielopolski et al., 1998].

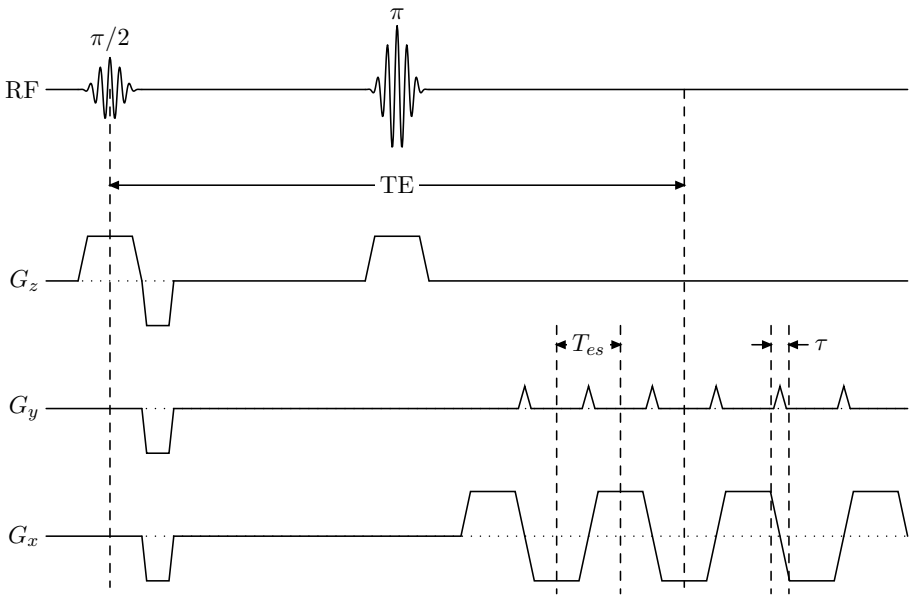

Figure 2.3: A spin echo EPI (SE-EPI) sequence. Note the 180° RF pulse at TE/2 that appears before the blipped EPI readout.

to T_2^* contrast by design and is widely used for observing BOLD signal in functional MRI scans [Stehling et al., 1991, Kwong, 1996, Schmitt, 2015]. In some applications, like diffusion MRI, it may be desirable to obtain a T_2-weighted contrast, for which the spin echo technique can be combined with EPI as shown in Fig. 2.3. Nonetheless, spin echo EPI (SE-EPI) also suffers from T_2^* blurring and intra-voxel dephasing of MR but these artifacts are less severe in SE-EPI [Wielopolski et al., 1998, Fischer and Ladebeck, 1998].

2.2.4 Low pixel bandwidth artifacts

Another effect of the long readout times in EPI is low pixel bandwidth, particularly along PED, which makes EPI sensitive to off-resonance effects [Fischer and Ladebeck, 1998]. Pixel bandwidth refers to the difference in the precession frequency of the protons between the center of the adjacent pixels (after application of the spatial encoding gradients) and is commonly expressed as the inverse of the time interval between sampling the extremum k-space samples along readout and PED[4] [Fischer

[4]The precession frequency at center of each pixel (and therefore the pixel bandwidth) is directly proportional to the strength of the applied encoding gradients [Haacke et al., 1999, Brown et al., 2014c]. Further, the strength of the encoding gradients control the time required to acquire samples in k-space. A stronger gradient lower the acquisition time as the interval between sampling of the extremum k-space samples according to eqs. (2.2) and (2.3) (assuming field of view and resolution to be the same). Hence, the pixel bandwidth is inversely proportional to the time interval between sampling of the extremum k-space samples.

and Ladebeck, 1998]. Following the discussion in the previous section, the pixel bandwidth along the readout (x) direction is expressed as $b_{RO} = 1/T_{RO}$, while that along PED is given by $b_{PED} \approx 1/T_{\text{Acq}} = 1/(N_y \times T_{es}) \approx 1/(N_y \times T_{RO}) = b_{RO}/N_y$. Hence, the pixel bandwidth along PED is lower than that along the readout direction by a factor of number of lines of k-space (N_y). Lower bandwidth causes higher sensitivity to the off-resonance effects (described below). Chemical shift artifact and geometric distortion are the two main effects of the off-resonance sensitivity in EPI [Fischer and Ladebeck, 1998, Bernstein et al., 2004, Brown et al., 2014a, Skare and Bammer, 2010].

As the precession frequency encodes the spatial location of protons in MRI, the pixel bandwidth (difference in the precession frequency between adjacent pixels) effectively controls the 'error' in the location of reconstructed signal due to the errors in the precession frequencies. The errors in the desired precession frequencies can originate because of various reasons including imperfections in the MRI system and tissue composition of the sample. The protons in water and fat are the primary sources of MR signal in the body; however most MR image reconstruction process operates at the precession frequency of water-protons. The fat-protons have a precession frequency that is 214 Hz lower than that of water-protons at 1.5 T, which introduces an error in the expected precession frequency [Haacke et al., 1999, Fischer and Ladebeck, 1998]. Let's take a typical example, where $N_y = 128$ and $T_{RO} = 0.6$ ms, then the corresponding pixel bandwidths would be $b_{RO} = 1667$ Hz and $b_{PED} = 13$ Hz. In this case, the errors in the reconstructed location of the signal coming from fat components would be $214/1667 \approx 0.13$ pixel along readout direction and $214/13 \approx 16.5$ pixels along PED. Hence, EPI acquisition of a sample containing both water and fat tissues would result in the fat signal to be *shifted* by 16.5 pixels along PED w.r.t. their true location in the reconstructed image (ignoring 0.13 pixels shift along readout direction). The resulting EPI image is an overlap of water-proton image and a shifted fat-proton image. This type of chemical composition dependent artifact is known as the chemical shift artifact. Further, this error scales proportionally with the field strength (the error in the location of reconstructed fat signal at 3 T would be twice the error at 1.5 T) and so the EPI sequences almost always make use of a water-selective excitation pulse to suppress signal from fat components [Fischer and Ladebeck, 1998, Bernstein et al., 2004, Brown et al., 2014a, Skare and Bammer, 2010].

Lower pixel bandwidth, particularly along PED, is also the prime reason for susceptibility-induced geometric distortion in EPI images. Next section describes this effect more rigorously.

2.3 Susceptibility-induced geometric distortion in EPI

In this section, we focus on the analytical understanding of the source of large geometric distortions in EPI images in the presence of imperfections in the homogeneity of the main magnetic field (B_0) over the imaging volume. Fig. 2.4 shows an example of distortion in T_2- and diffusion-weighted *in vivo*

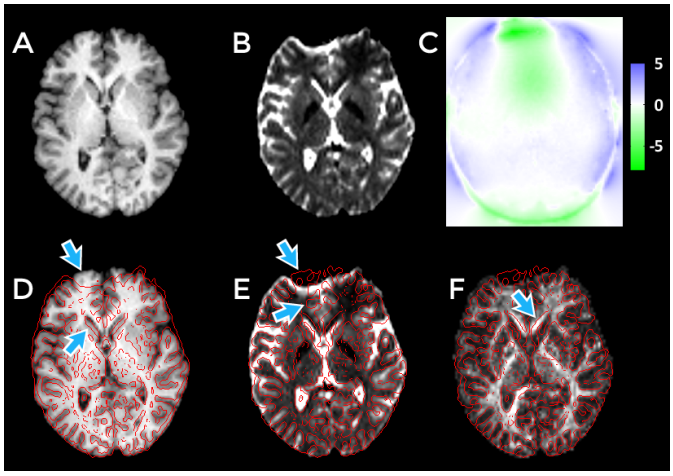

Figure 2.4: Example of distortion in a brain image acquired with EPI sequence. (A) An undistorted T_1-weighted anatomical image acquired using conventional imaging. (B) T_2-weighted image acquired with EPI (T2W-EPI) from a diffusion dataset. (C) The displacement map (in millimeters) computed from an acquired fieldmap. Edges from the T2W-EPI image are overlaid in red on the T_1-weighted image in (D) and vice-versa in (E) after rigid alignment (using INVERSION approach described in chapter 4). Arrows point to areas with substantial distortion. (F) The fractional anisotropy (FA) map derived from diffusion dataset acquired with EPI overlaid with edges from the T_1-weighted image in red.

dataset. Note that B_0 inhomogeneity can also cause some more undesirable artifacts including incorrect slice profile and exacerbated T_2^* effects – for more details see Brown et al. [2014b] and Schmitt et al. [1998].

The first source of inhomogeneity in B_0 could arise from the practical imperfection in the magnet itself due to limited length and other factors. However, the sample being imaged is usually also another source of B_0 inhomogeneity [Fischer and Ladebeck, 1998, Jezzard and Balaban, 1995]. Different regions of the imaging volume may have very different magnetic susceptibility, for example, a region with air will have different magnetic susceptibility than another region with brain tissue. This causes a change in the magnetic field (or density of the magnetic flux) near the interface of substance with different susceptibility, which is proportional to the susceptibility differences [Fischer and Ladebeck, 1998]. In the brain, areas near the frontal sinus and ear canal have such interface between air and tissue. Note that this inhomogeneity is spatially varying across the imaging volume and affects different parts of the image differently. Shimming of the main field, which adds or subtracts small magnetic field of high moments, is almost always used to reduce the inhomogeneity, but can not be entirely eliminated [Haacke et al., 1999, Fischer and Ladebeck, 1998].

Assuming homogeneous main magnetic field and ignoring any T_2 or T_2^* relaxation, the observed signal at time t after ADC is expressed by eq. (2.4) [Liang and Lauterbur, 2000, Brown et al., 2014c,

Jezzard and Balaban, 1995], which is reproduced here:

$$S(t) \propto \iint I(x,y)\; e^{-i\gamma\left(x\int_0^t G_x(t')\mathrm{d}t' + y\int_0^t G_y(t')\mathrm{d}t'\right)}\,\mathrm{d}x\,\mathrm{d}y \tag{2.5}$$

where, I is the unknown 2D image of the slice being imaged with the readout gradient along x-direction and the PED along y-direction. γ is the gyromagnetic ratio for hydrogen proton in units of radians per Tesla and $G_x(t')$ and $G_y(t')$ are the readout and phase-encode gradients respectively. In presence of a total B_0 inhomogeneity of $\Delta B_0(x,y,t)$ in units of Tesla[5], combined across external (magnet) and internal sources (sample itself), the observed signal is described by [Brown et al., 2014b, Fischer and Ladebeck, 1998, Jezzard and Balaban, 1995]:

$$S(t) \propto \iint I(x,y)\; e^{-i\gamma\left(x\int_0^t G_x(t')\mathrm{d}t' + y\int_0^t G_y(t')\mathrm{d}t' + \int_0^t \Delta B_0(x,y,t')\mathrm{d}t'\right)}\,\mathrm{d}x\,\mathrm{d}y. \tag{2.6}$$

To simplify the expression further, let's assume a uniform sampling in k-space, ignore any offset in k-space lines, ignore the ramps in the gradients (assume square gradients), assume that B_0 inhomogeneity does not change with time ($\forall t, \Delta B_0(x,y,t) = \Delta B_0(x,y)$) and assume that the observed signal $S(t)$ corresponds to discrete index (m,n) in the k-space. Then, using the pulse sequence from Fig. 2.2:

$$\int_0^t G_x(t')\mathrm{d}t' = m\,\Delta t\,G_x \tag{2.7}$$

$$\int_0^t G_y(t')\mathrm{d}t' = n\,\tau\,G_y \tag{2.8}$$

$$\int_0^t \Delta B_0(x,y,t')\mathrm{d}t' = (m\,\Delta t + n\,T_{es})\,\Delta B_0(x,y) \tag{2.9}$$

where, Δt is the time interval between sampling two adjacent k-space points, through ADC, along the readout (x) direction. Substituting above in eq. (2.6), we get

$$\begin{aligned} S(t) &\propto \iint I(x,y)\; e^{-i\gamma(m\Delta t G_x x + n\tau G_y y)}\; e^{-i\gamma(m\Delta t + nT_{\text{es}})\Delta B_0(x,y)}\,\mathrm{d}x\,\mathrm{d}y \\ &\propto \iint I(x,y)\; e^{-i\gamma m\Delta t G_x\left(x + \frac{\Delta B_0(x,y)}{G_x}\right)}\; e^{-i\gamma n\tau G_y\left(y + \frac{\Delta B_0(x,y)}{G_y}\frac{T_{\text{es}}}{\tau}\right)}\,\mathrm{d}x\,\mathrm{d}y. \end{aligned} \tag{2.10}$$

Next we use a substitution function $(x,y) = \Phi(x_e, y_e)$ to change the integration variables, with assumption of invertibility of the transforms, such that the inverse function (Φ^{-1}) maps (x,y) to (x_e, y_e), which

[5] In most of the literature the B_0 inhomogeneity map is referred to as 'fieldmap' and it is common to use the units of rad/sec (or Hz) for fieldmap [Chang and Fitzpatrick, 1992, Jezzard and Balaban, 1995, Kadah and Hu, 1998, Andersson and Skare, 2011, Andersson, 2014]. Fieldmap is generally measure by phase difference between two gradient echo images [Chang and Fitzpatrick, 1992, Jezzard and Balaban, 1995, Andersson, 2014, Nayak and Nishimura, 2000], which is equivalent to $\gamma\Delta B_0(x,y)$, where γ is the gyromagnetic ratio in units of rad/Tesla. Apart from phase differences, there are also other techniques for fieldmap estimation [Hernando et al., 2008, 2010, Nayak et al., 2001, Funai et al., 2008, Dagher et al., 2014].

are related as

$$x_e = x + \frac{\Delta B_0(x,y)}{G_x}$$
$$y_e = y + \frac{\Delta B_0(x,y)}{G_y}\frac{T_{es}}{\tau}. \tag{2.11}$$

Then by using the integration by substitution method the signal equation (2.10) can be expressed as

$$S(t) \propto \iint I(\Phi(x_e,y_e))\; e^{-i\gamma m \Delta t G_x x_e}\, e^{-i\gamma n \tau G_y y_e} \left|\frac{\mathrm{d}\,\Phi(x_e,y_e)}{\mathrm{d}(x_e,y_e)}\right| \mathrm{d}x_e\,\mathrm{d}y_e \tag{2.12}$$
$$\propto \iint I(\Phi(x_e,y_e)) \left|\frac{\mathrm{d}\,\Phi(x_e,y_e)}{\mathrm{d}(x_e,y_e)}\right| e^{-i\gamma m \Delta t G_x x_e}\, e^{-i\gamma n \tau G_y y_e}\, \mathrm{d}x_e\,\mathrm{d}y_e \tag{2.13}$$
$$\propto \iint \underbrace{I(\Phi(x_e,y_e)) \left|\frac{\mathrm{d}(x,y)}{\mathrm{d}(x_e,y_e)}\right|}_{=I_e(x_e,y_e)} e^{-i\gamma m \Delta t G_x x_e}\, e^{-i\gamma n \tau G_y y_e}\, \mathrm{d}x_e\,\mathrm{d}y_e \tag{2.14}$$
$$\propto \iint I_e(x_e,y_e)\, e^{-i\gamma m \Delta t G_x x_e}\, e^{-i\gamma n \tau G_y y_e}\, \mathrm{d}x_e\,\mathrm{d}y_e \tag{2.15}$$

where, $\left|\frac{\mathrm{d}(x,y)}{\mathrm{d}(x_e,y_e)}\right|$ is the determinant of the Jacobian of the transform $\Phi(x_e,y_e)$. Eq. (2.15) shows that the Fourier transform based reconstruction will obtain the image $I_e(x_e,y_e)$ which is related to the true unknown image $I(x,y)$ by

$$I_e(x_e,y_e) = I(\Phi(x_e,y_e)) \left|\frac{\mathrm{d}(x,y)}{\mathrm{d}(x_e,y_e)}\right|. \tag{2.16}$$

Let's consider the practical implications of the eq. (2.16) on the reconstructed EPI image. $I_e(x_e,y_e)$ represents the signal intensity at the coordinate location (x_e,y_e) of the obtained EPI image I_e. From the first part of the right-hand side of eq. (2.16), we see that the intensity in EPI image at coordinates (x_e,y_e) is related to the intensity in the original (unknown) image I at coordinates $\Phi(x_e,y_e)$. The function $\Phi : (x_e,y_e) \mapsto (x,y)$ maps the coordinates (x_e,y_e) in EPI image to the coordinates (x,y) in the original image, which is described by eq. (2.11)[6]. Eq. (2.11) shows that in the presence of non-zero inhomogeneity ($\Delta B_0(x,y) \neq 0$), the mapping between the coordinates is not an identity mapping and, hence, the geometry of the spatial locations are not preserved in EPI image (as compared to the original image). This is the source of the geometric distortion in EPI images. Further, the distortion in the geometry of the spatial location also varies spatially as $\Delta B_0(x,y)$ could be different at different locations because of the susceptibility differences. In addition to the geometric distortion, the EPI signal is also modulated by the determinant of the Jacobian term in the second part of the eq. (2.16). For example, if the map Φ results into stretching of the EPI coordinates in a local area (which means the

[6] We actually describe the inverse function (Φ^{-1}) in eq. (2.11) because it naturally follows from the change of the integration variables and is simple to describe. The expression of the forward function Φ can be more complicated to describe and is unnecessary for our purposes, as we will see later.

original coordinate was compressed to map to EPI coordinates), then the determinant of Jacobian is larger than one and results in hyper-intensity modulation in EPI images. Similarly, the compression of the EPI coordinates results into hypo-intensity modulation in EPI images.

In the above discussion, we assumed that both Φ^{-1} and Φ can be described easily. Φ^{-1} is described in eq. (2.11) in terms of ΔB_0 and other EPI parameters. Depending on the nature of ΔB_0, Φ^{-1} can be a one-to-one and onto mapping, in which case it is straightforward to describe Φ. However, in practice eq. (2.11) may not describe a one-to-one mapping (*i.e.* Φ^{-1} may be a non-injective mapping), in which case Φ is more complicated in nature and makes the correction of the geometric distortion in EPI images a non-trivial task. The implication of such a non-injective mapping is discussed in more details in section 2.4.

2.3.1 1-Dimensional approximation of EPI distortion

The distortion in 2D EPI images are commonly modeled as a 1-dimensional geometric distortion [Chang and Fitzpatrick, 1992, Weisskoff and Davis, 1992, Bowtell et al., 1994, Jezzard and Balaban, 1995, Jezzard, 2012, Andersson et al., 2003, Munger et al., 2000, Studholme et al., 2000, Andersson and Skare, 2011, Andersson, 2014, Bhushan et al., 2015b, 2014b, 2012]. Eq. (2.11) clearly shows that the mapping Φ is a 2D mapping between the coordinates and, hence, the distortion is present in both the readout and phase-encoding directions. There are two factors that differentiate the relative amount of distortion along x and y direction: the relative strength of the gradients G_x and G_y, and the ratio $\frac{T_{es}}{\tau}$ along PED. In practice, the strength of the gradients G_x and G_y are similar for blipped EPI (Eq. (2.9) and (2.11) may not hold correct for other types of EPI sequences). So, in general, the amount of distortion along the directions differ by a factor of $\frac{T_{es}}{\tau}$. From Fig. 2.2 we can see that this ratio is substantially larger than 1.0 and hence results in larger distortion along PED (y) direction. This effect is also directly related to the low pixel bandwidth along the PED as discussed in Sec. 2.2.4.

Let's consider some numbers to get the practical perspective on the amount of distortion in each encoding direction. At 3 T, gradient coils with strength $G = 25$ mT/m is commonly available and used [McNab et al., 2013a, Fischer and Ladebeck, 1998]. The bandwidth of the inhomogeneity in main magnetic field in the brain is typically around 100 Hz, which implies that for few pixels $\Delta B_0 = 100$ Hz$/(\gamma/2\pi)$ = 100/(42.56$\times 10^6$) T = 2.35 $\times 10^{-6}$ T. The echo spacing T_{es} is generally less than 1 ms and in comparison the blip duration τ is a fraction of T_{es} [Jezzard and Balaban, 1995], which gives us $\frac{T_{es}}{\tau} \approx 100$ for 128$\times$128 pixel image. Putting these values in eq. (2.11), we get a displacement of 0.094 mm and 9.4 mm along x and y, respectively. For commonly used 2 mm$\times$2 mm in-plane resolution, this translates to a displacement of approximately 0.05 and 5 pixels along readout and PED, respectively. Further, this shift depends on ΔB_0 and would typically be different at different locations and several imaging regions for the brain image can have larger displacements. Nonetheless, as seen above, the distortion along

PED is a much bigger concern than that along the readout direction. Hence, it is common to approximate the susceptibility induced distortion only along phase encoding direction, which approximates the coordinate-mapping to be a 1D mapping (see Munger et al. [2000] for a comparison with and without this approximation). The 1D approximation modifies the mapping (Φ^{-1}) between EPI coordinates (x_e, y_e) and original coordinates (x, y) as:

$$\begin{aligned} x_e &\approx x \\ y_e &= y + \frac{\Delta B_0(x,y)}{G_y}\frac{T_{es}}{\tau}. \end{aligned} \tag{2.17}$$

Under 1D approximation we get the determinant of the Jacobian as $\left|\frac{\mathrm{d}(x,y)}{\mathrm{d}(x_e,y_e)}\right| = \frac{\partial y}{\partial y_e}$, changing the relationship between the reconstructed image I_e and I to following:

$$I_e(x_e, y_e) = I\big(\Phi(x_e, y_e)\big)\frac{\partial y}{\partial y_e}. \tag{2.18}$$

2.3.2 Pixel-shift representation of EPI distortion

Eq. (2.17) describes the relationship between the EPI and original image coordinates. However, this expression may not be very useful in several clinical applications as the information about the exact values of gradient strength (G_y) and blip duration (τ) is seldom available from the MRI scanner console. We can express this with more commonly used parameters, such as pixel size and matrix size, by performing some simple mathematical manipulations. We know from Fourier reconstruction equations that spacing between k-space points along PED under square gradients assumption is given by [Liang and Lauterbur, 2000, Haacke et al., 1999]

$$\Delta k_y = \frac{\gamma}{2\pi}\int_0^{\tau} G_y(t')\mathrm{d}t' = \frac{\gamma}{2\pi}G_y\tau \implies \frac{1}{G_y\tau} = \frac{\gamma}{2\pi\,\Delta k_y}. \tag{2.19}$$

Further, from Nyquist sampling theorem we know that $\frac{1}{\Delta k_y} = L_y$, where L_y is the field of view along the y-direction (or more precisely, the spatial interval along y over which the reconstructed image repeats itself). If we define the pixel size along y as Δy and number of pixels along y as N_y, then $L_y = N_y\Delta y \implies \frac{1}{\Delta k_y} = N_y\Delta y$. Substituting this into the above equation we get:

$$\frac{1}{G_y\tau} = \frac{\gamma}{2\pi}N_y\Delta y. \tag{2.20}$$

Using eq. (2.20) in eq. (2.17), we get:

$$y_e = y + \frac{\gamma}{2\pi}\Delta B_0(x,y)T_{es}N_y\Delta y \tag{2.21}$$

$$\implies \frac{y_e}{\Delta y} = \frac{y}{\Delta y} + \frac{\gamma}{2\pi}\Delta B_0(x,y)T_{es}N_y \quad \text{(Dividing both sides by}\Delta y\text{)}$$

$$\implies \tilde{y}_e = \tilde{y} + \frac{\gamma}{2\pi}\Delta B_0(\tilde{x},\tilde{y})T_{es}N_y \quad \text{(Rewriting in terms of pixel coordinates)} \tag{2.22}$$

where, $\tilde{y}_e$ and $\tilde{y}$ represent the coordinates in the EPI and original image, respectively, in units of pixels. Hence, the pixel $(\tilde{x}, \tilde{y})$ in the original image is shifted by $\frac{\gamma}{2\pi}\Delta B_0(\tilde{x}, \tilde{y})T_{es}N_y$ pixels along the phase encoding direction due to the geometric distortion in EPI image.

2.3.3 Matrix operator representation of EPI distortion

Eq. (2.22) is a very useful expression that forms the basis of the widely used pixel-shift method [Jezzard and Balaban, 1995, Jezzard, 2012]. However, it is also desirable to express the forward model of distortion as matrix operation on the original image [Munger et al., 1998, 2000, Kadah and Hu, 1998, Andersson et al., 2003, Bhushan et al., 2013, 2014b]. The distortion correction problem is frequently an ill-posed problem, and matrix operator representation provides an opportunity to leverage a variety of advanced approaches for solving ill-posed linear inverse problems (see sec. 2.4.1 for a longer discussion). We can express the unknown original image I with a total of $N_v = N_x N_y$ pixels as a column vector $\mathbf{s}$ of length N_v. Similarly, the observed distorted EPI image I_e can be expressed as a column vector $\mathbf{d}$ of length N_v, which are related as

$$\mathbf{d} = \mathbf{D}\,\mathbf{s} \tag{2.23}$$

where, $\mathbf{D}$ is a $N_v \times N_v$ distortion matrix operator, which is constructed based on the knowledge of $\Delta B_0(x, y)$ and expresses eq. (2.18) as a single matrix operation. The matrix $\mathbf{D}$ is a highly sparse matrix because of the local nature of EPI distortion and can reflect relationship across several pixels easily, in a similar fashion as in Weis and Budinský [1990]. Note that the 1D approximation is not a requirement for the matrix $\mathbf{D}$ to be sparse, and even 2D (or 3D) modeling of the distortion could be represented as a sparse matrix operator [Kadah and Hu, 1998, Munger et al., 2000]. To obtain the corrected image $\mathbf{s}$, the linear system in eq. (2.23) can be solved using a variety of methods and can also be combined with known priors about the image [Bhushan et al., 2013, 2014b, Sutton et al., 2003, Andersson et al., 2003]. Here, we have represented the observation ($\mathbf{d}$) in the image domain, however, similar matrix operators can also be represented for the k-space data [Kadah and Hu, 1998, Weisskoff and Davis, 1992, Munger et al., 2000, Sutton et al., 2003].

2.4 Distortion correction approaches for EPI images

Section 2.3.1 and 2.3.2 provide the analytical expressions that establish the relation between the observed distorted EPI image I_e and the original (unknown) image I. Eq. (2.18) and (2.21) can be used to estimate I when all other parameters (γ, ΔB_0, T_{es}, N_y, Δy) are known and when the transformation Φ is invertible. Depending on the application or situation some of these conditions may not be satisfied. γ is the gyromagnetic ratio, which is a constant for proton and T_{es}, N_y, and Δy are all parameters of

the EPI acquisition itself, which are known. However, ΔB_0 is the field inhomogeneity map which can not be retrieved from a single arbitrary EPI image and generally requires additional image acquisition [Jezzard and Balaban, 1995, Jezzard, 2012, Andersson and Skare, 2011]. Several approaches have been developed for distortion correction[7] of EPI images and most of the approaches, and their respective correction quality, differ in the type of modeling and additional information that is used for the correction. The additional information could be an accurate knowledge of the fieldmap (through additional image acquisition) and/or prior knowledge about different characteristic of the image. In this section, we briefly describe some commonly used approaches to correct distortion in EPI images.

It should be noted here that eq. (2.10) and all other expressions derived from it, in this chapter and forthcoming chapters, are describing the relationship between complex-valued images (both distorted and undistorted). However, methods described here and in next chapters do not explicitly use the phase information from the complex-valued images as only magnitude images are available or used in most applications. Nonetheless, the use of complex-valued images provides additional phase information, which can be used to apply additional constrains for improved distortion correction [Gai et al., 2013, Sutton et al., 2003].

2.4.1 Pixel-shift method

When the fieldmap ($\gamma\Delta B_0$) is known, then it is straight forward to use eq. (2.18) and (2.21) to estimate undistorted image $\widehat{I}$ from distorted I_e, such that

$$\widehat{I}(x,y) = I_e\Big(\Phi^{-1}(x,y)\Big)\left.\frac{\partial y_e}{\partial y}\right|_{x,y}. \tag{2.24}$$

From eq. (2.17) and (2.21) we get $\Phi^{-1}(x,y) = \left(x, y + \frac{\gamma}{2\pi}\Delta B_0(x,y) T_{es} N_y \Delta y\right)$ and

$$\begin{aligned}\frac{\partial y_e}{\partial y} &= 1 + T_{es} N_y \Delta y \frac{\partial}{\partial y}\left(\frac{\gamma}{2\pi}\Delta B_0(x,y)\right)\\ &= 1 + T_{es} N_y \Delta y \frac{\mathrm{d}}{\mathrm{d}y}\left(\frac{\gamma}{2\pi}\Delta B_0(x,y)\right).\end{aligned} \tag{2.25}$$

Substituting these in previous equation we get the final expression of the estimated undistorted image $\widehat{I}$

$$\widehat{I}(x,y) = I_e\left(x, y + \frac{\gamma}{2\pi}\Delta B_0(x,y) T_{es} N_y \Delta y\right)\left(1 + T_{es} N_y \Delta y \frac{\mathrm{d}}{\mathrm{d}y}\left(\frac{\gamma}{2\pi}\Delta B_0(x,y)\right)\Bigg|_{x,y}\right). \tag{2.26}$$

[7] In some clinical applications, it may not be critical to correct the images for distortion as large structures such as a quadrant of the brain could be the region of interest and the diagnostic interpretation would be unlikely to change due to presence of distortion in such a large region.

Above equation can also be modified, in similar fashion as eq. (2.22), to completely operate in the pixel-coordinates of the images for computational convenience:

$$\widehat{\tilde{I}}(\tilde{x},\tilde{y}) = I_e\left(\tilde{x},\tilde{y}+\frac{\gamma}{2\pi}\Delta B_0(\tilde{x},\tilde{y})T_{es}N_y\right)\left(1+T_{es}N_y\,\frac{\mathrm{d}}{\mathrm{d}\tilde{y}}\left(\frac{\gamma}{2\pi}\Delta B_0(\tilde{x},\tilde{y})\right)\Big|_{\tilde{x},\tilde{y}}\right). \tag{2.27}$$

It should also be noted here that the fieldmap ($\gamma\Delta B_0$) in all above equations is assumed to be available in the correct/undistorted coordinates. Fieldmap is generally measured by a phase difference between two gradient echo images, which, unlike EPI images do not suffer from severe geometric distortion artifact [Andersson and Skare, 2011, Chang and Fitzpatrick, 1992, Jezzard and Balaban, 1995].

The pixel-shift representation in eq. (2.27) provides a simple and valuable analytical relationship which has been, and still is, widely used along with linear interpolation for distortion correction of EPI images [Weisskoff and Davis, 1992, Jezzard and Balaban, 1995, Jezzard, 2012, Andersson and Skare, 2011, Andersson, 2014, Studholme et al., 2000, Bhushan et al., 2015b, 2012, Pierpaoli et al., 2010]. However, there is an important implicit assumption made in this approach: the mapping between EPI and original coordinates is invertible, *i.e.* Φ and Φ^{-1} form a bijection. Unfortunately, this might not always be true. It is common for EPI brain images to have large distortions around the frontal sinuses and ear canal, which results in a mapping where several voxels in original image maps to 1-2 voxels in EPI image resulting in compression of information from several *true* voxels into few *observed* voxels. This causes the mapping to be non-invertible (*i.e.* many-to-one mapping – the classic case of an ill-posed problem) that can make eq. (2.27) unstable and inaccurate [Andersson et al., 2003, Jones and Cercignani, 2010]. This can be appreciated easily when the distortion correction problem is posed in matrix form, as described in sec. 2.3.3 [Munger et al., 1998, 2000, Andersson et al., 2003, Andersson, 2014].

Another factor that could limit the accuracy of correction using the pixel-shift method with linear interpolation is its 'perceived' raster nature [Weis and Budinský, 1990]. The original sample being imaged is continuous objects and hence the original image I is also a continuous image. Acquired EPI images are acquired at a finite resolution (generally 2-6 mm isotropic in-plane resolution), which provides approximately the ensemble of intensities in a pixel/voxel of the continuous image. The pixel-coordinates represents the center location of the pixel/voxel, which may not be sufficient to describe the full physical phenomenon of the distortion. Consider a situation when there is a large stretching in the geometry of the original image's coordinate locations due to EPI distortion. In this scenario, the signal from, say 2 pixels, would stretch to a larger number of pixels, say 20 pixels. For correction of these 2 pixels, the pixel-shift method [Jezzard and Balaban, 1995, Jezzard, 2012] with linear interpolation under 1D assumption would only make use of at most 4 pixels, which could be highly inaccurate.

The matrix representation, as described in sec. 2.3.3, allows the modeling of these types of effects

easily and accurately, where the distortion corrected image can be obtained by

$$\widehat{\mathbf{s}} = \mathbf{D}^{+}\mathbf{d} \tag{2.28}$$

where $\mathbf{D}^{+}$ is the Moore-Penrose pseudoinverse of $\mathbf{D}$. For well-posed problems, in the absence of any rasterization effects, both eq. (2.28) and (2.26) should produce the same results. See Weisskoff and Davis [1992] for a comparison of the pixel-shift and matrix operator method and Weis and Budinský [1990] for a detailed discussion about the continuous and raster interpolations.

In practice, the distortion correction problem (eq. (2.23)) may not be well-posed as the mapping between EPI and original coordinates described by eq. (2.17), could be a non-injective mapping. This causes the solutions of eq. (2.28) or (2.26) to be inaccurate or unreliable, in regions with non-injective mapping of the coordinates [Chang and Fitzpatrick, 1992, Andersson et al., 2003, Jones and Cercignani, 2010].

2.4.2 Reversed gradient method

The reversed gradient (RG) method addresses the ill-posed nature of the distortion-correction problem by using additional acquisitions to collect more information about the original image [Chang and Fitzpatrick, 1992, Bowtell et al., 1994, Andersson et al., 2003, Morgan et al., 2004, Holland et al., 2010, Embleton et al., 2010, Gallichan et al., 2010]. The main idea of RG method originates from the observation that if the polarity of the phase encoding blips is reversed in Fig. 2.2 then the direction of distortion (under 1D approximation) is also reversed. This observation can be explained by noticing the effect of the polarity of G_y in eq. (2.17). The RG method uses two EPI images with reversed phase encoding blips to estimate the undistorted image. This can be easily understood with matrix notations, but has been described and implemented in variety of ways (Eg. using line integrals and conservation of total integral in [Chang and Fitzpatrick, 1992, Bowtell et al., 1994, Morgan et al., 2004, Embleton et al., 2010]). Two "reversely" distorted images, $\mathbf{d}_{+}$ and $\mathbf{d}_{-}$, are acquired using the reversed phase encoding blips, such that the respective distortion matrix operators are $\mathbf{D}_{+}$ and $\mathbf{D}_{-}$ (subscripts denote the polarity of the blips). Then the undistorted image $\mathbf{s}$ can be estimated by solving the linear system:

$$\begin{bmatrix}\mathbf{d}_{+}\\ \mathbf{d}_{-}\end{bmatrix} = \begin{bmatrix}\mathbf{D}_{+}\\ \mathbf{D}_{-}\end{bmatrix}\mathbf{s}. \tag{2.29}$$

The RG method has one clear benefit – it uses two observations with different distortion matrices, and hence this linear system should be better posed than eq. (2.28) or (2.26) that generally obtains much better results than pixel-shift method [Bhushan et al., 2014b, 2013, Holland et al., 2010]. Another benefit of RG method is that the fieldmap can be estimated from $\mathbf{d}_{+}$ and $\mathbf{d}_{-}$ itself, dropping the requirement for an additional acquisition for fieldmap [Ruthotto et al., 2012, Holland et al., 2010, Morgan et al., 2004,

Bowtell et al., 1994, Andersson et al., 2003]. However, it should be noted that the RG method requires twice the number of EPI images as compared to the previous approaches, which could be limiting in some situations as the time required in acquiring twice the set of images could be much longer than the scan-time required for the fieldmap. Gallichan et al. [2010] proposed using a dual-echo approach to collect RG data where the second echo has reversed phase-encoding blips, so that the increase in scan time is modest (much lower than two-times). However, as the TE is different for both the echo, the second echo has larger T_2 weighting (*i.e.* different contrast) and lower SNR, which make the fusion of the information from two RG images challenging and non-trivial. Note that eq. (2.29) assumes that the same undistorted (unknown) image $\mathbf{s}$ is observed using two different distortion operators. Hence, RG is very challenging to apply in applications where the data is temporal in nature *i.e.* the information in the images is constantly changing with time, for example in fMRI experiments.

As described above, the conventional RG method uses images acquired with two different PEDs. However, the idea can be generalized to acquire images with more than two PEDs, at the cost of even longer scan time, to obtain much more accurate correction. For example, we use four different PED to obtain the reference images for comparison of different distortion correction methods in chapter 5. In particular, we obtain four differently distorted images, $\mathbf{d}_L, \mathbf{d}_R, \mathbf{d}_A$ and $\mathbf{d}_P$, with corresponding distortion matrices $\mathbf{D}_L, \mathbf{D}_R, \mathbf{D}_A$ and $\mathbf{D}_P$, which is used obtain the corrected image by solving the linear equation

$$\begin{bmatrix} \mathbf{d}_L \\ \mathbf{d}_R \\ \mathbf{d}_A \\ \mathbf{d}_P \end{bmatrix} = \begin{bmatrix} \mathbf{D}_L \\ \mathbf{D}_R \\ \mathbf{D}_A \\ \mathbf{D}_P \end{bmatrix} \mathbf{s} \tag{2.30}$$

where, subscripts L, R, A and P represents the phase encoding along Left-to-right, Right-to-left, Anterior-to-posterior, and Posterior-to-anterior, respectively (phase encoding and readout direction are swapped on the 2D plane to change PED from left-right to anterior-posterior). We refer to the corrected image thus obtained using 4 phase-encoded images as "4-PED full". In chapter 5, we present an interlaced q-space sampling scheme for diffusion MRI, which is a novel sub-sampling scheme for RG method that does not increase the scan-time at all as compared to the original acquisition while improving the quality of distortion-correction to that of RG method [Bhushan et al., 2014b, 2013].

2.4.3 Registration based approaches

Registration based methods are useful in applications where the fieldmap is not acquired, but other undistorted high-resolution anatomical images[8] are acquired. Several neuroimaging studies do not ac-

[8]Note that the anatomical images can also be affected by several artifacts, including susceptibility and gradient non-linearity, leading to the distortion of the images along all the three dimensions [Brown et al., 2014b, Jovicich et al., 2006], Bernstein

quire the fieldmap for a variety of reason such as lowering the scan time, but almost always acquire a high-resolution T_1- or T_2-weighted anatomical image. Registration-based approaches estimate the unknown fieldmap in a non-rigid image registration framework by making use of the undistorted T_1- or T_2-weighted anatomical image. In this framework the EPI image is undistorted with an estimated fieldmap (using eq. (2.26)) such that the similarity between the anatomical image and undistorted EPI image is maximized – *i.e.* in image-registration jargon, a deformation field is estimated using the anatomical image as the registration template while EPI image is warped according to eq. (2.26) to maximize the similarity between the two images [Kybic et al., 2000, Studholme et al., 2000, Irfanoglu et al., 2011, Tao et al., 2009, Huang et al., 2008, Bhushan et al., 2015b, 2012]. As compared to the classical image-registration there are two key difference in this approach that should be addressed before using an *off the shelf* image registration tool for this purposes. First, the deformation field, which is estimated by registration, should be constrained to only deform the EPI image along PED, as argued in Sec. 2.3.1[9]. Second, the un-warping of EPI should follow the physics of distortion *i.e.* the un-warping of EPI images should also apply the Jacobian modulation as in eq. (2.18). It should be noted here that in most applications, the contrast of anatomical image and EPI will not be identical, and so these approaches should have the robustness to contrast differences. Several registration-based methods have been developed for this purpose, and they differ in some of the choices they make: the contrast of anatomical image, the nature of the similarity metric, parameterization of the deformation field, the regularization model and the optimization metric [Kybic et al., 2000, Studholme et al., 2000, Irfanoglu et al., 2011, Tao et al., 2009, Huang et al., 2008, Bhushan et al., 2015b, 2012, Gholipour et al., 2006, Yao and Song, 2011, Ardekani and Sinha, 2005, Pierpaoli et al., 2010, Wu et al., 2008] (also see discussion in [Andersson and Skare, 2011, Andersson, 2014]). A more detailed discussion and review of registration-based methods are included in chapter 4.

It is useful to be aware of the relative performance of the two class of distortion corrections methods, registration-based and fieldmap-based, with *in vivo* images. Fig. 2.5 shows an example of correction using different approaches on an *in vivo* image, where distortion-corrected EPI images are overlaid with edges obtained from the high-resolution T_1-weighted anatomical image. The overlay images show that all corrected images have similar alignment of anatomical structures, however, there are some dif-

et al. [2004, Chapter 13]. However, the size of distortion in anatomical images acquired using conventional scheme is order of magnitudes smaller than that in EPI images in most cases [Brown et al., 2014b], Bernstein et al. [2004, Chapter 13]. Hence, in practice the anatomical images act as a good undistorted template.

[9]It can argued that 1-dimensional approach is an approximation and so the deformation field should be allowed to un-warp along both direction. However, the distortion along readout direction is typically in range of 1/20th of a voxel and in our experience allowing flexibility along both directions results into much lower quality of correction. In our opinion, 2D non-rigid registration shows such behavior because of the ill-posed nature of problem and so is more stable with 1D constraints. Also, vast majority of registration based distortion correction methods use 1D constrain (see chapter 4 and its references).

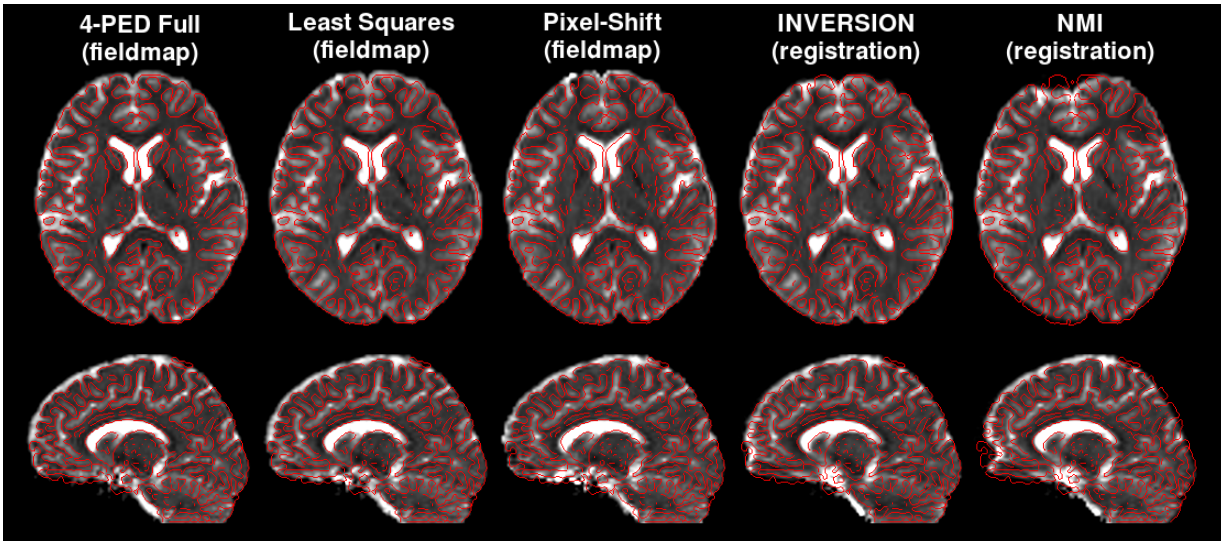

Figure 2.5: Qualitative examples of distortion corrected *in vivo* images with different fieldmap- and registration-based methods. Each column shows (top) an axial and (bottom) a sagittal slice of the distortion-corrected T_2-weighted EPI image using a particular method. All images are overlaid by edges from the anatomical T_1-weighted image in red. The original distorted T_2-weighted EPI is not shown. NMI is an acronym for normalized-mutual information [Studholme et al., 1999] and INVERSION is a registration method introduced in chapter 4. See text for more description.

ferences. It can be noticed that edges align better with anatomical information for images corrected with fieldmap-based methods (first three columns) as compared to registration-based methods (last two columns). This is expected since the fieldmap-based methods already have access to the information about the non-uniformity of the magnetic field. In contrast, registration-based methods estimate this information from the image registration process. Among fieldmap-based method, 4-PED full shows substantially better alignment than others as it uses 4-times more information than others (see eq. (2.30)) and can be practically used as a comparison reference for other methods. Least-squares and pixel-shift corrected images are obtained by solving eq. (2.28) and (2.27), respectively. As discussed in Sec. 2.4.1, we notice that least-squares approach shows better correspondence to anatomical edges than pixel-shift method, most likely due to the more accurate modeling of image distortion with the matrix representation. Among registration-based approaches, normalized mutual information (NMI) based method shows a poor performance in areas with severe distortion as can be seen in frontal areas of the brain, most likely due to challenges with optimization of the non-smooth NMI cost function (see chapter 4 for a detailed discussion). INVERSION (Inverse contrast Normalization for VERy Simple registratION) is a novel method based on the use of the simpler sum of squared differences cost function, that robustly aligns T_1- and T_2-weighted images by leveraging known contrast relationships between these two contrast in the

brain [Bhushan et al., 2015b, 2014a] (also see chapter 4). Note that we do not show exhaustive results for all fieldmap- or registration-based methods reported in the literature. However, Fig. 2.5 shows the representative qualitative performance of few of the approaches and could be useful for guiding the design of acquisition protocols for future studies.

2.4.4 Point spread function based approach

Point spread function (PSF) mapping methods use an estimate of the PSF at each pixel/voxel in the image for distortion correction [Chung et al., 2011, Zaitsev et al., 2004, Zeng and Constable, 2002, Robson et al., 1997]. The PSF at each pixel is mapped by acquiring several reference EPI scans, with additional phase encoding gradients [Robson et al., 1997, Zaitsev et al., 2004]. The PSF captures the effect of inhomogeneity which, unlike fieldmap, can be directly applied to the k-space data without the need for any phase unwarping and result in good distortion correction [Chung et al., 2011, Zeng and Constable, 2002]. However, the main limiting factor of PSF based approach is the requirement of several additional reference scans – for an ideal 1D PSF mapping along PED of a $N_x \times N_y$ image, N_y reference scans are required, resulting in N_y-fold increase in scan time (although some effort has been made to reduce scan time [Zaitsev et al., 2004, Zeng and Constable, 2002]). Another important factor is that the estimated PSF cannot be easily shared across images with different contrasts (even in case different images suffer from same inhomogeneity artifact) as the PSF is sensitive to phase changes and would require separate PSF mapping for each fMRI frame or diffusion-weighted image, making it impractical for these applications. See Andersson and Skare [2011] for a detailed discussion of these methods in the context of diffusion MRI.

2.4.5 Pulse sequence based approaches

There are several approaches that reduce EPI artifacts, including geometric distortion, by modifying the EPI pulse sequence to reduce the effective echo spacing (T_{es}) and acquisition time (T_{Acq}) [Andersson and Skare, 2011, Skare and Bammer, 2010, Pipe, 2014, Wielopolski et al., 1998]. Probably the most effective among these is the use of parallel imaging in conjunction with EPI, which can reduce the T_{Acq} approximately by a factor of, say, R by only acquiring every R^{th} k-space lines [Skare and Bammer, 2010]. It introduces an aliasing along PED that can be un-aliased by using the multi-channel information with techniques like SENSE and GRAPPA [Deshmane et al., 2012, Skare and Bammer, 2010]. The effective reduction in T_{Acq} helps to increase the bandwidth along PED and reduces several artifacts by a factor of R (geometric distortion, eddy current distortion, T_2^* effects, chemical shift). See Fig. 12.7 in Skare and Bammer [2010] for an example of parallel imaging that reduces the chances of misdiagnosis in an acute stroke patient. Similar to several parallel imaging techniques, this may also require the

acquisition of calibration scans, which can be achieved without large penalty on the total scan time. Another added advantage of using parallel imaging is that it can reduce the EPI scan time even further, allowing acquisition of more slices in the same overall repetition time.

Similar to parallel imaging, interleaved EPI increases the effective bandwidth along PED by only acquiring every R^{th} k-space lines after each RF excitation [Wielopolski et al., 1998, Schmitt and Wielopolski, 1998]. Interleaved EPI is different in the sense that it fills up the missing k-space lines by acquiring those lines in consecutive RF excitations [Wielopolski et al., 1998, Schmitt and Wielopolski, 1998]. This results in set of R interleaved k-space data, which are put together for reconstructing the EPI image – this, however, requires the tough task of matching the phases of different shots, which is done by acquiring an additional set of navigator scans [Skare and Bammer, 2010, Wielopolski et al., 1998]. A small mismatch of the phase information results in the appearance of several ghosts in the reconstructed image (similar effect to Nyquist ghosts) and may render the image useless [Skare and Bammer, 2010]. Interleaved EPI also needs longer scan times than SSEPI due to the requirement of several repeated acquisitions.

Another similar set of methods makes use of multi-echo segmented EPI approach, where a smaller segment of the k-space is acquired during each echo, which can reduce T_{es} for each segment [Andersson and Skare, 2011, Skare and Bammer, 2010, Pipe, 2014]. The short-axis readout propeller EPI (SAP-EPI) [Skare and Bammer, 2010] and Readout-segmented EPI (RS-EPI) [Pipe, 2014] are two such approaches. RS-EPI acquires the k-space segments along the readout direction while SAP-EPI acquires the segments in a propeller fashion (radially outward from the center of the k-space). SAP-EPI has an advantage that it acquires the center of the k-space in each segment and so is more robust for the correction of phase differences across segments without additional scans. RS-EPI, on the other hand, needs a navigator scan to help correct phase differences in each segment. Both methods achieve a substantial reduction in distortion and enable high-resolution imaging, however, requires much longer scan times than SSEPI due to the repeated acquisitions.

There are few more tricks to lower distortion in EPI images [Skare and Bammer, 2010, Wielopolski et al., 1998]. Another trick is to use *ramp sampling*, which samples the data also during the gradient ramps (so ADC would also be triggered during ramp in Fig. 2.1). This allows to shorten the total duration of readout gradients (T_{RO}) [Skare and Bammer, 2010], however this requires either non-uniform triggering of ADC during the ramp or re-gridding of k-space samples or both to get equidistant sampled k-space data, suitable for Fourier-based reconstruction [Schmitt and Wielopolski, 1998, Wielopolski et al., 1998]. See Fig. 12.15 in Skare and Bammer [2010] for an example of the effect of ramp sampling. Another approach, if possible, could be to get better hardware capable of higher gradient strength and faster slew rate (the rate at which gradient strength can be changed) [Fischer and Ladebeck, 1998]. Higher gradient strength directly lowers the distortion (eq. (2.11)), and faster slew rate lowers the time spent during the ramps – combination of both of them further lowers the total readout time (T_{RO}, T_{es} and T_{Acq}) reducing

several of the EPI artifacts. However, faster slew rate can also induce a larger eddy current resulting in larger eddy current distortion (see sec. 2.5.1).

It should be noted here that, in practice, a combination of several of these tricks and techniques, such as ramp sampling, parallel imaging, etc., are employed in clinical and research scans. This improves the image quality substantially, however, does not eliminate the artifacts, and images may still need additional artifact correction step for accurate analysis and interpretation.

2.5 Other artifacts in diffusion MRI

We described several artifacts in EPI image in previous sections of this chapter. EPI sequence is widely used for diffusion MRI experiments owing to EPI's fast image acquisition [Pipe, 2014, Miller, 2014, Skare and Bammer, 2010]. Diffusion MRI also suffers from some additional artifacts that are unique or more pronounced due to diffusion encoding [Pierpaoli, 2010, Jones and Cercignani, 2010, Skare and Bammer, 2010]. In this section, we briefly describe two common artifacts with diffusion MRI

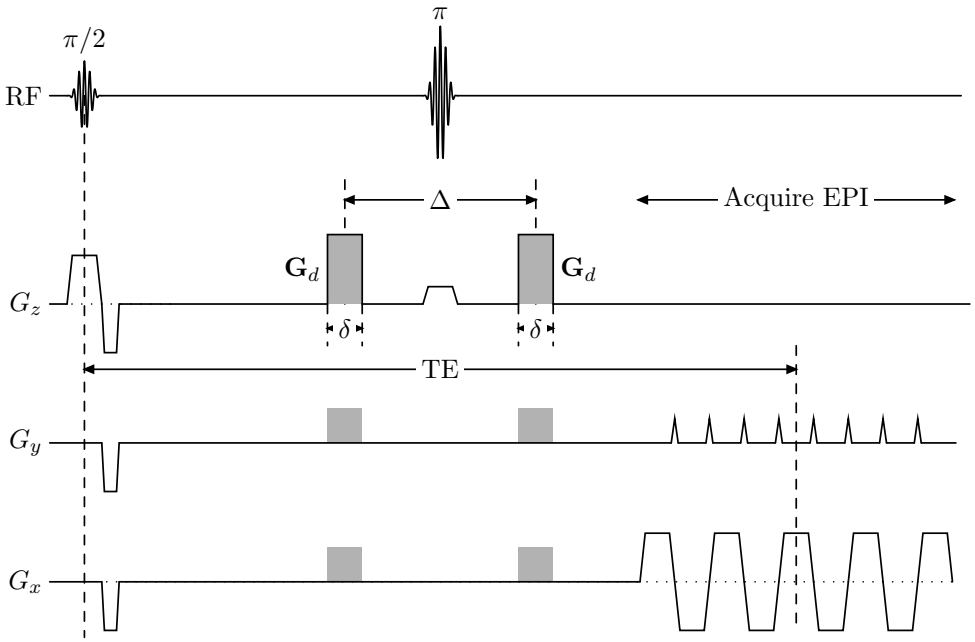

Figure 2.6: Conventional 'Stejskal-Tanner' spin echo pulse sequence for diffusion MRI. It is similar to spin echo EPI sequence shown in Fig. 2.3 with the addition of diffusion sensitization gradients, which are shown here as shaded gradients. The physical direction of the diffusion sensitivity in 3D can be adjusted by appropriately setting the G_x, G_y and G_z gradient in the shaded part, the vector sum of which is shown here as $\mathbf{G}_d$. Δ is the diffusion time – the interval over which protons are allowed to diffuse before observing their effect on the signal. δ is the time interval during which the diffusion sensitization gradients are turned on.

that are caused due to eddy current and subject motion. Note that there are a number of other artifacts that are also important to consider such as physiological noise (e.g., cardiac pulsation induced) [Pierpaoli, 2010], phase errors due to motion during diffusion encoding [Bammer et al., 2011], mechanical vibration [Yadav et al., 2011] etc., but are not described in this section (also see [Pierpaoli, 2010, Jones and Cercignani, 2010], [Jones, 2011, Section III]).

It is helpful to understand the basic nature of diffusion MRI experiment to fully appreciate the consequences of these artifacts on the interpretation of the diffusion data. Fig. 2.6 shows the conventional 'Stejskal-Tanner' spin echo pulse sequence, which encodes the diffusion processes along one direction $\mathbf{G}_d$. To gather the diffusion information in 3D, the diffusion MRI experiment generally acquires several of such EPI images by repeating the acquisition with unique $\mathbf{G}_d$ in each repetition (for more details see: Turner et al. [1991], Turner [1998], Pipe [2014] and Jones [2011]). Hence, the diffusion data consists of several 'diffusion-weighted' EPI images, each of which is a T_2-weighted spin echo image which is further weighted by the diffusion properties along a particular direction $\mathbf{G}_d$.

2.5.1 Eddy current induced distortion

As seen in Fig. 2.6, diffusion sequence heavily uses the gradient to achieve diffusion and spatial encoding. Such rapid change in magnetic field also induces a small electric current, referred to as eddy-current (EC), in the nearby conductor and coils, which in turn induces another small magnetic field gradients. These EC-induced gradients can be expressed as another set of inhomogeneity in the B_0 field which results in distortion with same principals as that described in sec. 2.3 (another interpretation could be that these EC-induced gradients are set of undesired spatial encoding gradients that affect the way k-space samples are collected). Under the simplistic assumption that these eddy currents are small and constant over the data acquisition, the reconstructed images are 'distorted' in relatively simpler fashion. EC-induced gradients along different directions affect the images differently – xy-shear (EC-induced gradients along readout x), compression/stretching along y (EC-induced gradients along phase encoding) and slice dependent y-shift (EC-induced gradients along z) [Andersson and Skare, 2011, Skare and Bammer, 2010]. In practice, it is a combination of all three of these, and so the EC-induced distortion is commonly parameterized by three parameters of a simple affine transformation for each EPI image, which are generally estimated using image registration approaches [Andersson and Skare, 2011, Pierpaoli, 2010, Skare and Bammer, 2010].

The nature of the exact set of EC induced in the coils would depend on the set of gradients which were used before the EPI readout. From Fig. 2.6 we can see that diffusion gradients are used immediately before the EPI readout, hence, the diffusion gradients will have the largest effect on the induced EC gradients. As the diffusion experiment, by design, uses different diffusion encoding gradients at each repetition, the EC induced distortion will also be different for each diffusion-weighted image. This can

cause different diffusion-weighted images to misalign (even if there was no subject motion) and can introduce inaccuracy when all diffusion-weighted images are combined for further analysis and processing without an EC correction step. EC-induced distortion is commonly corrected by using a registration-based approach, where each diffusion-weighted image volume is linearly aligned (affine transformation) to a common template (a volume without any diffusion weighting is a common choice) [Pierpaoli, 2010]. However, two things should be noted in the context of EC correction: First, the distortion depends on the location of the slice and the order in which the slices were acquired, and second the distortion can also cause intensity modulation due to stretching and compression [Jones and Cercignani, 2010]. Hence, the commonly used EC correction approach of a single affine transformation for each diffusion-weighted volume may not be sufficient or accurate (see Jones and Cercignani [2010] for detailed analysis of these effects). Further, EC-induced gradients can also affect the diffusion weighting gradient as there could be some residual EC from an earlier set of gradients, effectively introducing error in the desired diffusion weighting, which is not easy to correct using image processing methods [Pierpaoli, 2010].

An improved hardware design and use of advanced pulse sequences is generally more effective in minimizing eddy current effects. The split diffusion-weighting gradients with twice RF refocused pulses is a very effective way to substantially reduce the EC induced distortion in diffusion-weighted images with a small decrease in the efficiency [Pipe, 2014, Reese et al., 2003, Skare and Bammer, 2010].

2.5.2 Subject Motion

Diffusion MRI scans can require long scan time depending on the application, and it may not always easy for the subject to maintain a rigid posture, especially for unhealthy subjects. As diffusion MRI are almost always acquired using SSEPI, the result of subject motion is different from the conventional acquisition. SSEPI is very fast 2D imaging technique, so most subject motion do not corrupt the 2D image itself, but it may result in misalignment of different 2D slices and different diffusion-weighted images. Further, the desired diffusion encoding can also be affected, as the relative direction of diffusion sensitization gradients changes due to the subject motion. This could be corrected by appropriately applying the rotation (estimated from subject motion correction) to the diffusion encoding direction before further analysis [Jones and Cercignani, 2010]. When the subject motion is low, different diffusion-weighted images may appear out of alignment and can generally be corrected by a rigid alignment with 6 degrees of freedom. However, the choice of registration similarity measure can be very challenging as different diffusion-weighted images are sensitive to diffusion along different directions and can have very different contrast [Pierpaoli, 2010]. This can be partially addressed by interleaving several volumes without any diffusion weighting (which will have T_2-weighted contrast acquired with EPI; T2W-EPI) in the diffusion sequence and using the displacement parameters, under smooth motion assumption, estimated by co-registering these T2W-EPI images (which is easier as they all will have same contrast)

[Pierpaoli, 2010].

When the subject motion is large, as frequently in the case of fetal examination and in subjects with medical conditions such as Parkinson's, then the motion correction becomes more challenging because different slices of the same diffusion-weighted images may not align well. Further, the slice orientation may also change from one slice to other, and some areas of the imaging region may be acquired multiple times while other areas may go unobserved. Jiang et al. used a slice to volume registration approach to address such motion correction, where individual diffusion-weighted slices were registered to a reference 3D volume acquired using a multislice snapshot imaging [Jiang et al., 2009, 2007a,b]. Diffusion encoding directions were also corrected for individual slices and the aligned diffusion-weighted images were sampled in the coordinate location of the reference 3D volume. To address the possibility of the missing data, authors over-sampled the imaging region by repeating the diffusion scan 3-4 times with different diffusion encoding gradients, which increased the chances of sampling almost all the regions at least once [Jiang et al., 2007a].

Chapter 3

Review: Parcellation of the cerebral cortex

In this chapter, we review several approaches that have been used to study and map the microstructural organization of the brain. Section 3.1 reviews early histological approaches to studying and parcellating the brain, while section 3.2 reviews recent non-invasive approaches using MRI to obtain similar parcellations *in vivo*.

3.1 Brief history of architectonic mapping

Brain biochemistry, electrical properties, structural organization and connectivity have all been studied for the purposes of improving our understanding of how the brain works. These studies range across scales from molecular and single cell studies through mesoscale studies of groups of neurons to the whole brain and system-level models [Swanson, 2012, Arbib, 2002, Swanson and Bota, 2010, Pechura and Martin, 1991, Bear et al., 2007]. One important avenue of research is that of the structure of the cerebral cortex, the outermost layer of the cerebrum [Amunts and Zilles, 2015, Zilles and Amunts, 2010]. In the late nineteenth and early twentieth century several neuroanatomists, including Oskar Vogt, Cécile Vogt, Korbinian Brodmann, Otfried Foerster, Alfred Walter Campbell, Grafton Elliott Smith, Constantin F. von Economo and Georg N. Koskinas, used histological staining methods to investigate variations in the layered structure of the cerebral cortex [Geyer and Turner, 2013, Zilles and Amunts, 2010, 2012]. They primarily studied cytoarchitectonic patterns (cellular and laminar architecture of the cell bodies) using Nissl staining and myeloarchitectonic patterns (laminar architecture of the myelin sheaths) using Weigert staining [Zilles and Amunts, 2010, Elston and Garey, 2013, Nieuwenhuys, 2013, Amunts and Zilles, 2015]. These studies found that the cerebral cortex had consistent and marked regional variability, *i.e.* the cerebral cortex could be subdivided, or parcellated, into regions with locally homogeneous cyto- and myelo-architecture. These patterns were published as maps of cortical architecture [Nieuwenhuys, 2013, Elston and Garey, 2013, Zilles and Amunts, 2010, Zilles et al., 2015b,a, Zilles and Amunts, 2012].

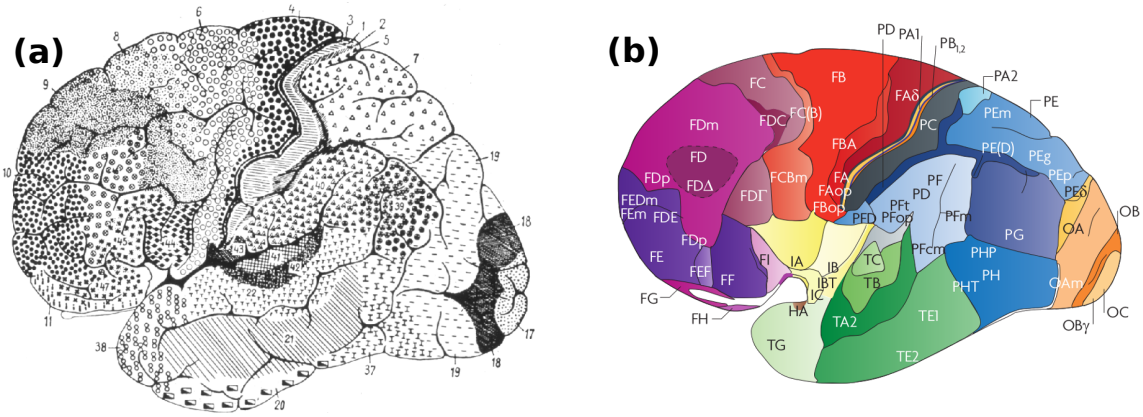

Figure 3.1: Cytoarchitectonic maps derived from histological studies by (a) K. Brodmann [Brodmann, 1909, Elston and Garey, 2013] and (b) C. F. von Economo [von Economo and Koskinas, 1925, Triarhou, 2013]. Areas with homologous cytoarchitecture are shown with same color or pattern. For a detailed discussion of each area please see respective references.

Among these, Brodmann's cortical map, shown in Fig. 3.1(a) [Brodmann, 2006, 1909], gained huge popularity and is still being used by neuroscientists as a reference map for localization of the *in vivo* data [Geyer and Turner, 2013, Zilles and Amunts, 2010].

Brodmann started his famous cytoarchitectonic work in 1901 along with the Vogts at their private brain research institute in Berlin (which later became part of Berlin University) [Nieuwenhuys, 2013, Elston and Garey, 2013]. Vogt's institute was also interested in understanding the theory of evolution in the brain [Zilles and Amunts, 2010, Brodmann, 2006, Geyer and Turner, 2013]. To this end, they started a comparative study of micro-architecture across brains of human, non-human primate and other mammals [Zilles and Amunts, 2010, Geyer et al., 2011, Brodmann, 2006, Geyer and Turner, 2013]. Brodmann started working on cytoarchitectonic mapping using Nissl staining technique and identified several architectonic patterns which were found across brains of several species. He used the same numbering scheme for all the brains (human and non-human) to indicate homologies between the cytoarchitecture of the regions. This resulted in a total of 44 areas in the human cortex, which are frequently referred as Brodmann's areas (BA) and is shown in Fig. 3.1(a), numbered from 1 to 52 with some gaps (as the cytoarchitectonic patterns corresponding to the missing numeric labels could not be identified in the human cortex) [Zilles and Amunts, 2010, Geyer et al., 2011, Triarhou, 2013, Zilles et al., 2015b].

During this time, the Vogts focused on studies of the myeloarchitecture in the cortex and, similar to Brodmann, identified several homologous regions (a total of around 200 regions; much more than Brodmann's but with comparable subdivisions of major cortical areas) [Geyer et al., 2011, Triarhou, 2013, Nieuwenhuys, 2013]. Vogt and Vogt also believed that "*the fact that all of the cortical areas distinguished display a specific structural organization indicates that all of these areas subserve a specific*

function" [Vogt and Vogt, 1919, Nieuwenhuys, 2013, Geyer et al., 2011]. They studied the functional significance of the architectonic areas in stimulation studies in monkeys, where they reported that the sites with similar stimulation response lay within same architectonic area and that the stimulation responses changed across architectonic areas [Geyer et al., 2011, Vogt and Vogt, 1919, Nieuwenhuys, 2013]. They produced maps of the motor specialization in human cortex by transferring the functional localization results in monkeys, obtained with electrical stimulation studies, through the cytoarchitectonic mapping they had obtained across human and non-human primates [Vogt and Vogt, 1926, Penfield and Boldrey, 1937, Clarke and Dewhurst, 1995]. These maps had a close resemblance to those produced by Otfrid Foerster, a German neurologist and neurosurgeon, through electrical stimulation of epilepsy patients [Vogt and Vogt, 1926, Penfield and Boldrey, 1937, Clarke and Dewhurst, 1995]. However, "*The Vogts and their associates knew, of course that some of these units are involved in particular sensory or motor functions, but in general they refrained from speculating on the specific functions of the remaining units.*" – [Nieuwenhuys, 2013]. It should also be noted here that not all the associates of Vogt's institute believed in the 'complete' functional segregation of the cortex, eg. Brodmann believed that higher level cognitive functions are not associated with one particular region and could employ several areas widely distributed across the cortex [Nieuwenhuys, 2013, Brodmann, 2006, 1909].

The study of the micro-architectonics in the cerebral cortex was not limited to the Vogt's institute even in the early 20th century (see Clarke and Dewhurst [1995] for a summary of work done from 1870 to 1936). Several other neuroanatomists, including Campbell, Smith, von Economo, and Koskinas, also independently mapped the cell architecture in the first half of the 20th century, which resulted in similar looking architectonic maps of the cerebral cortex [Zilles and Amunts, 2010, Geyer and Turner, 2013, Zilles and Amunts, 2012, Zilles et al., 2015a,b, Toga and Mazziotta, 2002, Clarke and Dewhurst, 1995]. Fig. 3.1(b) shows the cytoarchitectonic map delineated by von Economo and Koskinas [Triarhou, 2013] (see Zilles and Amunts [2010] and Zilles and Amunts [2012] for several other cortical maps). Despite the similarities, there were large differences between the maps which can most likely be attributed to individual differences in the subjects and differences in the staining and slicing techniques [Zilles and Amunts, 2010, Triarhou, 2013].

The later half of the 20th century saw several advancements in techniques to study brain which provided further evidence of the regional architectonic variations. The architectural parcellation of cortex was also indicated at the neurochemical level by imaging studies of the receptor binding sites for several neurotransmitters using autoradiography [Zilles et al., 1991, 2002a,b, Amunts and Zilles, 2015]. These studies also revealed that the boundaries defined by regional changes in receptor bindings matched the cytoarchitectonic boundaries in Brodmann's maps across several regions of the cortex [Zilles et al., 2002a,b, Zilles and Palomero-Gallagher, 2001, Amunts and Catani, 2015, Geyer et al., 2011]. With advances in electrophysiological technology the cytoarchitectonic studies were combined with intra-cortical mi-

crostimulation, similar to [Vogt and Vogt, 1919] but with sophisticated instruments, which replicated the earlier findings of the close correspondence between areas with homologous micro-architecture and stimulation responses in non-human primates [Luppino et al., 1991, Matelli et al., 1991, Zilles et al., 2002b, Iwamura et al., 1985, 1983a,b].

Non-invasive imaging technology matured rapidly in the late 20th and early 21st century, and today it has become possible to study anatomy and function *in vivo*, primarily by use of magnetic resonance imaging (MRI). However, despite several decades of development in MRI technology it is still challenging to study architectonics across the entire cortex *in vivo* [Geyer and Turner, 2013]. Current *in vivo* image quality is not sufficient to resolve cortical layers so that cyto- and myelo-architectonic regions must be inferred indirectly from currently available contrast mechanisms as we describe below. There are several advantages of studying the cortical architectonics *in vivo* [Geyer, 2013]. It would enable simultaneous mapping of architecture and function [Zilles et al., 2002b]. Like the brain, MRI images are 3D in nature and so are more suitable to study and represent the highly folded cortex as compared to 2D histological slices, which for morphological studies of layer thickness require that the laminar pattern matches the slicing orientation [Amunts et al., 2013, Triarhou, 2013]. Further, *in vivo* methods would allow studies of large populations, which could be instrumental in addressing the confounding issues with earlier studies with small samples size and inter-subject variability (see [Zilles et al., 2015a] and its references). In the next section, we will review recent promising approaches which aim to enable *in vivo* study and parcellation of the cerebral cortex based on architectonic variations.

3.2 Approaches for *in vivo* cortical parcellation using MRI

MRI enables *in vivo* acquisition of both functional and structural images and has emerged as a popular neuroimaging technique[1] [Rorden and Karnath, 2004, Turner and Geyer, 2014, Geyer and Turner, 2013]. The MRI signal is sensitive to a wide range of properties of the soft tissue including T_1-relaxation, T_2-relaxation, T_2^*-relaxation, water proton density, water diffusion, and blood oxygenation and allows versatile soft-tissue contrast by adjustment of the sensitivity to different properties. This versatility in imaging multiple tissue parameters *in vivo* makes MRI a powerful tool for studying the brain [Filler, 2009]. There are three broad classes of approach for cortical parcellation with MRI: (a) macroanatomy-based, which uses structural information visible to the naked eye such as sulcal and gyral landmarks, (b) microanatomy-based, which uses properties intrinsic to the microstructure such as cell/myelin density, pattern and chemical composition, and (c) connectivity-based, which uses properties extrinsic to the

[1] Several other techniques also allow 3D imaging of structure and/or function *in vivo* such as positron emission tomography (PET), Computerized tomography (CT), electroencephalogram (EEG), Magnetoencephalography (MEG) etc., however we will focus on MRI in this chapter.

(micro and macro) structure such as anatomical and functional connectivity.

3.2.1 Macroanatomy-based parcellation

T_1-weighted image provides excellent gray and white matter tissue contrast and is widely used to obtain anatomical landmarks in neuroimaging studies [Damasio, 2005, Brant-Zawadzki et al., 1992, Toga and Mazziotta, 2002, Toga, 2015]. The cortical folding pattern in human (and non-human) cortex is phylogenetically the oldest feature and is stable across subjects at a gross level [Fischl, 2013, Fischl et al., 2008, Mangin et al., 2015, Zilles and Palomero-Gallagher, 2015]. This means that similar sets of folding patterns can be identified between 3D MRI images of two cortices and can be used to establish a point-to-point mapping between the cortices. If one of the cortices is already labeled (by a procedure) then these labels can be transferred to the second unlabeled cortex through the established point-to-point mapping, as done in several popular registration-based methods and software tools [Yeo, 2015, Talairach and Tournoux, 1988, Collins, 1994, Evans et al., 1993, Miller et al., 1993, Thompson and Toga, 1996, Christensen et al., 1997, Collins et al., 1995, Joshi et al., 2012, 2009a, 2007, Shattuck and Leahy, 2002, Shattuck et al., 2013a,b, 2001, Tzourio-Mazoyer et al., 2002, Dale et al., 1999, Fischl et al., 2002, 2004, Fischl, 2012, Van Essen et al., 2012, Clarkson et al., 2010, Desikan et al., 2006]. The labeled cortex (and full brain) is generally referred to as the 'atlas', and the labeling of the atlas can be achieved by a variety of techniques such as manual delineation of gyrus, architectonic labeling, functional labeling etc. [Damasio, 2005, Yeo, 2015, Toga and Thompson, 2001]. This widely used approach provides a technique to parcellate the cortex (or full brain) using a labeled atlas, which is driven by the macro-anatomic landmarks and features [Toga and Thompson, 2001, Toga, 2015, Toga and Mazziotta, 2002].

One of the early spatial normalization approaches was developed by Talairach and Tournoux [Talairach and Tournoux, 1988]. They provided an atlas that was marked with coarse Brodmann areas (BAs) without borders and used simple rotation and piece-wise scaling along different directions to map a brain to their atlas [Talairach and Tournoux, 1988, Mazoyer, 2008, Brett et al., 2002]. Talairach normalization allowed reporting results in a standard coordinate space[2], which became popular in functional imaging. However, due to the use of simple piece-wise linear deformation model in this approach, the alignment of the brains were coarse in nature (only overall space and size) [Brett et al., 2002]. Since then several sophisticated deformation models have been developed that used non-rigid registration based approaches to align the volumetric 3D brain images [Johnson and Christensen, 2002, Woods et al., 1998, Friston et al.,

[2]The Montreal Neurological Institute (MNI) also published a series of MNI template brains which were created by averaging T_1-weighted images across several subject to reflect average neuroanatomy and was adopted by International Consortium of Brain Mapping (ICBM) as an international 'standard space', which has been widely used in neuroimaging studies [Brett et al., 2002, Collins, 1994, Evans et al., 1993, 1992]. Also see: http://imaging.mrc-cbu.cam.ac.uk/imaging/MniTalairach (Last accessed: January 20, 2016)

1995, Ashburner and Friston, 1999, Shen and Davatzikos, 2003, Joshi et al., 2007, Holden, 2008, Derek L. G. Hill and Hawkes, 2001, Oliveira and Tavares, 2012]. These approaches used information and landmarks in the 3D volume to drive the non-rigid registration and achieved overall better alignment of the anatomical information as compared to Talairach normalization [Johnson and Christensen, 2002, Woods et al., 1998, Friston et al., 1995, Shen and Davatzikos, 2003, Joshi et al., 2007]. Since these approaches did not explicitly model or constrain the cortical surfaces for the registration, the aligned images showed a poor correspondence of the cortical features across the brains [Fischl et al., 1999, Shen and Davatzikos, 2003, Joshi et al., 2007, Anticevic et al., 2008].

Estimation and modeling of the cortical surfaces from 3D volumetric images provide more natural and direct set of cortical features across different brains [Sandor and Leahy, 1997, Van Essen et al., 1998]. A number of normalization approaches were developed that used information derived from the cortical surfaces to drive the spatial normalization of the brain, which can be broadly categorized as landmarks-based and shape-based [Sandor and Leahy, 1995, Thompson and Toga, 1996, Sandor and Leahy, 1997, Thompson et al., 2000, Joshi et al., 2004, Wang et al., 2005, Fischl et al., 1999, Dale et al., 1999, Pantazis et al., 2010, Yeo, 2015]. The landmark-based approaches use manually or automatically defined cortical landmarks contours to constrain the registration and provide flexibility to be customized for a particular application [Joshi et al., 1997, Thompson et al., 2000, Thompson and Toga, 2002, Van Essen et al., 1998, Van Essen, 2004, 2005, Glaunès et al., 2004, Pantazis et al., 2010]. The shape-based methods use shape features such as surface curvature and sulcal depth over the cortex to drive the alignment and allows automated processing without any user input [Fischl et al., 1999, Tosun et al., 2004, Wang et al., 2005, Goebel et al., 2006, Joshi et al., 2012]. These surface-based approaches provided accurate identification of the anatomical regions by transferring information from a labeled atlas [Pantazis et al., 2010, Van Essen et al., 1998, Postelnicu et al., 2009, Joshi et al., 2012, Yeo, 2015]. Several of these volumetric and surface-based approaches for spatial normalization to a brain templates are also available as software tools including SPM[3] [Friston et al., 1995, Tzourio-Mazoyer et al., 2002], FSL[4] [Jenkinson et al., 2012, Jenkinson and Smith, 2001], BrainSuite[5] [Shattuck and Leahy, 2002, Joshi et al., 2007, 2012], and FreeSurfer[6] [Fischl et al., 2004, Fischl, 2012] (see https://www.nitrc.org/ for more exhaustive listing).

[3]SPM website: http://www.fil.ion.ucl.ac.uk/spm/ (Last accessed: January 20, 2016)
[4]FSL website: http://fsl.fmrib.ox.ac.uk/fsl/fslwiki/ (Last accessed: January 20, 2016)
[5]BrainSuite website: http://brainsuite.org/ (Last accessed: January 20, 2016)
[6]FreeSurfer website: http://freesurfer.net/ (Last accessed: January 20, 2016)

3D microarchitectonic atlas

Macro-anatomic features such as sulci and gyri also provided the topographic images for reporting localization results for much of the early micro-architectonic, stimulation, and lesion studies in the 20th century [Damasio and Damasio, 1989, Vogt and Vogt, 1926, Penfield and Boldrey, 1937]. Availability of high quality *in vivo* structural and functional MRI images motivated the use of macroanatomical landmarks to understand the relationship between *in vivo* findings and micro-architectonic details either by ad hoc visual comparison or through the use of Talairach/MNI coordinates. This direct comparison is useful, however, has several known limitations [Brett et al., 2002, Zilles and Amunts, 2010, Caspers et al., 2013, Geyer et al., 2011]. First, most of the architectonic maps, like Brodmann's, are based on a single individual, which does not account for variability across population [Zilles and Amunts, 2010, Caspers et al., 2013, Geyer et al., 2011, 1999, Amunts et al., 1999]. Second, the architectonic maps are reported on 2D projections of the topographical landmarks without a systematic spatial reference system, which limits their usability with 3D images or cortical surfaces as they cannot be warped [Fischl, 2013, Caspers et al., 2013, Geyer et al., 2011]. The BA labels in the Talairach atlas were not defined by histological study of the brain and were transferred by visual inspection of gross anatomy resulting in coarse labels without borders between labels, as noted in the original atlas – "*The brain presented here was not subjected to histological studies and the transfer of the cartography of Brodmann usually pictured in two dimensional projections sometimes possesses uncertainties.*" [Brett et al., 2002, Talairach and Tournoux, 1988]. Third, BAs were reported only on the outer exposed part of the cortex, missing the depiction on more than half of the intra-sulcal cortex hidden inside the cortical folds [Caspers et al., 2013, Geyer et al., 2011, Zilles et al., 1988, Triarhou, 2013]. Fourth and most importantly, the correspondence between the macroanatomic borders and microanatomic borders are known be limited outside few primary cortices as noted by Brodmann himself: "*The borders do not match, with a few exceptions, sulci and gyri of the cortical surface, or any other external morphological features.*" [Zilles and Amunts, 2010, Amunts et al., 2007, Zilles and Palomero-Gallagher, 2001, Caspers et al., 2013, Geyer et al., 2011, Geyer, 2013, Turner and Geyer, 2014, Fischl, 2013, Fischl et al., 2008]. All of these factors lead to the lack of quantitative certainty in *in vivo* studies using BA, which is defined based on gross anatomy [Amunts et al., 2000, 2007, Geyer et al., 2000].

An approaches to address some of the above mentioned limitations is to use a 3D atlas with labels derived from microanatomy [Zilles and Amunts, 2010, Amunts and Zilles, 2015, Roland et al., 1997, Roland and Zilles, 1998, 1994, Toga et al., 2006]. JuBrain[7] is the result of such an effort, which is a probabilistic atlas derived from 10 postmortem brains [Mohlberg et al., 2012, Caspers et al., 2013]. In this approach 10 postmortem brains are processed using histological staining for cell bodies to obtain

[7] JuBrain website: http://www.jubrain.fz-juelich.de/ (Last accessed: January 20, 2016)

cytoarchitectonic maps of the cortex and sub-cortical nuclei [Caspers et al., 2013, Bludau et al., 2014]. These histological slices are reconstructed together to get 3D histological volumes and cortical (inner and pial) surfaces for each individual brain, which are then spatially normalized to a template space to obtain the cytoarchitectonic labels in the template space [Bludau et al., 2014, Caspers et al., 2013, Fischl, 2013, Fischl et al., 2008]. This allows computation of a probabilistic measure of the presence of each cytoarchitectonically defined BA in each voxel/vertex of the template space, which can then be used for other studies [Mohlberg et al., 2012]. BigBrain[8] is a similar initiative where one postmortem brain is processed with a ultra-high resolution of 20 micrometers for histological studies and combined to obtained a cytoarchitectonically labeled 3D volume [Amunts et al., 2013]. Such ultra-high resolution allows analysis of microarchitecture along the entire cortical ribbon after 3D reconstruction, which is generally challenging with histological studies as not all cortical areas are cut orthogonal to the pial cortex [Amunts et al., 2013]. Amunts and Zilles [2015] provide a list of software packages which provides such microarchitectonic atlases.

Such microarchitectonic atlases allow *in vivo* parcellation of the cortex by transferring micro-anatomic labels of the atlas brain (probabilistic or discrete) to another brain by matching topographical landmarks [Amunts et al., 2014, Amunts and Zilles, 2015]. However, it would be preferable if the labels are derived directly from the individual's microstructure itself and then the inter-subject cortical mapping could be achieved by matching the microstructural features [Geyer, 2013, Geyer et al., 2011]. Methods discussed in the next section are geared towards this goal.

3.2.2 Microanatomy-based parcellation

Traditionally, the cortex has been parcellated microanatomically by studying the cyto-, myelo- and, more recently, receptor architectonics, all of which have been observed to have good lower level functional localization as we discussed in Sec. 3.1 [Zilles and Palomero-Gallagher, 2001]. The *in vivo* characterization of such microarchitectonic signals with MRI has been an active area of research over the past two decades [Turner and Geyer, 2014, Geyer and Turner, 2013]. MRI contrasts have been observed to be more sensitive to differences in myeloarchitecture as compared to that of cytoarchitecture [Eickhoff et al., 2005, Turner, 2013, Turner and Geyer, 2014, Geyer et al., 2011]. Myelin content affects several MR parameters of the associated protons including T_1, T_2, T_2^*, magnetization transfer and the water diffusion properties in the presence of bundles of myelinated axons [Barkovich, 2000, Geyer et al., 2011, Turner, 2013, Turner and Geyer, 2014]. Note that not all the studies, and particularly earlier approaches, reviewed in this section obtain a 'parcellation' *i.e.* microarchitectonic sub-division of the cerebral cortex. However, these studies provide very useful and important evidence that microarchitectonic features can

[8] BigBrain website: https://bigbrain.loris.ca/main.php (Last accessed: January 20, 2016)

be seen in *in vivo* and *ex vivo* MRI images, which could be later exploited to obtain such a parcellation.

3.2.2.1 Relaxation-based MR contrast

Most common MR sequences are sensitive to the indirect effects of the myelin content *i.e.* the observed signal is generated by 'myelin water' (MW), the water pool trapped inside the myelin sheaths, and not the myelin itself [Alonso-Ortiz et al., 2015, Wilhelm et al., 2012, Laule et al., 2007]. MW has restricted movement and is known to have relatively lower T_1 and T_2 relaxation times as compared to water outside myelin sheaths, hence MW generally causes hyper intensity in T_1-weighted images and hypo-intensity in T_2-weighted images [Barkovich, 2000, Laule et al., 2007, Alonso-Ortiz et al., 2015, Wilhelm et al., 2012]. MW also lowers T_2^* relaxation time, most likely due to local microscopic magnetic inhomogeneities introduced by myelin [Roth et al., 2015, Deistung et al., 2013, Hwang et al., 2010], and results into hypo-intensity in T_2^* maps and weighted images [Deistung et al., 2013, Hwang et al., 2010, Cohen-Adad, 2014, Cohen-Adad et al., 2012]. These properties of MW justify relaxation-based MR contrast as a popular choice to study microarchitectonic *in vivo* and indeed T_1 and T_2 parameters have been observed to be related to microstructural features [Harkins et al., 2015] and with myelin content [Barkovich, 2000, Laule et al., 2007, Ganzetti et al., 2014, Sereno et al., 2012, Lutti et al., 2014, Geyer et al., 2011, Geyer, 2013]. Several approaches have been proposed which use these properties to provide surrogate bio-markers of myelin in the cortex *in vivo* [Turner, 2013, Turner and Geyer, 2014, Ganzetti et al., 2014].

In order to directly observe the architectonic details in different cortical layers in MRI images, one would need ultra high resolution images, better than 200 µm or 0.2 mm with good SNR [Fischl, 2013], as the primate cortex has a highly folded structure and is on an average 2-4 mm thick with six cortical layers [Fischl, 2013, Turner, 2013, Geyer, 2013]. Few studies have been able to achieve such ultra-high resolution in *ex vivo* and/or *in vivo* images (see Turner [2013] and Fischl [2013] for a detailed review). The stria of Gennari is a heavily myelinated band of axons that runs parallel to the cortical surface in the striate cortex in occipital cortex, and many studies have tried to localize it in *in vivo* images. Clark et al. [1992] could identify the striate cortex in a 3 mm thick *in vivo* proton density weighted image with an in-plane resolution of $(0.391\ \text{mm})^2$ acquired at 1.5 T, which however required about 40 minutes of scan time per slice (4 averages). A decade later, Barbier et al. [2002] could acquire 62 T_1-weighted slices *in vivo* in about 45 minutes (8 averages) with voxel size of $0.35 \times 0.35 \times 0.6\ \text{mm}^3$, which visualized the stria of Gennari (also beautifully seen in the *ex vivo* proton density images they acquired with 110 µm isotropic resolution). The stria of Gennari was also visualized in *in vivo* anatomical scans by using T_1-contrast images with voxel size of $0.3 \times 0.3 \times 1.5\ \text{mm}^3$ at 3 T [Bridge et al., 2005, Clare and Bridge, 2005], where the authors also quantitatively compared its location to the primary visual cortex (V1) region identified using fMRI confirming that the visualization was not an imaging artifact. Duyn

et al. [2007] demonstrated the use of phase information from gradient-echo images with a voxel size of $0.24 \times 0.24 \times 1.0$ mm^3 to obtain very high contrast-to-noise ratio images of the cortical profile at 7 T, which also demonstrated a high-contrast profile for identification of the stria of Gennari. Turner et al. [2008] used *in vivo* quantitative T_1-maps at 3 T to visualize the stria of Gennari with almost isotropic voxels ($0.4 \times 0.4 \times 0.5$ mm^3), which allowed the exploration of the strias running along any direction in the folded cortex. Trampel et al. [2011] replicated this visualization at 7 T, yielding higher SNR images, using turbo spin echo sequence with $(0.5\,\text{mm})^3$ voxels and also demonstrated the presence of the stria of Gennari in congenitally blind subjects. The stria of Gennari has also been identified in healthy subjects using T_2^* maps, which also show a pattern of myelination similar to that of T_1-maps [Cohen-Adad et al., 2012, Cohen-Adad, 2014]. Sánchez-Panchuelo et al. [2012] studied the correspondence of the primary visual cortex (V1) as identified by high-resolution anatomical images (quantitative T_2^* maps with $(0.4\,\text{mm})^3$ voxels and T_1-weighted MPRAGE images with $0.4 \times 0.4 \times 0.6\,\text{mm}^3$ voxels) and with retinotopic mapping by using functional MRI at 7 T. They found that T_2^* maps show better contrast than MPRAGE in identifying the stria of Gennari, and it corresponds well with the functional region obtained by retinotopic mapping. Sánchez-Panchuelo and colleagues also studied the correspondence between functional response in somatosensory cortex (S1) to that of anatomical MR measurements (cortical thickness, magnetization transfer ratio and signal intensity in phase sensitive inversion recovery images) and found them to be correlated but not always significantly [Sánchez-Panchuelo et al., 2014].

Walters et al. [2003] used *in vivo* T_1-weighted images with $0.556 \times 0.556 \times 0.5$ mm^3 voxel size acquired at 1.5 T with surface coils to demonstrate that the intensity profiles across cortical laminar matched the myeloarchitectonic features in V1 and V5. In a similar approach, Eickhoff et al. [2005] compared the intensity profile across laminae in *in vivo* T_1-weighted image to that of in histologically stained slices and found that the T_1-weighted intensity profile matches myeloarchitecture better than cytoarchitecture. Sigalovsky et al. [2006] estimated quantitative $R_1 = 1/T_1$ map at $1.3 \times 1.0 \times 1.3$ mm^3 acquired at 1.5 T and found that high R_1 areas always contained the Heschl's gyrus and also showed hemispherical differences, suggesting myelinated auditory regions. Similarly, Sereno et al. [2012] used the whole brain quantitative R_1 maps acquired at 3 T with $(0.8\,\text{mm})^3$ voxels and demonstrated close correspondence in the spatial pattern over cortex to that of the early myelinating areas [Lutti et al., 2014]. Geyer et al. [2011] also demonstrated the presence of microarchitectonic features at 7 T in *in vivo* T_2^*-weighted images and T_1 maps, obtained from MP2RAGE sequence [Geyer, 2013, Bazin et al., 2014], acquired with voxels of size $(0.6\,\text{mm})^3$ and $(0.4\,\text{mm})^3$ respectively. Geyer et al. [2011] also used the image intensity values sampled at equidistant points between inner and pial-surface as a feature vector at each point on the cortical surface for automated segmentation of the primary visual cortex (V1) from the rest. Barazany and Assaf [2012] used a series of inversion-recovery image with variable inversion times (voxel size of approximately $0.43 \times 0.43 \times 1.5$ mm^3) to estimate T_1-relaxation time in each voxel, which

was used with k-means algorithm to automatically cluster different layers of the cortex in rat and human brain *in vivo*. The obtained clusters for the rat-brain were also compared with the histological stainings and were found to agree to a certain degree. Augustinack and colleagues explored the parcellation of medial-temporal cortices in *ex vivo* studies which provided more evidences that MR contrasts shows similar features as revealed by myelin and Nissl staining [Augustinack et al., 2010, 2013a,b, 2014].

Images with multiple MR contrasts have also been fused together to explore the myelin content in the cortex. Ratios of T_1- and T_2-weighted images (T1w/T2w ratio) has been popularly used as a surrogate for myelin volume in the cortex, and demonstrate close resemblance to the published early developmental myelin maps obtained using histological studies [Glasser and Van Essen, 2011, Glasser et al., 2014, Van Essen and Glasser, 2014, Shafee et al., 2015, Ganzetti et al., 2014, 2015]. The spatial variation in T1w/T2w ratio in human subjects also shows homologies with non-human primates [Glasser et al., 2014] and with probabilistic BA areas [Glasser and Van Essen, 2011], suggesting the measure's ability to capture similar information. Some recent improvements have also been suggested, which propose to use better calibration of intensities [Ganzetti et al., 2014] and model partial volume effects in T_1-weighted and T_2-weighted images [Shafee et al., 2015]. Similarly, ratios of T_1- and T_2^*-weighted images (T1w/T_2^*) has also been proposed as a surrogate for myelin content at 7 T, which allowed identification of the heavily myelinated regions in the medial Heschl's gyrus [De Martino et al., 2012, De Martino et al., 2015]. The intensities in T_1- and T_2-weighted images were also used as a set of two features for refined localization of the primary auditory cortex in a maximum likelihood framework, which was initially localized based on curvature [Wasserthal et al., 2014]. [Mangeat et al., 2015] proposed to fuse T_2^* and magnetization transfer ratio, after regressing out the variability which could be introduced by cortical thickness and B_0 orientation dependent contrast, to get another surrogate myelin measure.

It should be noted here that the approaches discussed in this section are insightful but assumes a very simple model of the underlying tissue structure in the cortex. The estimated relaxometry parameters and corresponding 'weighted' images assume a single compartment model, *i.e.* the tissue structure and composition are homogeneous inside each voxel. As seen in several stained histological slices, ultra-high resolution *ex vivo* images and electron micrographs, the micro-architecture of the cortex is very complex and contain several different types of components and cells including neurons, pyramidal cells, glia cells, astrocytes, nerve fibers, and blood vessels, resulting in the presence of a complicated combination of lipids, proteins and water in each voxel [DeFelipe et al., 2002, Laule et al., 2007, Amunts and Zilles, 2015, Alonso-Ortiz et al., 2015, Guleria and Kelly, 2014, Roth et al., 2015]. The MR signal is affected by several different properties of these components, for example, T_1 contrast is not only specific to the volume of myelin in a voxel but is affected by the axon diameter [Harkins et al., 2015] and iron concentration [Ogg and Steen, 1998]. The simple models, used in the approaches reviewed earlier in this section, are not very accurate for quantitative evaluation, can be difficult to interpret and can often lead

to confounding observations [Sandrone et al., 2015]. There are a number of approaches that do models these complexities and could be useful for more accurate quantification [Laule et al., 2007, Alonso-Ortiz et al., 2015, Wilhelm et al., 2012]. As we mentioned earlier, it is very difficult to directly image myelin, as the myelin lipids and cholesterol have extremely small T_1 and T_2 relaxation times at the field strength of most MR scanners [Alonso-Ortiz et al., 2015, Wilhelm et al., 2012, Laule et al., 2007]. So, most of the MR observation are indirect effects of myelin-water interactions which can confound any quantitative interpretations of myelin [Alonso-Ortiz et al., 2015, Wilhelm et al., 2012]. Wilhelm et al. [2012] explored a technique for direct detection and quantification of myelin by using ultra-short echo time for MR experiments, which is promising for the myeloarchitectonic quantification.

3.2.2.2 Diffusion-based MR contrast

A close observation of the myeloarchitectonic maps from stained histological slices (or from the early literature) shows that the microarchitectonic differences across different regions of the brain are not only limited to relative differences in myelin volume but more in the pattern of the myelination. Also, quite often theses difference are subtle and hence a simple single component relaxometry model may not be able to differentiate between these regions. Figure 3.2 shows an example of the histological slices with myelin staining from a macaque brain. Diffusion MRI is sensitive to the ensemble Brownian motion of the water molecules in the voxel that is undergoing restricted diffusion in the presence of different types of tissue structures [Jones, 2011, Basser and Jones, 2002, Beaulieu, 2014]. Hence the diffusion MRI contrast is directly affected by the volume, density, orientation and pattern of the neurons and myelinated sheaths in their axons[9], making it a very good candidate for studying microarchitectonic details in the cortex.

The highly folded nature of the cortex in adult human subjects makes it difficult to study diffusion properties with isotropic voxel resolution of about 2–3 mm, which is typically achievable in clinical scan times. Nonetheless, there has been considerable effort to study diffusion properties of the cortical gray-matter *in vivo* during the last 5-10 years. Diffusion properties in the cortex have been relatively widely studied in *in vivo* brain development studies, in part because pre-term fetal brains are substantially less folded than adult brains [McKinstry et al., 2002, McNab et al., 2013b]. These studies show that the diffusion properties in the developing cortex are maximally anisotropic at a gestation age of 26 weeks

[9]The exact relationship between the observed diffusion weighted signal in a voxel and the volume, density, orientation and pattern of the myelinated sheaths is quite complicated and can be affected by several other factors such as the presence of other cell bodies in the voxel and the experiment design [Beaulieu, 2002, 2014, Ackerman and Neil, 2014]. However, the presence of myelinated axons have been observed to affect the MR diffusion contrast across several studies [Beaulieu, 2009, Song et al., 2002, Tyszka et al., 2006] (see publications by Beaulieu [Beaulieu, 2002, 2009, 2011, 2014] and Jones [2011, Section II – The Basics of Diffusion MRI] for detailed and explanatory review of the topic).

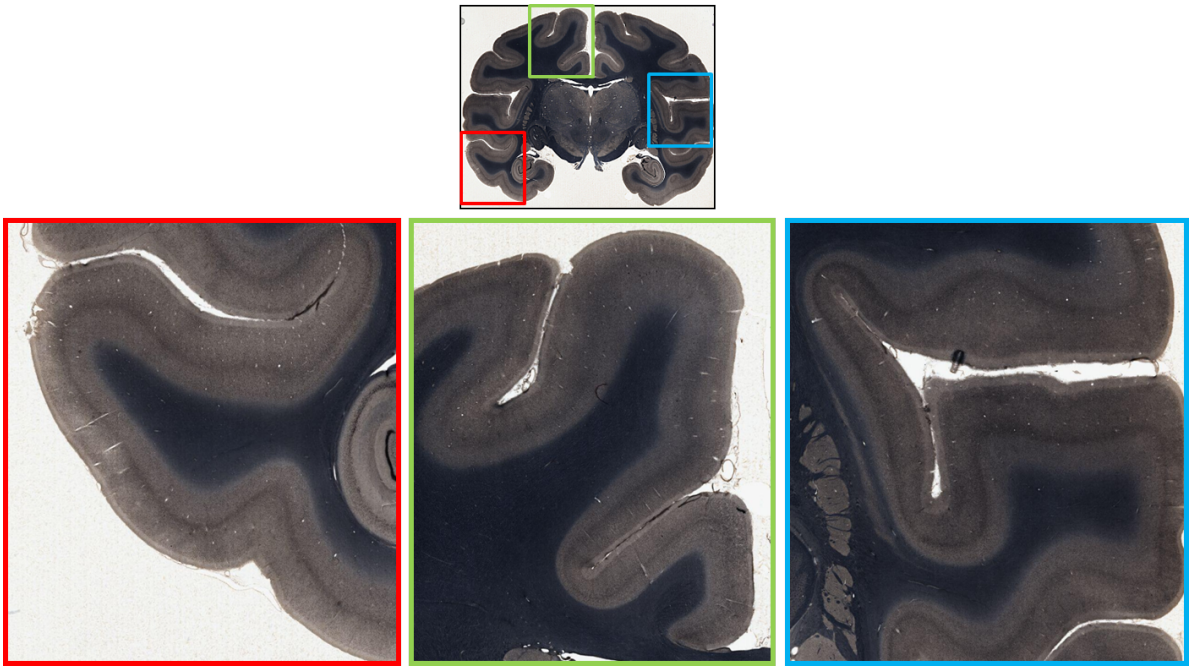

Figure 3.2: Example of histological slices with Weil myelin staining. The coronal view is shown in the top and zoomed in views of different regions (indicated by colored rectangles) are shown in the bottom row. The images of stained slices were obtained from brainmaps.org[10] [Mikula et al., 2007, Web].

and approaches isotropic behavior at a gestation age of about 36 weeks [McKinstry et al., 2002, Maas et al., 2004, Deipolyi et al., 2005, Mukherjee and McKinstry, 2006, Hüppi, 2011, Zhang et al., 2011, Dudink et al., 2015]. Cortical diffusion properties have also been studied in several *ex vivo* animal studies with fixed rat brain [Wedeen et al., 2004, Jespersen et al., 2010] and ferret brain [Kroenke et al., 2009, Jespersen et al., 2012]. These show anisotropic radial diffusion patterns in the cortex that are in close agreement with histological and microscopic results. Jaermann et al. [2008] used a dedicated miniature phased array detector at 3 T to obtain high-resolution *in vivo* diffusion images (2.5 mm thick slices with an in-plane resolution of $0.58 \times 0.58\,\mathrm{mm}^2$ at b-value of 1400 s/mm^2), which demonstrated anisotropic diffusion in the cortex perpendicular to the pial surface. McNab et al. [2009] demonstrated a similar radial anisotropic pattern in the cortex in an *ex vivo* study with fixed human brain. In contrast to previous studies, [Anwander et al., 2010] demonstrated that the diffusion processes are not always radial to the cortical surface in the cortex but are tangential in nature in somatosensory cortex in an *in vivo* study across 6 human subjects with voxel size of $(1.5\,\mathrm{mm})^3$ at b-value of 1000 s/mm^2 using a 3 T whole body MR scanner. This study was further extended by McNab and colleagues, where the authors

[10]Image are obtained under Creative Commons Attribution 3.0 License for academic purposes from: http://brainmaps.org/ajax-viewer.php?datid=21&sname=m21&vX=-287.5&vY=-123.198&vT=1 (Last accessed: January 20, 2016).

replicated the tangential behavior in the somatosensory cortex in an *in vivo* study with 6 human subjects (voxel size of 1.0 mm isotropic) and with one macaque (voxel size of 0.7 mm isotropic) at b-value of 1000 s/mm^2 on 3 T MR scanner [McNab et al., 2011, 2012, 2013b]. These studies also reported that the orientation of the principal diffusion component in most of the human cortex, except for somatosensory areas, is largely radial in nature.

Truong et al. [2014] used multishot constant-density spiral EPI to obtain *in vivo* images with 3 mm slice thickness and high in-plane resolution of $0.625 \times 0.625\,\text{mm}^2$ at 3 T and studied the variation of the anisotropy in the cortex as a function of cortical depth across three subjects. They found that most of the cortical regions showed primarily radial diffusion orientation and that the anisotropy is consistently highest in the middle of the cortical laminae. Haroon et al. [2010] examined the complexity of the diffusion processes by estimating the probability of observing 1, 2, 3 or >3 fiber orientations in each voxel using a model-based residual bootstrapping approach on the acquired diffusion data [Haroon et al., 2009]. The authors found that cortical gray matter voxels have a high probability of having 3 or more fiber orientations, indicating higher complexity of the diffusion processes, which was consistent across different subjects and different cortical regions (identified using macro-anatomical landmarks). Nagy et al. [2013] used features derived from first acquisition of the diffusion data to train a three-way classifier for three different cortical areas (extended middle temporal area, superior temporal sulcus, and angular gyrus determined either by retinotopic experiments or by using cortical folds), which they then used to classify the regions in a second acquisition of the same subject. The authors acquired diffusion data with a 3 T scanner with isotropic spatial resolution of 2.3 mm at b-value of 1000 s/mm^2 and computed a total of 27 orientation-invariant and cortical-normal dependent features, at each vertex on the cortex, derived from spherical-harmonic fitting of the apparent diffusion coefficient. They reported good classification accuracy, 80-82%, on the second acquisition of the same subjects showing good test-retest reproducibility of the diffusion features. They also tried k-means clustering on the computed features to cluster the whole cortex into 40 different clusters, which was inconclusive and did not obtain a meaningful set of clusters [Nagy et al., 2012, 2013].

High field MR scanners (>3 T) have also been used for exploration of the diffusion properties in the cortex. [Augustinack et al., 2010] acquired high-resolution *ex vivo* anatomical images at 7 T (0.1 mm isotropic resolution) and diffusion images at 4.7 T (0.3 mm isotopic resolution), which allowed direct visualization of the perforant pathway with two different fiber tracking methods. Fixed samples of visual cortex have been studied at 9.4 T to visualize the stria of Gennari in *ex vivo* diffusion images (spatial resolution of $0.188 \times 0.188 \times 0.376\,\text{mm}^3$, b=1159 s/mm^2, 4 averages), which showed that the voxels in and around the stria do not show a preferential principal diffusion direction while other regions of the cortex show preference along the perpendicular to the cortical surface [Leuze et al., 2011]. In a similar study at 11.7 T, the stria of Gennari was observed to have lower diffusion anisotropy than the rest of the

primary visual cortex using diffusion tensors at an isotropic spatial resolution of 0.3 mm [Kleinnijenhuis et al., 2011a]. These observations were further explored across two *ex vivo* samples by computing the fiber orientation distribution from the diffusion data, which demonstrated that the voxels in the stria of Gennari had two large fiber orientations, one perpendicular to the cortex and another primarily parallel to the cortex [Kleinnijenhuis et al., 2013a, 2011a]. The diffusion tensor anisotropy profile was also found to follow a similar pattern to the intensity profile of gradient-echo images along the normal to the cortical surface [Kleinnijenhuis et al., 2013a, 2011a]. [Leuze et al., 2014] used diffusion tractography in a fixed sample from visual cortex with an isotropic spatial resolution of 0.242 mm, where they identified different cortical layers that demonstrated different intra-cortical connectivity. The preferential diffusion direction, as observed in several *in vivo* and *ex vivo* human MR experiments, was also confirmed with histological staining for myelin and with polarized light imaging [Kleinnijenhuis et al., 2011a,b, Leuze et al., 2014]. Exploring the diffusion pattern in the visual cortex further through *ex vivo* studies, Kleinnijenhuis et al. [2013b] used NODDI, a multi-compartment tissue model [Zhang et al., 2012], and found that it has better sensitivity to microstructural details than fractional anisotropy maps derived from diffusion tensor modeling, and that the observed diffusion orientation pattern matches well with histological staining [Kleinnijenhuis et al., 2013c, Tariq et al., 2015]. Aggarwal et al. [2015] used a 3D diffusion-weighted gradient and spin echo sequence at 11.7 T to obtain a voxel size of $0.092 \times 0.092 \times 0.092\,\text{mm}^3$ with fixed samples from different brain regions coming from three subjects: prefrontal, primary motor, primary somatosensory and primary visual. They reported an important finding that these regions, which are known to have distinct microarchitectonic details, also show distinct and region specific diffusion MR signals as well as show good agreement with histological sliver impregnation of the same specimens.

Recent advances in diffusion acquisition now allow high-resolution full brain *in vivo* imaging at high-field in human subjects. Diffusion imaging at high-field strength is generally more challenging because single-shot EPI, which is widely used for diffusion imaging [Pipe, 2014, Miller, 2014], suffers from severe susceptibility-induced geometric and blurring artifact at higher field strengths. Heidemann et al. [2010] used segmented EPI with parallel imaging at 7 T to obtain diffusion images with less blurring and susceptibility artifacts at a spatial resolution of $1.1 \times 1.1 \times 3.0\,\text{mm}^3$ (b=1000 s/mm^2), which demonstrated the ability to study anisotropy in the cortex at high resolution. Improving the acquisition further, Heidemann et al. [2012] introduced an adapted EPI sequence with a combination of zoomed imaging and parallel acquisition (ZOOPPA) which allowed high-resolution (1.0 – 0.8 mm isotropic) diffusion imaging at 7 T of a partial field of view (50% view) in little over an hour with 60 diffusion encoding directions at b=1000 s/mm^2. ZOOPPA allowed high-resolution imaging of focused regions and revealed sub-millimeter details of the diffusion properties in both white-matter and cortical areas *in vivo*.

Most of the studies reviewed above are exploratory studies which visualize or demonstrate some in-

sightful properties of diffusion MRI in the cortex. However, with the exception of [Nagy et al., 2012, 2013], none of these methods obtain a parcellation of cortex based on diffusion properties. [Nagy et al., 2012, 2013] reported a parcellation based on k-means clustering of the features derived from the apparent diffusion coefficient, which, however, did not show a very meaningful parcellation. This could be an effect of several factors such as relatively lower spatial resolution (2.3 mm isotropic) of the diffusion data, a relatively simple diffusion model based on apparent diffusion coefficient, a limited set of derived features, or use of simple k-means based classification approach. Recent advances in multi-slice and super-resolution MR imaging allow reconstruction of *in vivo* diffusion images at an isotropic spatial resolution of 0.6-0.7 mm, which are promising for such cortical studies [Setsompop et al., 2015, Haldar et al., 2016, Setsompop et al., 2016]. There are also several advanced diffusion models which could be used such as the orientation diffusion function (ODF) [Tuch, 2004, Descoteaux et al., 2007, Haldar and Leahy, 2013, 2012], NODDI [Zhang et al., 2012], AxCaliber, Charmed, or the ball-and-stick model (see [Alexander, 2008, 2005] and Jones [2011, Section II and V]). A more advanced set of features such as axon diameter [Duval et al., 2014, McNab et al., 2013a] can also be used for clustering purposes. However, it should be noted that most publications use features that are orientation invariant and so are potentially not capturing all the information contained in the diffusion data which is inherently orientation dependent in anisotropic media. We present an advanced orientation normalization scheme for diffusion MRI dataset in chapter 7, which allows use of all the orientation dependent information for direct comparison across different points on the cortex. It should also be noted that several of the obtained features are correlated with the curvature of the cortex [Kleinnijenhuis et al., 2015], which probably should be regressed out before parcellation.

3.2.3 Connectivity-based parcellation

The approaches described in the previous section explore the ability of MRI to mimic microarchitectonic studies as classically performed with histological staining in early 20th century by Vogts, Brodmann, von Economo and others [Brodmann, 1909, Vogt and Vogt, 1919, von Economo and Koskinas, 1925]. These approaches were focused on studying the properties in the cortex that manifest due to the microarchitecture (cyto-, myelo-, and receptor-architecture) of the underlying tissue using MR images, which could later be used for parcellation of the cortex based on regional similarity of the microarchitecture. In this section, we discuss another class of approach that uses 'connectivity' based properties in the cortex to obtain a connectivity-based parcellation (CBP) using MRI images. The 'connectivity' in this context can be broadly defined as a set of input and output connections to a small local region of the cortex (or brain). CBP is inherently different from microarchitectonic approaches as it uses properties or "fingerprints" derived from its connection with *external* regions to drive the parcellation, whereas the microarchitectonic approach uses properties derived from its *internal* composition and architecture

[Behrens et al., 2010, Passingham et al., 2002]. CBP sub-divides the cortex (or region of interest) into small regions based on a similarity measure of their connectivity fingerprints to other parts of the cortex or brain. Historically, these connectivity fingerprints were first defined using diffusion MRI observations by computing connectivity between different regions of the brain using probabilistic or deterministic tractography [Behrens et al., 2003, Behrens and Johansen-Berg, 2005, Behrens et al., 2010]. There is also another type of CBP that uses "functional fingerprints" derived from correlation measures on resting functional MRI (rfMRI) to obtain the parcellation [Kim et al., 2010, Cohen et al., 2008, Eickhoff et al., 2015]. So the CBP approach can be classified based on structural connectivity (*i.e.* presence of axonal pathways connected to the region) or functional connectivity (*i.e.* presence of correlated functional or electrophysiological responses). In spite of the differences in the measure of connectivity in these two approaches, they are closely related [Johansen-Berg et al., 2005, Passingham et al., 2002, Johansen-Berg et al., 2004, Behrens and Johansen-Berg, 2005, Beckmann et al., 2009b, Knösche and Tittgemeyer, 2011].

The CBP approach is much more widely studied than the microarchitectonic approach with MRI and several different variations of CBP have been reported, in terms of the measure of connectivity or the region of interest to be sub-divided or a combination both, as can be found in several review papers [Eickhoff et al., 2015, Klein et al., 2014, Thirion et al., 2014, Sporns, 2014, Biswal, 2015, Eickhoff and Müller, 2015, Smith et al., 2013b, Cloutman and Lambon Ralph, 2012, Knösche and Tittgemeyer, 2011, Behrens et al., 2010, Margulies et al., 2010, van den Heuvel and Hulshoff Pol, 2010, Thirion et al., 2006, Behrens and Johansen-Berg, 2005]. In this section, we will briefly review the use of connectivity and functional fingerprinting for cortical parcellation. Note that large-scale brain network modeling and analysis is closely related to CBP but is not a focus of this chapter [Sporns, 2014, Wig et al., 2011]. Nonetheless, CBP is an important component of brain network analysis as the subdivisions obtained from CBP can form the nodes of a brain network or graph with the edges defined by a measure of connectivity across subdivisions [Sporns, 2014, Wig et al., 2011, Mars et al., 2016, Qi et al., 2015, Andellini et al., 2015, Stam, 2014, Taylor et al., 2014, Sporns, 2013, de Reus and van den Heuvel, 2013, van den Heuvel and Hulshoff Pol, 2010, Rubinov and Sporns, 2010].

Structural CBP is obtained *in vivo* by use of diffusion MRI images which allow non-invasive characterization of the long-range axonal pathways through a variety of diffusion models and tractography techniques [Jones, 2011, Section IV], [Johansen-Berg and Behrens, 2014, Section III]. A connectivity profile or fingerprint is obtained at each point in the region to be parcellated by using the point as a "seed point" through which the diffusion tracks are computed to obtain the connectivity information to either the entire brain or a predetermined subset of the brain. The later allows incorporation of prior knowledge from connectivity studies in animal models, histological and postmortem studies, which make the obtained parcellations easier to interpret [Behrens et al., 2003, Wiegell et al., 2003, Behrens and Johansen-Berg,

2005, Behrens et al., 2010, Cloutman and Lambon Ralph, 2012, Bzdok et al., 2013, Klein et al., 2007]. On the other hand computing connections across the entire brain allows parcellation without any prior hypothesis [Klein et al., 2014, Cloutman and Lambon Ralph, 2012, Moreno-Dominguez et al., 2014].

The connectivity profile, computed at each seed point, can be used to compute the similarity of each seed point to other seed points and expressed as a similarity matrix. This similarity matrix can be used in turn to obtain the set of final parcels using clustering techniques such as k-means, Gaussian mixture model, spectral clustering, or hierarchical trees [Knösche and Tittgemeyer, 2011, Klein et al., 2014, Cloutman and Lambon Ralph, 2012, Behrens et al., 2010]. This process obtains a parcellation for each individual separately, which can be advantageous as the obtained parcellation is directly related to individual's anatomy and connectivity. However, a meaningful parcellation should have consistent characteristics across subjects while still retaining individual differences [Knösche and Tittgemeyer, 2011, Klein et al., 2014]. Some method incorporate this assumption in the parcellation scheme itself and use multi-subject or population-based clustering, which improves the ability to use and interpret the resulting parcellation [Nanetti et al., 2009, O'Muircheartaigh et al., 2011, Lefranc et al., 2016, Knösche and Tittgemeyer, 2011, Chong et al., 2016, 2015]. One of the most crucial steps in the above process is the estimation of the connectivity fingerprinting, which depends on a combination of following: the quality of diffusion data, goodness of the diffusion model and the accuracy of the tracking algorithm [Johansen-Berg and Behrens, 2014, Knösche and Tittgemeyer, 2011]. Hence, it is important to optimize these depending on the application and region of the interest as well as understand its limitations [Jones et al., 2013, Jones, 2011, 2010, Jones and Cercignani, 2010, Johansen-Berg and Behrens, 2014, Knösche and Tittgemeyer, 2011]. Structural CBP has been used to parcellate sub-regions of the cortex (medial frontal cortex, inferior frontal cortex, precentral gyrus, postcentral gyrus, inferior parietal cortex), and sub-cortical gray matter structures (thalamus, basal ganglia, amygdala etc.) as well as the entire cortex [Klein et al., 2014, Cloutman and Lambon Ralph, 2012, Knösche and Tittgemeyer, 2011, Behrens et al., 2010, Klein et al., 2007]. These parcellations have been used to study differences between normal and diseased population [Wang et al., 2015, Schönknecht et al., 2013]. The parcellations obtained with structural CBP have also been found to have close agreement with histological parcellations [Bzdok et al., 2013, Johansen-Berg et al., 2005].

Functional CBP follows a similar method to structural CBP to obtain the parcellation but uses functional fingerprinting to obtain the similarity matrix [Eickhoff et al., 2015, Thirion et al., 2014, Biswal, 2015, Eickhoff and Müller, 2015, Smith et al., 2013b, Margulies et al., 2010, van den Heuvel and Hulshoff Pol, 2010, Thirion et al., 2006]. Resting functional MRI (rfMRI) uses spontaneous fluctuations in brain activity to obtain the fingerprint by computing the correlations of the rfMRI data between seed points and the rest of the brain [Cohen et al., 2008, Kim et al., 2010, Eickhoff et al., 2015]. The functional correlation matrix have been used to obtain the final set of parcels using a variety of clustering

techniques such as k-means, spectral clustering, and hierarchical clustering [Smith et al., 2013b, Thirion et al., 2014, Blumensath et al., 2013, Margulies et al., 2010, Craddock et al., 2012, Wig et al., 2014a,b, Yeo et al., 2011, Yeo, 2015]. It is also common to transfer the rfMRI data from several subject to a 'standard' space to obtain a functional parcellation in the standard space by combining the data across the population. This improves the sensitivity to functional fingerprinting differences by use of substantially more data and obtains better quality parcels as well as facilitating comparison of parcels across subjects [Shou et al., 2014, Calhoun et al., 2009, Beckmann et al., 2009a, Erhardt et al., 2011, Shen et al., 2010, Chong et al., 2016, 2015].

Another interesting approach, meta-analytic connectivity modeling (MACM), uses meta-data analysis of task fMRI activation maps [Eickhoff et al., 2011, Laird et al., 2013, Langner et al., 2014]. MACM uses meta-information reported in several thousand independent studies, from databases such as http://www.brainmap.org/, about the activations obtained in response to certain task/stimuli in fMRI experiments. MACM uses the reported meta-data to obtain a co-activation matrix, *i.e.* for each seed point, MACM finds all the brain voxels which have been reported to show coactivation across any task-experiment to form one row of the coactivation matrix. The co-activation matrix is then used as a similarity matrix for parcellation or the spatial maps corresponding to each seed point can be merged in a hierarchical fashion to obtain clusters [Eickhoff et al., 2011, Laird et al., 2013, Langner et al., 2014].

Connectivity-based parcellation is a rapidly evolving area of research, and several variations of the approaches described above have been used to explore brain connectivity and parcellation [Eickhoff et al., 2015, Klein et al., 2014, Thirion et al., 2014, Sporns, 2014, Biswal, 2015, Eickhoff and Müller, 2015, Smith et al., 2013b, Cloutman and Lambon Ralph, 2012, Knösche and Tittgemeyer, 2011, Behrens et al., 2010, Margulies et al., 2010, van den Heuvel and Hulshoff Pol, 2010, Thirion et al., 2006, Behrens and Johansen-Berg, 2005]. It should be noted that all the CBP methods are data driven and while the resulting parcellations explain the data in some way, they are not hypothesis driven and do not necessarily represent a 'true' neurobiological parcellation of the brain [Eickhoff et al., 2015, Craddock et al., 2013, Biswal et al., 1995, Biswal, 2015]. Among the different CBP approaches, structural CBP has the most direct neurobiological interpretation, *i.e.* the delineated parcels most likely reflect regions connected by true axonal pathways. As indicated earlier, the structural-connectivity based parcellations have also been found to show close agreement with some histological parcellation [Bzdok et al., 2013, Johansen-Berg et al., 2005].

Unlike the structural CBP, parcellations obtained from functional CBP and MACM are not as easy to interpret [Eickhoff et al., 2015]. The neurobiological nature of the spontaneous fluctuations in rfMRI and their relation to structural connectivity and function is not entirely understood [Eickhoff et al., 2015, Cloutman and Lambon Ralph, 2012], which confounds the interpretation of functional CBP parcels. Another confounding factor is the choice of cluster number, which is usually decided heuristically based on

an examination of results with several parameters [Eickhoff et al., 2015, de Reus and van den Heuvel, 2013]. Despite the difficulty in interpreting parcellations, CBP provides useful spatial maps of complex brain organization which can be used to generate spatial hypotheses for functional or structural segregation, which can be tested with a variety of other techniques and modalities to provide useful new insights into the cortical organization.

Chapter 4

Registration-based distortion correction of diffusion MR images

Diffusion MRI is a non-invasive imaging technique that can provide quantitative and qualitative information about microstructural tissue properties *in vivo* [Le Bihan and Johansen-Berg, 2012, Johansen-Berg and Behrens, 2009, Jones, 2011]. Neuroimaging studies frequently make use of high resolution T_1-weighted anatomical images to identify and delineate neuro-anatomical structures as well as study different properties of the brain such as thickness and volume [Toga and Mazziotta, 2002, 2000, Toga, 2015, Shattuck and Leahy, 2002, Shattuck et al., 2001, Joshi et al., 2007, 2012, Fischl, 2012, Fischl et al., 2004]. Quantitative information about diffusion processes can be combined with T_1-weighted anatomical images in order to quantify the microstructural characteristics of neuro-anatomical structures and the white matter connections between them. In order to jointly analyze these images, they must first be co-registered [Jones and Cercignani, 2010, Irfanoglu et al., 2012, Pierpaoli, 2010].

There are two primary challenges in accurate co-registration of T_1-weighted and diffusion images. First, diffusion MRI frequently uses EPI sequence for data acquisition, which results in localized susceptibility-induced distortions in the reconstructed diffusion weighted images (DWIs) as a result of inhomogeneities in the B_0 field [Pipe, 2014, Miller, 2014, Skare and Bammer, 2010]. As we discussed in chapter 2, these distortions can be particularly pronounced in regions where susceptibility is rapidly changing, such as at the interfaces of soft tissue, air and bone [Andersson and Skare, 2011, Jezzard and Clare, 1999, Jones and Cercignani, 2010]. Second, co-registration of T_1-weighted and diffusion images (distorted or undistorted) is difficult because the images are sensitive to different physical properties of the underlying tissue and exhibit very different image contrast [Pierpaoli, 2010]. This makes it an *inter-modal* registration problem [Oliveira and Tavares, 2012, Derek L. G. Hill and Hawkes, 2001, Jenkinson and Smith, 2001]. As reviewed briefly in chapter 2, when an accurate estimate of the B_0 fieldmap is available, several

methods can be employed for accurate correction of the localized susceptibility-induced EPI distortion [Andersson and Skare, 2011, Jezzard and Balaban, 1995, Jezzard, 2012, Jenkinson et al., 2012, Munger et al., 2000, Kadah and Hu, 1998, Bhushan et al., 2013, 2014b, Andersson et al., 2003, Gallichan et al., 2010]. However, accurate B_0 fieldmap information is not available in many neuroimaging studies because of variety of reasons such as limited scan time [Jezzard and Balaban, 1995, Jezzard, 2012, Jones and Cercignani, 2010].

In this chapter we present a novel registration-based technique for EPI distortion correction in absence of a fieldmap. Our technique can also be used for accurate rigid alignment with anatomical images.

4.1 Review of registration-based approaches

Image registration has been used to correct the distorted EPI image without a fieldmap in several reported methods [Studholme et al., 2000, Kybic et al., 2000, Ardekani and Sinha, 2005, Bhushan et al., 2012, Pierpaoli et al., 2010, Wu et al., 2008, Huang et al., 2008, Gholipour et al., 2006, Yao and Song, 2011, Irfanoglu et al., 2011, Tao et al., 2009]. In these methods the distortion field is generally estimated by a non-rigid alignment of the distorted EPI image with no diffusion weighting (*i.e.* a T_2-weighted (T2W) EPI image with a diffusion b-value of 0 s/mm^2) to an anatomical image with negligible geometric distortion. These methods differ in some of the assumptions and choice they make for the registration process: the contrast of anatomical image, the nature of the similarity metric, parameterization of the deformation field, the model of unwarping the distorted image, the regularization model and the optimization method. All of these choice have their own limitations and advantages and can have substantial impact the final outcome.

A T2W-EPI image is commonly used in registration-based methods because it shows similar image structure to an anatomical image, is almost always acquired in quantitative diffusion studies and manifests very similar distortion as different DWIs [Bhushan et al., 2012, Pierpaoli et al., 2010, Wu et al., 2008, Huang et al., 2008, Gholipour et al., 2006, Yao and Song, 2011]. Most methods use a T_2-weighted anatomical image since these have similar contrast to the T2W-EPI image [Kybic et al., 2000, Ardekani and Sinha, 2005, Pierpaoli et al., 2010, Wu et al., 2008, Huang et al., 2008]. However, we are interested to use T_1-weighted anatomical images as they are frequently acquired in brain-mapping studies to delineate cortex and sub-cortical anatomical structures [Shattuck and Leahy, 2002, Shattuck et al., 2001, Joshi et al., 2007, 2012, Fischl, 2012, Fischl et al., 2004]. Few previously reported method did use T_1-weighted anatomical images for this purpose [Studholme et al., 2000, Gholipour et al., 2006, Yao and Song, 2011], however there are some key difference between them. Yao and Song [2011] and Wu et al. [2008] did not use the constraints based on the physics of the EPI distortion, as described in chapter 2, which could limit the accuracy of the correction. Studholme et al. [2000] did use the physics-based

constraints but chose to not use spatial regularization during the registration process, which in our experience may lead to some severe singularities in some cases. Further, since the contrast of a T_1-weighted anatomical image is different from that of the T2W-EPI image, previous approaches using T_1-weighted images [Bhushan et al., 2012, Gholipour et al., 2006, Yao and Song, 2011] use standard inter-modality cost functions that are insensitive to contrast differences (e.g., mutual information (MI) [Maes et al., 1997, Viola and Wells III, 1997, Studholme et al., 1999] or correlation ratio (CR) [Roche et al., 1998]). However, it is known that both MI and CR lead to non-convex and non-smooth optimization problems that can be challenging to solve, specially in case of non-rigid registration [Oliveira and Tavares, 2012, Derek L. G. Hill and Hawkes, 2001, Pluim et al., 2003, Tsao, 2003, Pluim et al., 2004, Jenkinson and Smith, 2001, Jenkinson et al., 2002].

In this chapter, we propose a new approach, INVERSION (Inverse contrast Normalization for VERy Simple registratION), that exploits the approximately inverted contrast relationship between T_1- and T_2-weighted brain images to transform the contrast of one image into the contrast of the other. This means that the complicated *inter-modal* registration problem can be simplified to an *intra-modal* registration problem, which is easier to solve and is less sensitive to highly-misaligned images. INVERSION can be used for both co-registration of T_1-weighted anatomical and diffusion images and for fieldmap-free susceptibility-induced distortion correction[1]. INVERSION (along with NMI- and CR-based approach) is implemented in MATLAB (The MathWorks, Inc., USA) and the source code along with the pre-compiled binaries are available from http://brainsuite.org under the terms of the GNU General Public License, version 2.

4.2 Inter-modal image registration

Image registration finds a spatial transformation of a moving image (I_1) which aligns it to a static image (I_2). The spatial transform is typically represented as a deformation map $\phi : \mathbf{X_2} \rightarrow \mathbf{X_1}$ from the static image coordinate $\mathbf{X_2}$ to moving image coordinate $\mathbf{X_1}$. The optimal deformation map ($\widehat{\phi}$) can be estimated by solving [Derek L. G. Hill and Hawkes, 2001, Oliveira and Tavares, 2012]

$$\widehat{\phi} = \arg\min_{\phi} \left[\mathfrak{D}\left(I_2, I_1 \circ \phi\right) + \alpha\, \mathcal{R}(\phi) \right] \tag{4.1}$$

where $\mathfrak{D}(\cdot)$ measures dissimilarity between the images, $I_1 \circ \phi$ is the transformed moving image such that $\left(I_1 \circ \phi\right)\left(\mathbf{X_2}\right) = I_1\left(\phi(\mathbf{X_2})\right)$, $\mathcal{R}(\cdot)$ is a regularization function that penalizes non-smooth deformation maps, and α is a regularization parameter.

[1] Diffusion MRI images can also be subject to other forms of distortion and misalignment, e.g., due to eddy currents, gradient nonlinearities, motion etc. (see chapter 2 and it references). In this work, similar to previous approaches [Bhushan et al., 2012, Ardekani and Sinha, 2005, Gholipour et al., 2006, Yao and Song, 2011], we assume that these other sources of distortion are negligible.

The choice of dissimilarity measure $\mathfrak{D}(\cdot)$ is crucial for accurate registration of the images and it is desirable that $\mathfrak{D}(\cdot)$ be sensitive to slight differences in alignment between the images. Several intensity based dissimilarity measures have been developed, which are suitable for different applications and image modality. Here we briefly review few measures which are relevant to the distortion correction approaches (see Derek L. G. Hill and Hawkes [2001] and Oliveira and Tavares [2012] for broader review of different dissimilarity measures).

The sum of squared differences (SSD) is a simple and intuitive dissimilarity measure based on pixel/voxel intensity differences. If we express the moving image I_1 after transformation with deformation ϕ as $\overline{I}_1 \equiv I_1 \circ \phi$ for brevity of the notation, then the SSD dissimilarity is expressed as [Derek L. G. Hill and Hawkes, 2001]

$$\mathfrak{D}_{\text{SSD}}(I_2, \overline{I}_1) = \frac{1}{N_v} \sum_{\mathbf{X} \in \Omega} \left[I_2(\mathbf{X}) - \overline{I}_1(\mathbf{X}) \right]^2, \tag{4.2}$$

where Ω represents the set of voxels that are present in both the images and N_v is the cardinality of Ω. SSD is a well-behaved measure in images with similar contrast which may differ only by addition of Gaussian noise [Derek L. G. Hill and Hawkes, 2001, Viola, 1995]. SSD is a common choice for registration based distortion correction methods which use T_2 [Kybic et al., 2000, Ardekani and Sinha, 2005, Pierpaoli et al., 2010, Wu et al., 2008, Huang et al., 2008] However, SSD is generally not appropriate for inter-modal registration problems [Derek L. G. Hill and Hawkes, 2001, Viola, 1995].

Mutual information [Viola and Wells III, 1997, Maes et al., 1997] and correlation ratio [Roche et al., 1998] are common dissimilarity measures that depend on the relationship between the distributions of the image intensities and have been used widely in inter-modal registration [Oliveira and Tavares, 2012, Derek L. G. Hill and Hawkes, 2001, Jenkinson and Smith, 2001]. Normalized mutual information (NMI) is a variant of MI that is less sensitive to changes in the overlap in images as compared to MI itself [Studholme et al., 1999] and is defined as

$$\mathfrak{D}_{\text{NMI}}(I_2, \overline{I}_1) = \frac{H(\overline{I}_1, I_2)}{H(\overline{I}_1) + H(I_2)} \tag{4.3}$$

where $H(\overline{I}_1, I_2) = -\sum_{i,j} p(i,j) \log p(i,j)$ is the standard joint entropy computed from joint intensity histogram $p(i,j)$ of $\overline{I}_1$ and I_2; and $H(\overline{I}_1)$ and $H(I_2)$ are the marginal entropies computed similarly, but using the marginal histograms for $\overline{I}_1$ and I_2 in place of the joint histogram. We used a Parzen window estimate [Duda et al., 2001] for all histograms and used only the intensities from voxels in the overlapping region of the two images.

Correlation ratio (CR) measure the functional relationship between the images and is defined as [Roche et al., 1998]

$$\mathfrak{D}_{\text{CR}}(I_2, \overline{I}_1) = \frac{\sum_{k=1}^{K} N_k \operatorname{Var}(I_{2,k})}{N_v \operatorname{Var}(I_2)} \tag{4.4}$$

where $I_{2,k} = \{I_2(\omega); \omega \in \Omega_k\}$, $\Omega_k = \{\omega \in \Omega; \frac{(k-1)}{K} \leq \overline{I}_1(\omega) < \frac{k}{K}\}$ is the k^{th} iso-set of $\overline{I}_1$ in the image overlap region Ω, and N_v and N_k are the cardinalities of Ω and Ω_k respectively. In our implementation, we also used cost apodization for CR similar to that described in [Jenkinson et al., 2002].

The key difference between these dissimilarity measures is about assumption about the relationship between the intensities of the images (after alignment): SSD assumes intensity to be same, CR assumes a functional dependence (based on variance of the intensity distribution) and MI-based measures assume statistical dependence (based on entropy of the intensity distribution) [Sarrut et al., 2013]. Because of this, NMI and CR are suitable for inter-modal registration, however as noted earlier, these measure are not always well-behaved and can be challenging to optimize over large number of registration parameters as in case of non-rigid registration [Oliveira and Tavares, 2012, Derek L. G. Hill and Hawkes, 2001, Pluim et al., 2003, Tsao, 2003, Pluim et al., 2004, Jenkinson and Smith, 2001, Jenkinson et al., 2002]. We use the INVERSION approach, described next, to first transform the contrast of the T2W-EPI image to look like that of the T_1-weighted image (and vice versa), effectively matching the contrast of the images, which allows us to exploit the nice properties of the SSD cost function for distortion correction.

4.3 INVERSION

INVERSION is motivated by the fact that both T_1- and T_2-weighted images from the same subject have similar anatomical structure but have an approximately inverted contrast relationship. Specifically, the image intensities are ordered such that white matter > gray matter > CSF in a T_1-weighted anatomical image, while CSF > gray matter > white matter in a T_2-weighted image. In the INVERSION method, we define the dissimilarity measure between T_1-weighted anatomical image I_{T1} and a corresponding T2W-EPI image I_{EPI} as

$$\mathfrak{D}_{\text{INV}}(I_{\text{EPI}}, I_{\text{T1}}) = \mathfrak{D}_{\text{SSD}}\Big(\mathcal{F}_{I_{\text{T1}}}(I_{\text{EPI}}), I_{\text{T1}}\Big) + \beta\, \mathfrak{D}_{\text{SSD}}\Big(\mathcal{F}_{I_{\text{EPI}}}(I_{\text{T1}}), I_{\text{EPI}}\Big) \tag{4.5}$$

where $\mathcal{F}_{I_{\text{T1}}}(I_{\text{EPI}})$ transforms the intensity of I_{EPI} to match the contrast of I_{T1}, $\mathcal{F}_{I_{\text{EPI}}}(I_{\text{T1}})$ transforms the intensity of I_{T1} to match the contrast of I_{EPI} and β is a scalar weighting parameter determined experimentally. We assume, without loss of generality, that the intensities of both I_{T1} and I_{EPI} are normalized to lie in the range [0,1] and express the first contrast matching transform as

$$\mathcal{F}_{I_{\text{T1}}}(I_{\text{EPI}}) = \left[f_{I_{\text{T1}}, I_{\text{EPI}}}(1 - I_{\text{EPI}}) \cdot M_{I_{\text{EPI}}}\right] \tag{4.6}$$

where $M_{I_{\text{EPI}}}$ is a binary image representing the brain mask for the T2W-EPI image and $f_{I_{\text{T1}}, I_{\text{EPI}}}(\cdot)$ is a monotonically increasing histogram matching function which is computed by matching the histograms of intensities inside the brain masks of the anatomical image I_{T1} and the inverted T2W-EPI image $(1 - I_{\text{EPI}})$. $\mathcal{F}_{I_{\text{EPI}}}(I_{\text{T1}})$ is expressed in a similar fashion as $\mathcal{F}_{I_{\text{T1}}}(I_{\text{EPI}})$ *i.e.* by interchanging I_{T1} and I_{EPI}. We

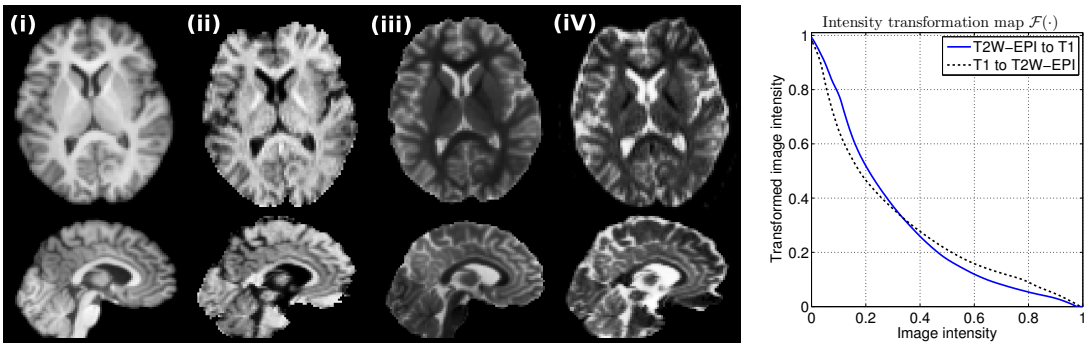

(a) (b)

Figure 4.1: An example of INVERSION in an *in vivo* dataset. (a) shows corresponding slices from (i) the T_1-weighted image, (ii) the intensity transformed T2W-EPI image, (iii) the intensity transformed T_1-weighted image, and (iv) the original T2W-EPI image. (b) Intensity transformation maps $\mathcal{F}(\cdot)$ in INVERSION for voxels inside the brain mask for the dataset shown in (a).

use histogram matching because both the T2W-EPI and T_1-weighted image are acquired for the same subject and should depict the same tissues and tissue boundaries, but may differ in the intensities of each tissue. As a result, an intensity transformation should be able to approximately match the histogram of the images. We used our implementation of the histogram matching method described in [Gonzalez and Woods, 2002] to estimate $f_{I_{\mathrm{T1}},I_{\mathrm{EPI}}}(\cdot)$. In our studies, the brain masks are obtained by intensity thresholding of the T2W-EPI image and by using the BrainSuite software [Shattuck et al., 2001] for the T_1-weighted image. An example of the INVERSION intensity transformation is shown in Fig. 4.1 for an *in vivo* dataset.

INVERSION is similar in concept to previous methods that estimate synthetic image contrast [Friston et al., 1995, Mercier et al., 2012, Choi et al., 2011, Miller et al., 1993, Roy et al., 2013, Meyer, 2007, Kroon and Slump, 2009, Guimond et al., 2001]. Specifically, some MRI-PET [Friston et al., 1995] and MRI-ultrasound [Mercier et al., 2012] co-registration methods also use image contrast transformations, though these transformations are generally quite complicated and depend on an initial tissue segmentation. Choi et al. [Choi et al., 2011] use a similar contrast transformation to enhance registration-based distortion correction, but do not use physics-based constraints on the non-rigid deformation field [Andersson and Skare, 2011, Studholme et al., 2000]. Other approaches use a multiple-contrast atlas to estimate image intensities for different modalities, either using a non-rigid registration framework [Miller et al., 1993] or using a patch-based sparse intensity prediction approach [Roy et al., 2013]. These approaches require solving large optimization problems, whereas INVERSION is computationally cheaper and does not require the construction of an atlas. INVERSION also has similarities to a histogram bin transformation approach [Meyer, 2007] for registration of MRI and CT images, although that approach requires user interaction to setup the intensity bin mapping between the histograms of the images while INVERSION

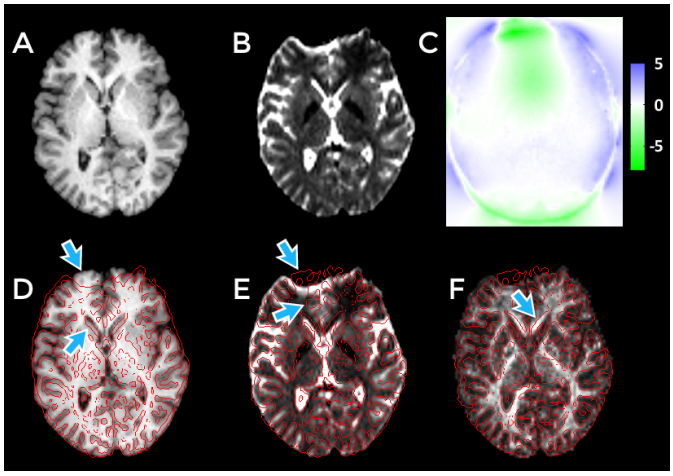

Figure 4.2: Example of distortion in a human brain T2W-EPI image acquired with EPI sequence. (A) An undistorted T_1-weighted anatomical image. (B) T2W-EPI image from a diffusion dataset. (C) The displacement map (in millimeters) computed from an acquired fieldmap. Edges from the T2W-EPI image are overlaid in red on the T_1-weighted image in (D) and vice-versa in (E) after rigid alignment (using INVERSION approach described later). Arrows point to areas with substantial distortion. (F) The fractional anisotropy (FA) map derived from diffusion dataset overlaid with edges from the T_1-weighted image in red.

is completely automated. In other similar registration methods, a contrast relationship is estimated by using the joint histogram [Kroon and Slump, 2009] or by assuming a polynomial relationship between the intensities of different images [Guimond et al., 2001]. Both these approaches perform nicely when the registration parameters are initialized well, but poorly otherwise. INVERSION uses an intensity mapping that matches the histograms of the two images so that registration works well even for large displacements between the two images.

4.4 Co-registration and distortion correction using INVERSION

As reviewed in section 2.3, EPI images can contain geometric distortions in the presence of B_0 inhomogeneity. An *in vivo* example is shown in Fig. 4.2: while the T_1-weighted image has negligible geometric distortion, the T2W-EPI image is substantially distorted. This leads to discrepancies between the two images when they are rigidly aligned to each other without distortion correction. Specifically, it can be noticed that image edges do not align correctly in distorted regions. We assume a standard DWI acquisition in which all images have the same EPI phase encoding direction (PED), as used in the vast majority of modern DWI acquisitions.[2]

[2]In cases where data is available with multiple different PEDs, the method described in this chapter is likely to be suboptimal relative to that described in chapter 5, which belong to class of more advanced methods that leverage additional information

Our registration-based distortion correction is initialized using a simple rigid alignment of the T2W-EPI and T_1-weighted anatomical images (described in Section 4.4.1), which is followed by non-rigid registration to estimate the distortion (described in Section 4.4.2). Note that even if the DWIs have been distortion corrected using other methods, a rigid alignment is required for co-registration of the T_1-weighted anatomical image and diffusion images. As a result, the rigid registration approach described in Section 4.4.1 is still useful in, e.g., cases where a B_0 fieldmap was acquired.

4.4.1 Rigid alignment using INVERSION

For rigid alignment, we set the T2W-EPI image (I_{EPI}) as the static image and we seek to estimate a rigid transformation $\phi_{R_1} : \mathbf{X}_{\text{EPI}} \rightarrow \mathbf{X}_{\text{T1}}$ that maps the EPI coordinate $\mathbf{X}_{\text{EPI}}$ to the corresponding T_1-weighted anatomical coordinate $\mathbf{X}_{\text{T1}}$. The optimal rigid transformation ϕ_{R_1} is estimated by solving

$$\widehat{\phi}_{R_1} = \arg\min_{\phi_{R_1}} \mathfrak{D}_{\text{INV}}\left(I_{\text{EPI}}, I_{\text{T1}} \circ \phi_{R_1}\right) \tag{4.7}$$

where $I_{\text{T1}} \circ \phi_{R_1}$ is the transformed T_1-weighted anatomical image. The rigid transformation ϕ_{R_1} is parametrized by a vectors of six elements, representing translational and rotational components. Note that the contrast matching functions $\mathcal{F}_{I_{\text{EPI}}}(\cdot)$ and $\mathcal{F}_{I_{\text{T1}}}(\cdot)$ are independent of rigid alignment and only need to be calculated once as a pre-computation before the actual registration process begins. In our experience, we found that the first contrast matching term in Eq. (4.5) is sufficient to obtain an accurate rigid alignment, so we set $\beta = 0$ in eq. (4.5) while solving Eq. (4.7), which also lowers the computational requirements.

We use a two step method to achieve robustness to local minima for large transformations while solving Eq. (4.7). Our first step involves a coarse grid search to quickly initialize with reasonable rotation parameters. Similar to other approaches [Oliveira and Tavares, 2012, Derek L. G. Hill and Hawkes, 2001, Jenkinson and Smith, 2001], we use the centroids (center of mass) of each image to define the origins of their respective coordinate systems. Then we evaluate the registration cost function for each of several different rotations from a coarse grid defined over the three Euler angles. To enhance computational speed, this step is performed using low resolution images, which are generated by applying a Gaussian blur with a full-width at half-maximum (FWHM) of 5mm, followed by downsampling. For typical datasets (such as those shown in our results), this first stage requires 15-20 seconds to search over 2197 different rotations (stepsize of 15° over range of -90° to 90° for each Euler angle) on a modern 4-core 2.10GHz processor.

The second step applies a simple gradient descent approach to refine the registration parameters, initialized with the best rotation parameters found in the first step. We use numerically-computed gradients

about the structure of multi-PED data [Bhushan et al., 2013, 2014b, Andersson et al., 2003, Gallichan et al., 2010, Chang and Fitzpatrick, 1992, Bowtell et al., 1994, Morgan et al., 2004, Holland et al., 2010].

and a multi-resolution approach. Our two-step approach does not guarantee finding the globally-optimal solution, but is both fast and simple. In addition, our experience suggests that the well-behaved nature of the INVERSION cost function makes our approach robust to local minima and increases the chances of accurately aligning the images.

4.4.2 Distortion correction using INVERSION

Susceptibility-induced geometric distortions in diffusion MRI images are commonly modeled as being 1-dimensional as they occur primarily along the PED and are generally negligible along the readout and slice directions (see section 2.3.1). We can express the deformation due to B_0 inhomogeneity as a map $\phi_{\Delta B_0} : \mathbf{X}_{\text{U}} \rightarrow \mathbf{X}_{\text{EPI}}$ which maps the coordinate $\mathbf{X}_{\text{U}} = (x_{\text{U}}, y_{\text{U}}, z_{\text{U}})$ in an ideal undistorted image to the erroneous coordinate $\mathbf{X}_{\text{EPI}} = (x_{\text{EPI}}, y_{\text{EPI}}, z_{\text{EPI}})$ in a distorted EPI image. Assuming that the PED is oriented along the y-axis, the ideal undistorted image I_{U} and distorted EPI image I_{EPI} are related as (see section 2.3.1 for details)

$$I_{\text{U}} \approx \frac{\partial y_{\text{EPI}}}{\partial y_{\text{U}}} \left(I_{\text{EPI}} \circ \phi_{\Delta B_0} \right). \tag{4.8}$$

Further,

$$\begin{aligned} \mathbf{X}_{\text{EPI}} &= \phi_{\Delta B_0}(x_{\text{U}}, y_{\text{U}}, z_{\text{U}}) && (4.9) \\ &= \left(x_{\text{U}},\ y_{\text{U}} + \gamma \Delta B_0(x_{\text{U}}, y_{\text{U}}, z_{\text{U}}) N T_{es} \lambda_y,\ z_{\text{U}} \right) && (4.10) \end{aligned}$$

where ΔB_0 is the B_0 inhomogeneity (units of T), γ is the gyromagnetic ratio (42.57×10^6 Hz/T for protons), T_{es} is the echo spacing in seconds, N is the number of phase encoding steps in the EPI acquisition and λ_y is the spatial resolution of each voxel along the PED in appropriate units.

In the absence of a fieldmap, we estimate ΔB_0 by registering the distorted I_{EPI} to the undistorted anatomical images[3] I_{T1} in a non-rigid registration framework. This requires estimation of a non-rigid deformation map ($\phi_{\Delta B_0}$) which would undistort I_{EPI} and a rigid transformation $\phi_{R_2} : \mathbf{X}_{\text{U}} \rightarrow \mathbf{X}_{\text{T1}}$ which would align I_{T1} to the undistorted image I_{U}. The optimal map is obtained by solving

$$[\widehat{\phi}_{R_2}; \widehat{\phi}_{\Delta B_0}] = \underset{[\phi_{R_2}; \phi_{\Delta B_0}]}{\arg\min} \left[\mathfrak{D}_{\text{INV}} \left(\frac{\partial y_{\text{EPI}}}{\partial y_{\text{U}}} \left(I_{\text{EPI}} \circ \phi_{\Delta B_0} \right), I_{\text{T1}} \circ \phi_{R_2} \right) + \alpha\, \mathcal{R}(\phi_{\Delta B_0}) \right] \tag{4.11}$$

where $\mathcal{R}$ is a regularizer explained later and α is a scalar weighting parameter determined experimentally. $\mathfrak{D}_{\text{INV}}(\cdot)$ is defined in eq. (4.5) with β equal to the ratio of mean intensities of I_{T1} and I_{EPI}. In principle, we

[3] Note that the anatomical images can also be affected by several artifacts, including susceptibility and gradient non-linearity, leading to the distortion of the images along all three dimensions [Brown et al., 2014b, Jovicich et al., 2006], Bernstein et al. [2004, Chapter 13]. However, the size of distortion in anatomical images acquired using conventional scheme is order of magnitudes smaller than that in EPI images in most cases [Brown et al., 2014b], Bernstein et al. [2004, Chapter 13]. Hence, in practice the anatomical images act as a good undistorted template.

could have estimated a rigid transformation that maps the undistorted EPI image to the T_1 image, instead of the other way around. The choice shown in Eq. (4.11) was motivated by computational efficiency. We parameterize $\phi_{\Delta B_0}$ as the outer product of 1D cubic B-spline kernels with uniformly spaced control points and coefficients $\mathbf{C}_{i,j,k}$ corresponding to the $(i,j,k)^{\text{th}}$ control point, such that [Rueckert et al., 1999]

$$\begin{aligned}\phi_{\Delta B_0}(\mathbf{X}_U) &= \phi_{\Delta B_0}(x_U, y_U, z_U) \\ &= \sum_{i,j,k} \mathbf{C}_{i,j,k}\, \mathcal{B}\left(\frac{x_a}{\delta} - i\right) \mathcal{B}\left(\frac{y_a}{\delta} - j\right) \mathcal{B}\left(\frac{z_a}{\delta} - k\right)\end{aligned} \tag{4.12}$$

where $\mathcal{B}$ is the cubic B-spline kernel [Bartels et al., 1987] and δ is the spacing between the control points in all the directions. In order to constrain the deformation along the PED, we only allow the y-coefficient of $\mathbf{C}_{i,j,k}$ to change while solving Eq. (4.11). We repeat and interpolate the end control points so that the deformation field is well-behaved everywhere, including along the boundary [Bartels et al., 1987]. We use a regularizer that penalizes the roughness of the control-point coefficients as described in [Chun and Fessler, 2009]. In our framework it is expressed as

$$\mathcal{R}(\phi_{\Delta B_0}) = \frac{1}{2} \sum_{i,j,k} \sum_{\mathbf{n} \in \mathcal{N}(\mathbf{C}_{i,j,k})} ||\mathbf{C}_{i,j,k} - \mathbf{C}_{\mathbf{n}}||^2 \tag{4.13}$$

where $\mathcal{N}(\mathbf{C}_{i,j,k})$ is the set of control-points that are neighbors of $\mathbf{C}_{i,j,k}$. This penalty encourages smoothness of the deformation field [Chun and Fessler, 2009].

We solve Eq. (4.11) using a multi-resolution approach, which helps to avoid local minima and enables faster computation [Oliveira and Tavares, 2012, Derek L. G. Hill and Hawkes, 2001]. Prior to solving Eq. (4.11), we rigidly align the T_1-weighted image to the distorted T2W-EPI image using the method described in sec. 4.4.1. The contrast matching functions $\mathcal{F}_{I_{\text{EPI}}}(\cdot)$ and $\mathcal{F}_{I_{\text{T1}}}(\cdot)$ depend on the estimate of $\phi_{\Delta B_0}$ (as the intensities in the T2W-EPI image are modulated by the Jacobian of the transformation) and so they should, ideally, be updated at each iteration. However, we found that changes in the contrast matching function were negligible at each iteration and so we only compute once at the beginning of each level of the multi-resolution approach. In our implementation the B-spline control points are refined twice, starting from a separation of 28mm to final separation of 7mm, in a multi-resolution approach using the Lane-Riesenfeld Algorithm [Lane and Riesenfeld, 1980]. We use a simple gradient descent method for all the optimization and use analytical expressions for the gradients for efficient computation.

	Dataset-1	Dataset-2	Dataset-3
T1-weighted	TE=3.09ms	TE=3.09ms	TE=3.5ms
	TR=2530ms	TR=2530ms	TR=2500ms
	TI=800ms	TI=800ms	TI=1200ms
	$1\times1\times1$ mm^3	$1\times1\times1$ mm^3	$1\times1\times1$ mm^3
Diffusion	TE=88ms	TE=115ms	TE=85ms
	TR=10000ms	TR=10000ms	TR=6000ms
	T_{es}=0.85ms	T_{es}=0.69ms	T_{es}=0.81ms
	$2\times2\times2$ mm^3	$2\times2\times2$ mm^3	$1.4\times1.4\times3.0$ mm^3
	b=1000s/mm^2	b=2500s/mm^2	b=1000s/mm^2
	GRAPPA 2$\times$	–	GRAPPA 2$\times$
B_0 Fieldmap	TE_1=10ms	TE_1=10ms	TE_1=4.92ms
	TE_2=12.46ms	TE_2=12.46ms	TE_2=7.38ms

Table 4.1: Acquisition parameters for the *in vivo* datasets used for evaluation. The diffusion datasets differ mainly in echo spacing (T_{es}), the use of parallel imaging, contrast parameters (TE, TR, and TI), b-values and resolution.

4.5 Datasets for evaluation

4.5.1 Simulation data

We evaluated the performance of the INVERSION method using simulated and multiple *in vivo* datasets. For simulations, we used images available from BrainWeb (http://brainweb.bic.mni.mcgill.ca/brainweb/) [Cocosco et al., 1997]. Although the BrainWeb phantom is artificially simple in contrast and image features, the availability of ground truth offers useful insight into the performance of the method. We used a simulated T_2-weighted spin echo image (TR=10000m, TE=120ms, Flip angle=90°, 2mm slice thickness) as the undistorted T2W-EPI image and also simulated a corresponding T_1-weighted MPRAGE image with 1mm isotropic resolution. To simulate EPI distortion, we used a real B_0 inhomogeneity map taken from an *in vivo* scan as ground truth distortion map and used a least-squares time segmentation approach to model the effects of field inhomogeneity on k-space data [Sutton et al., 2003, Gai et al., 2013]. We also added Gaussian noise to the modulus distorted image (in the image domain). The simulated distorted EPI image is shown in Fig. 4.7(b).

4.5.2 Experimental data

We also evaluated performance using a total of 22 *in vivo* single-shot EPI diffusion brain scans. All scans were acquired on 3T scanners and B_0 fieldmaps were used as references to evaluate the registration-

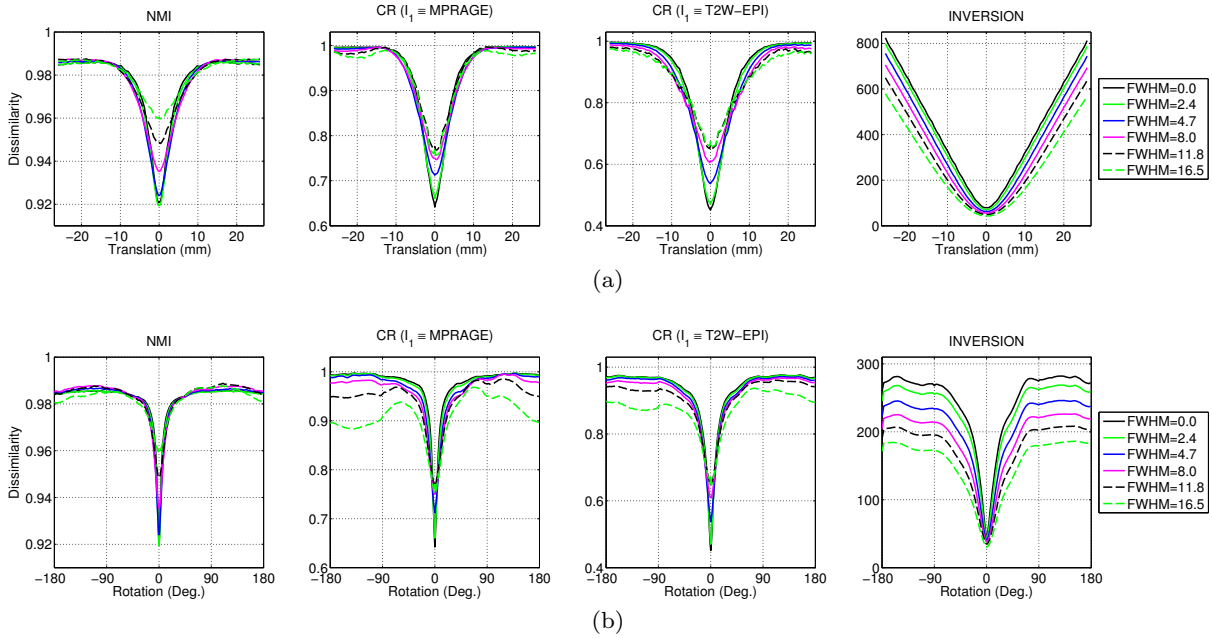

Figure 4.3: Behavior of different dissimilarity measures as a function of misalignment by (a) translation along the x-axis and (b) rotation along the x-axis. Different lines represent different level of smoothing applied to both images and illustrate behavior at different resolutions. The full-width at half-maximum (FWHM) of the Gaussian smoothing is reported in units of millimeters (mm).

based deformation estimates. These 22 scans are divided into three different groups with different acquisition parameters, as summarized in Table 4.1. The differences in acquisition parameters ensures a more comprehensive evaluation of the proposed method.

Dataset-1 was a single-subject dataset, with the acquisition specifically designed to yield a good distortion-corrected reference image. Specifically, we used a specialized acquisition scheme for dataset-1 where we acquired each diffusion image with 4 different PEDs, which were combined to form a distortion-corrected reference image using the accurate 4-PED full method described in [Bhushan et al., 2014b]. Datasets-2 and 3 represent typical diffusion images from ongoing neuroscience studies. Dataset-2 includes 10 subjects that were scanned at the University of Southern California under a grant to Hanna Damasio, PI, from the Air Force Office of Scientific Research (FA9620-10-1-109). Dataset-3 includes 11 subjects obtained from the NKI-Rockland sample [Nooner et al., 2012].

4.6 Results

4.6.1 Evaluation of dissimilarity measures

We studied the behavior of the different dissimilarity measures by observing how the different measures change when a T_1-weighted image is misaligned from a corresponding co-registered T2W-EPI image. We used the accurate 4-PED full distortion corrected T2W-EPI image from dataset-1 for these experiments in order to avoid confounding factors due to distortion present in the diffusion datasets. To generate a gold standard co-registration, the T_1-weighted image was rigidly registered to the T2W-EPI image using a manual procedure in Rview (http://rview.colin-studholme.net). The co-registered image pair was visually confirmed to have accurate alignment. Figure 4.3 illustrates the behavior of the different dissimilarity measures as we misalign the T_1-weighted image by applying translation or rotation. Since multi-resolution approaches are commonly used for registration, this comparison is performed with several different degrees of Gaussian smoothing. Since CR is not a symmetric measure [Roche et al., 1998], *i.e.*, $\mathfrak{D}_{\text{CR}}(I_1, I_2) \neq \mathfrak{D}_{\text{CR}}(I_2, I_1)$, we have plotted the two different versions of the CR measure that result from the two different possible choices of I_1. For the INVERSION measure, we use $\beta = 0$ in these experiments as both the terms in eq. (4.5) are based on SSD and we observed no improvement in performance by including the second term for rigid registration.

We show the behavior of misalignment with only translational components in Fig. 4.3(a) and with only rotational components in Fig. 4.3(b). The translation experiment (Fig. 4.3(a)) shows that the behavior of all cost functions is smooth when the Gaussian smoothing is large. Having a smooth cost function makes it easier to accurately solve the optimization problem, and helps justify the use of a multi-resolution approach. However, we observe that both the CR and NMI measures exhibit non-convex behavior when the translation is large. In contrast to CR and NMI, the INVERSION dissimilarity measure has a convex appearance even for large translational misalignment. The shape of this function suggests that it might be better-suited than CR and NMI for robustly finding the translational components.

The rotation experiment (Fig. 4.3(b)) shows similar behavior *i.e.* all cost functions are smooth when the Gaussian smoothing is large. However, all cost functions show non-convex behavior at large rotational misalignment and have local minima away from the globally-optimal solution for all levels of Gaussian smoothing. This means all the method could struggle to converge to the optimal solution using local optimization methods. This justifies our use of coarse grid search in Sec. 4.4.1 to find a good initialization with a limited number of cost evaluations. Fig. 4.3(b) shows that among all measures, the INVERSION measure has the widest area around the optimal solution which is well-behaved, especially for large Gaussian smoothing. This suggests that it has a higher chance of finding a good initial estimate in the coarse search over the rotation parameters and could avoid the need for multi-start optimization.

Expanding on our previous experiment, we next examined the characteristics of the different dis-

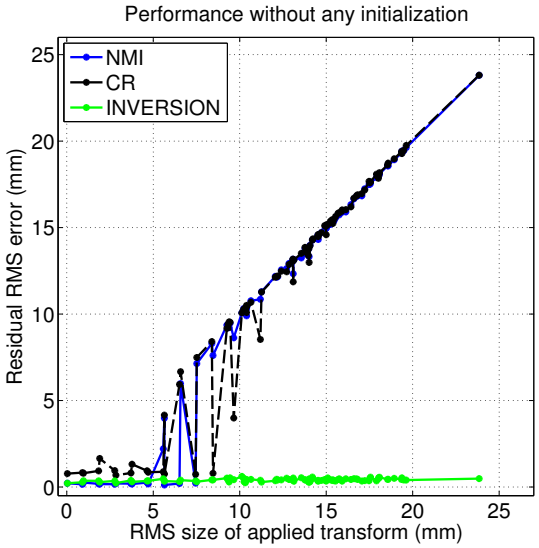

Figure 4.4: Performance of different dissimilarity measures as a function of the applied transformation in a rigid registration experiment without any initialization.

similarity measures by performing rigid registration, without any initialization, of the T_1-weighted and T2W-EPI images after applying known rigid transformations to the T_1-weighted image. Specifically, we applied 96 known rigid transformations: 32 with only translation, 32 with only rotation and 32 with both translation and rotation. For each trial and each dissimilarity measure (NMI, CR, and INVERSION), a 6-parameter rigid registration was performed without any initialization and the residual root mean square (RMS) error in the rigid alignment was computed for each trial. The RMS errors were computed using the method described in [Jenkinson and Smith, 2001, Jenkinson, 2000] where we represent the rigid transformations as 4×4 affine matrices. Specifically, for each applied (known) rigid transformation $\mathbf{A}$, we obtain an estimated transformation $\widehat{\mathbf{A}}$ from the registration procedure. The RMS error in millimeters is then given by $d_{\text{RMS}} = \sqrt{\frac{1}{5}a^2\,\text{Tr}(\mathbf{M}^\top\mathbf{M}) + \mathbf{t}^\top\mathbf{t}}$ where a is the radius of the brain region (with a spherical approximation), while $\mathbf{M}$ is a 3×3 matrix and $\mathbf{t}$ is a column vector of length 3 computed according to $\left[\begin{smallmatrix}\mathbf{M} & \mathbf{t}\\ 000 & 0\end{smallmatrix}\right] = \widehat{\mathbf{A}}^{-1}\mathbf{A} - \mathbf{I}$. For CR based registration, we used the T2W-EPI image as I_1, since as suggested by Fig. 4.3, this leads to a better-behaved cost function and higher accuracy.

The results of this evaluation are shown in Fig. 4.4. In the absence of any initialization, the CR and NMI based methods perform well for small misalignments (approximately less than 10 mm) but perform poorly when the misalignment is large. This observation is consistent with the relatively flat behavior of these measures and presence of local minima that was observed in Fig. 4.3. In contrast, the INVERSION method consistently showed good performance across all transformations and was robust to large transformation even without any initialization. This demonstrates the well-behaved nature of INVERSION over a wider region around the optimal solution. However, it should be noticed that whenever the NMI

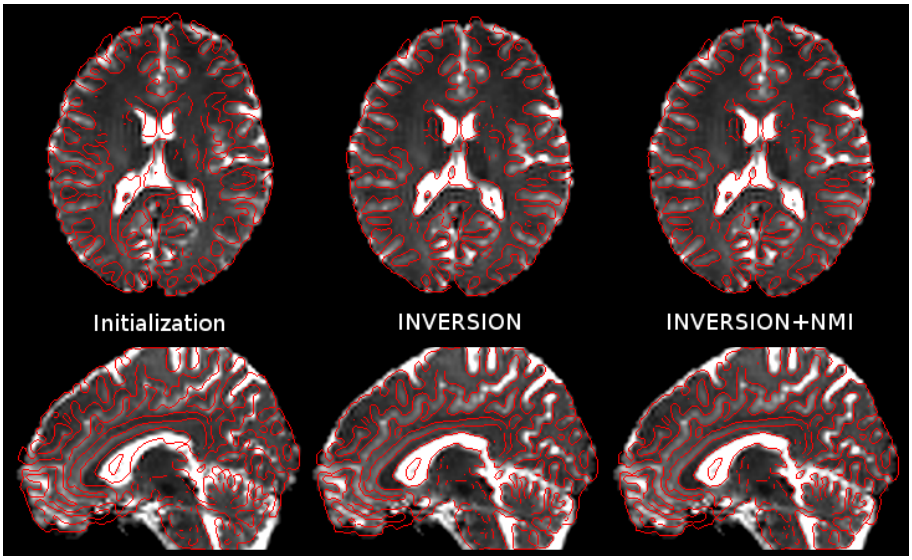

Figure 4.5: Result of the rigid registration procedure an *in vivo* image from Dataset-2 dataset (after distortion correction using fieldmap). The T2W-EPI image is overlaid by edge maps from the MPRAGE image in red (left) after initialization, (center) after INVERSION, and (right) after NMI-based refinement. NMI-based refinement adds a very subtle improvement which can be best noticed around edges of ventricles. Note that all other results presented in this chapter do not use any NMI-based refinement.

based measure performed well, it showed lowest error among all the measures. This could probably be explained by the fact that it makes the fewest assumptions about the different images, and is therefore the least sensitive to assumption violations. This motivated us to use the NMI based registration as a refinement step after INVERSION in our implementation in BrainSuite Diffusion Pipeline (BDP) software (http://brainsuite.org/). Fig. 4.5 shows a result of such refinement (note that all other results presented in this chapter do not use any NMI-based refinement). It can be noticed that most edges are well aligned with sulci and gyri after INVERSION and the NMI-based refinement adds a very subtle improvement.

4.6.2 Comparison with existing methods for rigid-alignment

We also compared INVERSION to two registration methods provided in the FMRIB Software Library (FSL) [Jenkinson et al., 2012] in a rigid registration experiment similar to that described in the previous section. We used the default settings with 6 degrees of freedom on FMRIB's Linear Image Registration Tool (FLIRT version 6.0) as the first method which uses a CR-based cost function in a hybrid global-local optimization approach for inter-modal rigid-registration [Jenkinson and Smith, 2001, Jenkinson et al., 2002]. For the second method we used EPI-Reg (http://fsl.fmrib.ox.ac.uk/fsl/fslwiki/FLIRT/UserGuide#epi_reg) which uses a boundary-based cost function [Greve and Fischl, 2009] along with FLIRT's global-local optimization approach. These two methods were selected for comparison be-

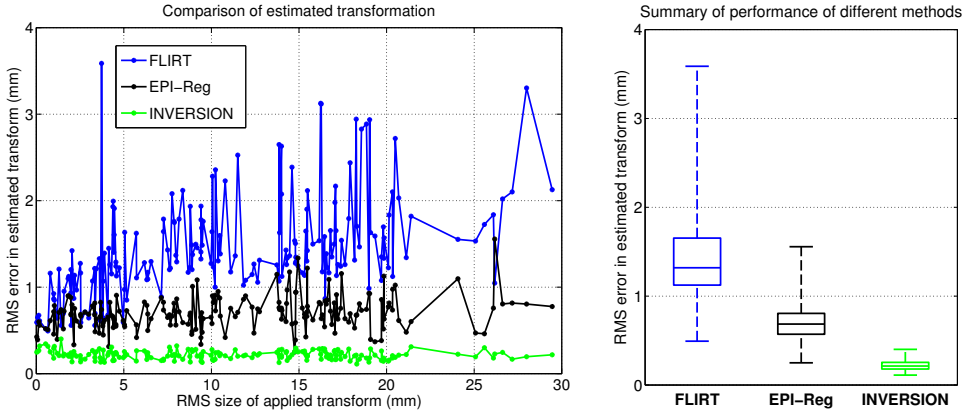

Figure 4.6: (a) Comparison of INVERSION to existing methods in a rigid registration experiment. (b) Box-and-whisker plot showing the summary of performance of different methods. The line inside the box represents the median RMS error and the whiskers extend to minimum and maximum RMS error.

cause FLIRT is widely used for affine registration by brain-mapping community and because EPI-Reg is specifically designed for registration of EPI images to anatomical (e.g. T_1-weighted) images. We applied 194 known (randomly generated) rigid transformations to the pre-registered T_1-weighted MPRAGE image from the previous section and used all the methods to estimate the rigid deformation. We used the accurate 4-PED full distortion corrected T2W-EPI image from dataset-1 as the static image for all the methods to avoid confounding factors due to distortion. Fig. 4.6(a) and (b) compares the performance of different methods in this experiment. The results show that all the three methods show low RMS error across all applied transformations. EPI-Reg performs better than FLIRT in most cases, which is expected as EPI-Reg is specifically tailored for registration with EPI images and uses a sophisticated tissue classification for boundary-based cost function. The proposed INVERSION method shows consistent behavior and the lowest RMS error for most of the applied transformation. Fig. 4.6(b) summarizes of the performance across all the applied transformation and indicates that the INVERSION based method outperforms all the other methods in this comparison.

4.6.3 Evaluation of INVERSION-based distortion correction

We first evaluated the proposed distortion correction method using the BrainWeb simulation data, comparing the distortion field estimated by INVERSION with the ground truth B_0 inhomogeneity map. Fig. 4.7(a) shows this comparison as a joint-histogram, which was computed using a Parzen-window estimate of the binned voxel counts. For ideal distortion correction, the joint histogram should be concentrated along the 45° line where the estimated distortion is equal to the true distortion. As seen in

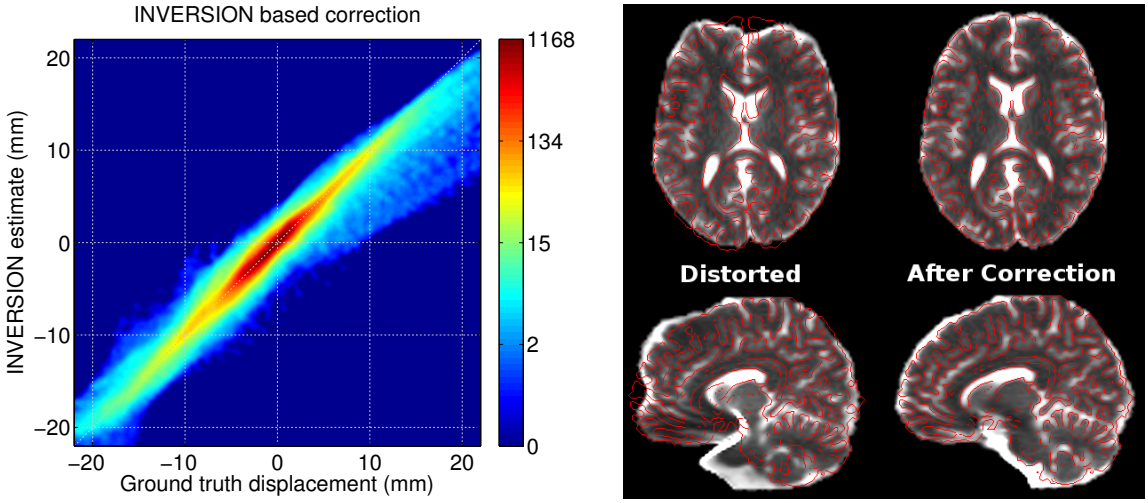

Figure 4.7: Performance of INVERSION-based distortion correction in the simulated BrainWeb dataset. The scatterplot of estimated displacement versus ground true displacement (calculated from the applied fieldmap) is shown as a joint histogram in (a). Note that the colorbars use a logarithmic scale to enhance visualization of the results for both minimally and severely distorted voxels. (b) Qualitative result of the INVERSION based correction in (top) an axial and (bottom) a sagittal slice. T2W-EPI images are overlaid with edge maps from the T_1-weighted MPRAGE image in red.

Fig. 4.7(a) our distortion estimate closely follows the ground truth. The mean absolute error in the displacement estimate was 0.8 ± 1.4 mm inside the brain mask. Fig. 4.7(b) shows a qualitative result of the corrected T2W-EPI images with edge maps from the anatomical image overlaid in red. It can be noticed that edges align well with sulci and gyri accurately after INVERSION based distortion correction.

Next, we evaluated the performance of the proposed registration-based distortion correction method using several *in vivo* datasets. We measured performance by comparing the INVERSION displacement field against that from the corresponding fieldmap. We also compared the performance of the proposed method to that of a NMI-based distortion correction method, described in [Bhushan et al., 2012]. A MI-based method was used for this comparison because it has been used for EPI distortion correction in several previous approaches [Studholme et al., 2000, Pierpaoli et al., 2010, Wu et al., 2008, Bhushan et al., 2012, Gholipour et al., 2006, Yao and Song, 2011] and because MI-based methods are widely used for inter-modal registration [Studholme et al., 1999, Viola and Wells III, 1997, Oliveira and Tavares, 2012, Derek L. G. Hill and Hawkes, 2001]. We present the results using the two methods for dataset-1 in Fig. 4.8. Fig. 4.8(a) shows the joint-histogram of the displacement estimates and the reference inside the brain-mask. As seen in the figure, the NMI-based method performs well for small distortions, but has large deviations from the 45° line for larger distortions. In contrast, the joint histogram for the INVER-

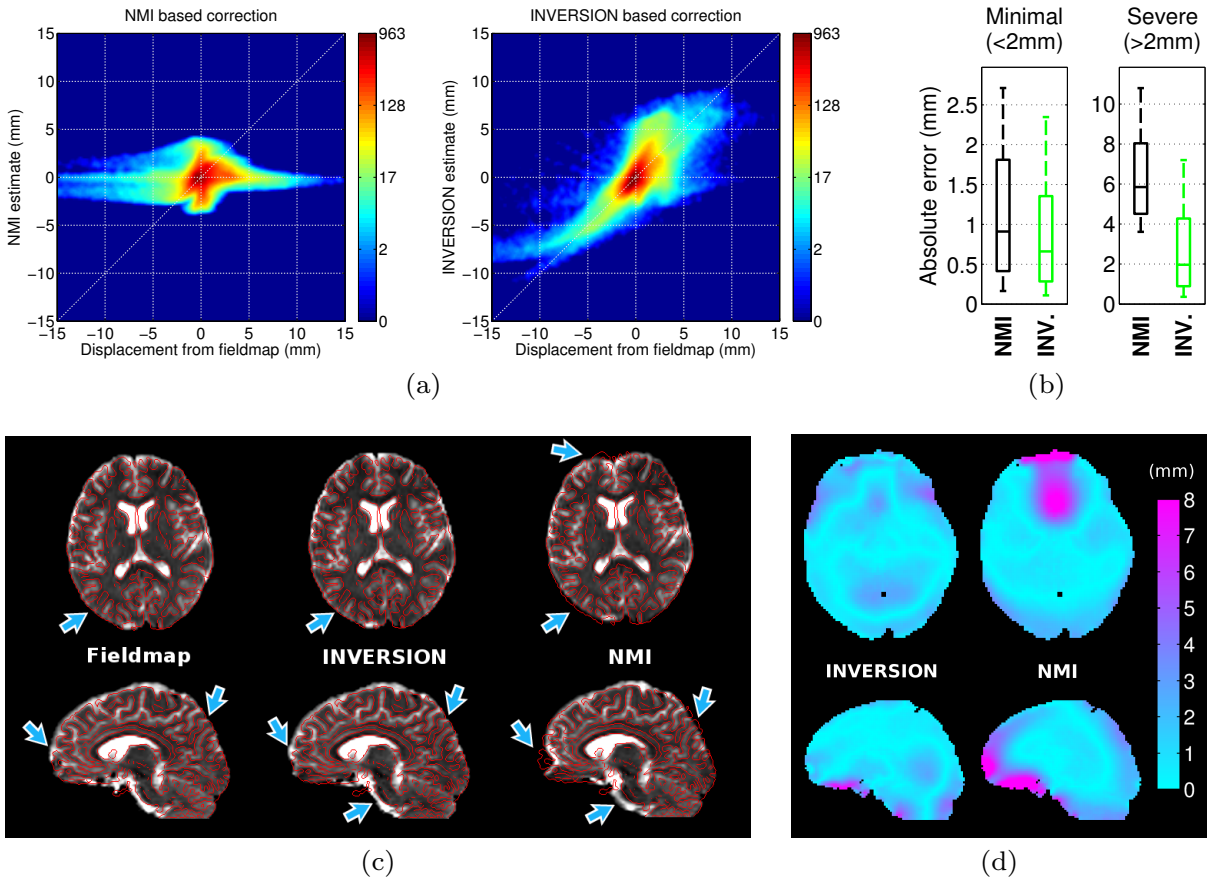

Figure 4.8: Performance of registration-based distortion correction in dataset-1. (a) The joint-histogram of the reference displacement (calculated from the fieldmap) and estimated displacement using (left) NMI and (right) INVERSION based method. (b) Box-and-whisker plots showing the absolute error in displacement estimated using NMI and INVERSION based distortion correction methods across (left) minimally distorted and (right) severely distorted voxels. The box extends from 25^{th} to 75^{th} percentile with the interior line representing the median and the whiskers extending from 10^{th} to 90^{th} percentile. (c) Qualitative comparison of distortion correction methods in (top) an axial and (bottom) a sagittal slice. Fieldmap based correction is shown as a reference for comparison. The distortion-corrected T2W-EPI images are shown overlaid with edge maps from the T_1-weighted MPRAGE image in red. Arrows point to areas with inaccurate distortion correction in the NMI-based correction. (d) Visualization of the absolute errors (in mm) in displacement relative to the fieldmap estimated by INVERSION and NMI-based methods in (top) an axial and (bottom) a sagittal slice.

SION method is more concentrated around the 45° line indicating overall better estimation of distortion field in most areas. Fig. 4.8(b) summarizes the performance of both the methods across all the voxels. For easier comparison we divide all the voxels in two sets, one set with minimal distortion (less than 2mm of reference displacement) and the other with severe distortion (more than 2mm of reference displacement). The INVERSION approach shows overall lower absolute error in the displacement estimates for all the voxels as compared to NMI-based distortion correction. Fig. 4.8(c) shows a qualitative comparison of the corrected T2W-EPI images with edge maps from the anatomical image overlaid in red. We also show the corrected T2W-EPI images using the acquired fieldmap for reference. From the overlay images, it can be noticed that both the registration-based methods show similar alignment of anatomical structures, however there are some differences. The NMI based correction shows poorer performance in areas with severe distortion as can be seen in frontal and occipital areas of the brain. The INVERSION based distortion correction shows better correspondence than NMI to the reference correction, as seen in regions indicated by arrows. Fig. 4.8(d) shows absolute errors in the displacement estimates as compared to that calculated from the fieldmap. The NMI based method shows larger errors around air-tissue boundaries, especially in frontal areas of the brain, while INVERSION based correction shows overall lower errors in all areas.

Next we compared the performance of INVERSION and NMI relative to the measured fieldmap using 21 scans from datasets-2 and 3. Fig. 4.9(a) shows the pooled joint-histogram of displacement estimates and reference displacement values for all subjects. Similar to previous observations, the joint histogram for the INVERSION method follows the 45° line indicating overall better estimation of distortion as compared to NMI-based method. Fig. 4.9(b) shows the histogram of absolute errors in the displacement estimates as compared to the fieldmap displacement for minimally and severely distorted voxels. Both registration methods show good and similar performance for minimal distortion. However, the NMI-based method had substantial error for severely distorted voxels. A summary of performance of both the method for individual subjects is shown in Fig. 4.9(c) for severely distorted voxels (performance was similar for both the methods for minimally distorted voxels). Of the two methods, INVERSION shows lower median error and lower range of absolute errors for all subjects. Runtimes for the INVERSION-based approach were in the range of 6-15 minutes for all subjects, while the NMI-based method had runtimes from 10-30 minutes. Both methods were implemented in MATLAB on a 4-core 2.10GHz processor.

4.7 Discussion

Our results demonstrate that INVERSION can accurately co-register diffusion MRI and T_1-weighted anatomical images. INVERSION improves the robustness of co-registration by using the simpler and

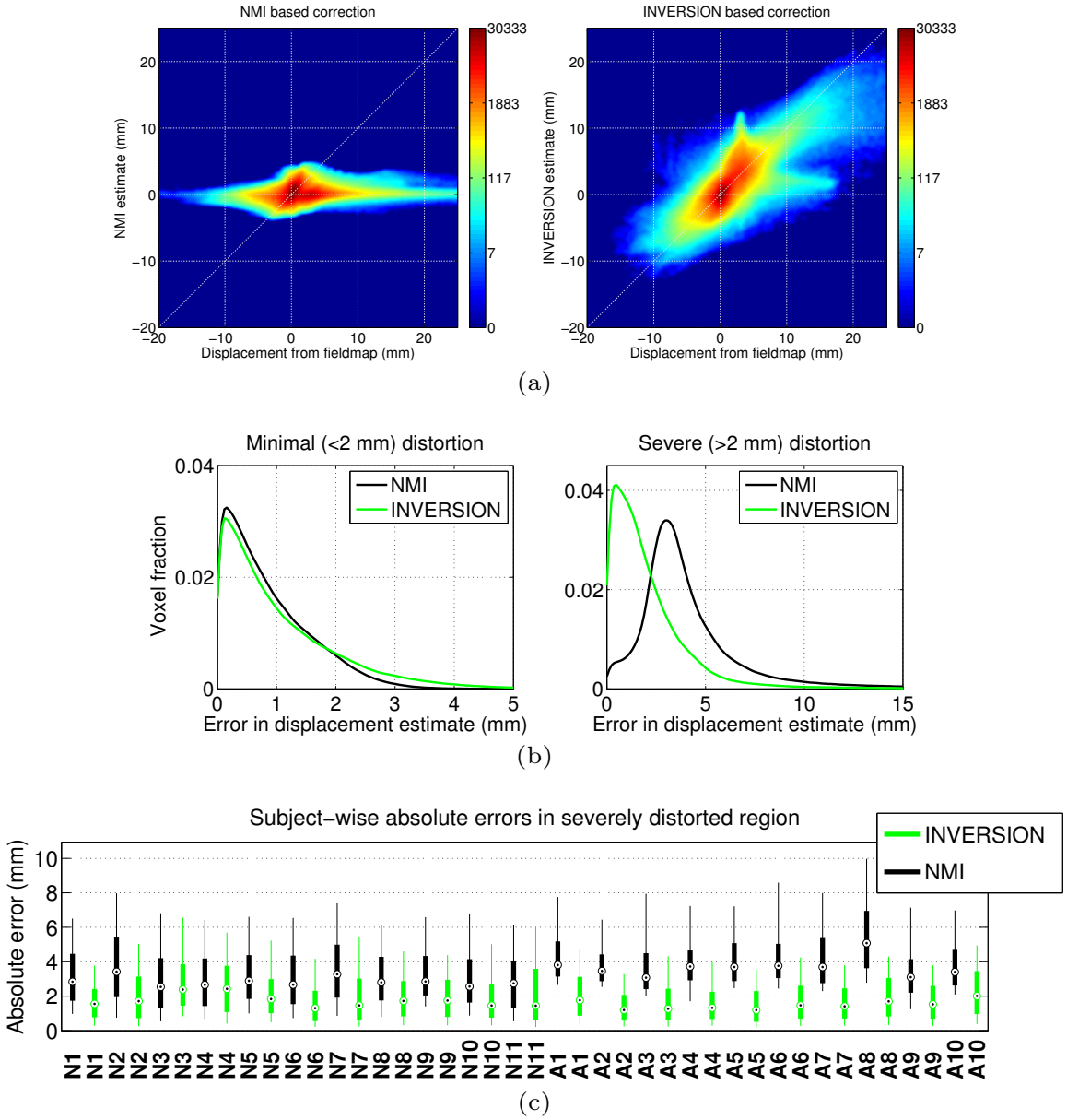

Figure 4.9: Performance of registration-based distortion correction with 21 subjects from dataset-2 and 3. (a) The pooled joint-histogram of the reference displacement (calculated from the fieldmap) and estimated displacement using (left) NMI and (right) INVERSION based methods for all subjects. Note that the colorbars use a logarithmic scale. (b) Histogram of the absolute errors in displacement estimate for (left) minimally and (right) severely distorted voxels. (c) Box-and-whisker plot showing the absolute error in the displacement estimated in severely distorted areas for each subject using NMI and INVERSION based distortion correction method. The box extends from 25th to75th percentile with the dot inside the box representing the median error and the whiskers extend from 10th to 90th percentile. Subjects from dataset-2 have labels starting with 'A' and subjects from dataset-3 have labels starting with 'N'.

smoother SSD dissimilarity measure by exploiting the approximately inverted contrast relationship in T_2- and T_1-weighted images of the human brain. This approach could also be applied to other multi-modal registration problems with similar contrast relationships.

It should be noted that more accurate correction of distorted EPI images can be performed in the presence of a fieldmap and/or more advanced acquisition schemes [Andersson and Skare, 2011, Jezzard and Balaban, 1995, Jezzard, 2012, Jenkinson et al., 2012, Munger et al., 2000, Kadah and Hu, 1998, Bhushan et al., 2013, 2014b, Andersson et al., 2003, Gallichan et al., 2010]. Hence, we recommend the use of these approaches when they are available. However, even in such cases, INVERSION can still be useful for rigid alignment of the diffusion images to the T_1-weighted anatomical image.

The intensity transformation used by INVERSION is only approximate, and this is especially true in regions with partial voluming between different tissue types. This is evident when looking at the boundaries between the white matter and the ventricles in Fig. 4.1. This difference is caused by both mismatched resolution and the fact that INVERSION should ideally be applied to white matter and cerebrospinal fluid separately when both are present within the same voxel (the inverse of the sum is not the same as the sum of the inverses). For rigid transformations, the low dimensionality of the transform appears to provide some level of robustness against this problem so that the final registration errors are small as shown in Fig. 4.6. For nonrigid transformations, we found that the symmetric measure, where we map intensities from T_1 to EPI as well as from EPI to T_1, reduces sensitivity to this effect producing improved results relative to mapping in only one direction.

INVERSION uses a coarse search for initialization of rotation parameters followed by a local optimization strategy to solve Eq. (4.7), which does not guarantee to find the optimally-global solution. Multi-start hybrid global-local optimization approaches [Jenkinson and Smith, 2001, Jenkinson et al., 2002] could be used in place of our search-based initialization scheme. However, as shown in the results section, the smoothness of our dissimilarity measure makes the search-based initialization followed by local optimization robust to local minima.

Use of INVERSION requires a background segmentation as the background does not contribute any MR signal and should appear dark in both the diffusion and anatomical images. This pre-processing step is straightforward for most images with reasonable SNR, as the background can be easily detected based on intensity thresholding.

Another factor which can limit the use of INVERSION are images with inhomogeneous intensities resulting from bias fields, severe susceptibility-induced distortion, and other related sources. Bias fields are uncorrected intensity nonuniformities that can have a variety of causes [Sled and Pike, 1998, Simmons et al., 1994]. In case one of the images suffers from a severe bias field, the inverted contrast relationship may no longer be a reasonable approximation. However the confounding effects of bias field are not limited to the INVERSION approach, and other dissimilarity measures based on MI and CR will

also have similar problems resulting from bias fields. Our acquired *in vivo* data had minor bias fields, but we did not notice any issues with INVERSION. In principle, bias field correction software [Shattuck et al., 2001, Sled et al., 1998] can be applied in cases where the scanner produces images with severe bias fields.

Similarly, areas affected by severe susceptibility-induced distortion may not follow the inverted contrast relationship, since susceptibility-induced distortion can change local tissue intensities. It is possible that severely distorted voxels may bias results when they are included in estimation of the contrast matching function. In order to reduce the effects of these severe intensity distortions, the contrast matching function could be estimated at each iteration while solving Eq. (4.11). Another approach could be to identify the severely distorted voxels and exclude them from the estimation of the contrast matching function. However, in our experience, the number of highly distorted voxels was small compared to the number of minimally distorted voxels in our images and the estimation of the histogram-matching function did not change substantially because of these voxels.

4.8 Conclusion

We described a new method for the correction of susceptibility-induced distortion in diffusion images and the co-registration of diffusion images with T_1-weighted anatomical images. Our method combines an appropriate mathematical model based on the physics of distortion in EPI images, with prior information about the contrast relationships between T_1 and T_2-weighted brain images. Evaluations of our method with *in vivo* datasets demonstrate improved distortion correction relative to normalized mutual information in diffusion weighted images in the absence of a fieldmap and robust alignment with T_1-weighted anatomical images. Our methods are implemented in a freely available software (http://brainsuite.org/).

Chapter 5

B_0-distortion correction in diffusion MRI using interlaced q-space sampling and constrained reconstruction

Diffusion MRI provides quantitative information about tissue microstructure that is not available through any other noninvasive imaging technology, and is routinely used in a wide variety of clinical and neuroscience applications [Jones, 2011, Tournier et al., 2011, Le Bihan and Johansen-Berg, 2012]. Quantitative diffusion MRI experiments acquire multiple Diffusion Weighted Images (DWIs) corresponding to different q-space samples. These DWIs are typically acquired using fast pulse sequences like Echo-Planar Imaging (EPI) to reduce acquisition time and minimize certain motion artifacts. As described in Sec. 2.3, EPI is sensitive to B_0 inhomogeneities because of low bandwidth along the phase encoding direction (PED). This leads to geometric distortion in reconstructed EPI images, which is particularly strong near the frontal sinuses and in the temporal lobes in the brain. Geometric image distortions can confound interpretation of the data and limit the accuracy of multimodal image analyses [Jones and Cercignani, 2010, Irfanoglu et al., 2012].

Multiple methods have been proposed to correct distortion in EPI images, as briefly reviewed in Sec. 2.4. One common approach, described in Sec. 2.3.2, uses a measured B_0 fieldmap to model the geometric warping observed in the EPI images, and generates a corresponding unwarping transform which is used to correct the distortions [Jezzard and Balaban, 1995]. This approach, which we will refer to as the 'single-PED method,' is widely used, but can be inaccurate in areas of substantial distortion [Jones and Cercignani, 2010].

There are two typical ways that severe geometric distortion artifacts manifest in EPI images: signal pile-up and signal stretching [Jezzard and Balaban, 1995]. Signal pile-up occurs when signal from

multiple spatial locations is erroneously mapped to the same spatial location. On the other hand, signal stretching occurs when signal that should be mapped to one voxel is spread across multiple voxels. Of these two, stretching is a one-to-many mapping that is relatively easy to correct, while pile-up correction is an ill-posed many-to-one mapping that is very difficult to correct using the single-PED method [Jones and Cercignani, 2010, Munger et al., 2000]. Distorted EPI brain images often contain both pile-up and stretching artifacts simultaneously in different image regions [Jezzard and Balaban, 1995].

In EPI, geometric distortions occur primarily along the PED (see Sec. 2.3.1), and a pile-up artifact can be converted into a stretching artifact (and vice versa) by reversing the PED [Morgan et al., 2004, Chang and Fitzpatrick, 1992][1]. The previously proposed reversed-gradient (RG) method, described in Sec. 2.4.2, uses this fact to substantially improve distortion correction relative to the single-PED method. The RG method acquires two DWIs for each q-space sample, each with a different PED so that they have opposite distortion characteristics. The complementary information from these two images allows substantially better distortion correction than the single-PED method [Jones and Cercignani, 2010, Morgan et al., 2004, Andersson et al., 2003]. However, the main limitation of the RG method is that it requires twice as many images, which increases the total scan time by a factor of two. This increased acquisition time can be prohibitive in many applications. Figure 5.1 illustrates typical results obtained by applying the RG and single-PED methods to an image from an EPI diffusion experiment. Note that the RG method yields corrected images with more uniform image intensity and better geometric fidelity to the undistorted anatomical reference.

This work proposes a new accelerated strategy for distortion correction which, similar to the RG method, uses information from multiple PEDs to improve the performance of distortion correction. However, unlike the RG method, the proposed approach does not require each q-space sample to be acquired multiple times. Instead, we propose to acquire each q-space sample once, using an interlaced sampling scheme that uses different PEDs for different q-space samples. This kind of subsampling is possible because neighboring q-space samples share a substantial amount of information, meaning that there is redundancy in the RG dataset if the distortion correction problem is formulated in an appropriate way. In the proposed approach, the acquired PED-interlaced DWIs are corrected for distortion using a constrained joint-reconstruction method that exploits the smoothness of diffusion data in q-space. Our results with simulated and experimental data suggest that the proposed method yields substantially better performance than the single-PED method, and can offer similar performance to the RG method while using only half the scan time. An implementation of the proposed method is also available from http://neuroimage.usc.edu/neuro/Resources/IPED.

[1] In this chapter, we use the term 'PED' to denote both the axis and the polarity of the phase encoding gradients.

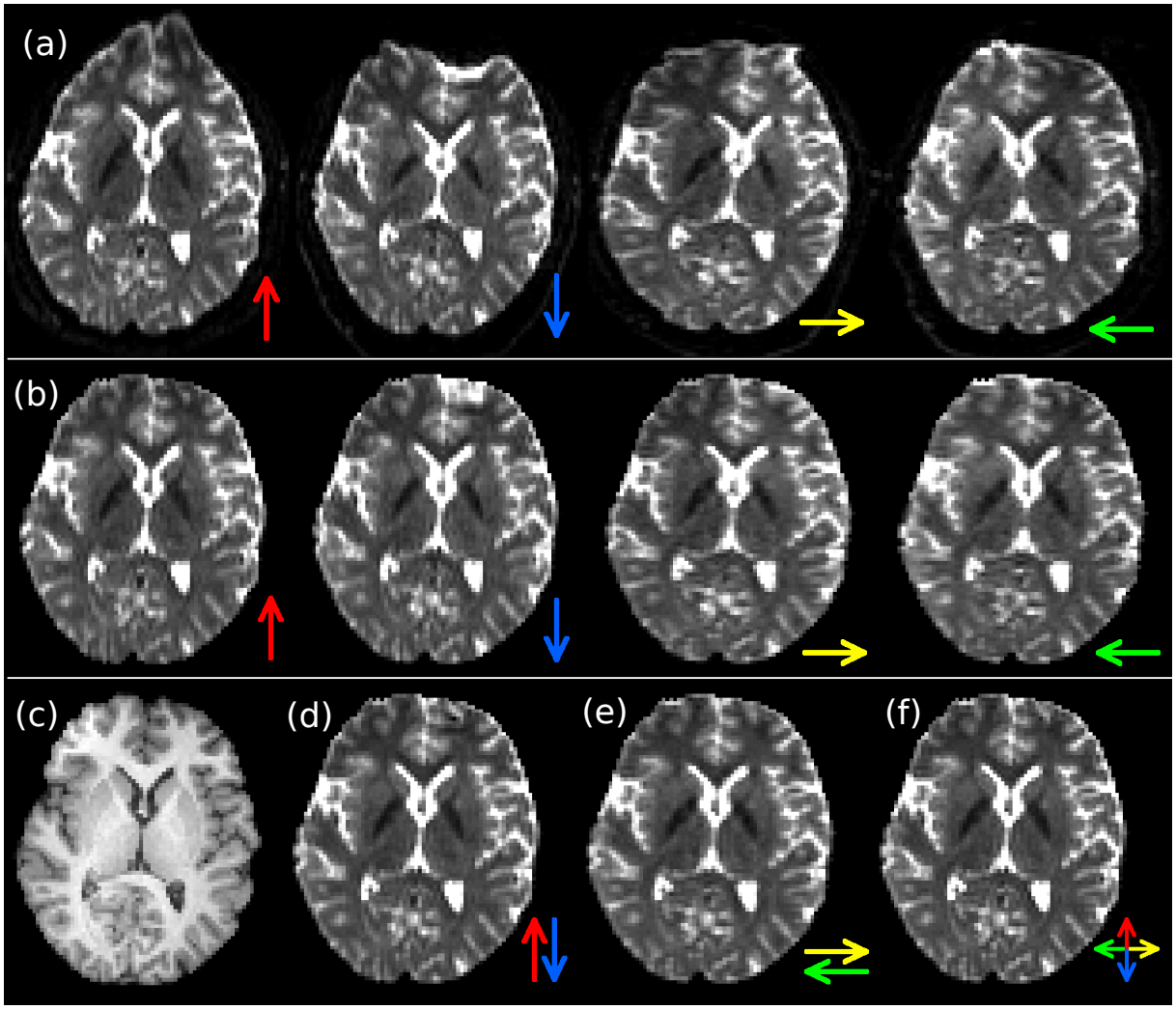

Figure 5.1: Overview of susceptibility-induced EPI distortion with single-PED and RG correction methods. (a) The same axial b=0 s/mm^2 brain image acquired with different EPI PEDs (represented by colored arrows). Note the presence of substantial geometric distortion, particularly in the frontal lobe. (b) Distortion-corrected images using the single-PED method. (c) Undistorted anatomical MPRAGE image for reference. Distortion-corrected images using the RG method are shown based on PEDs along the (d) A/P direction and (e) L/R direction. (f) Generalized RG distortion correction using all four PEDs ('4-PED Full').

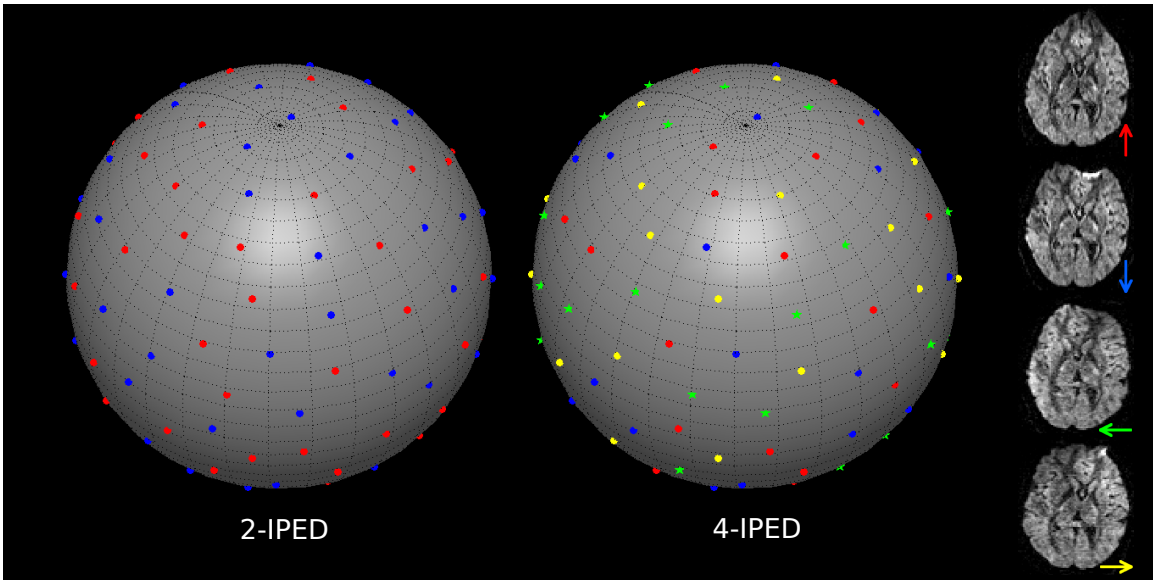

Figure 5.2: 2-IPED and 4-IPED examples of our proposed q-space sampling scheme assuming that data is sampled at 64 points on a sphere (i.e., a single b-value). Each q-space sample is shown as a dot on the surface of the sphere, where the color of each dot represents the PED for that particular diffusion encoding. The rightmost column of images shows how the different colors are mapped to different PEDs (represented by colored arrows).

5.1 Theory

In the traditional RG method, described in section 2.4.2, distortion correction is performed independently for each q-space sample [Chang and Fitzpatrick, 1992, Andersson et al., 2003]. As a result, it is necessary to acquire each point in q-space with two different PEDs. Our proposed method is based on the observation that nearby q-space samples are generally related to each other, and share a substantial amount of structure. This conceptual breakthrough allows for distortion correction of different DWIs to be performed jointly, which can substantially reduce the amount of data needed for high-quality results.

A variety of different dependencies have been previously observed between the DWIs for different q-space samples. For example, it has been observed that image edge locations are highly correlated between different DWIs (see Haldar et al. [2013] and its references), and that DWIs possess approximately low-rank structure (see Lam et al. [2013] and its references). For simplicity, we will not focus on these kinds of constraints in this work, though note that they are potentially powerful in this context. Another constraint, which we use extensively in the proposed method, is that the diffusion signal is generally smooth in q-space. This smoothness assumption is frequently used in high angular resolution diffusion imaging (HARDI) modeling [Descoteaux et al., 2007, Hess et al., 2006, Anderson, 2005], and is implicit in most of the parametric models of the diffusion signal like Diffusion Tensor Imaging (DTI) [Jones, 2011, Tournier et al., 2011, Le Bihan and Johansen-Berg, 2012].

Based on the assumption of q-space smoothness, our proposed method acquires different q-space samples with different PEDs in an interlaced manner: each q-space location is only measured once, and PEDs are assigned to each q-space location so that neighboring q-space samples have different PEDs. In addition, we construct the sampling pattern so that the samples associated with each unique PED are distributed as evenly as possible in q-space. Examples of our interlaced PED (IPED) q-space sampling scheme are shown in Fig. 5.2. By acquiring the data in an interlaced fashion, we do not require any additional scan time, but still obtain information from DWIs with similar contrasts that have been distorted in different ways. Note that unlike the RG method, which always uses 2 PEDs, we do not place any restrictions on the number of distinct PEDs that are used in the acquisition (though, for simplicity, the examples we present either use 2 or 4 PEDs). We will respectively refer to IPED data acquired with 2 and 4 PEDs as '2-IPED' and '4-IPED' data in the rest of the paper.

To enable distortion correction with our IPED q-space sampling scheme, we represent the geometric distortion process as a linear operator on an undistorted image, and formulate distortion correction as a regularized least-squares problem. In particular, assuming that each DWI has V voxels, that there are Q-different DWIs, and that we have an estimate of the B_0 fieldmap, we obtain distortion-corrected images by solving:

$$[\widehat{\mathbf{s}}_1, \cdots, \widehat{\mathbf{s}}_Q] = \underset{[\mathbf{s}_1, \cdots, \mathbf{s}_Q] \in \mathbb{R}^{V \times Q}}{\arg\min} \left(\underbrace{\sum_{q=1}^{Q} \|\mathbf{D}_q \mathbf{s}_q - \mathbf{d}_q\|_{\ell_2}^2}_{\text{data consistency}} + \underbrace{R(\mathbf{s}_1, \cdots, \mathbf{s}_Q)}_{\text{regularization}} \right), \tag{5.1}$$

where $\mathbf{d}_q \in \mathbb{R}^V$ and $\mathbf{s}_q \in \mathbb{R}^V$ are respectively the measured distorted image and the corresponding unknown distortion-free image for the q^{th} sample in q-space, $\mathbf{D}_q$ is the corresponding $V \times V$ geometric distortion operator (a function of the PED for the q^{th} DWI and the measured fieldmap), and $R(\cdot)$ is a regularization penalty function that stabilizes the distortion correction procedure by enforcing additional constraints. Similar formulations for EPI distortion correction based on least-squares approaches have previously been explored [Munger et al., 2000, Andersson et al., 2003], though these did not incorporate joint reconstruction of different q-space samples, regularization, or multiple PEDs.

Careful choice of the function $R(\cdot)$ is essential, since the use of IPED sampling was predicated on leveraging the shared structure between different q-space samples, and regularization is the only mechanism in our formulation for imposing shared structure. Note that without regularization in Eq. (5.1), the distortion correction of different q-space samples is completely decoupled when using IPED sampling. As already described, distortion correction of a single DWI from a single-PED dataset can be ill-posed.

The proposed formulation in Eq. (5.1) is quite general, and can be adapted to arbitrary q-space sampling schemes through the choice of an appropriate $R(\cdot)$ function that couples together the distortion correction of different q-space samples. However, the choice of $R(\cdot)$ must also be compatible with the

q-space sampling pattern. For simplicity, we will assume in this paper that diffusion data is sampled on the surface of a sphere in q-space (i.e., a conventional single-shell acquisition with multiple diffusion encoding directions and a single b-value), and that the q-space signal varies smoothly on the surface of the sphere. Based on this assumption, we will adopt the Laplace-Beltrami q-space smoothness regularization penalty that is commonly used for this kind of data when estimating HARDI signals [Descoteaux et al., 2007, Hess et al., 2006, Anderson, 2005]. Similar to previous approaches, we implement the Laplace-Beltrami operator in a computationally-efficient manner by using a representation of the DWIs in the spherical harmonic (SH) basis. In particular, we assume that the $V \times Q$ image matrix $\mathbf{S} = [\mathbf{s}_1, \cdots, \mathbf{s}_Q]$ is represented as $\mathbf{S} = \mathbf{CY}$, where $\mathbf{C}$ is a $V \times N$ matrix whose v^{th} row contains the N different SH coefficients (truncated at a predetermined user-chosen SH order [Descoteaux et al., 2007, Hess et al., 2006, Anderson, 2005]) for the v^{th} voxel, and $\mathbf{Y}$ is the $N \times Q$ matrix whose rows are computed by sampling the SH basis functions along each of the Q different diffusion encoding directions. In order to further stabilize the distortion correction procedure, we also encourage the spatial smoothness of each DWI. Combining the SH representation with Laplace-Beltrami (spherical) q-space smoothness and spatial smoothness penalties, we arrive at our proposed optimization formulation:

$$\widehat{\mathbf{C}} = \underset{\substack{\mathbf{C}\in\mathbb{R}^{V\times N} \\ \text{s.t. } \mathbf{S}=\mathbf{CY}}}{\arg\min} \left(\sum_{q=1}^{Q} \|\mathbf{D}_q\mathbf{s}_q - \mathbf{d}_q\|_{\ell_2}^2 + \underbrace{\sum_{v=1}^{V} \alpha_v \|\mathbf{L}\mathbf{c}_v\|_{\ell_2}^2}_{\text{spherical smoothness}} + \underbrace{\beta \sum_{q=1}^{Q} \|\mathbf{F}\mathbf{s}_q\|_{\ell_2}^2}_{\text{spatial smoothness}} \right), \tag{5.2}$$

and then obtaining $\widehat{\mathbf{S}}$ by setting $\widehat{\mathbf{S}} = \widehat{\mathbf{C}}\mathbf{Y}$. In Eq. (5.2), $\mathbf{c}_v$ is the transpose of the v^{th} row of $\mathbf{C}$, $\mathbf{L}$ is a diagonal matrix that applies the Laplace-Beltrami operator to SH coefficients [Descoteaux et al., 2007, Hess et al., 2006, Anderson, 2005], $\mathbf{F}$ is a first-order finite difference matrix of size $2V \times V$, that computes the horizontal and vertical spatial image derivatives at each image voxel, and α_v and β are scalar regularization parameters that respectively control the strength of the spherical and spatial smoothness constraints. See Appendix 5.A for more specific details about the SH representation, the Laplace-Beltrami operator, and the associated matrix definitions that are used in Eq. (5.2).

Equation (5.2) is quite similar in structure to a variety of different constrained image reconstruction methods (e.g., Haldar et al. [2013] and its references), and reduces to a simple linear least squares problem (shown in Appendix 5.B that can be solved using standard iterative least squares algorithms. Despite the relatively large scale of the optimization problem, computationally-efficient implementations can be obtained by using sparse matrix representations that enable fast matrix-vector multiplications (note that $\mathbf{D}$, $\mathbf{L}$, and $\mathbf{F}$ are all sparse). We solved all linear least squares problems in this paper using the iterative LSQR algorithm [Paige and Saunders, 1982] in MATLAB 7.14 (The MathWorks, Inc., USA).

In practice, the regularization parameters α_v and β must be chosen appropriately to achieve good performance. Small values of α_v will only weakly impose coupling between different DWIs in the

distortion correction procedure, which could lead to performance that is more similar to single-PED distortion correction than to the RG method. On the other hand, excessively large values of α_v will lead to a bias towards isotropic diffusion characteristics. It should be noted that we are allowing α_v to vary as a function of spatial location, since the coupling between different DWIs will be more critical in spatial image regions that are more highly distorted. Similarly, small values of β can cause the reconstructed DWIs to be more sensitive to noise, while excessively large values of β can lead to substantial loss of spatial resolution. Spatially-varying choices of β can also be used to achieve additional performance benefits [Haldar et al., 2013], though for simplicity, we will use a spatially-invariant β in this work.

5.2 Evaluation methods

5.2.1 Simulation data

To evaluate the proposed method, we simulated a 20-direction diffusion MRI dataset acquired with a single-shot EPI readout for two different levels of geometric distortion. Small and large distortions were generated by simulating a fully-sampled 128×128 EPI trajectory (without any parallel imaging) with echo spacings of 0.35ms and 0.55ms, respectively. The echo spacings used in our simulation are similar to typical 'effective' echo spacings for *in vivo* acquisitions. We used distortion-corrected experimental human brain data (TE=88s, TR=10000ms, b=1000 s/mm^2, 2mm isotropic resolution) as a ground truth for the simulation. The ground truth for the simulation was specifically constructed based on 10 contiguous DWI slices from a brain region with minimal B_0 field inhomogeneity, to ensure that the ground truth had negligible geometric distortion artifacts. To yield even better geometric accuracy, these images were also corrected using a data sampling and distortion correction scheme we refer to as '4-PED Full' (see Eq. (2.30) in chapter 2). Specifically, 4-PED Full samples each q-space sample 4 times with 4 different PEDs which encodes the highly distorted image regions even more comprehensively than the RG method. Note that 4-PED Full uses twice as many images as the RG method, and four times as many as the single-PED schemes. Distorted images were simulated based on the ground truth images using a B_0 fieldmap acquired on a 3T scanner from a different subject (fieldmap values ranged from approximately -75 Hz to 130 Hz, leading to maximum signal displacements of approximately 11 mm and 18 mm for the small and large distortion simulated datasets, respectively) and a least-squares time segmentation approach to model the effects of field inhomogeneity on measured k-space data [Fessler et al., 2005, Sutton et al., 2003, Gai et al., 2013].

Simulated data was generated for each of the four different PEDs shown in Fig. 5.1, for a total of 80 simulated DWIs. Acquisitions corresponding to single-PED, RG, 2-IPED, 4-IPED, and 4-PED Full sampling schemes were constructed by subsampling this data (80 DWIs for 4-PED Full, 40 DWIs for

the RG acquisition, and 20 DWIs for the single-PED, 2-IPED, and 4-IPED acquisitions). Note that while 4-PED Full distortion correction was used for the construction of the ground truth images for the simulation, we used a distinct distortion model to generate the simulated distorted images. Specifically, the simulated distorted images were constructed using a distinct fieldmap with larger inhomogeneity, and distortion was simulated in k-space rather than image space. As a result, the simulation would not be expected to be biased toward 4-PED Full reconstruction, and 4-PED Full reconstruction of the simulated data would not be expected to be perfect.

PEDs for each of the 20 DWIs in the interlaced acquisitions were assigned to achieve a fairly even distribution in q-space by using a variation of the electrostatic repulsion method for distributing q-space samples evenly on the sphere [Jones et al., 1999]. In particular, we first used electrostatic repulsion to distribute the 20 q-space samples evenly on the sphere. Subsequently, keeping the q-space sampling locations fixed, we chose PED labels for each q-space location to minimize the electrostatic potential energy for the subsets of q-space samples sharing the same PED. Global optimization of this energy is not computationally tractable, but we obtained reasonable PED distributions using Monte Carlo methods (see Appendix 5.D for the gradient/PED table). Note that our approach has similarities to a recent method developed for designing multi-shell diffusion acquisitions [Caruyer et al., 2013], though was derived independently.

5.2.2 *In Vivo* data

The proposed method was also evaluated with *in vivo* data. We acquired a set of 20 DWIs (using the same gradient/PED tables as the simulations) on a 3T scanner (single-shot EPI, 6/8ths partial Fourier, GRAPPA with 2$\times$acceleration, TE=88ms, TR=10000ms, b=1000s/mm^2, 60 slices, isotropic 2 mm resolution, 0.85ms echo spacing) for each of four different PEDs. The use of GRAPPA makes the 'effective' echo spacing (for distortion modeling) equal to 0.425ms. The $b = 0$s/mm^2 images for the four PEDs were shown in Fig. 5.1(a). A B_0 fieldmap was also estimated from two gradient echo images (TE=10.0ms and 12.46ms, respectively, with image resolution and FOV matched to the DWI acquisition, and a total acquisition time of approximately 2 minutes).

Similar to the simulation, we subsampled the *in vivo* DWI dataset to create single-PED, RG, 2-IPED, and 4-IPED datasets. Since the ground truth is unavailable for *in vivo* data, we used distortion-corrected DWIs based on 4-PED Full data (using our own implementation of a generalized version of the RG method with appropriate modifications to use 4 PEDs instead of only 2) as a reference for comparison. This choice is justified by our simulation results (to be presented later), which quantitatively demonstrate very accurate distortion correction performance when using simulated 4-PED Full data. An example of 4-PED Full correction was shown in Fig. 5.1(f).

5.2.3 Comparisons

The performance of different distortion correction methods on the simulated and *in vivo* data was assessed both qualitatively and quantitatively. The distortion correction results were evaluated for accuracy with respect to the ground truth images for the simulated data, while the results were evaluated with respect to 4-PED Full distortion corrected images for the *in vivo* data (due to the lack of a ground truth in this case).

Quantitative performance was assessed by computing the following error measures between the distortion-corrected images and the ground truth (for simulated data) or 4-PED Full images (for *in vivo* data): (i) Mean Absolute Error (MAE)[2] of the DWI voxel intensities, (ii) log-Euclidean distances (LED) between DTI fits of the diffusion data [Arsigny et al., 2006] (see Appendix 5.C for the definition of LED), and (iii) MAE of the fractional anisotropy (FA) values derived from the DTI fit. These three measures each reflect different features of the different distortion correction methods. Since different spatial regions are distorted by different amounts in different spatial locations, we also compared these errors as a function of the relative amount of local image distortion.

We compared results for several different distortion correction schemes. We performed single-PED distortion correction for each of the 4 different PEDs, using our own implementation of the non-iterative unwarping procedure described in Ref. [Jezzard and Balaban, 1995], which is not based on regularized least squares optimization. We also performed RG distortion correction with Left-Right (L/R) and Anterior-Posterior (A/P) PEDs (see Fig. 5.1(d,e)). Our implementation of the RG method is similar to the method described in Ref. [Andersson et al., 2003], except that we used spatial smoothness regularization to improve performance, and used a separate B_0 field measurement (instead of estimating the B_0 fieldmap directly from the distorted data). In particular, our RG implementation used the data consistency and spatial regularization terms (but no spherical regularization) from Eq. (5.2), with appropriate modifications to the data consistency term to accommodate two PEDs for each q-space sample. We also used Eq. (5.2) without spherical regularization to correct distortions in the 4-PED Full data (also used as reference image for comparison for the *in vivo* data), with similar modifications to the data consistency term to accommodate four PEDs for each q-space sample. For the proposed IPED method, we evaluated the performance with 2-IPED (for both L/R and A/P PEDs) and 4-IPED acquisitions. Regularization parameters, when not specified, were chosen empirically for each method and dataset (to minimize the MAE of the DWI voxel intensities) to ensure a fair comparison.

In most of our results (and unless specified otherwise), the regularization parameters α_v in Eq. (5.2) were chosen heuristically to be larger in spatial regions with more substantial geometric distortion,

[2] MAE was chosen over mean-squared error because it is more robust to outliers. However, results with both MAE and mean-squared error were qualitatively similar in all of our experiments.

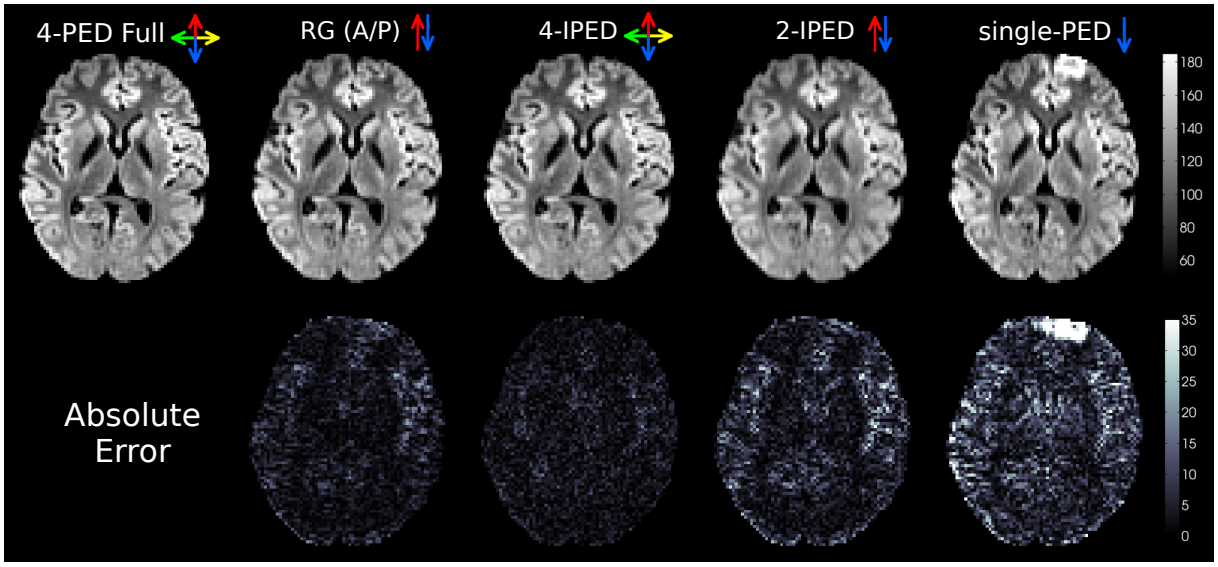

Figure 5.3: Representative comparison of applying different distortion correction methods to *in vivo* data. (top) The average of all distortion-corrected DWIs from the same axial slice shown in Fig. 5.1(a). (bottom) Corresponding MAE of the DWI image intensities, with respect to the 4-PED Full images (used as a reference since no ground truth exists for the *in vivo* data). Colored arrows indicate the PED(s) used for each method.

though we also performed a comparison with spatially-uniform α_v. In the spatially-varying case, we chose α_v to be a monotonic function of the amount of distortion in each voxel, and used the magnitude of the spatial gradient vector of the B_0 fieldmap to quantify the amount of distortion for each voxel. In particular, if W_v is the magnitude of the gradient of B_0 at the v^{th} voxel, then we set $\alpha_v = \alpha\Lambda_v$, where

$$\Lambda_v = \begin{cases} \eta & W_v \leq \eta \\ W_v & \eta < W_v < \Gamma \\ \Gamma & W_v \geq \Gamma. \end{cases} \tag{5.3}$$

The threshold parameters η and Γ were chosen manually to avoid under- and over-regularization, respectively, and were set at approximately η=1.5Hz/mm and Γ=16Hz/mm in our experiments. We evaluated performance for a range of different α and β values.

5.3 Results

5.3.1 Qualitative comparisons

Each of the methods performed similarly on simulated and *in vivo* data, and while we will present quantitative results in both cases, we will only show qualitative results for *in vivo* data. A representative qualitative comparison between methods for *in vivo* data is shown for an axial slice including the

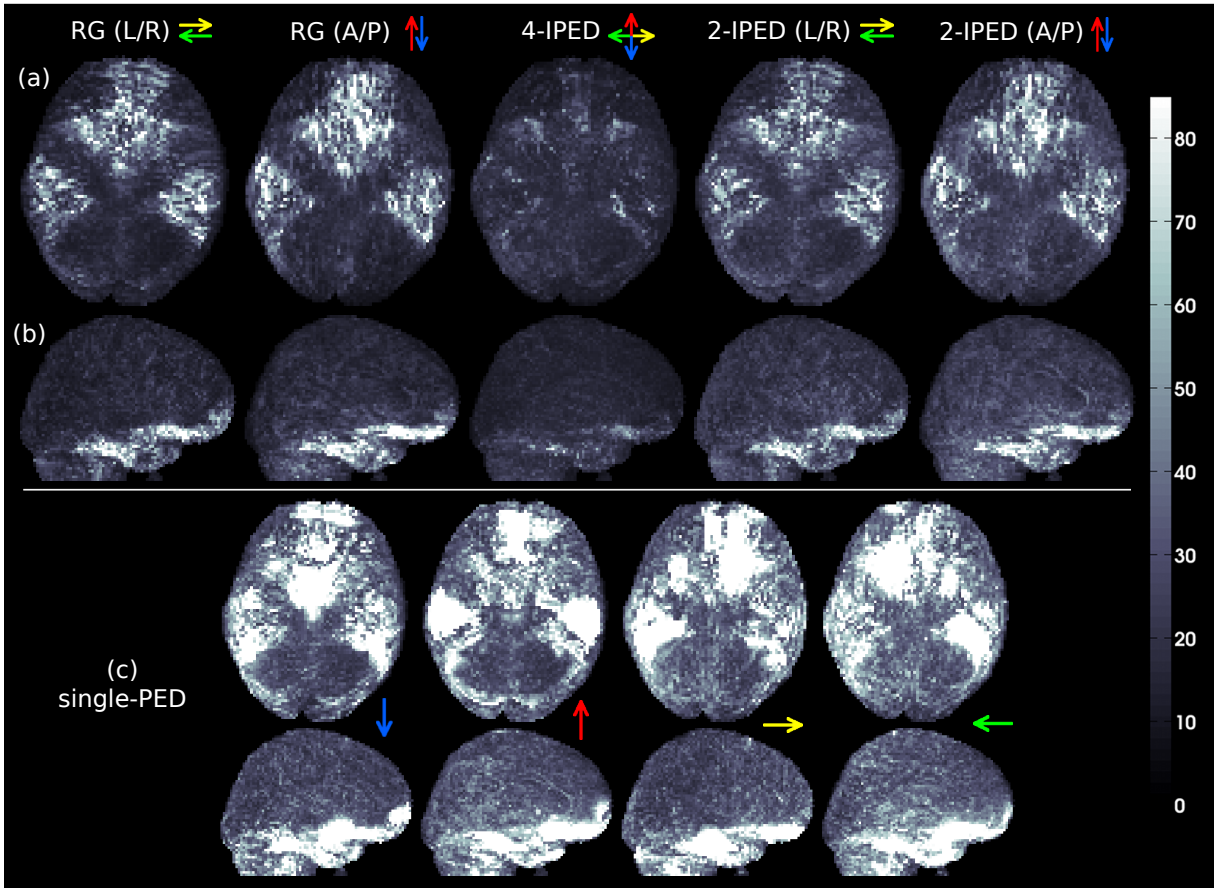

Figure 5.4: Whole-brain MIP images of image-intensity error maps computed after applying different distortion correction methods to the *in vivo* data. (a) Axial MIP images. (b) Sagittal MIP images. (c) Axial and sagittal MIP images for single-PED acquisitions. Colored arrows indicate the PEDs used for each method. Error images are computed using 4-PED Full data as a reference, since there is no ground truth available for *in vivo* data.

frontal lobe in Fig. 5.3. We observe that the single-PED method performs poorly compared to the other approaches, and has significant errors in the frontal lobe where the distortion was relatively large. As expected, the RG method performs substantially better and recovers the structure in the frontal lobe quite accurately. Our proposed interlaced methods (both 2-IPED and 4-IPED) perform similarly to the RG method, with the 4-IPED images actually demonstrating better performance than the RG method. This enhanced performance is notable, given the fact that the RG method used twice as many DWIs and would require twice the scan time as the 4-IPED approach. Maximum intensity projection (MIP) images of whole-brain DWI intensity and FA error maps are shown in Figs. 5.4 and 5.5, respectively, and have features that are similar to those observed in the single-slice comparison.

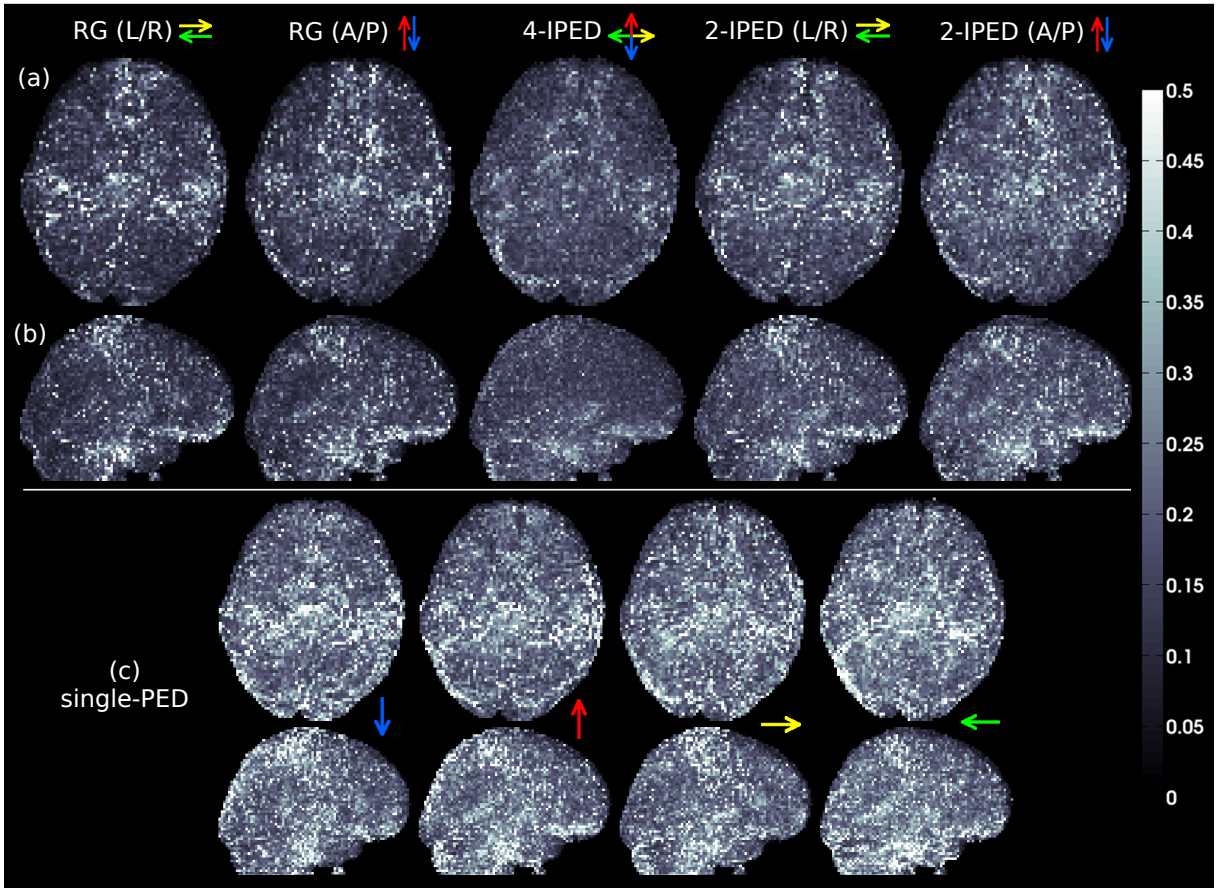

Figure 5.5: Whole-brain MIP images of FA error maps computed after applying different distortion correction methods to the *in vivo* data. (a) Axial MIP images. (b) Sagittal MIP images. (c) Axial and sagittal MIP images for single-PED acquisitions. Colored arrows indicate the PEDs used for each method. Error images are computed using 4-PED Full data as a reference, since there is no ground truth available for *in vivo* data.

5.3.2 Quantitative comparisons

Quantitative performance comparisons are shown in Fig. 5.6 for the two simulation datasets. The errors are quantified individually for different image regions based on a partition of W_v, noting that increasing values of W_v correspond to increasing levels of local image distortion. We define image regions with minimal, moderate, and severe distortion by finding voxels with W_v values in the ranges of 0-2 Hz/mm, 2-6 Hz/mm, and >6 Hz/mm, respectively. As expected, single-PED data has the worst performance across all error measures, while the 4-PED Full data (which acquires the most data and requires the longest acquisition time) consistently outperforms all other methods for all regions and error measures, and both the RG (L/R) and RG (A/P) methods perform substantially better than the single-PED method. We observe that performance with our proposed interlaced methods was substantially better than

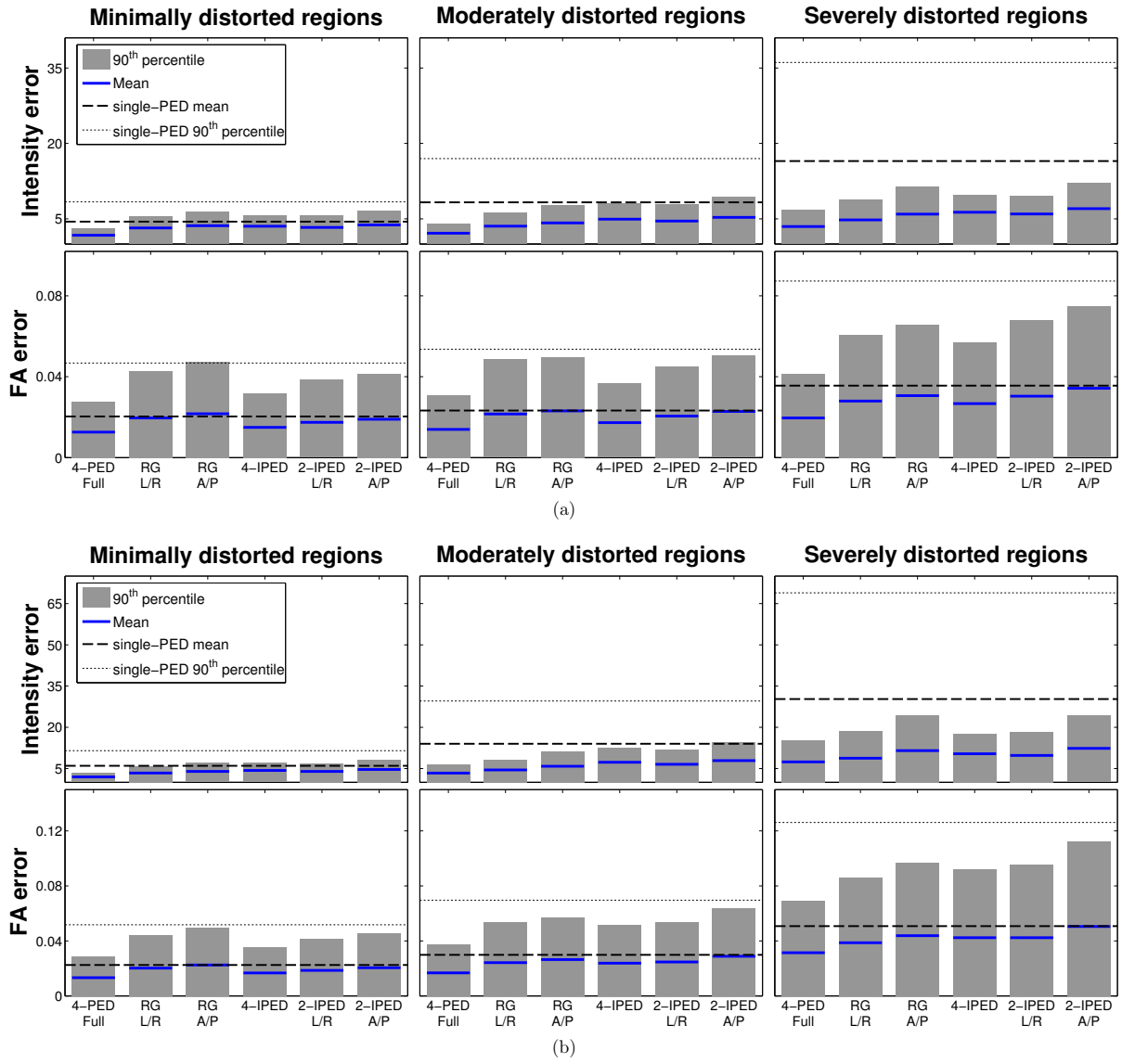

Figure 5.6: Quantitative performance of different methods (measured separately for groups of voxels that experience different amounts of local image distortion) for simulated data with (a) small and (b) large distortion in comparison to the ground truth images. The height of each bar plot shows the 90th percentile of the computed error measure for each region, while the solid blue line shows the mean value of the error measure. The thin and thick dashed lines correspond to the 90th percentile and the mean, respectively, of the error measure in the region for the single-PED methods (all single-PED methods had similar error numbers, and we show the average value of the four).

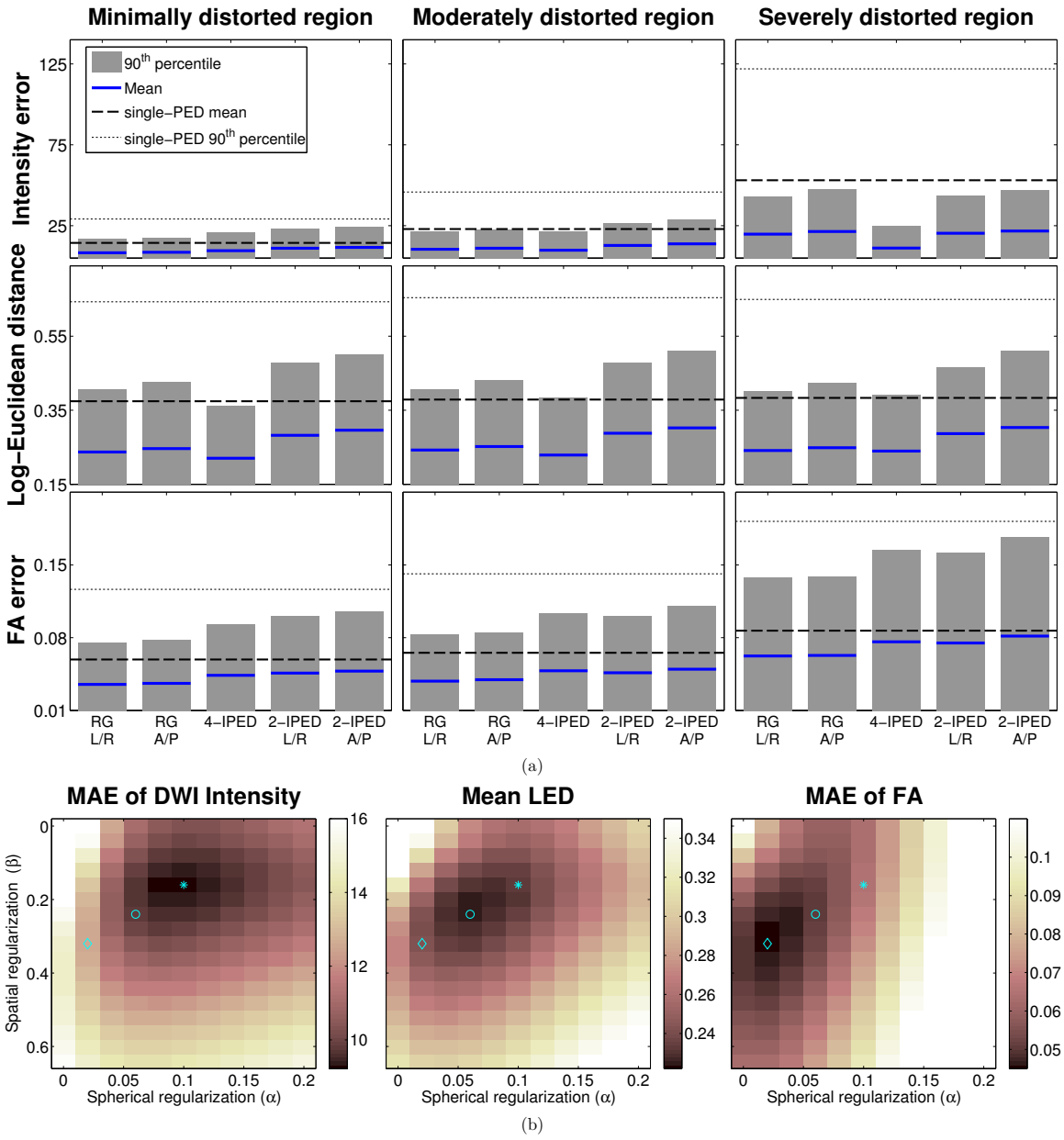

Figure 5.7: (a) Quantitative performance of different methods (measured separately for groups of voxels that experience different amounts of local image distortion) for *in vivo* data, in comparison to the 4-PED Full images which were used as a reference. The height of each bar plot shows the 90th percentile of the computed error measure for each region, while the solid blue line shows the mean value of the error measure. The thin and thick dashed lines correspond to the 90th percentile and the mean, respectively, of the error measure in the region for the single-PED methods (all single-PED methods had similar error numbers, and we show the average value of the four). (b) Mean values of several distortion correction error measures across all voxels as a function of the spherical smoothness (α) and spatial smoothness (β) regularization parameters. Regularization parameters corresponding to minimum error measures are marked by an asterisk ($*$) for the MAE of DWI Intensity, by a circle ($\circ$) for the Mean LED, and by a diamond ($\diamond$) for the MAE for FA.

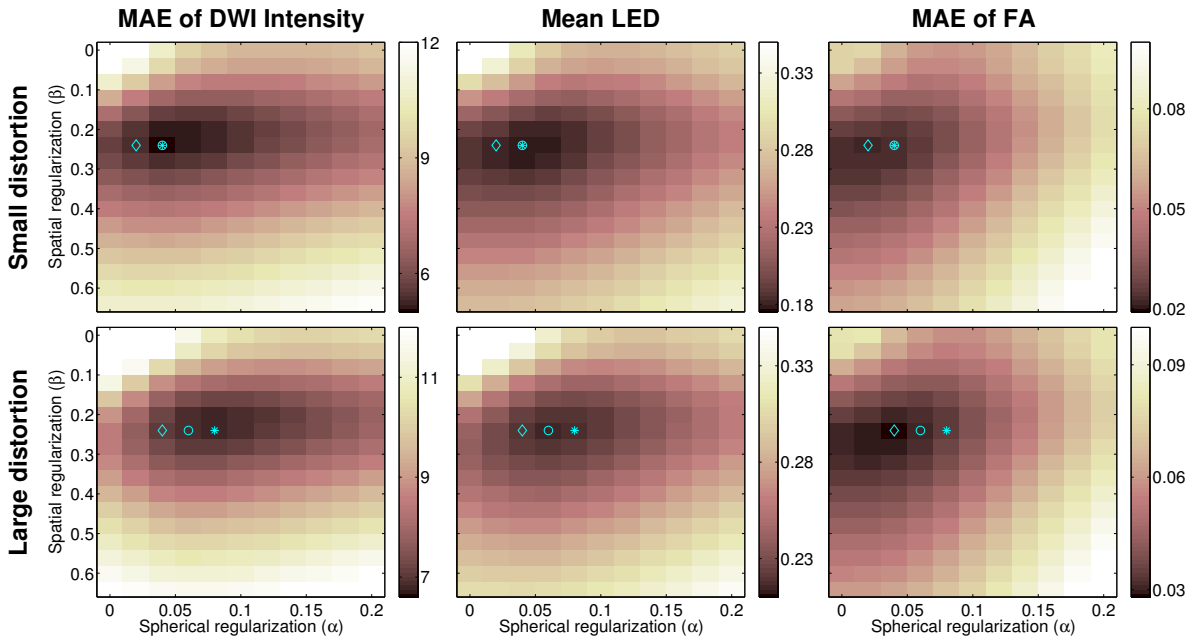

Figure 5.8: Mean values of several distortion correction error measures across all voxels as a function of the spherical smoothness (α) and spatial smoothness (β) regularization parameters, computed for (top) the 4-IPED small distortion simulation data and (bottom) the 4-IPED large distortion simulation data in comparison to ground truth images. Regularization parameters corresponding to minimum error measures are marked by an asterisk ($*$) for the MAE of DWI Intensity, by a circle ($\circ$) for the Mean LED, and by a diamond ($\diamond$) for the MAE for FA.

with the single-PED methods, and that the 4-IPED acquisition was generally better than the two 2-IPED acquisitions. Notably, the 4-IPED acquisition performed similar to and frequently better than both RG methods, despite using half as much data. It should be noted that the 2-IPED performance was either similar to or slightly worse than for the RG methods, as would be expected since the 2-IPED acquisition uses a subset of the data from the RG method. The 4-IPED acquisition has the capability to improve on the RG method because it measures a more diverse set of PEDs (4 different types of distortion, instead of the 2 different types of distortion that the RG method uses). The spherical regularization in the proposed method makes it possible to use this information for distortion correction without increasing the scan time, and allows 4-IPED acquisition to perform better than the RG method on some error measures. Similar quantitative performance comparisons are shown for the *in vivo* data in Fig. 5.7(a), and reflect similar trends.

5.3.3 Choice of regularization parameters

In order to illustrate the impact of the different regularization terms in Eq. (5.2), we show quantitative error measures when using the 4-IPED acquisition for a range of different choices of α and β for *in vivo*

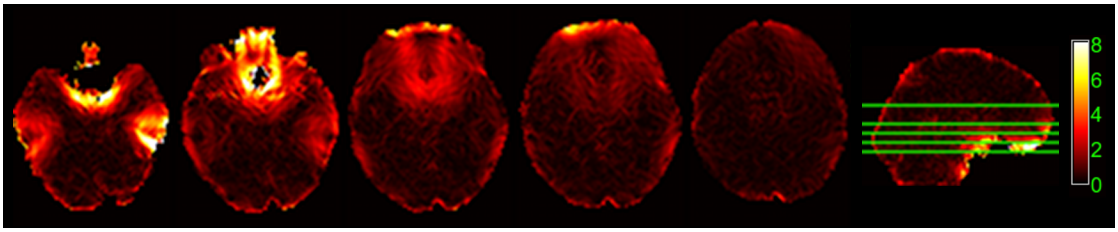

(a)

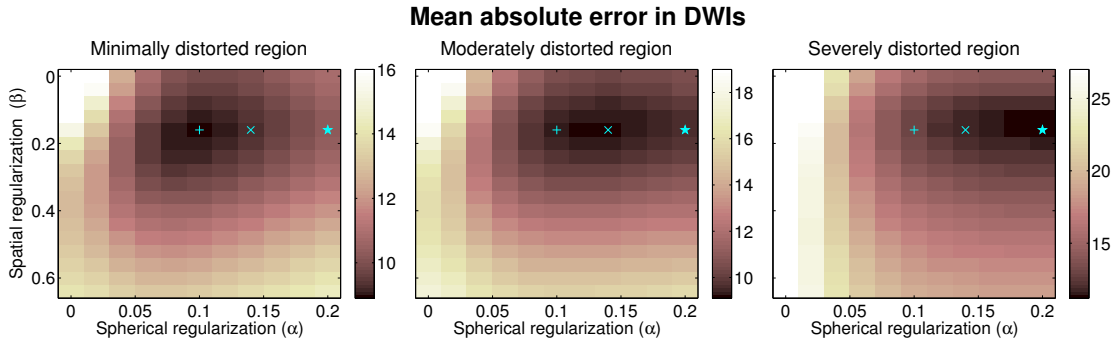

(b)

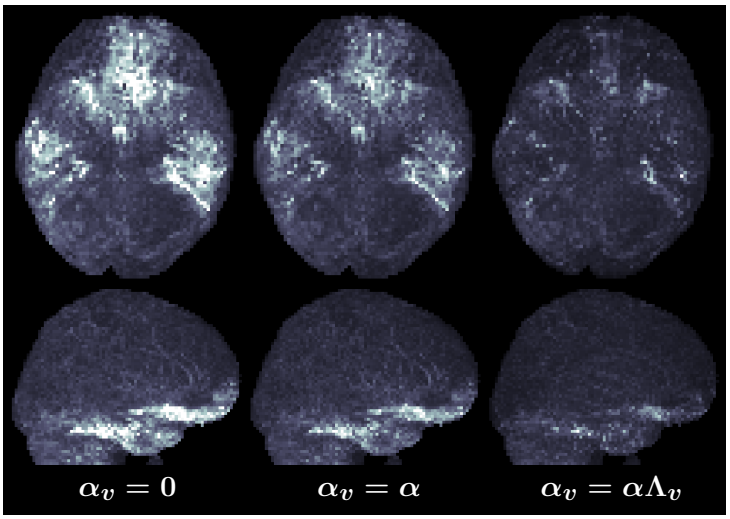

(c)

Figure 5.9: (a) Magnitude of the spatial gradient vector of the B0 fieldmap (W_v) for several axial slices (units of Hz/mm). (b) MAEs of the distortion corrected image intensities, as a function of the amount of local geometric distortion and the spherical-smoothness and spatial-smoothness regularization parameters α and β. Regularization parameters corresponding to minimum MAE are marked respectively by a plus sign (+), a cross ($\times$), and a star ($\star$) for minimally, moderately, and severely distorted regions. (c) Whole-brain MIP images of the image-intensity error maps resulting from (left) no spherical smoothness regularization ($\alpha_v = 0$ for all v), (center) spatially-invariant spherical smoothness regularization ($\alpha_v = \alpha$ for all v), and (right) spatially-varying spherical smoothness regularization ($\alpha_v = \alpha\Lambda_v$). (top row) Axial MIP images. (bottom row) Sagittal MIP images. Error images were computed with respect to 4-PED full data, since no ground truth exists for *in vivo* data.

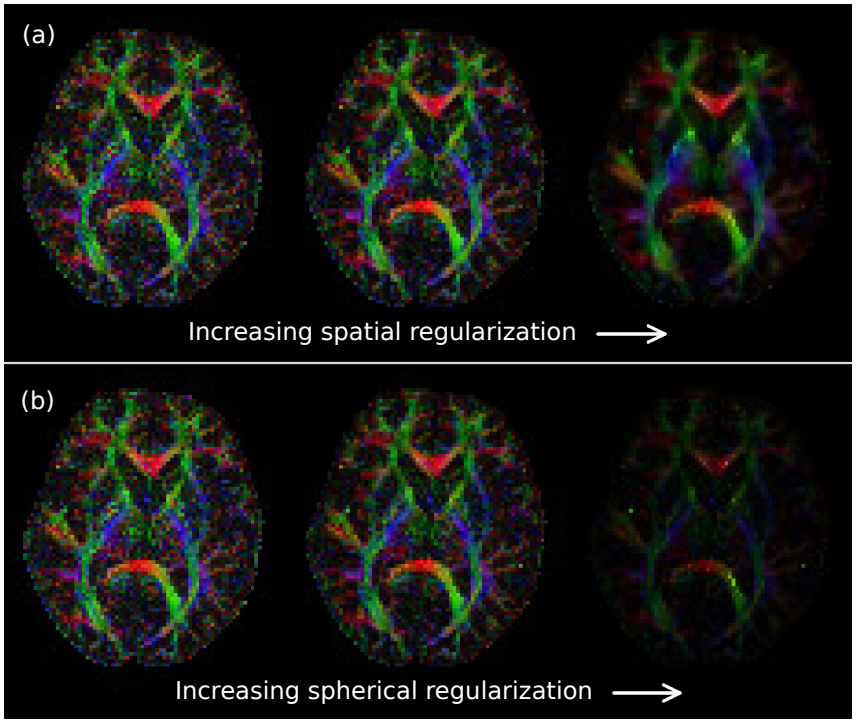

Figure 5.10: Color-coded FA maps shown as a function of the (a) spatial-smoothness regularization parameter β and the (b) spherical-smoothness regularization parameter α. (left) Regularization parameters that are too small lead to noisy results. (center) Reasonable regularization parameters lead to reasonable results. (right) Regularization parameters that are too large lead to over-smoothing.

data (Fig. 5.7(b)) and the simulations (Fig. 5.8). We observe that the use of regularization substantially reduces all of the error measures for all of the datasets, and observe that the best performance is obtained when using spatial and spherical regularization together ($\alpha \neq 0$ and $\beta \neq 0$). However, as indicated in Fig. 5.7(b) and Fig. 5.8, we also observe that the optimal choice of regularization parameters is different for different error measures. This observation is consistent with previous regularized processing of diffusion data [Lam et al., 2013], and is a reflection of the fact that different estimated diffusion parameters are more or less sensitive to different features of the diffusion data. This suggests that for optimal performance in a given application, the choice of regularization parameters should be tuned based on the subsequent data analysis procedures.

Our choice to use spatially-varying regularization was motivated by the fact that distortion correction is more ill-posed in highly distorted regions than in less-distorted regions. Figure 5.9 illustrates this in more detail with the 4-IPED *in vivo* data. In particular, Fig. 5.9(a) shows W_v (the magnitude of the gradient of B_0) for several slices of the *in vivo* data, and Fig. 5.9(b) plots the MAE of the DWI intensities as a function of the amount of local image distortion. This was achieved by partitioning the

image into mildly, moderately, and severely distorted regions based on W_v, identical to the partition used for Figs. 5.6 and 5.7(a). For easier interpretation of these plots, we did not use spatial weights for the spherical smoothness constraint, i.e., $\alpha_v = \alpha$ for all v instead of $\alpha_v = \alpha\Lambda_v$. The figure demonstrates that imposing the spherical q-space smoothness constraint becomes more important as the amount of distortion increases, which is consistent with our use of spatially-varying α_v. In addition, we observe that the optimal β is not highly dependent on the amount of distortion. We compare the use of spatially-varying α_v with spatially invariant α_v for the *in vivo* data in Fig. 5.9(c), and observe that the use of spatially-varying α_v substantially improves distortion correction in severely distorted brain regions in the frontal and temporal lobes.

A further illustration of the impact of the regularization parameters is presented in Fig. 5.10, which shows the color-coded FA images that result when α or β are too large or too small. As expected from theory, we observe that when either of the regularization parameters is too small, the resulting color FA maps are quite noisy. On the other hand, setting the regularization parameters too high leads to over-smoothing. As predicted, over-smoothing manifests as a loss in spatial resolution for the case of spatial regularization, and as a reduction in anisotropy for the case of spherical regularization.

5.4 Discussion

Our results demonstrated that the proposed PED-interlaced methods can accurately correct DWI distortion without increasing scan time, and that the 4-IPED acquisition yields the best performance. The approach uses a relatively small modification of a conventional acquisition, and can be implemented from the console (without changing pulse sequence code) if the existing diffusion pulse sequence allows flexible choice of the PED. For example, the IPED acquisition can easily be implemented in this case by dividing the acquisition into two or more segments, where each segment is acquired separately using a different PED and a different diffusion gradient table. With this setup, the PEDs would be interlaced in q-space, but not in time. Note that the proposed IPED approach could also be implemented with more than 4 PEDs, with potential for additional gains in performance.

Since our proposed approach involves changing PEDs, it is relevant to mention that different PEDs can be associated with different incidence rates for peripheral nerve stimulation (PNS) [Ehrhardt et al., 1997]. No subjects experienced PNS during our experiments with using multiple EPI PEDs, though results may vary on different scanners with different pulse sequence protocols.

Similar to other regularized methods, the performance of the proposed approach depends on the choice of regularization parameters. In this work, we selected the optimal parameters by comparing our corrected images with accurate reference images. However, this approach is impractical for real applications. One approach to avoiding this problem could be to use automatic regularization parameter

selection techniques [Kilmer and O'Leary, 2001]. However, it should be noted that optimal regularization parameters will depend on the choice of error measure, and that automated parameter selection techniques might not available for many of the error measures that would be most relevant to diffusion MRI. We expect that optimal regularization parameters will be relatively consistent for data collected with the same sequence on the same scanner, so that reasonable regularization parameters would only need to be calibrated once.

Our proposed method can also be modified to use more advanced regularization constraints, including the use of the previously mentioned edge- and rank-constraints [Haldar et al., 2013, Lam et al., 2013]. This could, for example, be achieved by augmenting the cost function in Eq. (5.2) with appropriate additional penalty terms. The proposed approach can also be used with q-space data that is not sampled on a sphere (e.g., multi-shell acquisitions [Caruyer et al., 2013] or diffusion spectrum imaging [Wedeen et al., 2005]), as long as an appropriate regularization penalty is used to couple the reconstruction of neighboring q-space samples together. In addition, our proposed method can also be modified to use more advanced noise models. Our proposed formulation used the ℓ_2-norm to measure data consistency, which is the optimal choice when the noise is Gaussian. Since the noise in MR magnitude images is approximately Gaussian at high SNR, our choice was appropriate for high-SNR experiments. However, low-SNR is frequently encountered in certain diffusion imaging scenarios, particularly when acquiring data with high b-values. For these cases, the noise is more appropriately modeled using Rician or non-central chi signal distributions. Our proposed approach is easily adapted to these cases by replacing the ℓ_2-norm data consistency term in Eq. (5.2) with an appropriate Rician or non-central chi log-likelihood function, and using efficient algorithms to optimize the resulting cost function [Varadarajan and Haldar, 2013].

In principle, our proposed q-space smoothness constraint could also be applied to fully-sampled RG or 4-PED acquisitions. We studied this possibility, but only observed minor improvements in quantitative performance. This is not unexpected, since the main purpose of the q-space smoothness constraint in our proposed IPED scheme was to compensate for information that is missing with the IPED acquisition, but which is present in fully-sampled non-interlaced acquisitions. Another interesting observation from our study is that the fully-sampled 4-PED acquisition can lead to even better performance than the RG method. This is not surprising, since it uses twice as much data and more comprehensive encoding of distorted image regions.

In this work, we demonstrated good performance of our proposed IPED approach with an acquisition that sampled a relatively small number of q-space samples. However, it should be noted that our assumption that neighboring q-space samples have similar image structure and contrast will become more accurate as the q-space sampling density increases. As a result, we would expect even better distortion correction for large numbers of q-space samples, e.g., as in HARDI acquisitions. On the other

hand, our assumptions might not be accurate enough for fewer than 20 q-space samples, though this issue remains to be investigated. However, it should also be noted that most quantitative diffusion experiments perform best when more than 20 q-space samples are acquired, even in the absence of significant image distortions [Jones, 2004].

The proposed method relies on accurate models of geometric distortion that are computed based on B_0 fieldmaps. However, our distortion model may be inaccurate if the fieldmap is noisy and/or if there are significant geometric distortion artifacts that are not related to B_0 inhomogeneity (i.e., from concomitant fields, non-linear gradients, or eddy currents [Andersson and Skare, 2011]), and an inaccurate distortion model can severely degrade the performance of all fieldmap-based distortion methods. The effects of noisy fieldmaps can be minimized by acquiring higher-quality field mapping data and/or using regularized fieldmap estimation [Hernando et al., 2010]. If eddy current or concomitant field artifacts were present in the data, we would ideally want to also model their effects in the $\mathbf{D}_q$ geometric distortion operators. This was not necessary in our experiments, since the data was acquired axially at 3T and had negligible concomitant field effects, and because the acquisition used a twice-refocused spin-echo sequence to significantly reduce eddy current effects [Reese et al., 2003].

In our experiments, the fieldmaps were estimated from two gradient echo images, which requires a moderate amount of extra acquisition time. However, we should note that the details of fieldmap estimation are not essential to the proposed IPED method, and that there are other potentially faster B_0 fieldmap estimation schemes. For example, many previous RG methods [Andersson et al., 2003, Holland et al., 2010, Gallichan et al., 2010] were able to estimate accurate B_0 fieldmaps directly from the distorted DWI data, without any increase in acquisition time. Similar B_0 fieldmap estimation techniques could also be used with IPED data (e.g., from two b=0s/mm^2 images acquired with opposite PEDs).

5.5 Conclusions

We have proposed and evaluated a novel distortion correction method for DWIs that enables high-quality distortion correction without measuring q-space samples more than once. The proposed method combines a novel q-space sampling scheme (in which neighboring q-space samples are acquired with different PEDs) with a novel constrained reconstruction approach that leverages the fact that DWIs from neighboring q-space samples are related to each other. Our results demonstrated that the proposed method provides substantially better distortion correction performance than the single-PED method, and similar performance to the RG method while using only half as much data. We expect that this accelerated approach to highly-quality distortion correction will make accurate geometric distortion correction methods more practical for a range of different experimental contexts.

Appendices

Appendix 5.A Spherical harmonics and the Laplace-Beltrami operator

As described in the Theory section, we represent the distortion-free signal $\mathbf{S} \in \mathbb{R}^{V \times Q}$ (unknown, and to be estimated using Eq. (5.2)) using a SH representation to simplify the use of spherical q-space smoothness constraints. Our SH modeling representation is identical to that described in Ref. [Descoteaux et al., 2007]. These details from Ref. [Descoteaux et al., 2007] are repeated here for the sake of completeness.

We assume that diffusion data is sampled on the surface of the sphere along Q different gradient orientations, which are defined in terms of the standard polar angles ($\theta_q \in [0, \pi], \phi_q \in [0, 2\pi]$) for $q = 1, 2, \ldots, Q$. As with all data sampled on the sphere, it is possible to represent the element in the v^{th} row and q^{th} column of the $\mathbf{S}$ matrix (i.e., the diffusion data for the v^{th} voxel and q^{th} q-space sample) in an orthonormal basis of spherical harmonics according to

$$[\mathbf{S}]_{v,q} = \sum_{n=1}^{N} [\mathbf{C}]_{v,n} \, [\mathbf{Y}]_{n,q} \quad , \tag{5.4}$$

where $[\mathbf{C}]_{v,n}$ is the n^{th} SH coefficient for the v^{th} voxel, $[\mathbf{Y}]_{n,q} = Y_n(\theta_q, \phi_q)$ is the n^{th} modified (real and symmetric) SH basis function sampled along q^{th} diffusion encoding direction [Descoteaux et al., 2007], and N is the number of SH basis functions used in the representation. The modified SH basis functions are defined in terms of the order-L truncation of the even-order standard SH basis functions $Y_\ell^m(\theta, \phi)$, which are given by

$$Y_\ell^m(\theta, \phi) = \sqrt{\frac{2\ell + 1}{4\pi} \frac{(\ell - m)!}{(\ell + m)!}} \, P_\ell^m(\cos\theta) \, e^{im\phi} \tag{5.5}$$

for $\ell = 0, 2, 4, \ldots, L$ and $m = -\ell, -(\ell - 1), \ldots, 0, \ldots, (\ell - 1), \ell$, where $P_\ell^m(\cdot)$ is the associated Legendre polynomial of order ℓ and degree m. The truncated modified SH basis function $Y_n(\theta, \phi)$ is obtained by defining the index n in terms of ℓ and m according to $n = (\ell^2 + \ell + 2)/2 + m$, and setting

$$Y_n = \begin{cases} \sqrt{2} \, \text{Re}\left(Y_\ell^{|m|}\right) & m < 0 \\ Y_\ell^m & m = 0 \\ (-1)^{m+1} \sqrt{2} \, \text{Im}\left(Y_\ell^{|m|}\right) & m > 0 \end{cases} \tag{5.6}$$

for $\ell = 0, 2, 4, \ldots, L$ and $m = -\ell, -(\ell - 1), \ldots, 0, \ldots, (\ell - 1), \ell$. Note that $N = (L + 1)(L + 2)/2$.

The SHs have the special property that they are eigenfunctions of the Laplace-Beltrami operator. As a result, applying the Laplace-Beltrami operator in the SH domain is equivalent to multiplying the N

SH coefficients for each voxel by an $N \times N$ diagonal matrix $\mathbf{L}$. The n^{th} diagonal element of $\mathbf{L}$ is equal to $\ell_n(\ell_n + 1)$, where ℓ_n is the spherical harmonic order used in Eq. (5.6) when constructing $Y_n(\theta, \phi)$ [Descoteaux et al., 2007]. This result is used in the spherical smoothness term from Eq. (5.2).

Appendix 5.B Linear least squares formulation

The solution to Eq. (5.2) can be obtained by solving the following equivalent linear least squares problem:

$$\widehat{\mathbf{c}} = \arg\min_{\mathbf{c}} \left\| \begin{bmatrix} \mathbf{D}\mathcal{S} \\ \sqrt{\beta}(\mathbf{I} \otimes \mathbf{F})\mathcal{S} \\ (\mathbf{A} \otimes \mathbf{L}) \end{bmatrix} \mathbf{c} - \begin{bmatrix} \mathbf{d} \\ \mathbf{0_F} \\ \mathbf{0_L} \end{bmatrix} \right\|_{\ell_2}^2 . \tag{5.7}$$

In this expression:

- The vector $\mathbf{c}$ is the length-VN concatenation of the SH coefficient vectors for each voxel $\mathbf{c}_v$ for $v = 1, \ldots, V$;
- The vector $\mathbf{d}$ is the length-VQ concatenation of the distorted DWIs $\mathbf{d}_q$ for $q = 1, \ldots, Q$;
- The linear operator $\mathcal{S}$, which can also be expressed as a sparse matrix of size $VQ \times VN$, converts a vector of SH coefficients into the undistorted DWI vectors $\mathbf{s}_q$ for $q = 1, \ldots, Q$ according to Eq. (5.4), and then concatenates the $\mathbf{s}_q$ vectors into a single length-VQ vector;
- $\mathbf{D}$ is a $VQ \times VQ$ block-diagonal matrix with Q diagonal blocks. The diagonal blocks are each of size VxV, and are equal to $\mathbf{D}_q$ for $q = 1, \ldots, Q$. $\mathbf{D}_q$ is a function of the PED for the q^{th} q-space sample, and the number of unique $\mathbf{D}_q$ matrices is equal to the total number of PEDs used;
- $\mathbf{A}$ is a $V \times V$ diagonal matrix with v^{th} diagonal entry equal to $\sqrt{\alpha_v}$;
- $\mathbf{0_F}$ and $\mathbf{0_L}$ are zero vectors of length $2VQ$ and VN, respectively;
- $\mathbf{F}$ and $\mathbf{L}$ are defined in eq. (5.2) and Appendix 5.A, respectively;
- $\mathbf{I}$ is the $Q \times Q$ identity matrix; and
- The symbol $\otimes$ denotes the standard Kronecker product.

Appendix 5.C Log-Euclidean distance

The similarity-invariant Log-Euclidean distance between diffusion tensors $\mathbf{S}_1$ and $\mathbf{S}_2$ is defined as [Arsigny et al., 2006]:

$$\text{dist}(\mathbf{S}_1, \mathbf{S}_2) = \sqrt{\text{Trace}\left(\{\log \mathbf{S}_1 - \log \mathbf{S}_2\}^2\right)}, \tag{5.8}$$

where $\log(\cdot)$ denotes the matrix logarithm. See Arsigny et al. [2006] for implementation details and further discussion of this metric.

Appendix 5.D Gradient and PED table

The gradient orientations and PEDs used for the simulation and *in vivo* experiments are shown in Table 5.1. We show only the L/R version of the 2-IPED scheme. The 2-IPED A/P scheme can be derived from the L/R scheme by replacing L and R with A and P, respectively.

Gradient Orientation			PED	
x	y	z	2-IPED	4-IPED
1.00	0.00	0.00	L	L
0.00	1.00	0.00	R	R
-0.0310	0.8034	-0.5947	R	P
0.8554	0.4976	0.1441	R	A
0.8348	0.3138	-0.4523	R	A
0.8348	-0.3138	-0.4523	L	P
0.8554	-0.4976	0.1441	R	R
0.8239	-0.0045	0.5668	L	P
0.5508	0.4313	0.7146	L	R
0.4666	0.8370	0.2858	R	P
0.5144	0.8121	-0.2754	L	L
0.3919	0.5211	-0.7582	L	P
0.4789	-0.0036	-0.8779	R	R
0.3919	-0.5211	-0.7582	L	L
0.5144	-0.8121	-0.2754	R	A
0.4666	-0.8370	0.2858	L	L
0.5508	-0.4313	0.7146	R	A
0.1102	-0.2686	0.9569	L	R
0.1102	0.2686	0.9569	R	L
0.0310	0.8032	0.5949	L	A

Table 5.1: Table of the gradient orientations and PEDs used for the simulation and *in vivo* experiments.

Chapter 6

Temporal non-local means filtering for functional MRI

6.1 Visualization of function MRI on the cortex

Low frequency fluctuations in BOLD activity during resting functional MRI (rfMRI) exhibit correlations between cortical regions that are known to be physiologically related, as first shown by Biswal et al. [Biswal et al., 1995, Smith et al., 2009]. These correlations are the basis for identification of functional networks from rfMRI in individuals and groups [Smith et al., 2013b, 2009, Blumensath et al., 2013, Craddock et al., 2012]. There are a large number of methods available for identification of functional networks from rfMRI BOLD data, including seed-based correlation, independent components analysis (ICA) and cortical parcellation methods [Smith et al., 2013b]. Prior to resampling onto a cortical surface, rfMRI data are typically preprocessed with a pipeline that includes compensation for susceptibility-induced distortion, slice timing and subject motion, as well as high-pass filtering of individual time series and removal of ICA-identified temporal noise components [Smith et al., 2013a, Glasser et al., 2013, Chambers et al., 2015]. However, when visualized as a time series or movie of cortical images, correlated patterns of BOLD variation reflecting time-varying brain activity are not readily visible in the data, even after preprocessing. Rather, the local intensity variations across the brain at each time point obscure larger scale correlated activity, as shown in Fig. 6.1(a) and the corresponding movie M1 (Sec. 6.C).

To reduce noise in fMRI it is common to spatially smooth the data, typically with an isotropic kernel applied in the volumetric space [Smith et al., 2013a, Blumensath et al., 2013, Wig et al., 2014b, Craddock et al., 2012]. Isotropic linear smoothing will inevitably mix signals from different areas, including areas that are not directly adjacent with respect to the cortical geometry, for example blurring occurs across the void from one side of a sulcal bank to the other. To avoid this problem, data can be smoothed directly

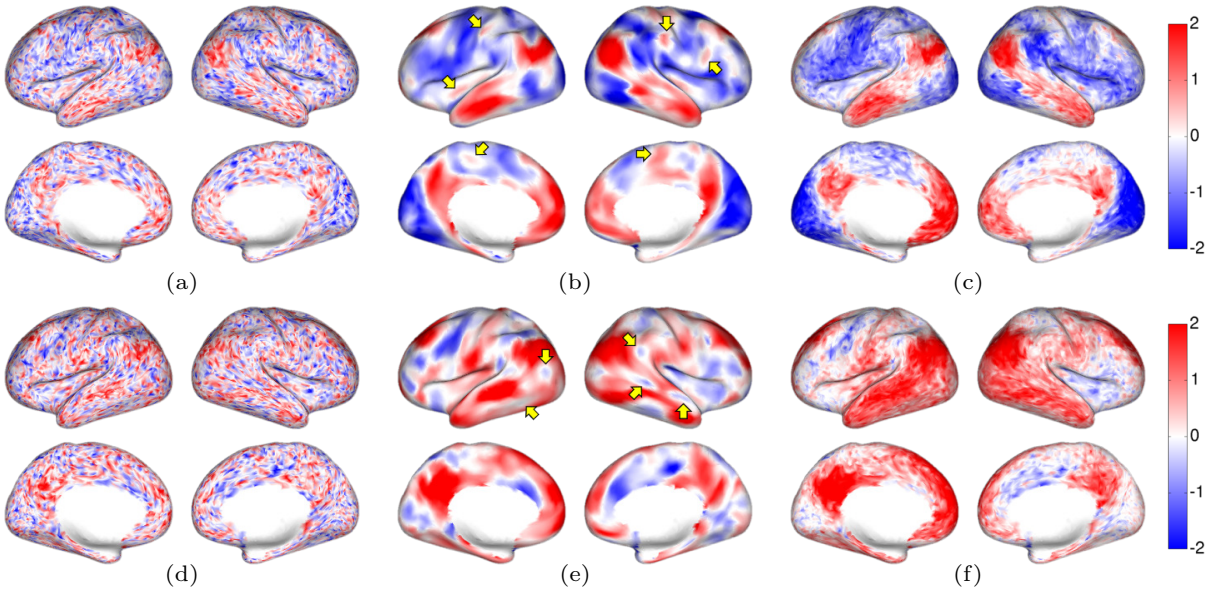

Figure 6.1: Illustration of smoothing effects on cortical BOLD signal intensity in rfMRI in a single subject, shown at a single time point: (a) no filtering, (b) LB filtering ($t = 4$) and (c) tNLM filtering ($h = 0.72$). Color scale shows positive (red), negative (blue) and zero (white) BOLD signal intensity. 3 minute real-time movies showing the un-filtered, LB- and tNLM-filtered rfMRI data can be found in the Sec. 6.C (M1–M3). It is difficult to detect spatial structure in the original unfiltered data, even if there are hints that can be discerned. By applying either LB or tNLM filtering, however, the noise is reduced and coherence in local activation/deactivation with respect to the underlying anatomy of the cerebral cortex is revealed. We see synchronous bilateral activity (in red) for both filtering methods in brain regions associated with the anterio-medial, posterio-medial and dorso-lateral regions of the default mode network (DMN). LB filtering (b) however, shows some additional small isolated patches in the fronto-lateral cortex, anterior insula, and the pre and post-central gyri, as indicated by the arrows. Interestingly, most of these isolated patches lie in regions that have been reported to show strong negative correlations to the DMN [Buckner et al., 2008, Fox et al., 2005, Vincent et al., 2008, Fransson, 2005], and so are unlikely to be synchronous with DMN regions. Similar behavior can be observed at another time point when (d) the original rfMRI data is filtered with (e) LB and (f) tNLM, where most of the DMN regions again show synchronous BOLD signal intensity in red. The tNLM results appear clearer in the sense that contrast in the images and movies appears to more closely follow discrete anatomical regions than do the LB results. The differences between the two methods is more readily evident in the movies of continuous resting state recording (see Sec. 6.C, M1–M3). Note in particular the different dynamic of the changes in brain activity – LB filtered images change smoothly from one brain state to the next while the tNLM images depict a more burst like change across consecutive brain states.

in the 2D manifold of the cortical surface. This is achieved by the Laplace-Beltrami operator which accounts for local surface curvature to generalize the 2D Gaussian smoothing kernel to an arbitrary smooth manifold [Angenent et al., 1999].

While Laplace-Beltrami (LB) smoothing can avoid blurring across sulcal banks, the smoothing is

still linear and isotropic so that sharp spatial features on the surface are smoothed, blurring boundaries between distinct functional regions. As we demonstrate below, the resulting signal mixing can also confound cortical parcellation methods, introducing artifactual parcels purely as a result of isotropic smoothing. An example of Laplace Beltrami smoothing is shown in Fig. 6.1(b) and in the corresponding the movie M2 (Sec. 6.C).

The primary contribution of this chapter is to describe an alternative nonlinear filtering method based on a novel adaptation of non-local means that reduces noise while also respecting functional boundaries on the cortical surface. As we illustrate in Fig. 6.1(c) and in corresponding movie M3 (Sec. 6.C), this results in the ability to directly visualize cortical brain activity and networks in resting state by playing back the filtered data on the cortical surface. The nonlinear filtering approach also significantly improves the identification of functional networks as demonstrated in the comparison presented below to task activation maps and probabilistic Brodmann areas.

Non-local means (NLM) is an edge-preserving filtering method that uses the weighted average of pixels in a large neighborhood where these weights are chosen adaptively depending on the structural similarities in the local neighborhoods of each pixel [Buades et al., 2005]. As a result NLM reduces noise through averaging while simultaneously retaining spatial structure by averaging only over pixels that have similar local structure. NLM filtering has previously been applied to structural [Manjón et al., 2008, Coupé et al., 2008, Manjón et al., 2009], functional [Xing et al., 2013, Zuo and Xing, 2011, Bernier et al., 2014], and diffusion [St-Jean et al., 2014, Wiest-Daesslé et al., 2008] MRI data. Modified NLM methods tailored to MRI data have also been developed including block-wise filtering and automatic adaption of weights based on SNR [Coupé et al., 2008, Wiest-Daesslé et al., 2008, Manjón et al., 2008], multi-compartment extension [Manjón et al., 2009], and use of multiple angular components for HARDI MRI [St-Jean et al., 2014]. All of these approaches use spatial similarity over one or more images as the basis for NLM smoothing. While this approach can be applied to fMRI time series [Bernier et al., 2014, Xing et al., 2013, Zuo and Xing, 2011], filtering each temporal frame separately with NLM will produce a time-varying smoothing kernel, confounding subsequent time-series analysis.

We have developed a novel variation on NLM which we refer to as temporal NLM (tNLM). Our method directly exploits the temporal information in the data by replacing the standard spatial similarity weighting in NLM with a weighting that is based on the correlation between time series. As a result we reduce noise by averaging only those pixels that have similar time series. This has the effect of not smoothing across functional boundaries, since the time series in different functional areas will be less strongly correlated than within each distinct functional region. The practical qualitative effect of this approach is illustrated in Fig. 6.1(c) and the corresponding movie M3 (Sec. 6.C). A related approach was used by one of the authors for denoising dynamic PET data by combining local spatial and temporal information to compute NLM weights [Dutta et al., 2013].

In addition to demonstrating the impact of tNLM on the spatio-temporal structure of rfMRI data, we illustrate its utility through one application: functional cortical parcellation. A number of parcellation methods have recently been described that include spectral clustering, hierarchical clustering, edge detection, and snow-balling [Blumensath et al., 2013, Smith et al., 2013b, Craddock et al., 2012, Wig et al., 2014b, Thirion et al., 2014]. Our goal here is to investigate the effect on cortical parcellation of tNLM filtering and compare its performance to linear filtering and no-filtering of the rfMRI data. For this purpose we use a spectral clustering method based on normalized cuts [Yu and Shi, 2003, Shi and Malik, 2000], although tNLM could also be used as part of a pre-processing pipeline and combined with other parcellation methods.

6.2 Temporal non-local means (tNLM)

Non-local means (NLM) is a widely used technique for edge-preserving filtering of images [Buades et al., 2005]. In common with conventional linear filtering, NLM uses weighted spatial averaging to reduce noise. However rather than using a fixed set of weights applied to pixels in a local neighborhood, the NLM weights are based on a measure of similarity of a small neighborhood, or a patch, surrounding each pixel [Buades et al., 2005]. When the patches around two pixels are similar the weight is large; and when they are dissimilar, the weight is low. In this way, the weighted averaging tends to reinforce spatial structure while removing noise.

In this work, we are interested in identifying functional regions that share common temporal variations. For this reason tNLM uses a weight based on the similarity of the time series rather than a spatial patch to filter the data. Specifically, let $d(s,\tau)$ denote the rfMRI data at surface vertex s at time τ. Then the corresponding tNLM-filtered rfMRI is given by

$$f(s,\tau) = \frac{1}{\sum_{r\in\mathcal{N}(s)} w(s,r)} \sum_{r\in\mathcal{N}(s)} d(r,\tau)\, w(s,r)\ , \tag{6.1}$$

where $\mathcal{N}(s)$ denotes a set of vertices lying in a large neighborhood surrounding vertex s and $w(s,r)$ is the weight applied to vertex $r \in \mathcal{N}(s)$ when filtering the rfMRI data at vertex s. We parameterize the neighborhood of a vertex on the cortical mesh by the linked distance parameter D such that the set $\mathcal{N}(s)$ contains all vertices, including itself, which are at a linked distance of D or less from the vertex s (we use $D = 11$ in all our results). The weights $w(s,r)$ are given by

$$w(s,r) = \exp\left(-\frac{\frac{1}{T}||\underline{\mathrm{d}}(s) - \underline{\mathrm{d}}(r)||^2}{h^2}\right) \tag{6.2}$$

where $\underline{\mathrm{d}}(s) = [d(s,1),\cdots,d(s,T)]^\top$ is a vector of length T representing the time series at vertex s and h is scalar parameter which determines the rate at which the weights decrease with (dis)-similarity of the

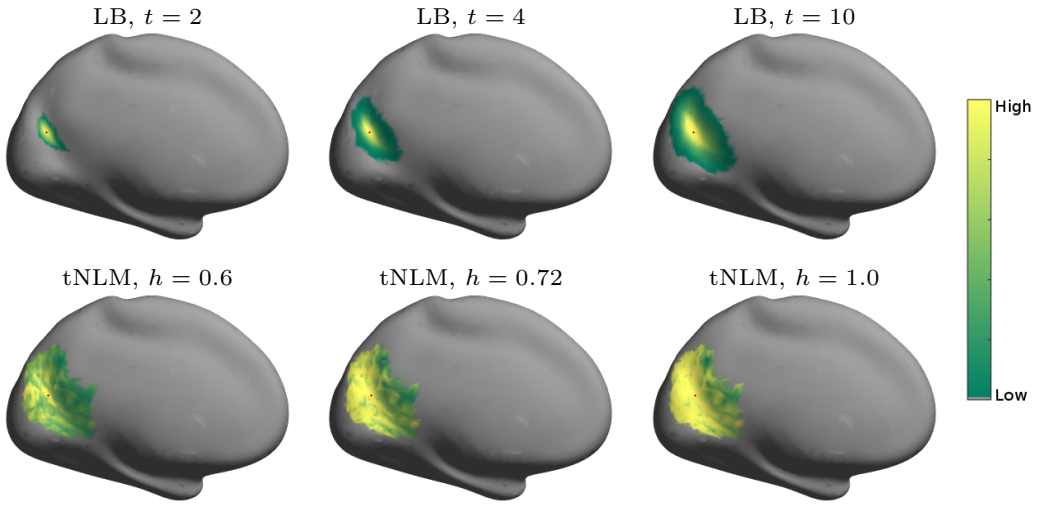

Figure 6.2: Qualitative differences in spatial weights applied to the neighboring vertices while filtering *in vivo* rfMRI data at a vertex, shown as a red dot, with (top row) LB filtering and (bottom row) tNLM filtering. The (red) vertex is chosen to lie in visual cortex near the boundary of visual cortex and posterio-medial cortex (PMC). The weights for LB filtering were computed using the original surface's geometry but are shown on smooth surfaces for easy visualization (which causes the LB weights to appear spatially anisotropic). The weights for tNLM filtering are shown for a neighborhood of maximum linked distance of $D = 11$ from the (red) vertex.

two time series. Since we pre-process the time series at each vertex to have zero mean and unit variance, the weights in eq. 6.2 are equivalent to using Pearson's correlation coefficient corr $(\underline{\mathrm{d}}(s), \underline{\mathrm{d}}(r))$ between $\underline{\mathrm{d}}(s)$ and $\underline{\mathrm{d}}(r)$, as $\frac{1}{T}||\underline{\mathrm{d}}(s) - \underline{\mathrm{d}}(r)||^2 = 2 - 2 \times \mathrm{corr}\,(\underline{\mathrm{d}}(s), \underline{\mathrm{d}}(r))$.

Fig. 6.2 illustrates the difference between the LB and tNLM approach when filtering the rfMRI data at a vertex. In order to highlight the differences between the methods, a vertex from visual cortex is selected such that it lies near the boundary of visual cortex and posterio-medial cortex (PMC) as these regions are known to have functionally different characteristics [Yeo et al., 2011, Lee et al., 2013, Buckner et al., 2008, Smith et al., 2009]. The relative values of the spatial weights are shown for increasing levels of smoothing, which is controlled by the time parameter t for LB filtering (see 6.A for details) and by the scalar parameter h for tNLM filtering[1]. The LB weights decrease isotropically (with respect to the original un-smoothed surface) with distance from the vertex point being filtered. In contrast, the tNLM weights (bottom row) show a spatial distribution that is highly asymmetric around the vertex such that the vertices in visual cortex have higher weights than vertices in PMC. As a result, LB filtering at that vertex will result in approximately equal mixing of signals from visual cortex and PMC. On the other hand, tNLM filtering will place substantially more weight on signals coming from visual cortex, irrespective

[1]The size of the neighborhood $\mathcal{N}$, as parameterized by the maximum link distance D, also affects the nature of tNLM filtering. We use $D = 11$ in all results included here as it shows empirically good results with reasonable computational cost.

of geodesic distance on the surface. Section 6.4.3 addresses the choice of smoothing parameters h and t.

6.3 Identification of cortical networks

To explore the impact of LB and tNLM filtering on cortical parcellation we used a graph-based spectral clustering method to identify a set of functional networks for each subject. We represent the spatio-temporal rfMRI data as a graph $G = (V, A)$ where the set of vertices of the cortical tessellation are the nodes $v \in V$ of the graph and A is the adjacency (edge) matrix such that any two vertices $u, v \in V$ are connected by an undirected edge of strength $A(u, v) = \exp(\underline{\mathrm{d}}^\top(u)\underline{\mathrm{d}}(v)/T)$.

The normalized-cuts (N-cuts) algorithm [Yu and Shi, 2003] subdivides the graph G into K sub-graphs by subdividing the nodes (or vertices on the tessellated cortical surface), V, into K disjoint subsets $V_1, V_2, \cdots, V_K$ so that $\cup_{i=1}^{K} V_i = V$ and $\forall i \neq j$, $V_i \cap V_j = \varnothing$. N-cuts partitions the graph to maximize the average "normalized association" within each of the K sub-graphs, which can be expressed as a cost function:

$$\mathrm{Nassoc}(\{V_1, \cdots, V_K\}) = \frac{1}{K} \sum_{i=1}^{K} \left(\frac{\sum_{u,v \in V_i} A(u, v)}{\sum_{u \in V_i, v \in V} A(u, v)} \right) \tag{6.3}$$

Yu and Shi [Yu and Shi, 2003, Shi and Malik, 2000] show this cost is equivalent to minimizing the average normalized cut cost. N-cuts therefore finds the set of K sub-graphs that have the weakest normalized average connectivity between sub-graphs and the maximum connectivity within each sub-graph. In this chapter, we use the implementation of N-cuts provided by the authors[2].

Note that the graph definition described above produces a fully connected graph that contains no explicit spatial information about each vertex's neighborhood structure. It is common to explicitly introduce spatial neighborhood information for functional clustering of rfMRI data, typically, by making the adjacency matrix A sparse [Blumensath et al., 2013, Smith et al., 2013b, Craddock et al., 2012]. In preliminary evaluations (not shown) we found that the fully connected graph produced more reliable parcellation with tNLM, presumably because the fully connected graph contains far more information about functional similarity of nodes/vertices than the sparser spatially constrained graph. The fully connected graph also allows clustering of spatially disjoint nodes/vertices in a single subgraph V_i allowing direct identification of functional networks rather than just producing a spatially contiguous cortical parcellation.

[2] Version January 22, 2010, obtained from http://www.cis.upenn.edu/~jshi/software (last accessed: December 04, 2015).

6.4 Performance evaluation

We compare the performance of different smoothing approaches using a variety of qualitative and quantitative methods. In this section, we describe the dataset used, background and technical details for the evaluation approaches. Detailed results corresponding to these are presented in the next section.

6.4.1 Dataset and preprocessing

All of the results in this chapter used the minimally pre-processed rfMRI data from 40 unrelated subjects, available from the Human Connectome Project (HCP)[3] [Van Essen et al., 2013, Glasser et al., 2013, Smith et al., 2013a]. Functional MRI data sets were acquired for four independent resting state sessions of 15 minutes each (TR=720ms, TE=33.1ms, $2 \times 2 \times 2$ mm voxel) and the subjects were asked to relax and fixate on a projected bright cross-hair on a dark background [Van Essen et al., 2013]. HCP's minimal preprocessing primarily corrects the rfMRI data for acquisition artifacts, resamples the data on cortical surface and performs a "non-aggressive" spatio-temporal cleanup [Glasser et al., 2013, Smith et al., 2013a]. The artifacts correction step allows compensation for head motion and spatial distortion caused due to gradient non-linearity and B_0 field inhomogeneity. The corrected functional data is then co-registered with corresponding structural images and resampled onto the 32K Conte-69 cortical mesh in the native subject space (resampling process also applies a 2mm FWHM Gaussian surface smoothing) [Smith et al., 2013a, Van Essen et al., 2012]. Next, a spatio-temporal processing is used to remove residual effect of scanner and motion artifacts and non-neuronal physiological artifacts, which includes a weak high-pass temporal filtering (>2000s FWHM; no low-pass filtering) followed by regressing out the artifactual temporal time-courses identified by using ICA-FIX on the volumetric data. The only additional preprocessing step we introduced prior to tNLM or LB filtering was to normalize the time series associated with each cortical vertex to zero mean and unit variance.

The functional parcellation results presented below are also evaluated using the probabilistic Brodmann areas and the task-localizers, as made available by the HCP. Task-based fMRI data for six major task domains [Barch et al., 2013] were obtained for the same 40 subjects, which included somatosensory and motor systems, language processing, social cognition, relational processing, emotion processing and decision making (see Fig. 6.4). We used HCP's pre-processed and analyzed task-fMRI data, with different levels of Gaussian smoothing, resampled on the 32K Conte-69 cortical mesh, which yielded a total of 17 statistical task-pair activation maps (analysis details for extraction of statistical task activation maps are described in [Woolrich et al., 2001, Barch et al., 2013]).

[3]Data were provided [in part] by the Human Connectome Project, WU-Minn Consortium (Principal Investigators: David Van Essen and Kamil Ugurbil; 1U54MH091657) funded by the 16 NIH Institutes and Centers that support the NIH Blueprint for Neuroscience Research; and by the McDonnell Center for Systems Neuroscience at Washington University.

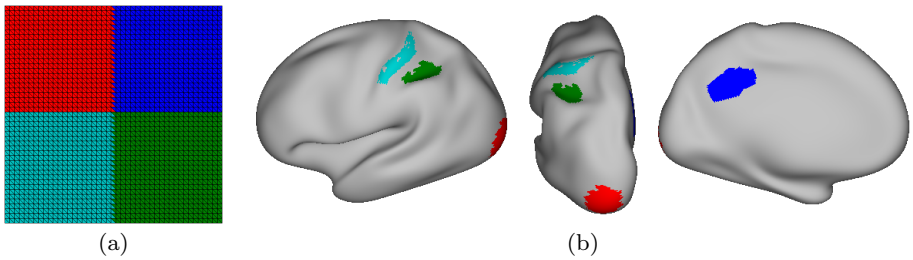

(a) (b)

Figure 6.3: Simulation setup: (a) The square surface on which smoothing and parcellation is performed. The four quadrants are color-coded for easy identification and represents functionally distinct regions. (b) The location of the four regions on cortex from which the time series for each quadrant are drawn.

6.4.2 Simulated rfMRI dataset

We used a simulated data set to investigate the effect of the different filtering methods, tNLM and LB, on identification of functionally distinct areas. We simulated a square surface patch with four quadrants, where each quadrant corresponds to a functionally distinct region. Vertices in each quadrant were assigned rfMRI time series data drawn from a small cortical region in an *in vivo* rfMRI data from a single subject. These cortical regions were chosen to lie in well known prominent networks (visual, motor, default mode and task positive networks), shown in Fig. 6.3, such that each region was locally homogeneous, based on the mean correlation with neighboring vertices, and functionally distinct from other regions.

6.4.3 N-cuts networks: parameters, visualization and boundaries

We studied the effect of filtering rfMRI data on cortical parcellation by comparing the classification of cortical networks using N-cuts with a large range of parameters. The N-cuts clustering approach sub-divides all the vertices into K disjoint sets as described in Sec. 6.3. We assign a unique label ID to all vertices which are clustered in the same set and visualize them with a unique color on the cortical surface (so that a clustering result with K classes will have K unique colors). We performed N-cuts classification, with several values of K, on a total of 160 *in vivo* rfMRI dataset (40 subjects $\times$ 4 sessions) without filtering and with LB and tNLM filtering. For both filtering types, we present results with three different level of smoothing: $h = 0.60, 0.72, 1.73$ for tNLM and $t = 2, 4, 10$ for LB filtering. The values of parameter h for tNLM were chosen based on visual inspection of the resulting smoothed data and a preliminary performance study. For qualitative comparisons of tNLM and LB filtering, we choose values of the LB parameter t by approximately matching the mutual information of LB filtered results with tNLM results for each value of h. Based on the preliminary study we chose a value of $h = 0.72$ for tNLM filtering for the majority of the qualitative results presented below (the corresponding LB

parameter was found to be $t = 4$). We note that the nature of smoothing with tNLM and LB is very different (see Fig. 6.14, supplemental results) and hence matching of smoothing levels/parameters across tNLM and LB only serves qualitative purposes. Our quantitative evaluations, described later, compare across all parameter values.

In order to enable color-coded visualization and comparisons of cortical parcellations obtained with a fixed value of K but with different filtering approaches or subjects, we first identify equivalent sub-networks by using our parcellation matching method described in 6.B, which is based on the Gale-Shapley stable matching algorithm [Gale and Shapley, 1962]. The matching method establishes a one-to-one matching between two parcellations allowing us to use the same color to represent equivalent parcels across subjects or methods.

We also investigated how the boundaries of functional regions changed with the number of networks K and the filtering approach used. For each parcellation, we obtained a binary boundary map by defining a triangle on the tessellated cortical mesh as a 'boundary' triangle if its vertices lie in more than one cluster. We summarized the boundaries across values of $K = 2, 3, 4, 5, 6, 7, 8, 9, 10, 15, 30, 40, 50, 60, 80$ by computing the cumulative boundary map across parcellations obtained with these values of K for each filtering approach and each subject. In the cumulative boundary map, the value at each triangle represents the number of times that triangle has been identified as a boundary triangle across all values of K. We also summarized the cumulative boundary maps across population by computing the population average across 40 subjects for both tNLM and LB filtering.

6.4.4 Agreement with task activation labels

As the ground-truth parcellation is absent in *in vivo* data, we evaluate the quality of the functional parcellations by performing quantitative comparisons with task activations for each subject. We used 17 different statistical task-pair activation maps, available for all 40-subjects from HCP, to obtain a discrete task label map for each subject. We first thresholded each task-pair activation map at Z-score ≥ 3.0 (one-tailed uncorrected p-value ≤ 0.00135) and merged them into a single cortical map with a unique label for each task-pair. If a vertex has Z-score ≥ 3.0 in more than one task-pair activation maps then we assigned the task label corresponding to the most significant activation. The labeled map was then cleaned by removing isolated labeled patches of size 40 vertices or less to obtain the final task label map for each subject. An example of the task label map obtain using above procedure is shown in Fig. 6.4(a) for a single subject. Only nine task-pairs survived statistical and spatial thresholding and hence we only present results with these task-pairs. Also note that the task-fMRI data was pre-analyzed with different levels of Gaussian smoothing (FWHM of 2mm, 4mm, and 8mm) to produce three different task-activation statistical maps. Here, we present results with FWHM of 4mm, however results with all other level of smoothing are included in the supplemental results (Fig. 6.20).

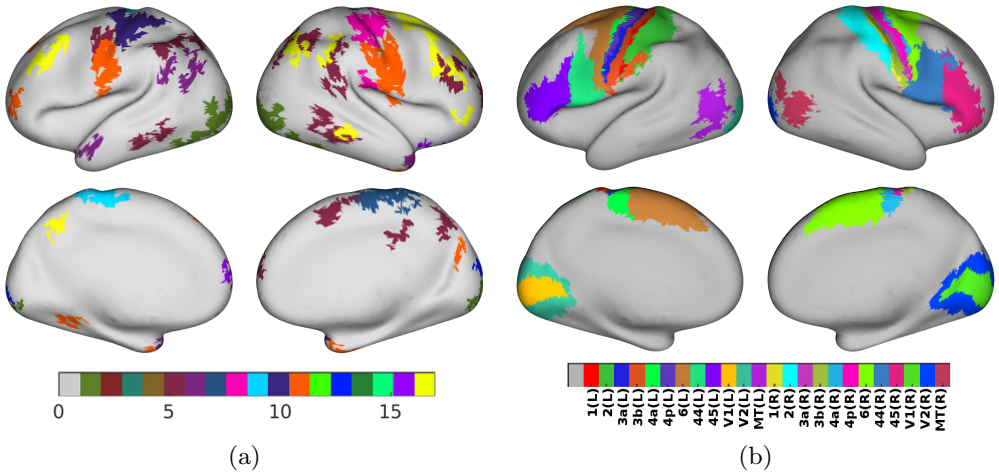

(a) (b)

Figure 6.4: (a) An example of task labels for a single subject obtained from 4mm smoothed task fMRI data (see Sec. 6.4.4 for details). The task-pair for each label-ID is shown in Fig. 6.20(d) (supplemental results). (b) An example of (thresholded) probabilistic Brodmann areas, mapped back to the subject's cortical surface.

We computed label-wise agreement between the task label maps and N-cuts parcellation using the matching method described in 6.B (we use task label as A and N-cuts parcellation as B). The agreement measure is defined as the fraction of vertices for each task label that correspond to the N-cuts parcel to which that task is matched. We computed the label-wise agreement measure separately for each parcellation, and used these measures to compare across filtering methods and parameters.

6.4.5 Agreement with probabilistic Brodmann areas

Since, it is believed that the cytoarchitectonic areas reflect functional specialization in cerebral cortex [Zilles and Amunts, 2010], it is also interesting to study how the functional parcellations obtained from rfMRI data compare with probabilistic Brodmann areas (BA). Probabilistic BA were obtained using histology studies of 10 postmortem human brains and were transferred to the subject's 32K Conte-69 cortical mesh, which are available from HCP as discrete labels (after thresholding) for each subject [Fischl et al., 2008, Van Essen et al., 2012]. An example of the discrete Brodmann label map is shown in Fig. 6.4(b). Similarly to our task based analysis, we computed label-wise agreement between BA labels and N-cuts parcellations to study the effect of different filtering approaches.

6.4.6 Test-retest reliability

To investigate the consistency of parcellations across different scan sessions of the same subject, we computed the concordance between all 6 possible pairings of the parcellation results for each of the four 15 min sessions. Concordance is a measure of consistency between parcellations and is described in

details in 6.B. The concordance measure was computed over all 40 subjects for each method and several parameter setting.

6.5 Results

6.5.1 Visualization of brain activity from rfMRI signal

We first show the resting-state time series as a series of still images and movies of BOLD signal intensities on the cortical surface for each of the following: unfiltered data, data with tNLM filtering and data with LB filtering. The movies are created by concatenating individual still images at each time point and are played back at a real-time rate *i.e.* the included movies (M1-M3, Sec. 6.C) show 3 minute of brain activity played back over 3 minutes. We render the movies at 10 frames per second by linearly interpolating the rfMRI image frames which are spaced by a TR=720ms (see Sec. 6.4.1 for preprocessing details). The signal intensities are visualized on a smoothed cortical surface using a colormap with transitions from blue (negative) to white (zero) to red (positive). The concatenated frames are encoded using the H.264 codec to produce mp4 movies.

The results of tNLM and LB smoothing are shown in the Figs. 6.1 and 6.5 first two images with detailed descriptions in the legends. In Figure 6.1 we show the cortical BOLD signal for a single subject before and after smoothing using LB and tNLM. Associated movies M1-M3 (Sec. 6.C) show 3 minutes of spontaneous brain data for the same subject. The effect of different degrees of smoothing (varying parameter h in tNLM and t in LB) are shown in Fig. 6.14 (supplemental results). In Fig. 6.5 we show examples of images obtained at different time points with tNLM filtering. Images at corresponding time points are shown in Fig. 6.13 (supplemental results) for unfiltered data and LB smoothing. As described in the legends, Figs. 6.1 and 6.5 illustrate the qualitative differences between unfiltered and tNLM and LB filtered data, with the tNLM images revealing activation at various time points that is more consistent than LB with known cortical networks. LB filtering does not use information about the time course to filter at each point in time and so can mix signals across neighboring vertices with very dissimilar time courses as seen in Fig. 6.1 and 6.13 (supplemental results). tNLM filtering on the other hand uses weights based on similarity of the time series and so largely avoids mixing of signals from dissimilar vertices. The movies similarly show qualitative differences as well as a real-time indication of the complex dynamics of resting brain activity. We interpret the irregular levels of activity, the spottiness and burst-like appearance of the anatomical regions involved, separately and in conjunction, as possibly corresponding, to what the actual brain activity during a period of undirected mind-wandering [Antrobus et al., 1970, Buckner and Vincent, 2007], so characteristic of the resting state, might look like.

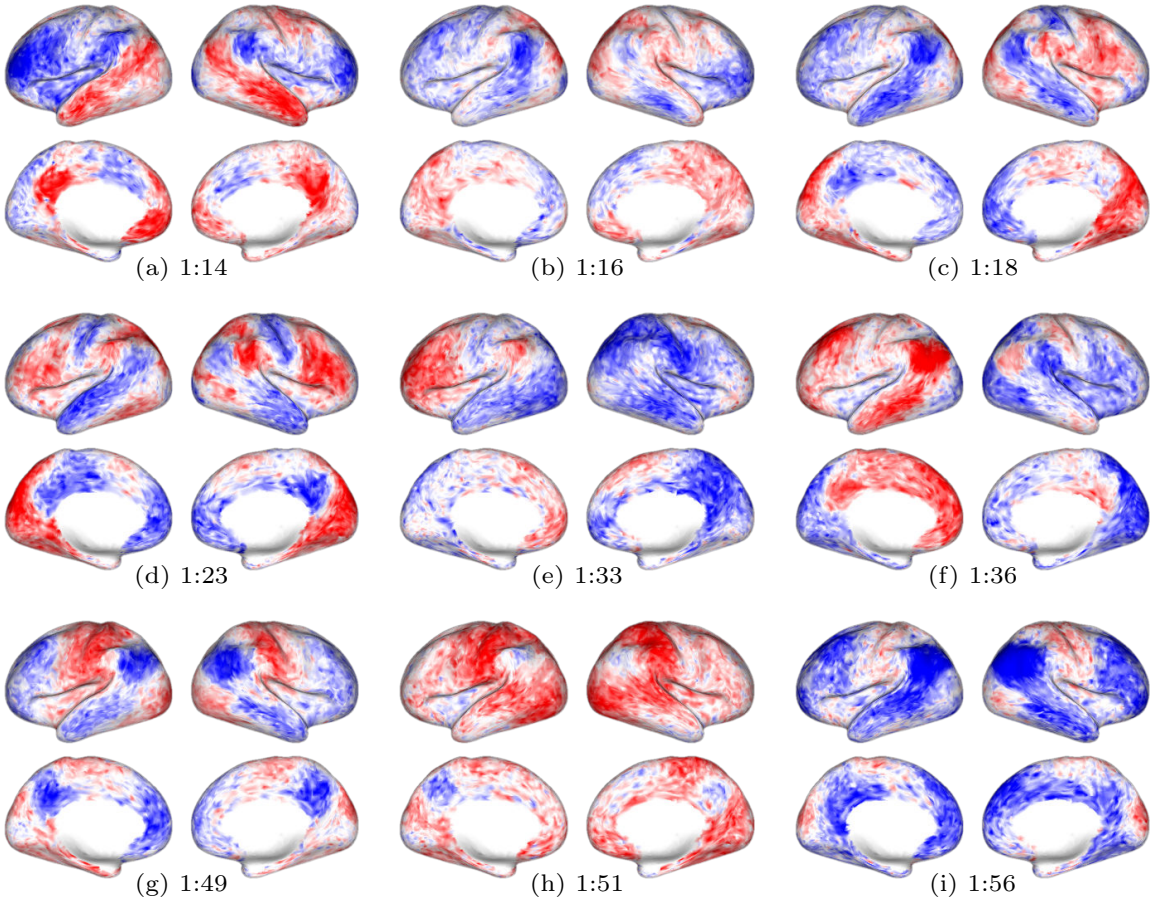

Figure 6.5: Cortical maps of BOLD intensity from a single subject at different time points with tNLM filtering ($h = 0.72$, same colorscale as fig. 6.1). The video time (min:sec) for the corresponding movie M3 (Sec. 6.C; supplemental videos) is shown for each subfigure. The video illustrates dynamic brain activity at "rest" where activation shifts from one network to another network, which can be most easily noticed around DMN and anti-correlated DMN. These networks consist predominantly of large regions distributed throughout the brain that are spatially separate but have synchronous temporal activity. In (a), at 01:14, we see activity above the mean in the DMN nodes, similar to the one seen in Fig. 6.1 (different time point), but here more symmetrical. The rest of the brain shows mostly activity below the mean, with the exception of the upper half of the sensory-motor cortices (SMC) which, on the right, show some activity above the mean; (b) only 2 seconds later the lateral temporal and parietal nodes of the DMN show activity clearly below the mean, while the activity in the PMC is still above the mean, but less so, and the activity in the mesial frontal regions is now mostly below the mean; (c) another 2 seconds later, all of the DMN nodes are clearly below the mean, while mesial occipital regions are now above the mean as are the right dorsolateral frontal and supra-marginal gyrus (SMG); so is the right insula; (d) five more second have passed and the image is almost the reverse of what was seen in (a); the DMN nodes show clear negativity, as do both SMC, while the rest of the brain, including both insulae, is clearly above the mean; (Contd. to next page)

Figure 6.5: (Contd. from previous page) (e) after 10 seconds, the activity is clearly asymmetric, with only a small region of the mesial superior frontal above the mean in the right hemisphere; left is close to the mean on the mesial aspect but it is split on the dorsolateral aspect: the frontal lobe, a small area of the SMG and the insula are above the mean, while the remainder of the hemisphere is below the mean; (f) after another 3 seconds the DMN nodes in the left hemisphere are well above the mean, the occipital lobe below, and the insula and SMC close to the mean; the right hemisphere shows an entirely different image: the angular gyrus, PMC and SMC are mildly positive while the rest of the hemisphere is clearly negative; the nodes of the DMN have definite asymmetric activity; (g) at 01:49 the DMN nodes are negative and symmetrically so, while the SMC shows activity clearly above the mean, more so on the left, and so do the occipital lobes and the left insula; (h) three seconds later the brain activity is in general above the mean with three interesting exceptions: the PMC and angular gyri show activity below the mean favoring the left hemisphere, and the left insula is also below the mean; (i) five seconds later, at 01:56, the brain is massively negative with a few exceptions where the activity approximates the mean.

6.5.2 Simulation: Effect of smoothing on clustering

We used the simulated dataset described in Sec. 6.4.2, where we know the location of the four functional regions. The correspondence between the four quadrants of the simulated surface and the locations on the cortex from which each quadrant was sampled are shown in Figs. 6.3(a) and (b). We applied N-cuts on the simulated rfMRI data using the graph structure described in Sec. 6.3 to find $K = 4$ and $K = 8$ networks without filtering and with LB and tNLM filtering (Fig. 6.6).

The results are almost perfect for $K = 4$ in both cases (Figs. 6.6(a) and (c)) and, indeed, also were for the unfiltered data (not shown) since the four regions were chosen to be internally homogeneous with respect to their time series but with a low or negative correlation between the time series in different regions. However, the clustering with $K = 8$ produces very different results as shown in Fig. 6.6(b) and (d). The linear mixing across quadrant boundaries using LB filtering produces intermediate regions that internally have a higher correlation than they do with the two regions from which the data originated. The resulting parcellation includes new contiguous regions at the boundaries between quadrants that were not present in the original data (Fig. 6.6(b), clusters in light-green, yellow and violet). When these clusters are mapped back to the surface vertices on the cortex from which they were drawn, we see they appear distributed across more than one functional area (for example elements in the light-green parcel appear in DMN, visual and motor areas). This clearly demonstrates that the contiguous regions at the boundaries between quadrants are solely an artifact of mixing from LB smoothing and do not reflect true underlying patterns of functional similarity in the rfMRI time series. We believe this in an important observation as the creation of false parcels resulting from LB smoothing could lead to erroneous interpretation of parcellations in *in vivo* data.

In contrast, tNLM filtering shows a strong pattern of sub-division of functionally distinct areas when

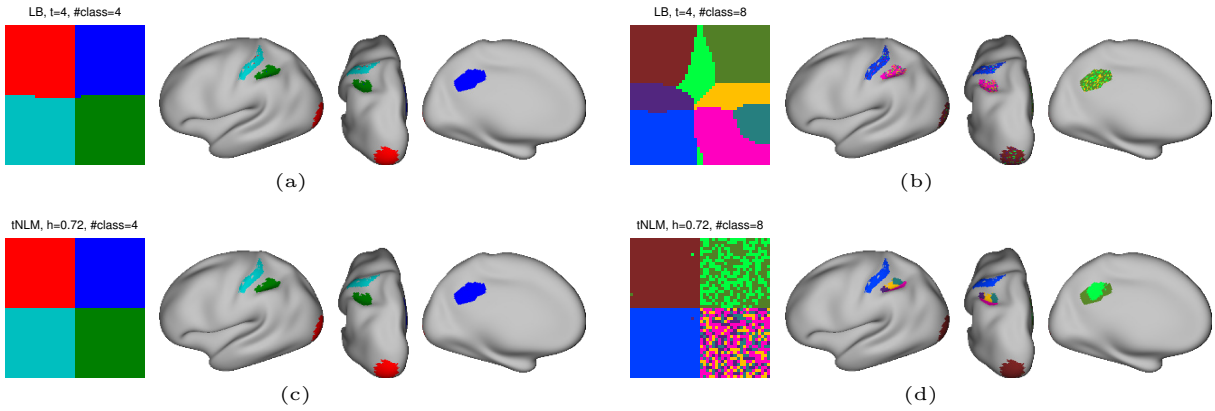

Figure 6.6: Simulation results: The result of N-cuts parcellation of LB filtered data into (a) $K = 4$ and (b) $K = 8$ clusters are also shown on the simulated square surface as well as on the original cortex, on the right, by mapping back the color-coded vertices from the square mesh to its original location on the cortex. Similarly, the results of N-cut parcellation for tNLM filtered data into (c) $K = 4$ and (d) $K = 8$ clusters are shown on square surface and on the original surfaces.

$K = 8$ class clustering was used, Fig. 6.6(d): vertices in the top right quadrant (corresponding to DMN) get sub-divided into two parcels (light and dark green) and vertices in the bottom right quadrant (task positive network, TPN) get sub-divided into four parcels which are distinct from those in the top right quadrant. While the spatial organization of these clusters in the square image appears random, when they are mapped back to the area on the cortex, from which they were drawn, we see that the clustering result actually sub-parcellates the DMN and TPN regions. This result demonstrates the "non-local" nature of tNLM - smoothing is performed based on similarity in time series rather than spatial proximity. For this reason, subsequent partitioning based on a fully connected graph can identify groups of pixels with similar time-series in the original data rather than producing false parcels as a result of local mixing of signals across functional areas as seen with LB filtering. This edge preserving nature of tNLM also allows accurate sub-division of functional regions when clustering is performed with larger value of K, as seen in the cortical map in Fig. 6.6(d).

We do not include results for unfiltered data for the simulation since they are qualitatively very similar to those obtained using tNLM for both $K = 4$ and $K = 8$. Since each quadrant was selected to have clearly distinct time series from all other quadrants, the N-cuts algorithm, even without smoothing, was able to reliably partition the data for $K = 4$. Further, the unfiltered data produced a very similar sub-parcellation for $K = 8$ to that shown in fig. 6.6(d), which indicates that there is evidence for these sub-parcellations in the data and these results are not an artifact of the nonlinear tNLM smoothing. As we show below, this similarity between tNLM and unfiltered data does not occur when N-cuts is applied to the complete set of *in vivo* data.

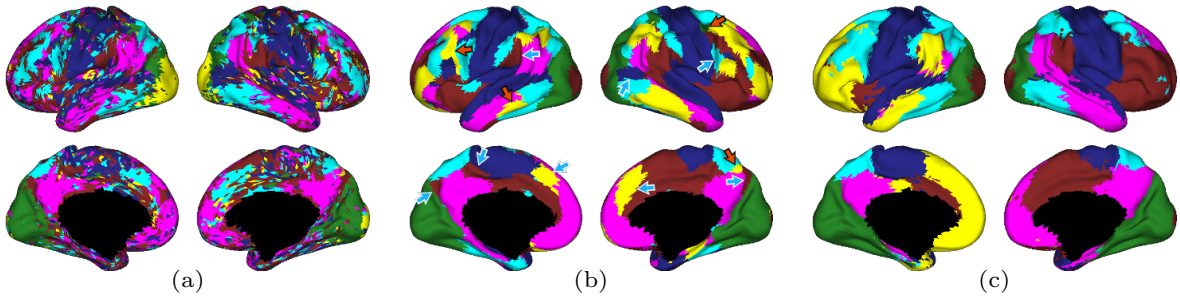

Figure 6.7: Cortical parcellations using N-cuts on a fully connected cortical surface graph for a single subject to partition cortex into $K = 6$ networks with (a) unfiltered data, (b) LB filtering (t=4), and (c) tNLM filtering (h=0.72). In each case a distinct color represents one of the $K = 6$ networks. Arrows in (b) illustrate regions lying between two large parcels that are classified as a separate network and appear similar to the false regions resulting from linear smoothing shown in the simulation in Fig. 6.6(b).

6.5.3 Qualitative evaluation of cortical networks

Figure 6.7 shows the result of N-cut clustering with six classes for a single subject. Clusters obtained from the original unfiltered data, Fig. 6.7(a), yields default mode (pink), visual (yellow/green), and somatomotor (dark blue) networks. However, the clusters are noisy and disjointed. In contrast, tNLM smoothed data shows networks with large contiguous regions, Fig. 6.7(c). In addition to the networks identified in the original data we can also identify the visual system (dark green) and and the cingulo-opercular (dark red) networks. We can also identify the fronto-parietal network, often described as anti-correlated to the default mode network (light blue), which includes the frontal eye field, left middle frontal gyrus, superior parietal lobule, and the lateral-posterior regions of the temporal lobe [Fox et al., 2005, 2006, Vincent et al., 2008, Fransson, 2005, Buckner et al., 2008]. It is also noticeable that the DMN seems to be sub-divided in two clusters (in yellow and pink) in the tNLM parcellation. At smaller values of K, we do expect both hemispheres of the DMN to be grouped into a single label, as seen in tNLM N-cuts clustering with four classes, Fig. 6.15 (supplemental results). With progressive increases of N-cut classes, K, we should see the network systems to continue to subdivide.

LB filtering, Fig. 6.7(b), produces similar networks to those identified by tNLM, however some of the networks separate into a larger number of non-contiguous parcels, which appear as patches of small parcels through out the cortex. Notice in the lateral surface of the frontal lobe, we see a mix of smaller patches of the yellow, pink, light blue, and dark blue labels which are isolated away from the large, spatially continuous portion of each label. This makes it difficult to judge whether the yellow label is a sub-division of the DMN or of the pre-frontal cortex. We also see that the inferior frontal gyrus (part of the language network) is fragmented into five different labels. At a coarse parcellation of the cortex into only six labels, we do not expect this system to be sub-divided. In contrast, tNLM seems to preserve

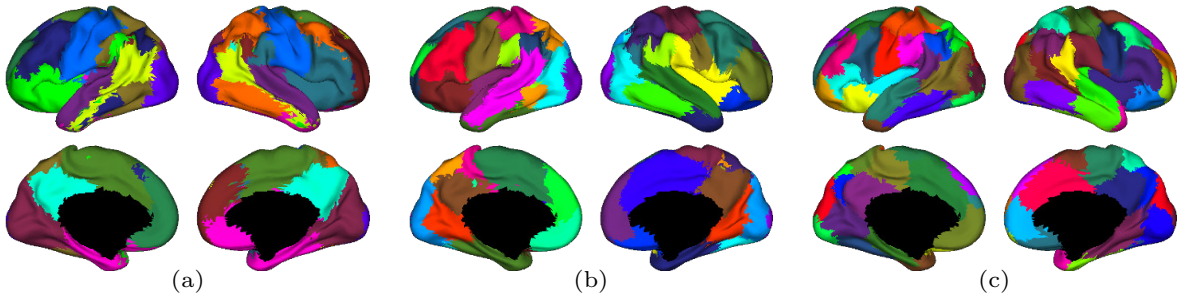

Figure 6.8: Cortical parcellation N-cuts applied to tNLM filtered (h=0.72) data for the same subject as in Fig. 6.7 for (a) $K = 15$, (b) $K = 30$ and (c) $K = 60$ clusters. See Fig. 6.15 (supplemental results) for equivalent images for unfiltered and LB filtered data.

the area as a part of larger cluster. Further, it can be also be noticed that several regions between two large networks are classified as a separate network as indicated by the arrows. A greater number of patchy regions in the LB result, particularly near boundaries of known networks, is consistent with the formation of additional false parcels in the simulation study in the previous section. Such behavior is largely absent in tNLM results.

As the number of subgraphs increases with (a) K=15, (b) K=30, and (c) K=60, we notice that boundaries are frequently preserved and regions are sub-divided with tNLM filtering (Fig. 6.8) while the equivalent results for unfiltered data become increasingly noisy, and LB filtering continues to produce apparently spurious regions which appear as patches of small clusters around boundaries of larger networks (Fig. 6.15 supplemental results). For example, for tNLM results, the somatosensory and motor cortices are initially identified as a single network (blue) for $K = 15$ classes (Fig. 6.8(a)). When the number of classes is doubled, this area sub-divides into the right upper (violet), and left upper (pink), and the lower (brown) somatomotor cortices (Fig. 6.8(b)). Increasing the number of classes to 60, the right lower somatomotor cortex (red) separates from the left hemisphere, and further divides into the ventral premotor cortex (blue) and the ventral motor cortex (dark red) (Fig. 6.8(c)). Similar patterns of progressive subdivision can be observed in other primary networks including the visual network.

In Fig. 6.9 we illustrate how the boundaries of the clusters vary across several parcellations with different number of classes in both tNLM and LB. Fig. 6.9(a) and (b) shows cumulative boundaries for a single subject over different number of classes. The tNLM results show consistent boundaries delineating the ventro-medial prefrontal cortex, posterio-medial cortex (PMC) and the visual cortex. The LB results are quite similar, however, we notice larger number edges running through the primary network regions (for example, several edges are seen in the interior of PMC and similarly some edges are seen in the interior of the medial side of visual cortex running parallel to the boundary between visual cortex and PMC on both hemispheres). When cumulative edges are averaged across the population of 40 subjects,

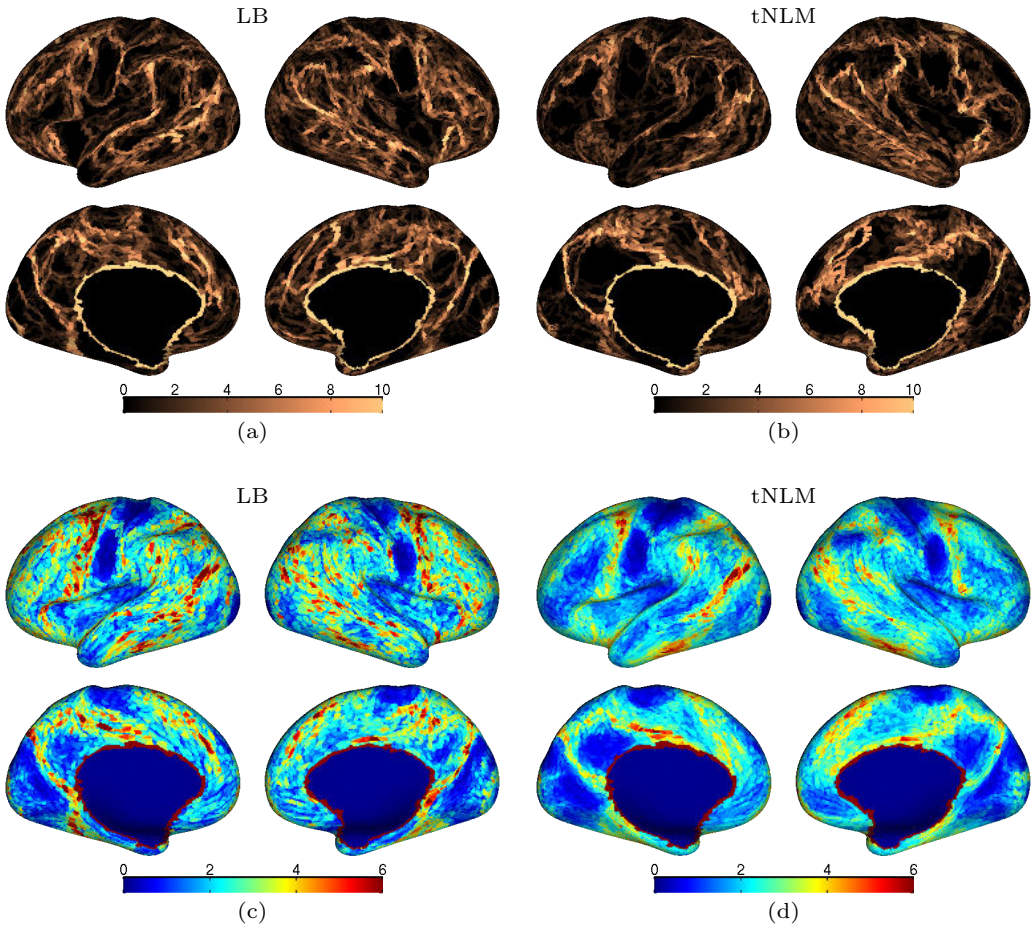

Figure 6.9: Cortical map of the cumulative boundaries of N-cut parcellations over fifteen different values of K in a single subject with (a) LB ($t = 4$) and (b) tNLM ($h = 0.72$) filtering. The population average cumulative boundary map across the 40 subjects are also shown with (c) LB ($t = 4$) and (d) tNLM ($h = 0.72$) filtering. The value at each triangle represents total number of times that triangle was a identified as a boundary triangle across fifteen different clustering results ($K = 2, 3, 4, 5, 6, 7, 8, 9, 10, 15, 30, 40, 50, 60, 80$). The boundary maps are thresholded at an upper boundary count of 10 for single subject and 6 for the population average.

Fig. 6.9(c) and (d), we notice differences between the methods more clearly, with boundaries occurring more consistently across different values of K with tNLM filtering than with LB filtering. In both cases the upper and lower sensorimotor areas are consistently identified, as evidenced through the absence of boundaries in these regions. However, tNLM shows clearer boundaries than LB, particularly for the PMC, the visual cortex and the ventrolateral prefrontal cortex. Higher order association cortices also clearly show marked internal consistency with tNLM. LB shows boundaries spread across frontal and lateral posterior temporal-occipital region, again, possibly reflecting the introduction of false parcels near boundaries between functional areas as illustrated earlier in the simulation study.

Additional results showing the distribution of the number and size of clusters in LB and tNLM N-cuts parcellations are included as Fig. 6.16 – 6.19 (supplemental results). These results support the general observation that LB results tend to produce more, smaller contiguous clusters than tNLM.

6.5.4 Quantitative comparison with task fMRI labels

We quantify the quality of parcellations obtained with different filtering approaches by computing the agreement of rfMRI parcellation with task labels for each subject (see Sec. 6.4.4 for details). An example of task labels for a single subject are shown in Fig. 6.4(a). For each subject, we investigate the agreement of each task label across several rfMRI parcellations obtained with different number of classes ($2 \leq K \leq 400$) and with different filtering approaches: unfiltered, LB filtering ($t = 2, 4, 10$) and tNLM filtering ($h = 0.60, 0.72, 1.73$). Fig. 6.10(a) shows the mean agreement fraction of an example task label, left foot motor task, with clustering results across the population. Similar plots for other task labels are included in the supplemental results (Fig. 6.23). For the tongue motor task, we also studied the performances by subdivided the tongue region into two regions, one on each hemispheres, because the N-cuts clustering frequently sub-divided the clusters across hemisphere for $K > 15$. We see that mean agreement fraction varies substantially with number of classes K for all filtering approaches and all task labels. LB and tNLM show similar behavior for very smaller number of classes ($K < 10$), however tNLM filtering achieves larger agreement than LB across a wider range of K.

The performance of different filtering peaks at different values of K for different tasks. This behavior is expected as the value of K and smoothing parameters controls the quality of the resulting clusters. Here, we define the 'best' parcellation as the set of clustering and filtering parameters (K for unfiltered; K and t for LB; K and h for tNLM) that achieves the largest mean agreement across the population for a particular task. We compared the performance of different filtering approaches for their 'best' parcellation for each task label in Fig. 6.10(b). This comparison shows substantial improvement in performance over unfiltered data with LB or tNLM but overall tNLM filtering achieves a larger mean agreement fraction. More complete overall results for different levels of smoothing of the task data are shown in supplemental results (Fig. 6.21 with detailed results for individual tasks in Figs. 6.22 – 6.24).

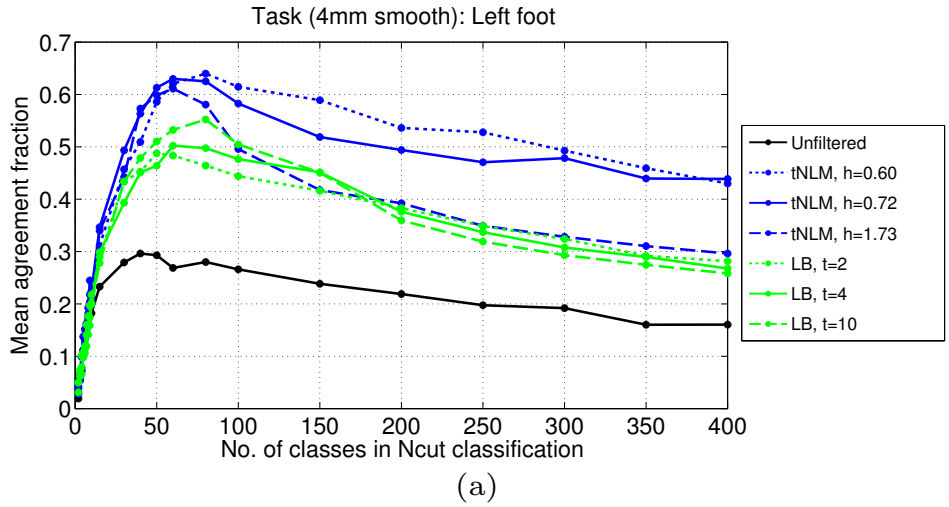

(a)

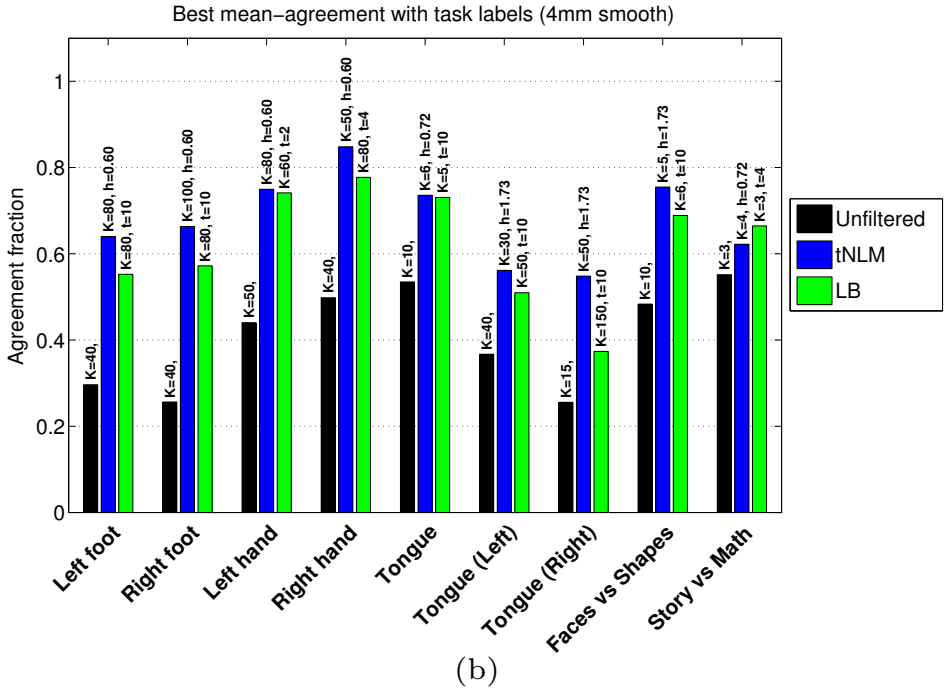

(b)

Figure 6.10: (a) Mean agreement fraction, across 40 subjects $\times$ 4 session, of an example task label (Left foot, motor task) with N-cuts parcellations obtained using unfiltered, LB filtered and tNLM filtered rfMRI data. See supplemental results (Fig. 6.23) for corresponding plots for all task labels. (b) Best performance of different filtering approaches across different task labels. For each task and each filtering approach, we select the parameters which achieves the highest mean agreement fraction. The grouped bar plot shows the highest mean agreement fraction and the text on top shows the corresponding parameters.

Task-pair (ID)	Alternate hypothesis	Rank-sum p-values	Signed-rank p-values
Left foot (7)	tNLM > LB	8.399×10^{-4}	7.588×10^{-9}
Right foot (9)	tNLM > LB	3.3557×10^{-4}	1.7304×10^{-7}
Left hand (8)	LB > tNLM	0.053848	0.0039957
Right hand (10)	tNLM > LB	1.0452×10^{-4}	2.7763×10^{-13}
Tongue (11)	LB > tNLM	0.31327	0.0016967
Tongue (Left)	tNLM > LB	0.04225	3.4968×10^{-6}
Tongue (Right)	tNLM > LB	1.1488×10^{-10}	6.995×10^{-20}
Faces vs. Shapes (1)	tNLM > LB	6.1754×10^{-6}	1.8794×10^{-9}
Story vs. Math (6)	LB > tNLM	0.0031035	9.4594×10^{-9}

Table 6.1: Statistical tests for improved agreement with task labels: Table of (uncorrected) p-values for one-sided tests for 'best' performance of LB and tNLM filtering (see text for detailed description). For each task label, the best performance parameters for both filtering approaches are reported in Fig. 6.10(b). The agreement fractions across population, computed with these filtering parameters, are used as the performance metric for the tests. The alternate hypothesis "tNLM>LB" means that the median agreement fraction of the tNLM approach is greater than the median agreement fraction of the LB approach; and similarly for "LB > tNLM".

We also performed two non-parametric tests to examine the statistical differences between the 'best' parcellations of LB and tNLM filtering for each task label, the results of which are presented in table 6.1. For the first test we used a one-sided Mann-Whitney U (rank-sum) test [Gibbons and Chakraborti, 2003] with the null hypothesis that there is no difference between the agreement fraction corresponding to 'best' parcellation of LB and tNLM across all subjects. We used the one-sided Wilcoxon signed-rank paired test [Gibbons and Chakraborti, 2003] as the second test with a null hypothesis of no subject-wise difference in 'best' performances between LB and tNLM filtering. The alternate hypotheses for both of the one-sided tests (*i.e.* which tail to test) were decided by the value of the population median of agreement fractions and are reported in Table 6.1 for each task-pair. These statistical tests indicate that tNLM filtering significantly improves the agreement with several task labels when compared with LB filtering.

6.5.5 Quantitative comparison with probabilistic Brodmann areas (BAs)

We also computed quantitative agreement of N-cuts parcellations with probabilistic BAs. Fig. 6.11 shows the summary of the best performances for different filtering approaches for each BA. Consistent

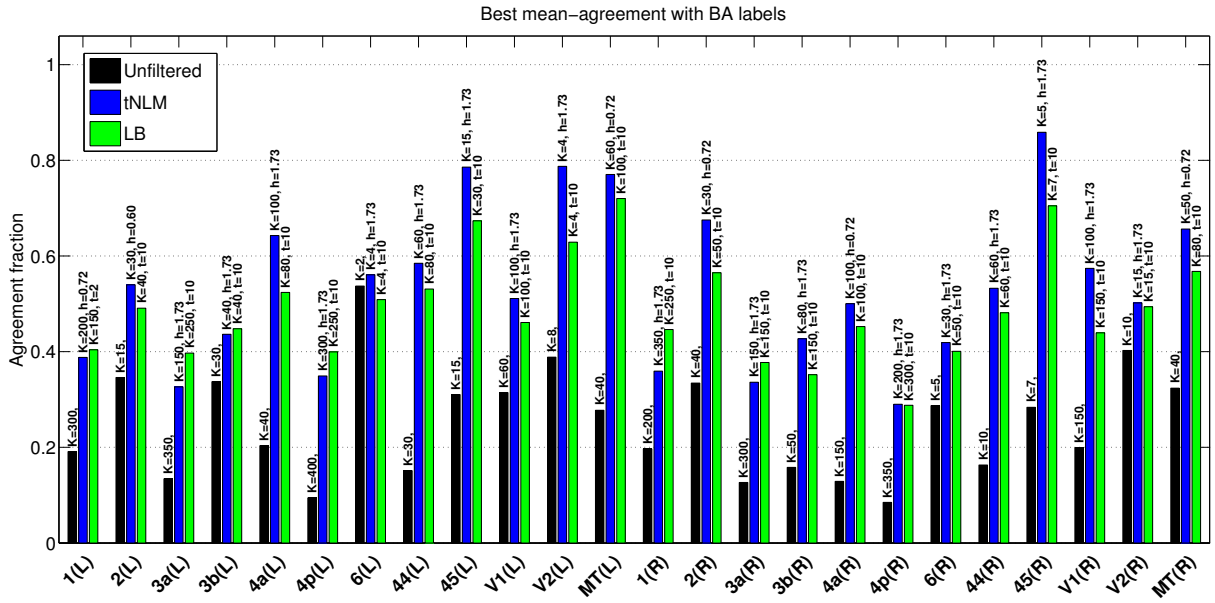

Figure 6.11: Best performance of different filtering approaches across different probabilistic Brodmann areas (BA). For each BA and each filtering approach, we select the parameters which achieves the highest mean agreement fraction. The grouped bar plot shows the highest mean agreement fraction and the text on top shows the corresponding parameters. Detailed BA-wise performance results are included in Fig. 6.25 (Supplemental results).

with our previous observation for task fMRI, tNLM achieves the highest agreement fraction across several BA (for 18 out of 24 BAs). We also performed the two non-parametric (one-sided) statistical tests with the same null hypothesis as the task analysis. The results and alternate hypothesis of the statistical tests are reported in table 6.2 which reveal that tNLM filtering significantly improves the agreement of several BA labels with the parcellation results as compared with LB filtering. There are few BA labels, such as BA 3a (L), for which LB parcellations shows higher median agreement than tNLM. More complete data are included in Fig. 6.25 (supplemental results) in which mean agreement is plotted for each method and parameter for each of the BAs.

6.5.6 Quantitative test-retest reliability

In Fig. 6.12 we show within-subject agreement over all six possible pairs of parcellations from the four 15-min rfMRI sessions per subject. The agreement between a pair of parcellation is quantified by the concordance measure, described in 6.B, which measures the fraction of vertices which agree between the parcellations. We plot the median concordance, over the six pairs per subject and the 40 subjects, as a function of the number of cuts, K, for three different smoothing parameters for LB and tNLM. Non-parametric Mann-Whitney U (rank-sum) tests for significant differences (uncorrected) between median

Brodmann areas	Alternate hypothesis	Rank-sum p-values	Signed-rank p-values
1(L)	LB $>$ tNLM	0.119	0.0517
2(L)	tNLM $>$ LB	0.00997	0.00997
3a(L)	LB $>$ tNLM	0.0306	4.07×10^{-4}
3b(L)	LB $>$ tNLM	0.581	0.666
4a(L)	tNLM $>$ LB	1.04×10^{-9}	2.74×10^{-11}
4p(L)	LB $>$ tNLM	2.13×10^{-7}	1.61×10^{-6}
6(L)	tNLM $>$ LB	0.0059	7.69×10^{-7}
44(L)	tNLM $>$ LB	0.00234	0.00243
45(L)	tNLM $>$ LB	1.57×10^{-12}	8.77×10^{-7}
V1(L)	tNLM $>$ LB	0.0098	0.00861
V2(L)	tNLM $>$ LB	1.06×10^{-7}	1.74×10^{-8}
MT(L)	tNLM $>$ LB	7.22×10^{-5}	0.000313
PH(L)	tNLM $>$ LB	0.00232	0.00521
1(R)	LB $>$ tNLM	7.18×10^{-11}	2.77×10^{-11}
2(R)	tNLM $>$ LB	3.46×10^{-10}	6.49×10^{-10}
3a(R)	LB $>$ tNLM	5.96×10^{-4}	0.00121
3b(R)	tNLM $>$ LB	2.36×10^{-20}	9.9×10^{-19}
4a(R)	tNLM $>$ LB	9.34×10^{-4}	2.07×10^{-4}
4p(R)	tNLM $>$ LB	0.178	0.272
6(R)	tNLM $>$ LB	0.131	0.07
44(R)	tNLM $>$ LB	2.79×10^{-4}	6.91×10^{-4}
45(R)	tNLM $>$ LB	2.35×10^{-13}	5.25×10^{-10}
V1(R)	tNLM $>$ LB	8.1×10^{-15}	2.84×10^{-14}
V2(R)	LB $>$ tNLM	0.621	0.865
MT(R)	tNLM $>$ LB	2.06×10^{-4}	3.07×10^{-4}
PH(R)	tNLM $>$ LB	0.105	0.146

Table 6.2: Statistical tests for higher agreement with probabilistic Brodmann areas: Table of (uncorrected) p-values for one-sided tests for 'best' performance of LB and tNLM filtering (parameters of 'best' parcellation are reported in Fig. 6.11). The procedure and description of the non-parametric tests are same as that of task labels in table 6.1.

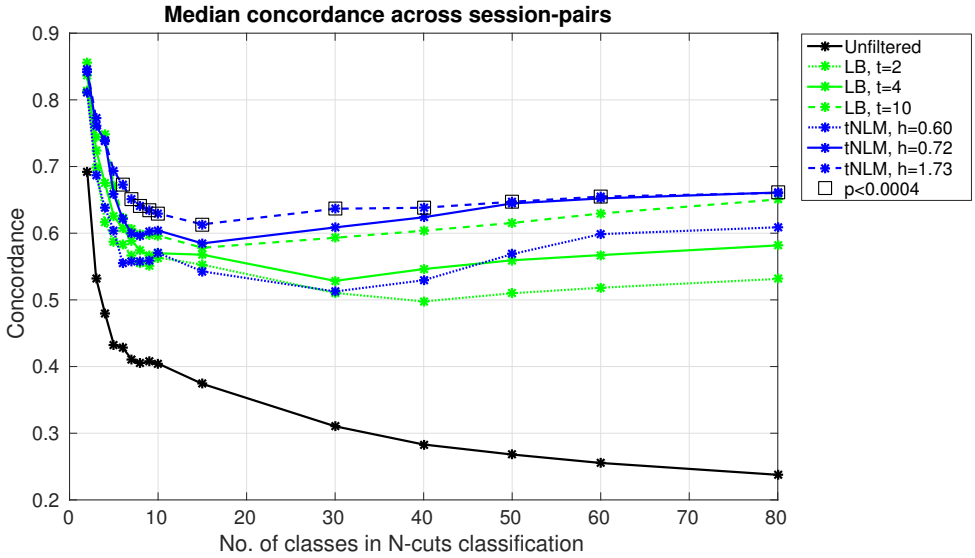

Figure 6.12: Test-retest reliability: Median concordance of parcellation results over the pairs of rfMRI sessions (40 subject $\times$ 6 session pairs) as a function of the number of cuts, K = 2 to 80, for different filtering approaches. Square boxes indicate significant differences (uncorrected p-value < 0.0004) between best of tNLM and LB median concordance values, as tested with Mann-Whitney U (rank-sum) test.

performances of tNLM and LB were also performed and the square boxes indicate values of p-value < 0.0004. These results show concordance for LB and tNLM roughly decreases until $K = 10$, and then remains relatively stable but with a slow increases as K increases to 80. The unfiltered data results are far worse than either LB or tNLM. Over the range from K=6 to 80, tNLM with $h = 0.72$ and $h = 1.73$ consistently outperform the other methods and settings. Qualitatively, tNLM with $h = 0.72$ and LB with $t = 4$ produced the best apparent results, and there is a clear difference in performance here between these two over the same range ($K = 6$ to 80). While it is initially surprising that the concordance improves with K (this trend continues for $K > 80$ with LB ultimately given significantly larger concordance than tNLM for $K > 130$, see Fig. 6.26 in supplemental results), we believe this is simply a result of the decreasing size of the networks and the nature of the matching algorithm used to compute concordance (6.B). Consider the limiting case where K = *number of vertices*. Then each surface vertex forms a different parcel. In this case, the matching algorithm would achieve a perfect match and 100% consistency. The supplemental results (Figs. 6.16 – 6.19) show that cluster-sizes of LB parcellations are substantially smaller than tNLM, especially for $K > 130$. Cluster-size distribution in Fig. 6.16 (top) shows that tNLM has several clusters which are substantially larger than LB for $K \geq 100$. The cortical distribution of cluster-size in Fig. 6.18 shows this effect more clearly, where we see that

tNLM results have substantially larger clusters as compared to LB across most of the cortex[4]. Since the average size of the clusters in LB for a fixed K is substantially smaller than that for tNLM, we believe there is an increased chance of a (random) good match between pairs of parcellations (with the matching algorithm in 6.B). Figures 6.27 and 6.28 (supplemental results) illustrate the spatial distribution of concordance/disagreement in region boundaries for tNLM and LB as a function of K.

6.6 Discussion

The tNLM filtering results shown in Fig. 6.1 appear qualitatively quite different from both the unfiltered noisy data and the result of linear LB smoothing. While the images are smoother in the latter, the regions appearing coherently activated are more patchy, which results in the apparently spurious clustering results as seen in Fig. 6.7(b) and (e). An example of how these spurious clusters can be formed as a result of LB smoothing is shown in the simulation example, Fig. 6.6. The presence of spurious clusters around boundaries of large networks can also be appreciated by comparing Figs. 6.18 and 6.19 for $K = 50$ and 100 in the supplemental results, which show the average cluster-size before and after breaking networks into contiguous parcels. The filtered images obtained with tNLM filtering appear to allow more direct identification of components of known networks. In Fig. 6.5 a sequence of images at short intervals shows how coherent co-activation changes between networks. As activity in one network increases and that in an adjacent network decreases, the effect of LB smoothing across the boundary between these networks produces an apparent boundary or wave moving from one network to the other. This behavior is apparent in the LB movie. With tNLM, since only surface elements with similar time series are averaged to denoise the data (as demonstrated in Fig. 6.2), when two adjacent networks have distinct time series then they will not be blurred through smoothing and this wavelike effect does not occur. Instead, the impression is that of irregular, burst like activity, which might be expected during a period of undirected mind-wandering [Antrobus et al., 1970, Buckner and Vincent, 2007]. Qualitatively, there are clearer boundaries in tNLM relative to LB, although it is also evident that even within networks, activation is not always synchronous. The ability of tNLM to denoise data while respecting functional boundaries makes it a potentially attractive processing tool both for data exploration and as a precursor to network identification or parcellation.

There are relatively few examples showing real time rfMRI whole-brain activity in the form of either single frame images or movies in the literature. An early example[5] from Vincent et al. shows real-time

[4]Both tNLM and LB results have same number of clusters for a fixed K (Fig. 6.18, supplemental results). However, tNLM results seems to consistently have several large clusters as well as several small clusters. LB results on the other hand seems to uniformly divide the whole cortex in approximately equal size for large K. This can also be seen in cortex-size distribution plots in Fig. 6.16 (top).

[5]Available online: https://youtu.be/VaQ66lDZ-08 and https://youtu.be/3nCBLw9Z-xU (last accessed: December 04, 2015).

brain dynamics from data used to explore resting networks [Fox et al., 2006, Vincent et al., 2006] but the dynamics do not clearly show coherent activity in regions forming the default mode and other networks. Kundu et al. [Kundu et al., 2013] have developed a method for denoising multi-echo fMRI data that distinguishes BOLD from non-BOLD signals based on echo-time dependence. The resulting denoised data show dynamic activation in DMN and other networks in real-time[6] similar to that shown in Figs. 6.1 and 6.5. However this approach explicitly requires a multi-echo sequence and unlike tNLM cannot be applied to standard fMRI protocols. The dynamics shown in the movies in also share similarities with those in Zalesky et al. [Zalesky et al., 2014] who explore the HCP resting data data using dynamic regional network efficiency measures, computed from time-resolved connectivity estimates, to produce movies of brain dynamics. Their results show "a consistent set of functional connections (with) pronounced fluctuations in their strength over time". The authors also note spontaneous increases in spatially distributed regions over brief intervals, observations that can be also be made from the movies in the Sec. 6.C.

While all examples shown here are restricted to cortex, tNLM filtering can also be applied to volumetric or grayordinate [Glasser et al., 2013] representations of the data. Similarly, tNLM could be applied as a denoising tool in event-related functional MRI studies which may result in improved resolution of focal activation relative to methods based on conventional isotropic linear smoothing. The tNLM method could also be extended to include a spatial component, so that the weighted average depends on a combination of temporal and spatial similarity. It would also be interesting to explore a dynamic version in which the similarity measure is computed of restricted time-window, rather than the entire time-course as was the case in the results presented above.

We illustrated the potential utility of tNLM through cortical parcellation studies based on N-cuts spectral graph partitioning. Our approach parcellates a single subject using a fully connected graph with edge strengths based on pairwise correlations between the time series on the surface elements. Most previous applications of graph-cuts in brain parcellation have used locally connected graphs to ensure spatially contiguous parcels [Blumensath et al., 2013, Craddock et al., 2012]. While this appears necessary for unfiltered data (Fig. 6.7(a)), the denoising effect of tNLM allows use of the fully connected graph while still producing a piece-wise contiguous parcellation (Fig. 6.7(c)). This has the advantage of using all correlations for parcellation rather than a restricted subset, thus using more information. LB smoothed data can also be parcellated using the fully connected graph (Fig. 6.7(b)) but the resulting networks appear to contain regions that may not actually belong. We explored this issue further in the simulations shown in Sec. 6.5.2. LB smoothing applied to the four quadrant configuration in Fig. 6.6 produced mixing of signals across quadrant boundaries that it turn resulted in artifactual networks that arise purely as a result of filtering. This finding indicates that care should be taken when using linear smoothing in combination with parcellation methods based on pairwise correlations to ensure that parcels

[6] Available online: https://youtu.be/D_UUfIF49Vc (last accessed: December 04, 2015).

are not produced solely as an artifact of smoothing.

Changes in parcellation as a function of the number of networks was investigated in Fig. 6.8 for tNLM (with equivalent results in Fig. 6.15 for LB and unfiltered data). A well known problem with N-cuts is that the algorithm tends to produce cuts of similar size if the graph (and its adjacency matrix) does not contain sufficient information to unambiguously support a single K-way partition [Blumensath et al., 2013]. We note that this does seem to be the case even for the relatively large number of networks ($K = 60$) as shown in Fig. 6.8. The plots of cluster-size distribution in Fig. 6.16 and 6.18 (supplemental results) also shows similar evidences. To investigate consistency as a function of the number of networks, we averaged edge locations over multiple values of K in Fig. 6.9. It is interesting that the resulting individual edge maps (Fig. 6.9(a)) bear a strong resemblance to the group functional connectivity gradients shown in Fig. 10 in [Smith et al., 2013a].

Quantitative comparisons with task labels and Brodmann areas in Sec. 6.5.4 and 6.5.5 demonstrate that tNLM filtering achieves significant improvement over LB filtering across most task labels and BA and wide range of K. It is interesting to note that both filtering approaches show peak performance around similar number of classes K.

6.7 Conclusion

The results shown above support the primary claim of this chapter: that temporal non-local means (tNLM) filtering is able to denoise resting fMRI data while also retaining much of the spatial structure that reflects ongoing dynamic brain activity. Correlated variations in activity are directly visible in the movies of cortical activity, which appear to reflect the underlying dynamics of large-scale brain networks. This ability to visualize real-time whole-brain networks may facilitate exploratory data analysis leading to new insights into the dynamics of spontaneous brain activity. Temporal NLM can also be used as a preprocessor for resting fMRI for exploration of dynamic brain networks and achieves significant improvement over traditional isotropic smoothing in quantitative agreement with task-based labels and probabilistic Brodmann areas.

Appendices

Appendix 6.A Laplace-Beltrami filtering

Gaussian filtering is frequently used to isotropically smooth volumetric 3D data in functional and task based fMRI studies. Isotropic smoothing can also performed on a 2D manifold such as the cortical surface. Because cortical surfaces have an intrinsic curvature that prevents them being mapped without distortion onto the plane, isotropic smoothing requires that curvature be taken into account. The Laplace-Beltrami (LB) operator, which generalizes the 2D Gaussian smoothing kernel from the plane to an arbitrary smooth manifold [Angenent et al., 1999], can produce isotropic smoothing on cortex.

In this approach, a solution of the heat equation $\frac{\partial f(p,t)}{\partial t} = \Delta f(p,t)$ with initial condition $f(p,0) = Y(p)$ is used to smooth the data $Y(p)$, where Δ is the LB operator on the cortical manifold parameterized by p [Joshi et al., 2009b, Seo et al., 2010, Seo and Chung, 2011]. The parameter t represents the diffusion time for the heat equation. The degree of smoothing increases with t. The solution is given by [Rosenberg, 1997, chap. 1]

$$f(p,t) = \int Y(q)\, K_t(p,q)\, \mathrm{d}q \tag{6.4}$$

where, $K_t(p,q)$ is the heat kernel which can be expressed in terms of ordered eigen-functions $\phi_0, \phi_1, \phi_2, \cdots$ and corresponding eigen-values $\lambda_0, \lambda_1, \lambda_2, \cdots$ of the Laplace-Beltrami operator Δ as [Rosenberg, 1997, Seo et al., 2010, Seo and Chung, 2011]

$$K_t(p,q) = \sum_{n=0}^{\infty} \mathrm{e}^{-\lambda_n t} \phi_n(p)\, \phi_n(q). \tag{6.5}$$

The solution at time t can therefore be expressed as

$$\begin{aligned} f(p,t) &= \int Y(q) \sum_{n=0}^{\infty} \mathrm{e}^{-\lambda_n t} \phi_n(p)\, \phi_n(q)\, \mathrm{d}q \\ &= \sum_{n=0}^{\infty} \mathrm{e}^{-\lambda_n t} \phi_n(p) \int Y(q)\, \phi_n(q)\, \mathrm{d}q \end{aligned} \tag{6.6}$$

Eq. (6.6) can be expressed in discrete form as a square matrix of dimension equal to the number of vertices on the cortical surface using a truncated eigen-function expansion of the LB operator (we use the first 800 eigenfunctions in all results with LB filtering in this chapter). The level of smoothing of the final solution is parameterized by the time parameter t. Fig. 6.2 shows example of weights applied to neighboring vertices for a particular vertex for different values of t, which can be intuitively interpreted as the smoothing kernel at the vertex. This approach allows efficient computation of filtered images as the eigen-decomposition needs to be computed only once irrespective of number of rfMRI volumes or level of smoothing.

Appendix 6.B Mapping and measures between parcellations

Assume we have two parcellations A and B for a set of vertices V: $A = \{A_i : i \in \mathbb{Z}_M\}$ parcellates V into M parcels where $\mathbb{Z}_M = \{1, 2, \cdots, M\}$ such that $\cup_i A_i = V$ and $\forall i \neq j,\ A_i \cap A_j = \varnothing$ and $B = \{B_i : i \in \mathbb{Z}_N\}$ parcellates V into N parcels where $\mathbb{Z}_N = \{1, 2, \cdots, N\}$ such that $\cup_i B_i = V$ and $\forall i \neq j,\ B_i \cap B_j = \varnothing$.

Label-wise agreement

Agreement is a label-wise measure of the fraction of vertices that agree between two parcellations A and B. Specifically agreement of parcel $A_i \in A$ with the corresponding parcel in B is given by

$$\text{Agreement}_{(A,B)}(A_i) = \frac{\left|A_i \cap B_{S(i)}\right|}{|A_i|} \tag{6.7}$$

where $|\cdot|$ represents the cardinality of a set and $S : \mathbb{Z}_M \mapsto \mathbb{Z}_N$ is a mapping of parcels in A to B as described later. The agreement measure ranges from 0 (no agreement) to 1 (perfect agreement).

Concordance: consistency between parcellations

Concordance is a global measure of consistency between two parcellations A and B. It is defined as fraction of vertices between the two parcellations that agree:

$$\text{Concordance}(A, B) = \frac{\sum_{i \in \mathbb{Z}_M} \left|A_i \cap B_{S(i)}\right|}{\sum_{i \in \mathbb{Z}_M} |A_i|} \tag{6.8}$$

where $|\cdot|$ represents the cardinality of a set and $S : \mathbb{Z}_M \mapsto \mathbb{Z}_N$ is mapping of parcels in A to B as described next. The concordance measure ranges from 0 (no agreement) to 1 (perfect agreement).

Mapping between parcellations

Given the two parcellations A and B, we aim to match each parcel in A to a unique parcel in B. Let $g(A_i, B_j)$ be a measure of the goodness of the match of A_i to B_j such as the Dice coefficient or Jacard index. We want a map $\widehat{S} : \mathbb{Z}_M \mapsto \mathbb{Z}_N$ such that we maximize the goodness of match across all parcels:

$$\widehat{S} = \underset{S:\mathbb{Z}_M \mapsto \mathbb{Z}_N}{\arg\max} \left[\sum_{i \in \mathbb{Z}_M} g\left(A_i, B_{S(i)}\right) \right]. \tag{6.9}$$

The exact solution of eq. (6.9) is combinatorial and scales approximately as $n!$ where $n = \max(M, N)$).

We use an approximate solution of eq. (6.9) by noting its similarity to the famous stable matching problem [Gale and Shapley, 1962]. Stable matching finds a match between elements of two sets of equal

size when a preference order of matching is specified for each element. A match is stable if there does not exists a pair (a, b) in the match in which both a and b have higher preference elements which also prefer a and b respectively over their current match. We use the Gale-Shapley algorithm [Gale and Shapley, 1962] after transforming our parcel mapping to a stable matching problem as described below. We will match each parcel in A to a unique parcel in B: In the language of the Gale-Shapley algorithm, elements in A are suitors and the elements in B are reviewers.

1. Compute an $M \times N$ matrix $\mathbf{G}$ such that the $(i, j)^{\text{th}}$ element $\mathbf{G}(i, j) = g(A_i, B_j)$.

2. The Gale-Shapley algorithm works with sets of the same size. Hence, we define an $n \times n$ matrix $\widetilde{\mathbf{G}}$ by appending appropriate number of row or columns to $\mathbf{G}$. All the elements of appended rows/columns are set to $\delta = \min(\mathbf{G}) - \epsilon$, where ϵ is a small positive constant. This modifies our problem by adding dummy suitors/reviewers which can be easily ignored.

3. Next, we compute the preference order of each element from $\widetilde{\mathbf{G}}$. There are a total of n suitors and n reviewers. We define the preference order for each suitor by arranging the indices of the elements in the corresponding row in $\widetilde{\mathbf{G}}$ in the descending order of magnitude of their entries. Similarly, we define the preference order of each reviewer as the indices of the elements of the columns arranged in descending order of magnitude of their entries. If two elements have same preference, then we break the tie by randomly assigning a preference order.

4. We use the resulting preference order from the last step to find a stable match $\widetilde{S}$ using the Gale-Shapley algorithm [Gale and Shapley, 1962]. The map $\widetilde{S} : \mathbb{Z}_n \mapsto \mathbb{Z}_n$ is modified to get $\widehat{S} : \mathbb{Z}_M \mapsto \mathbb{Z}_N$ as follows: If $M = N$ then $\widehat{S} \equiv \widetilde{S}$; If $M < N$ then all the appended dummy suitors are ignored in $\widetilde{S}$; If $M > N$ then all suitors which are matched to an appended dummy reviewer in $\widetilde{S}$ is modified to match to an empty set so that $B_{\widehat{S}(i)} = \varnothing$.

The matching solution obtained by the above procedure is the suitor-optimal solution (in the sense of preference order). If a reviewer-optimal solution is required A and B should be swapped [Gale and Shapley, 1962]. Further, the solution obtained is an approximation of eq. (6.9) as the Gale-Shapley algorithm is blind to the absolute values of $g\left(A_i, B_{S(i)}\right)$ and only uses relative preference order, which may not always maximize the total cost. Nonetheless, in our experience, this approximate solution produces reasonable matching and is more computationally tractable than combinatorial approaches.

Appendix 6.C Supplemental videos

The supplemental videos (M1– M3) can be found at http://neuroimage.usc.edu/~chitresh/fmri/.

Appendix 6.D Supplemental results

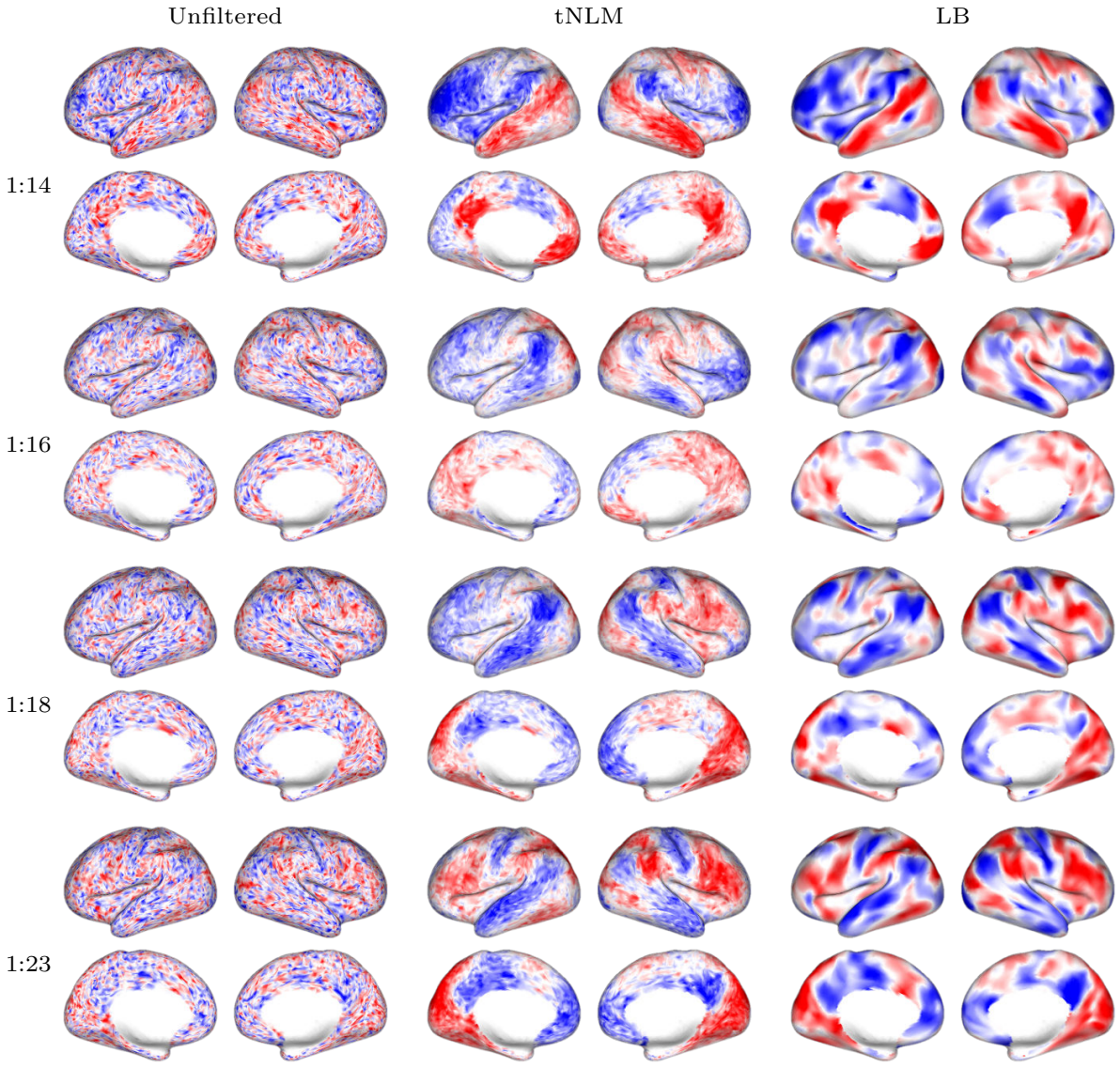

Figure 6.13: Cortical distribution of the signal intensity of rfMRI data from a single subject at different time points (left) without filtering, (center) with tNLM filtering (h=0.72) and (right) with LB filtering (t=4). The video time points of corresponding movies (M1–M3) are shown in left-most column. (Contd. to next page)

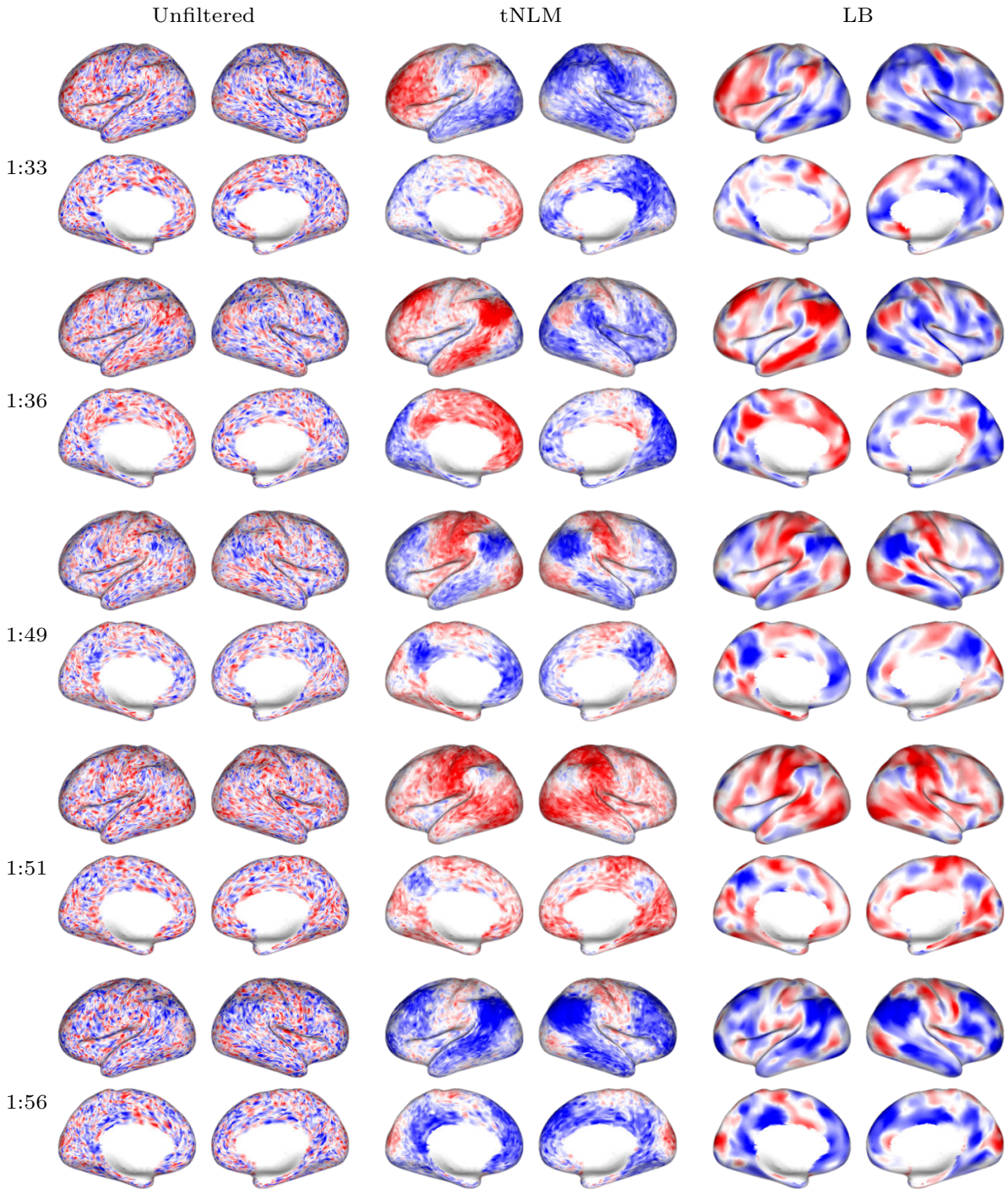

Figure 6.13: (Contd. from previous page) Cortical distribution of the signal intensity of rfMRI data from a single subject at different time points (left) without filtering, (center) with tNLM filtering (h=0.72) and (right) with LB filtering (t=4). The video time points of corresponding movies (M1–M3) are shown in left-most column.

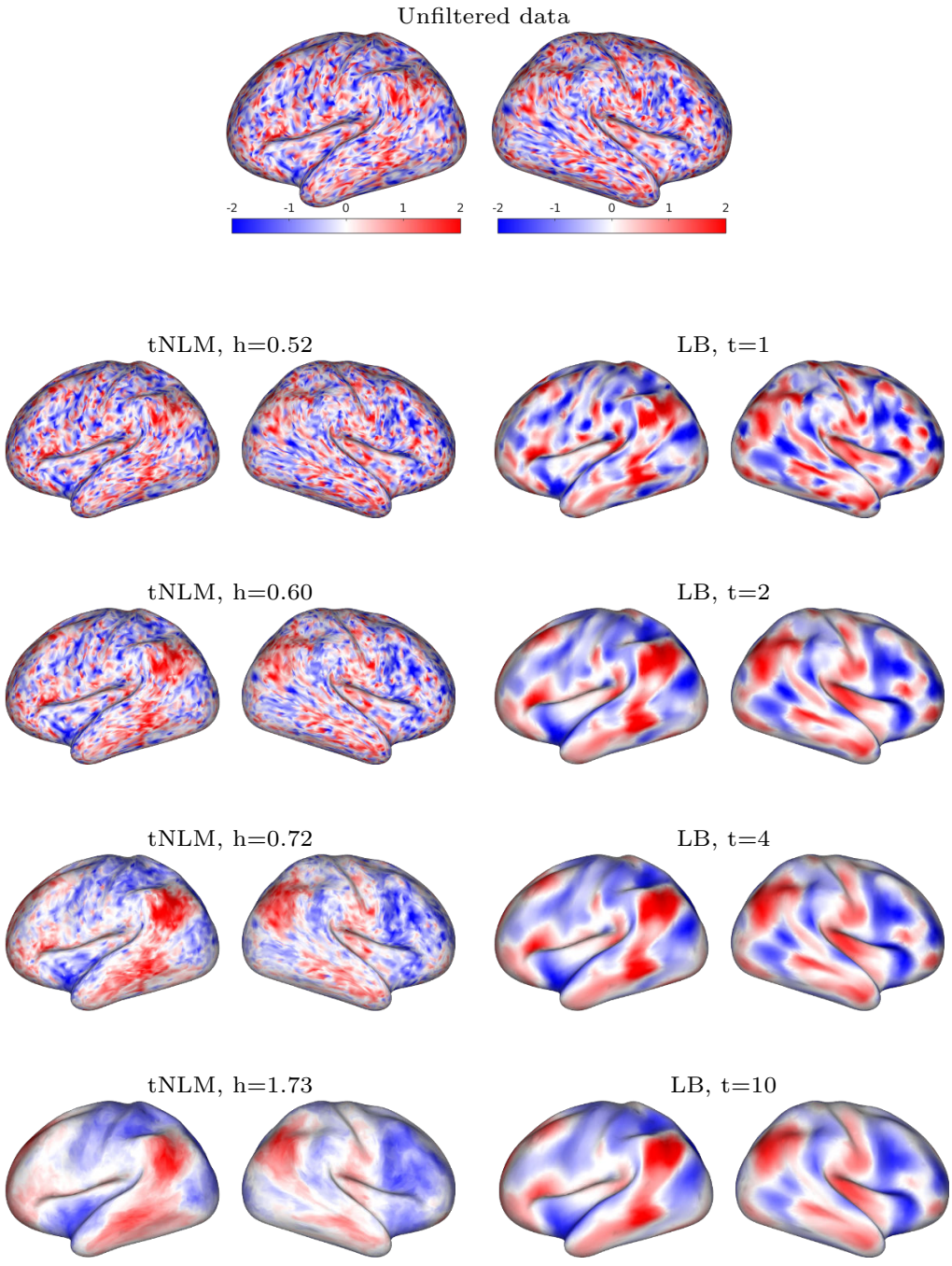

Figure 6.14: Effect of tNLM and LB parameters on smoothing of the signal intensity of rfMRI data on the cortical surface. The original unsmoothed data is shown in the top image for one particular time instant. The result of filtering the original data with LB and tNLM ($D = 11$) with different parameters are shown in left and right column. All the individual time series, unfiltered and filtered, were normalized to zero mean and unit variance before displaying as the signal intensity on the cortical surface.

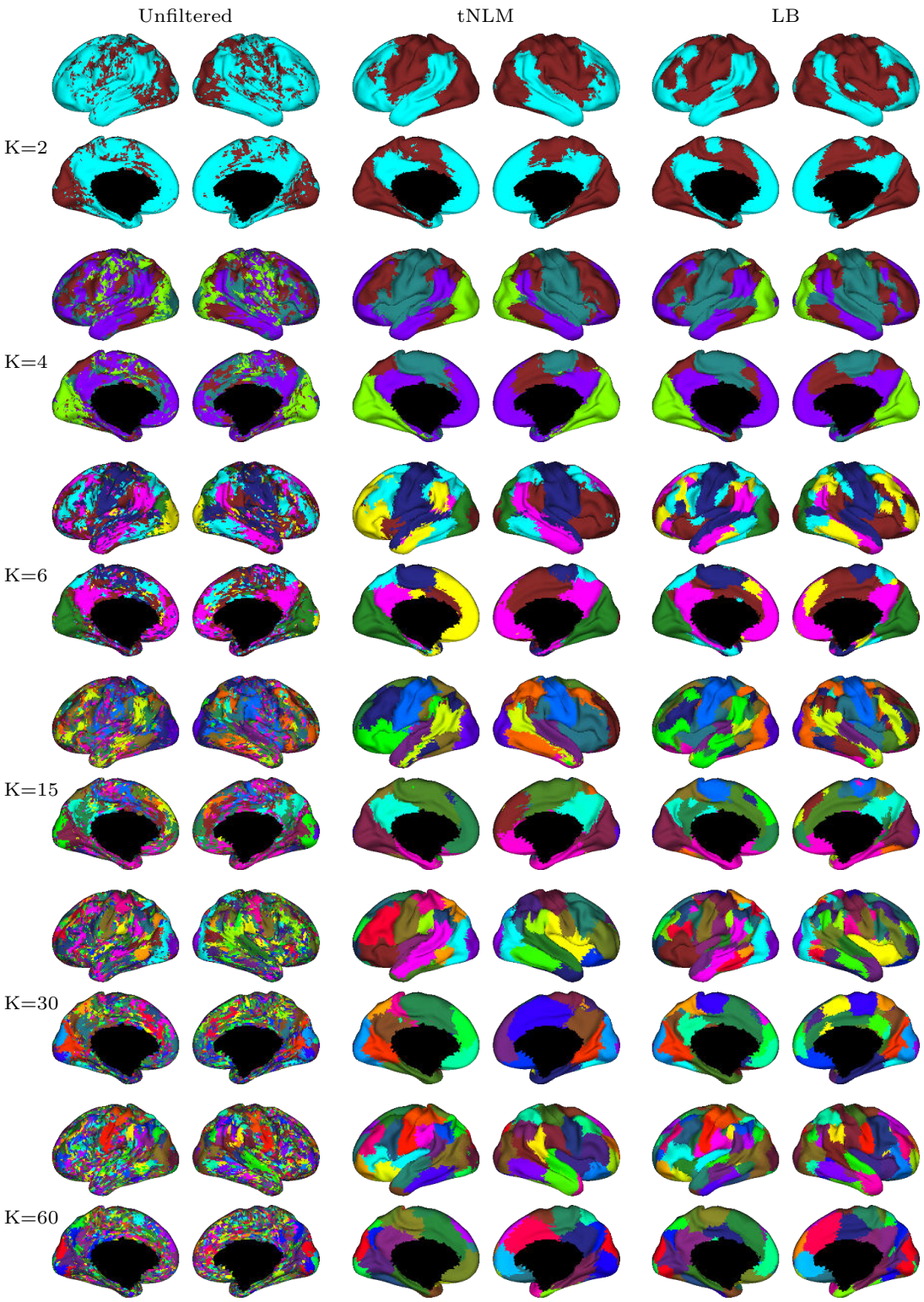

Figure 6.15: Examples of cortical parcellation using full-graph with N-cuts obtained with unfiltered data, tNLM filtering (h=0.72) and LB filtering (t=4). The number of N-cuts classes (K) is shown in left-most column. Each N-cuts cluster is shown in a unique color such that a the clustering result with K-classes will have K unique colors.

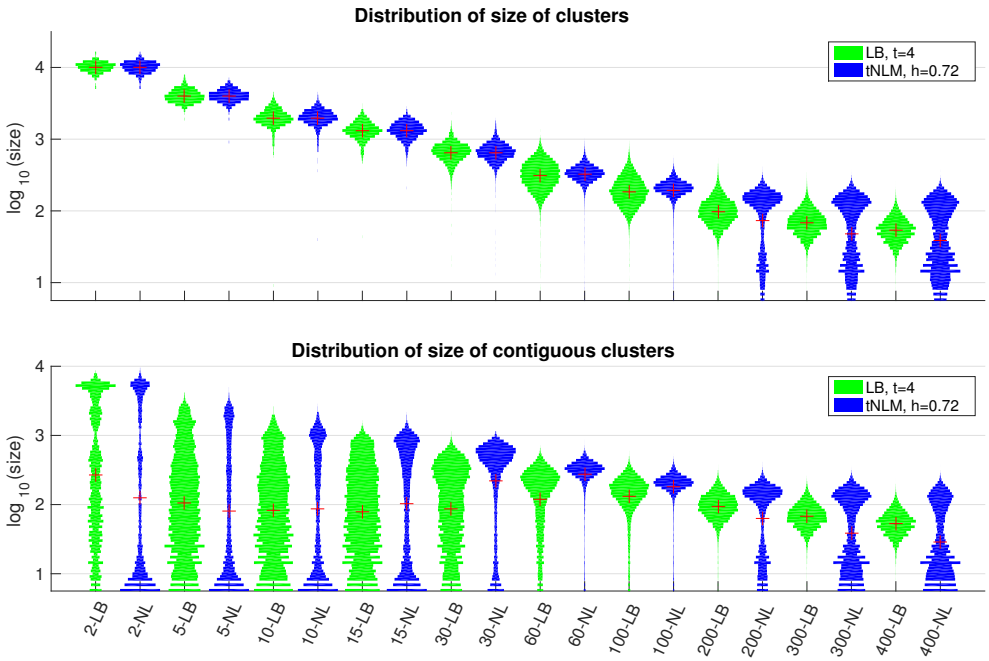

Figure 6.16: Distribution of cluster-size over different values of K in N-cuts clustering with LB (t=4) and tNLM (h=0.72) smoothing across 40 subjects with 4 sessions each ($40 \times 4 = 160$ N-cuts clustering results). (Top) plot shows the cluster-size (vertex count) distribution for the clusters obtained by N-cuts. (Bottom) plot shows the cluster-size distribution of the *contiguous* clusters (obtained by breaking the N-cuts clusters into spatially contiguous parcels). The red $+$ mark shows the mean size for each plot. Note that the cluster-size (y-axis) is reported on logarithmic scale.

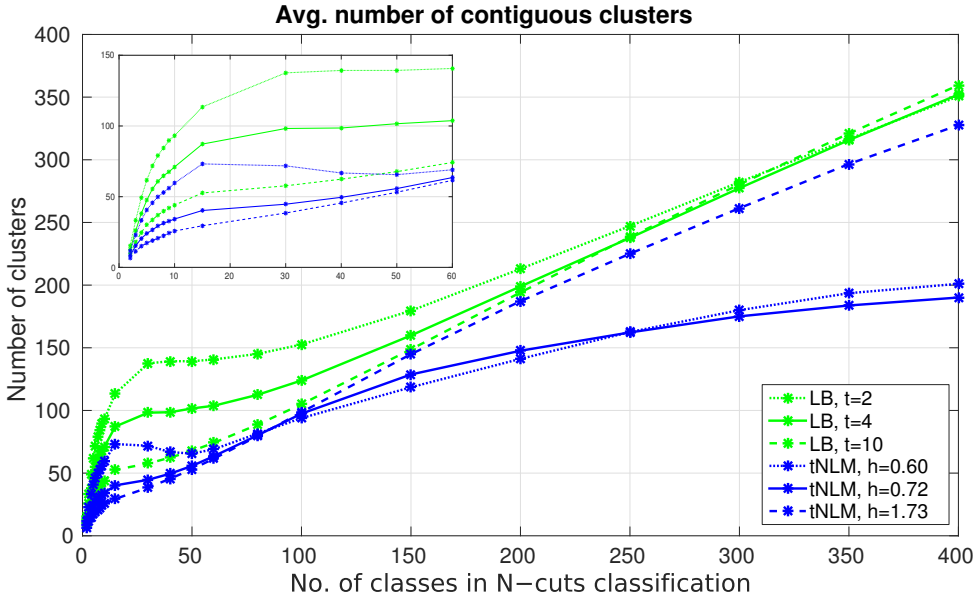

Figure 6.17: Average number of *contiguous* parcels obtained using LB and tNLM filtering over different values of K in N-cuts clustering (the average is computed over 40 subjects $\times$ 4 sessions = 160 N-cuts clustering results). *contiguous* clusters are obtained by breaking N-cuts clusters into spatially contiguous parcels. The inset shows the zoomed-in view of the lower left corner. We have ignored all the contiguous parcels which have less than 20-vertices in the above count. Most of the ignored vertices lie in areas known for signal dropout in BOLD-EPI images (near sinus and ear-canal) as can be seen in fig. 6.19 (K=300,400).

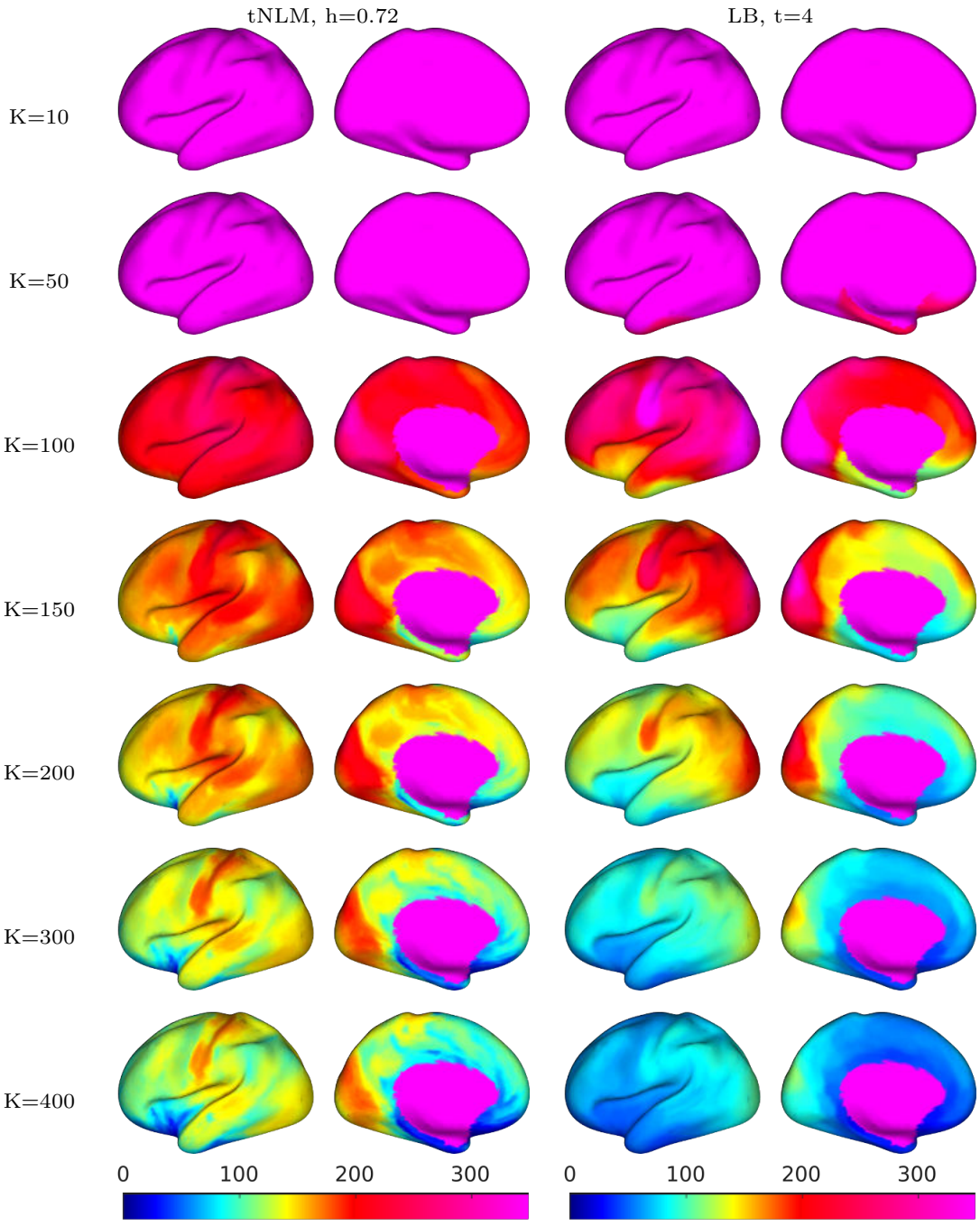

Figure 6.18: Average size of N-cuts clusters, measured by average number of vertices in each cluster across $40 \times 4 = 160$ N-cuts clustering results (left) with tNLM filtering (h=0.72) and (right) with LB filtering (t=4). The value at each vertex represents the average size of the cluster to which that vertex belonged across all subjects/sessions. The map is thresholded at upper vertex count of 350.

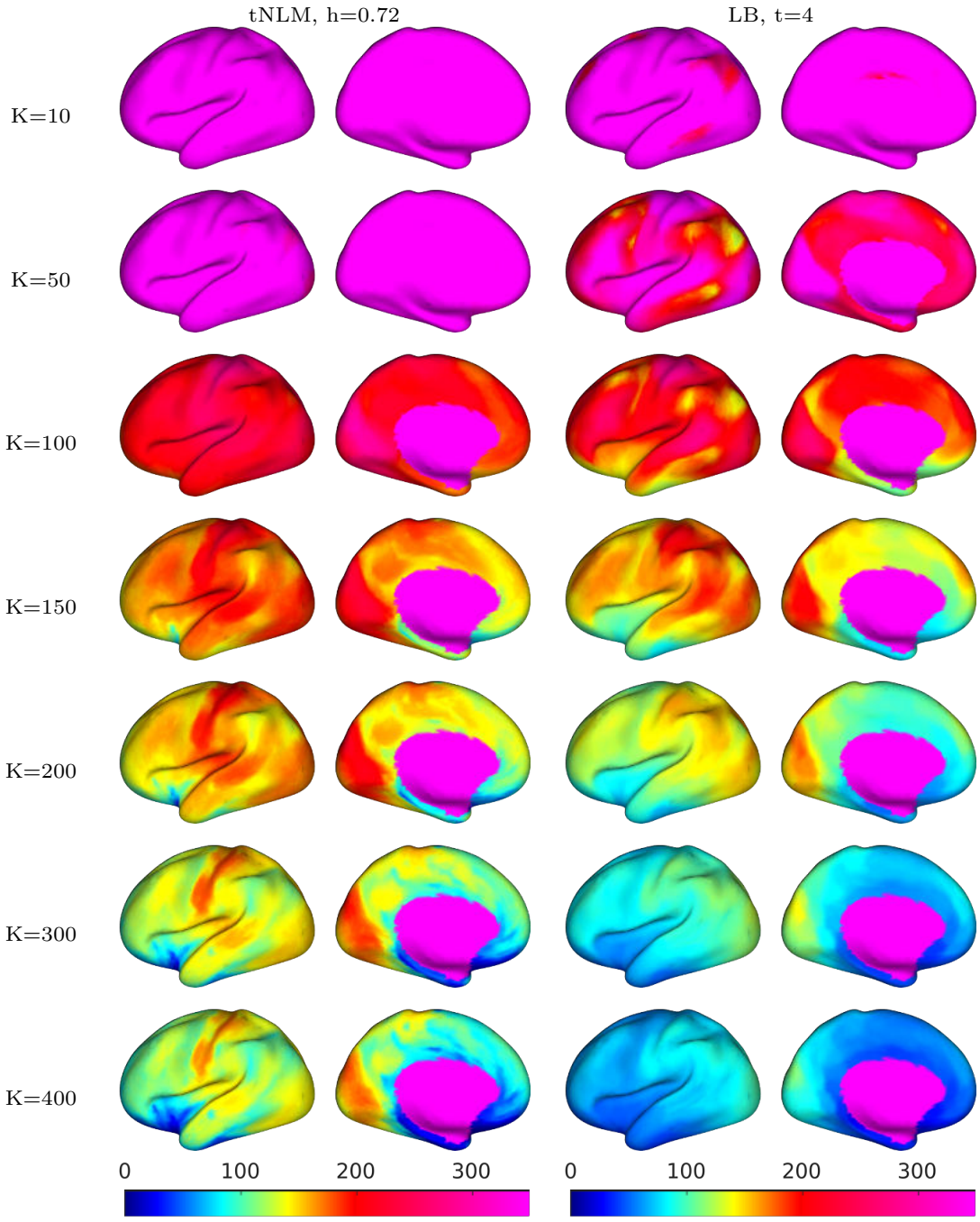

Figure 6.19: Average size of *contiguous* parcels – the cluster-size computation is same as that in Fig. 6.18 except that the N-cuts clusters are first broken into *contiguous* parcels. The images use the same colorscale as Fig. 6.18.

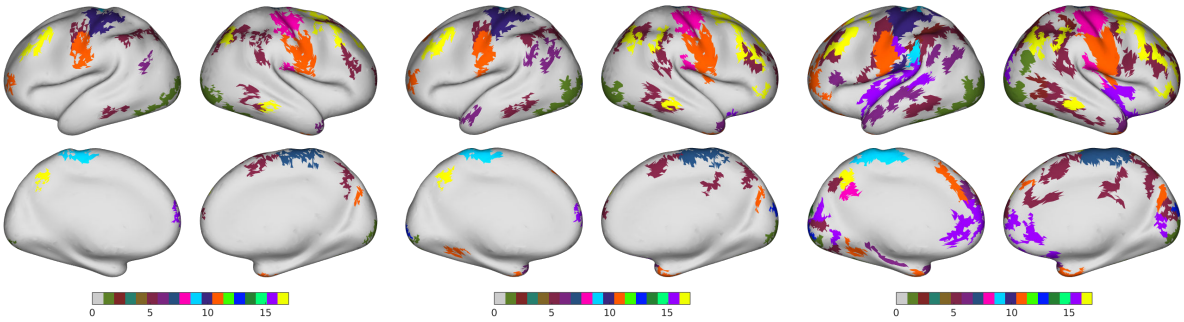

(a) 2mm Smoothed task fMRI (b) 4mm Smoothed task fMRI (c) 8mm Smoothed task fMRI

Task-pair	Label
Faces vs. Shapes	1
Shapes vs. Faces	2
Punish vs. Reward	3
Reward vs. punish	4
Math vs. Story	5
Story vs. Math	6
Left foot	7
Left hand	8
Right foot	9
Right hand	10
Tongue	11
Match vs. Rel.	12
Rel. vs. Match	13
Random vs. Tom	14
Tom vs. random	15
0-back vs. 2-back	16
2-back vs. 0-back	17

(d) Table of task-pair activation and label-IDs.

Figure 6.20: An example of task labels for a single subject obtained by thresholding the task activation statistical maps at Z-score of 3.0 followed by ignoring all connected components with less than 40-vertices (see section 2.4.3 for more details). A total of 17 task-pair activation maps were obtained for each subject from HCP's processed data, which were computed by processing the task fMRI data with three different level of smoothing: (a) 2mm, (b) 4mm, and (c) 8 mm. The task-pairs corresponding to each task label is reported in (d). The 4mm smoothing result is also shown in Fig. 4 in the body of the paper and used for subsequent quantitative analysis in Fig. 10 and Table 1.

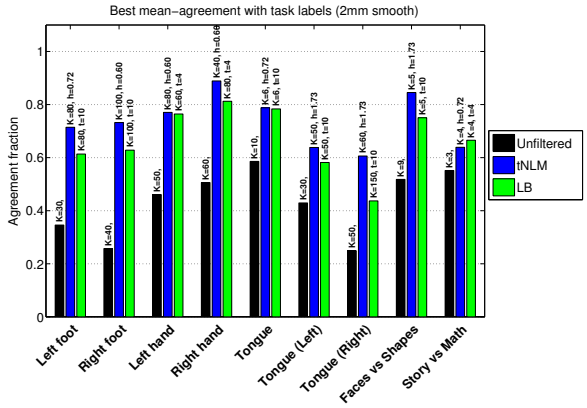

(a) 2mm Smoothed task fMRI

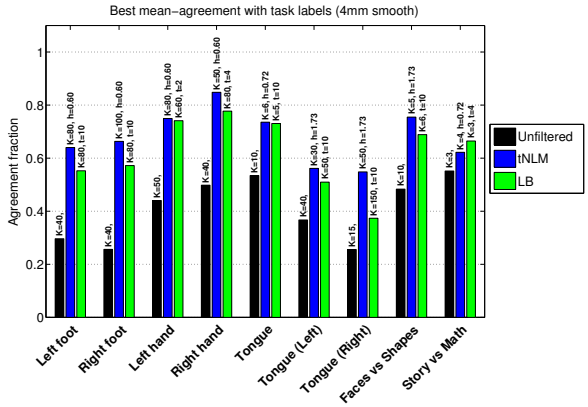

(b) 4mm Smoothed task fMRI

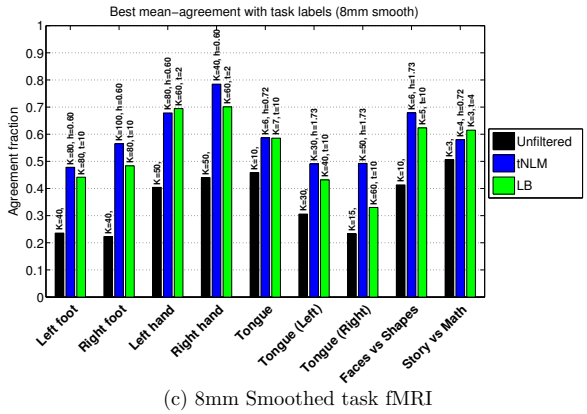

(c) 8mm Smoothed task fMRI

Figure 6.21: Task-based evaluation: Best performance of different filtering approaches (no filtering, tNLM and LB) across different task labels, which were obtained by processing the task fMRI data with different levels of smoothing, shown in each sub-figure. For each task and each filtering approach, we select the parameters which achieves the highest mean agreement fraction (see Sec. 3.4 for more details). The grouped bar plot shows the highest mean agreement fraction and the text on top shows the corresponding parameters: h for tNLM and t for LB filtering and number of classes K in N-cuts. Figs. 6.22 – 6.24 shows detailed performance all filtering approaches across several parameters. Only a subset of these results are included in the body of the paper. Specifically, overall performance results for 4mm smoothing (Fig. 10(b)) and mean agreement fraction for left foot task and 4mm smoothing (Fig. 10(a)).

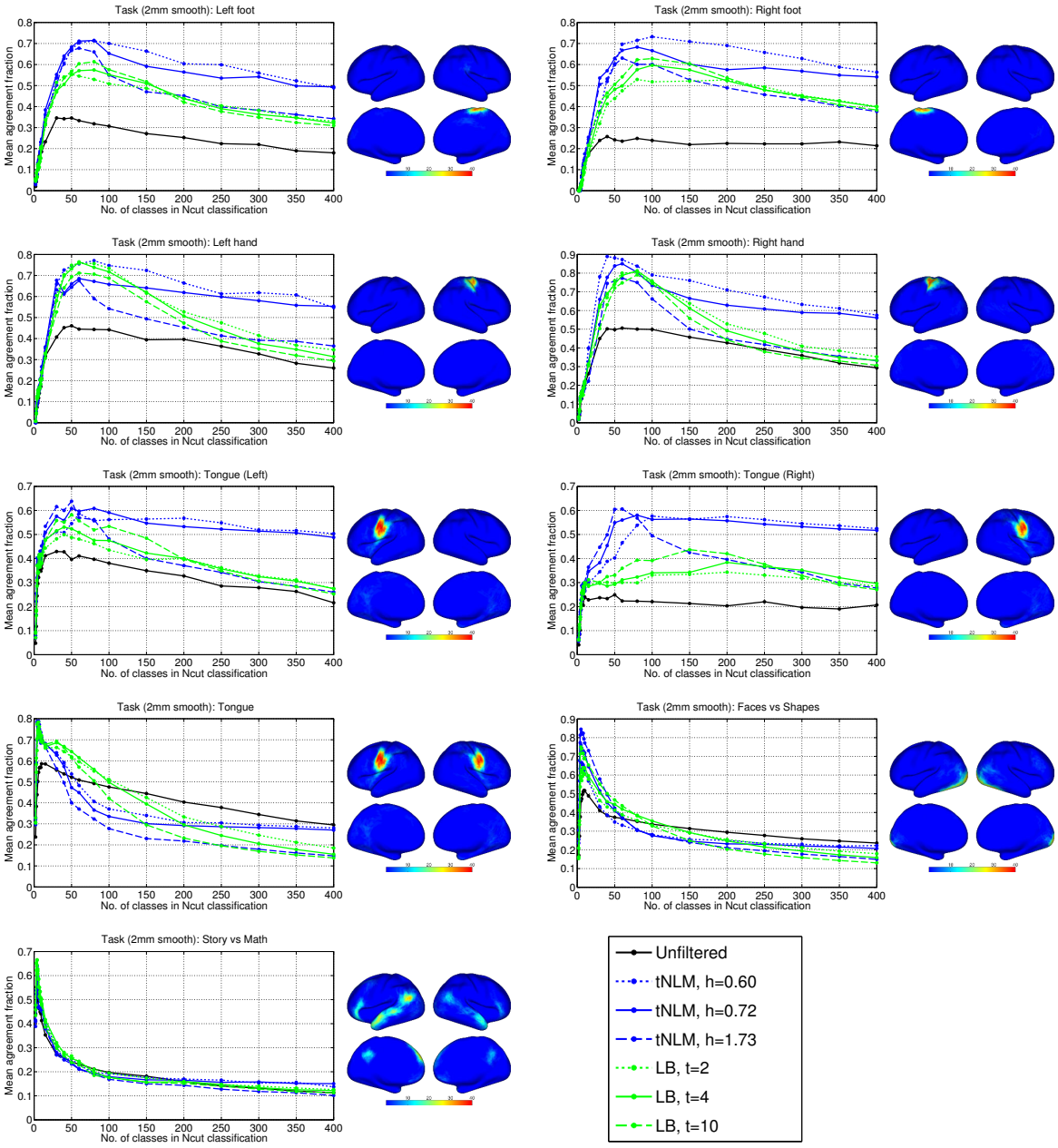

Figure 6.22: Task-based evaluation: Detailed performance of all filtering approaches across several parameters for task-labels obtained by 2mm smoothing of task fMRI data. Line plots show the mean agreement of N-cuts clusters with 2mm-smoothed task labels across 40 subjects with 4 sessions each ($40 \times 4 = 160$ N-cuts clustering results). For each task, we also show the spatial histogram of the task label across the 40 subjects. Only seven tasks, shown above, could survive the statistical and contiguity thresholding (see section 2.4.3 for more details), and can also be seen in Fig. 6.20. The tongue task was also studied after with breaking the activation maps into two parts, each lying on one hemisphere of the brain.

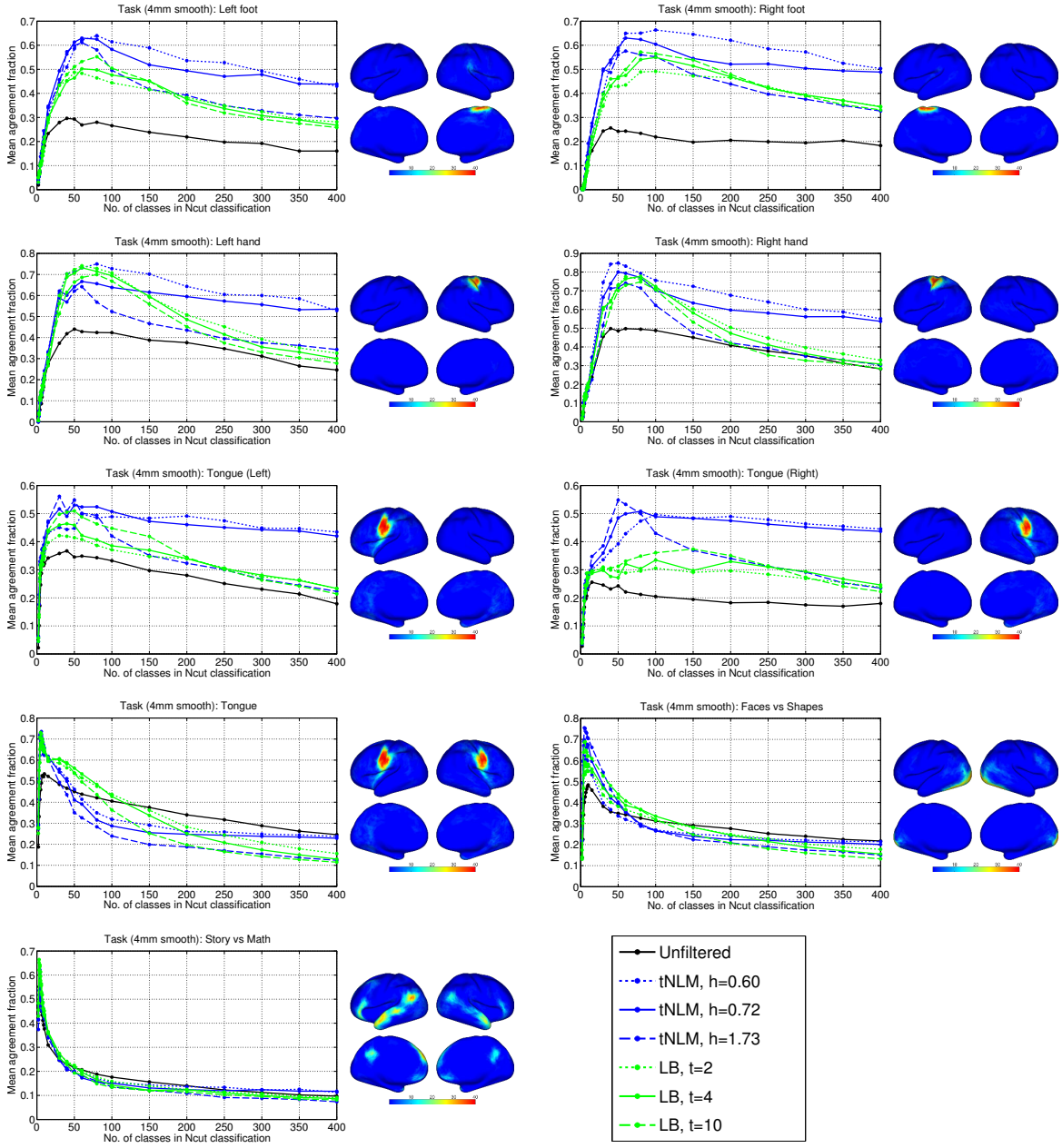

Figure 6.23: Task-based evaluation: (Same as Fig. 6.22, but with 4mm smoothing) Detailed performance of all filtering approaches across several parameters for task-labels obtained by 4mm smoothing of task fMRI data.

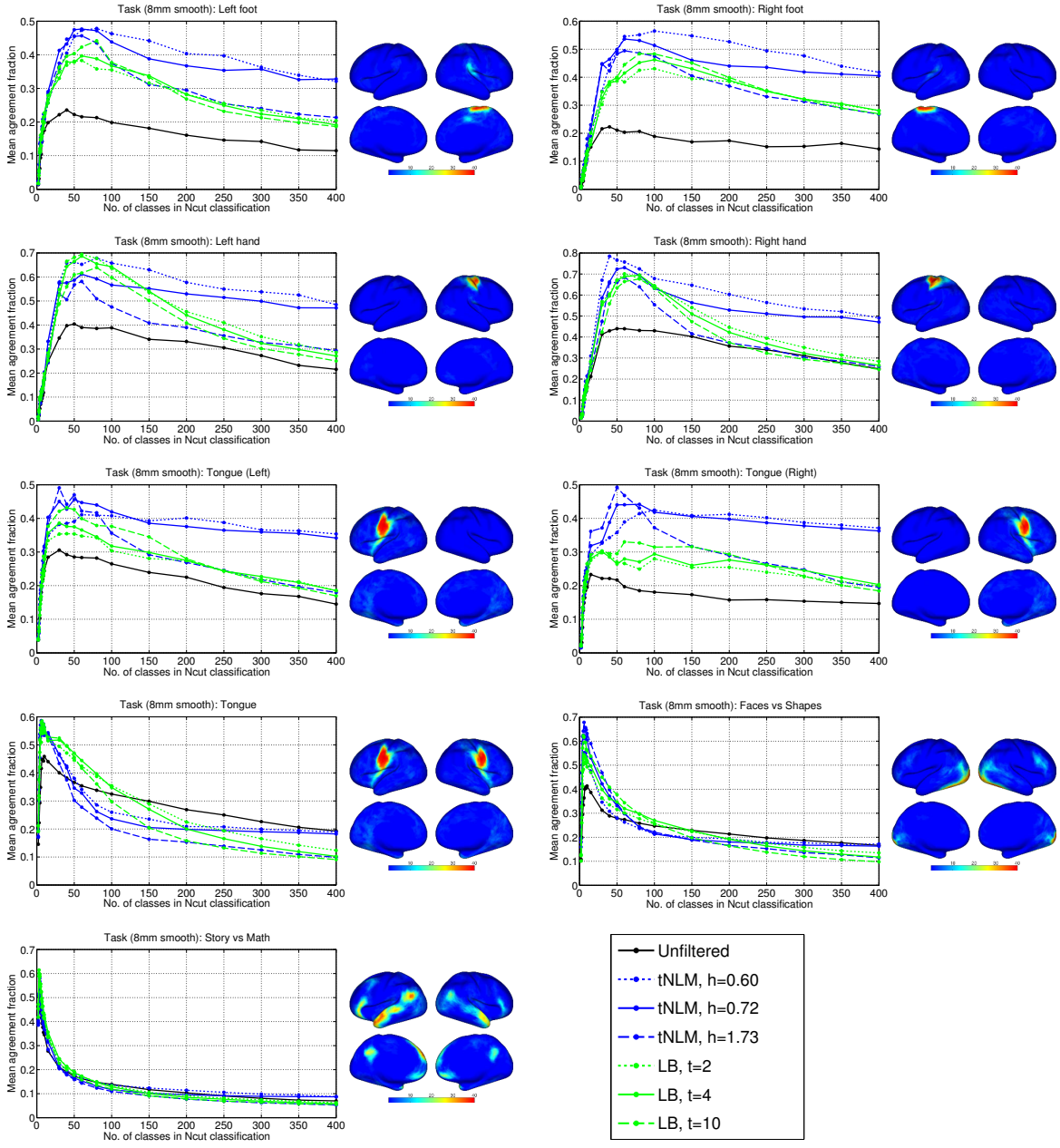

Figure 6.24: Task-based evaluation: (Same as Fig. 6.22, but with 8mm smoothing) Detailed performance of all filtering approaches across several parameters for task-labels obtained by 8mm smoothing of task fMRI data.

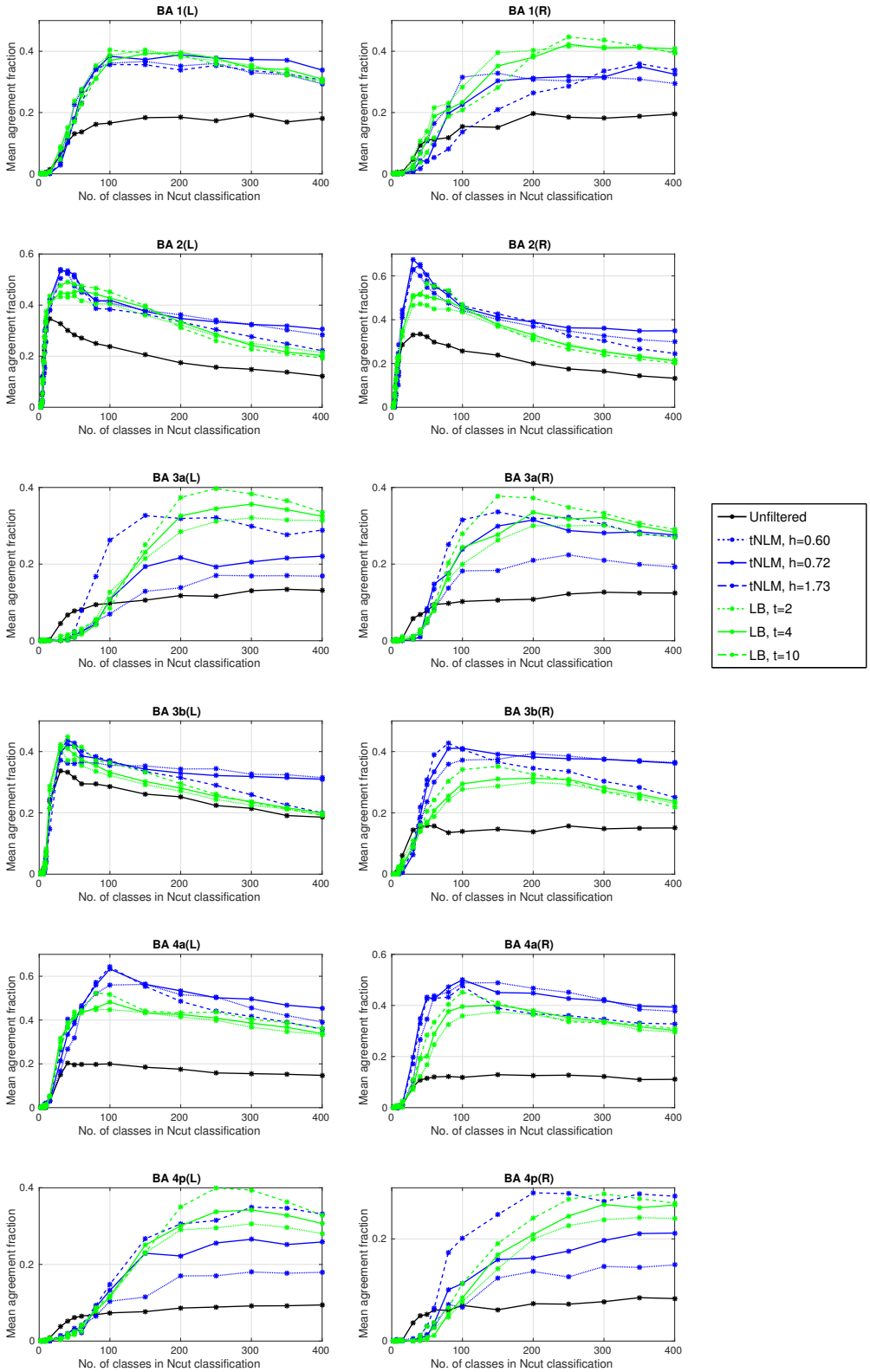

Figure 6.25: Probabilistic Brodmann area based evaluation: Detailed performance of all filtering approaches across several parameters for Brodmann areas (BAs). Line plots show the mean agreement of N-cuts clusters with BAs across 40 subjects with 4 sessions each ($40 \times 4 = 160$ N-cuts clustering results). Left and right column shows agreement for BAs in left and right hemisphere respectively. (Contd. to next page)

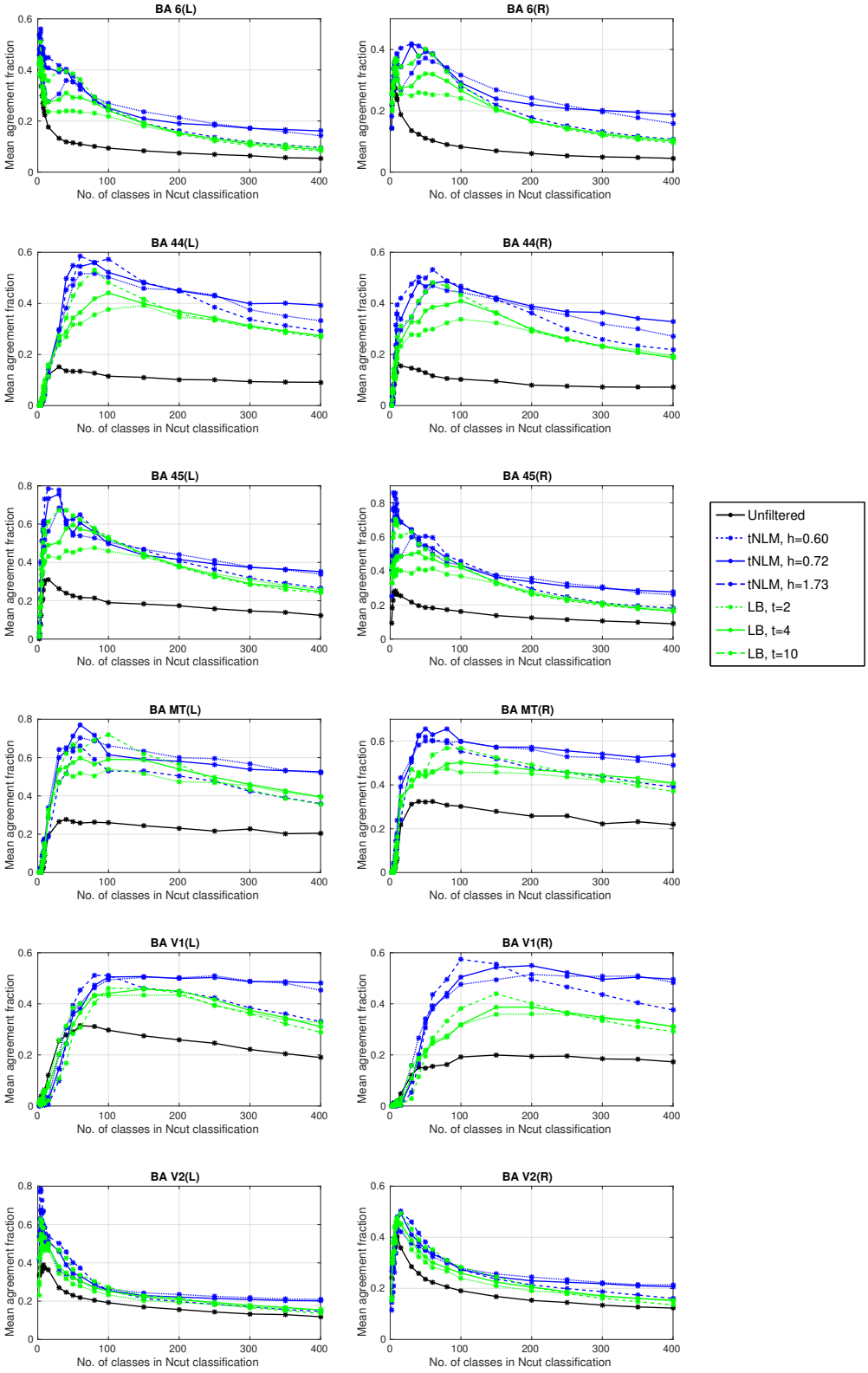

Figure 6.25: (Contd. from previous page) Probabilistic Brodmann area based evaluation: Detailed performance of all filtering approaches across several parameters for Brodmann areas (BAs). Line plots show the mean agreement of N-cuts clusters with BAs across 40 subjects with 4 sessions each ($40 \times 4 = 160$ N-cuts clustering results). Left and right column shows agreement for BAs in left and right hemisphere respectively.

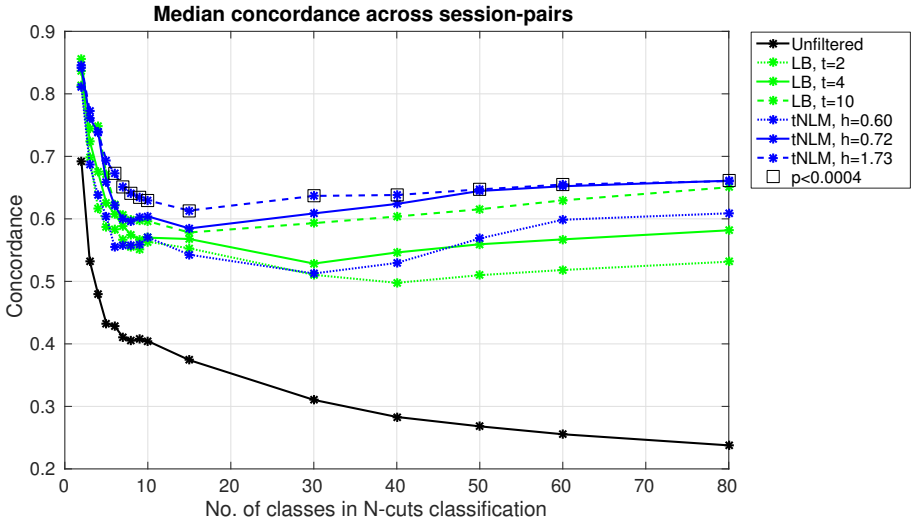

(a)

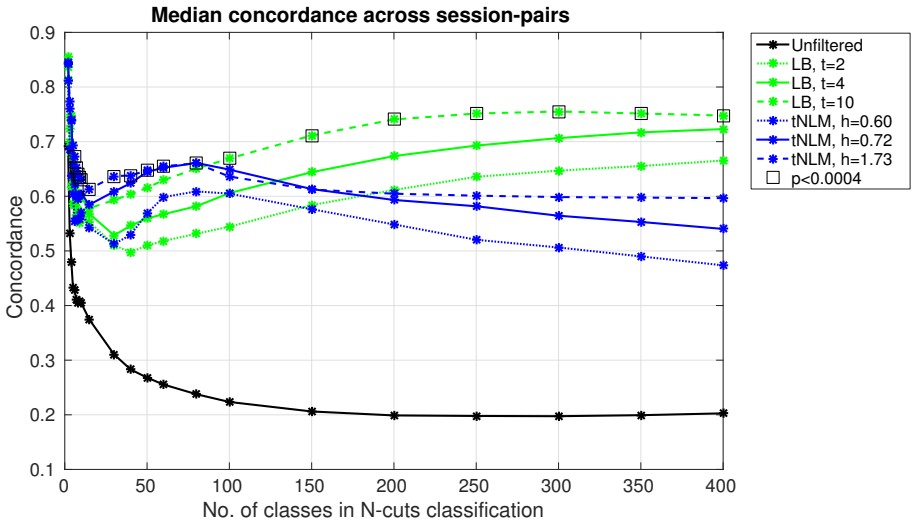

(b)

Figure 6.26: Test-retest reliability: (a) Median concordance (agreement between parcellations) over the six pairs of rfMRI sessions per subject and the 40 subjects as a function of the number of cuts, K = 2 to 80, for different filtering approaches. Mann-Whitney U (rank-sum) tests for significant differences between performances of tNLM and LB filtering were performed for each K separately and the square boxes indicate values of p-value < 0.0004. (b) Same as (a) but the concordance value are reported range for a K = 2 to 400. See Sec. 2.4.5 and 3.6 in paper for details. Note (a) is identical to Fig. 12 but repeated here for reference to (b).

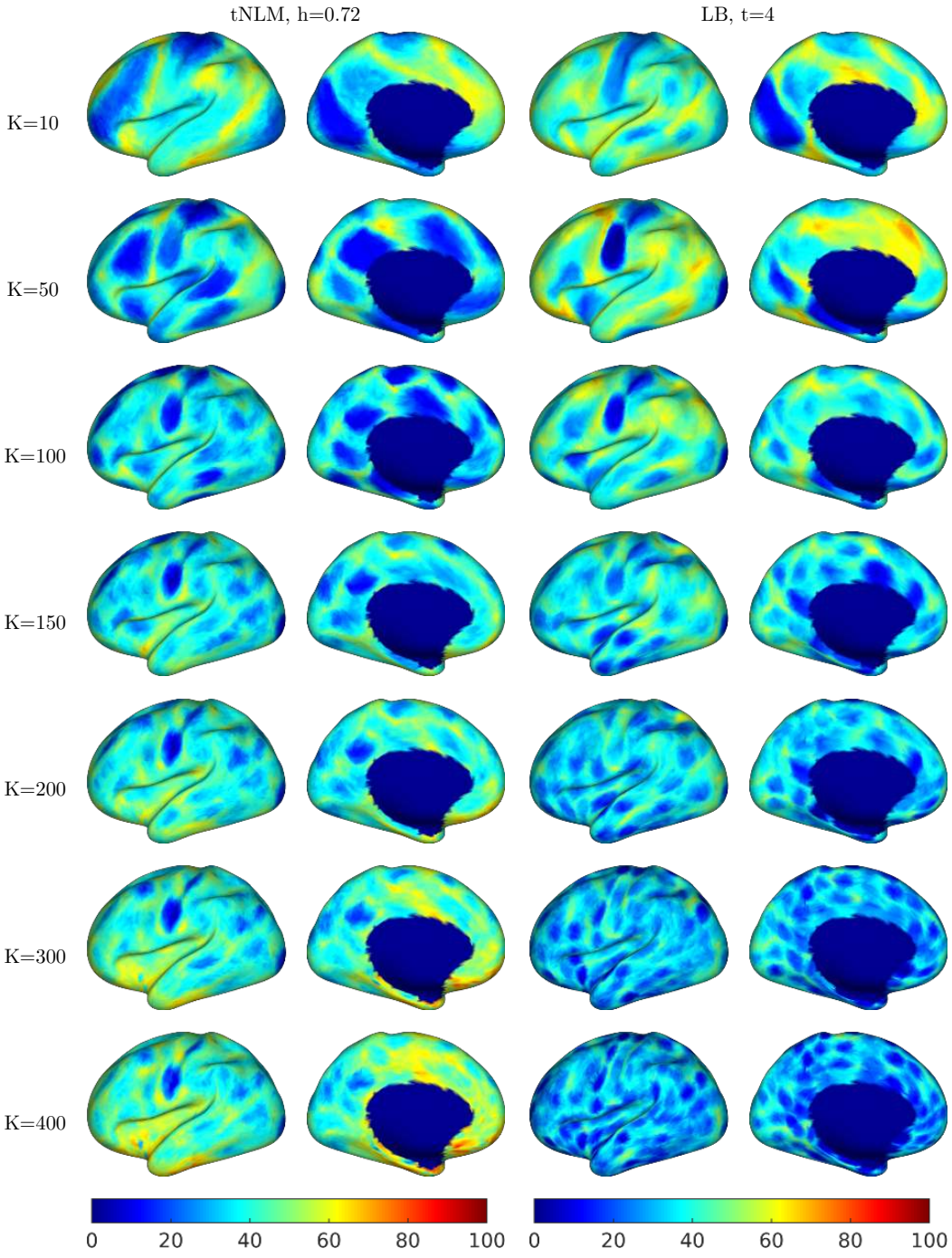

Figure 6.27: Test-retest variability: Cortical maps of frequency of disagreement between parcellations across independent rfMRI sessions of same subject (left) with tNLM filtering (h=0.72) and (right) with LB filtering (t=4). The value at each vertex represents the percentage of times (over 40 subjects $\times$ 6 sessions-pairs) that vertex had been assigned different labels across N-cuts parcellations using rfMRI data from a pair of independent sessions. Also, notice the corresponding size of the N-cuts clusters in Fig. 6.18 which would affect the parcellation matching. See Fig. 6.28 for several similar plots with $K \leq 80$.

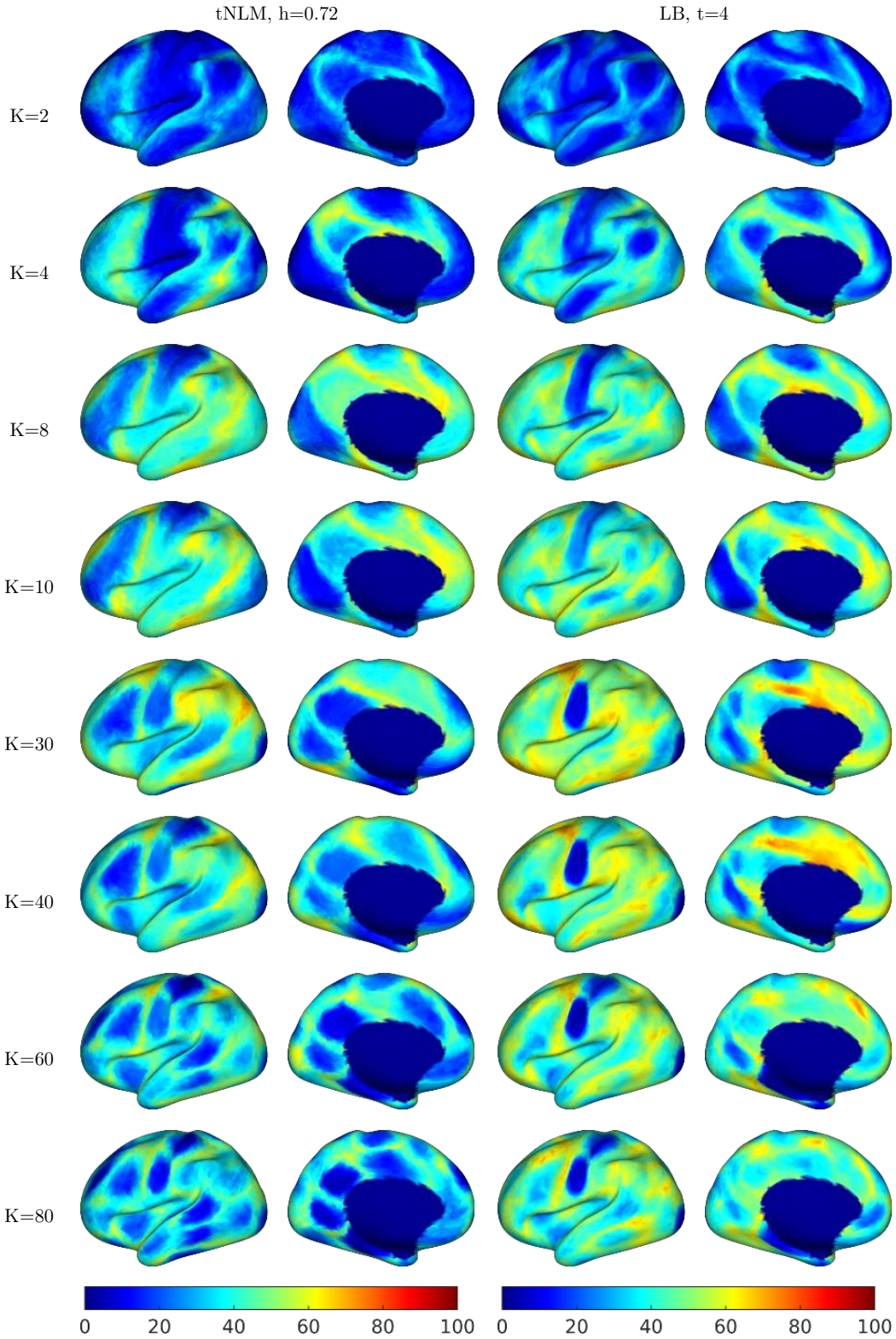

Figure 6.28: Test-retest variability: (Same as Fig. 6.27 but with N-cuts classes $K \leq 80$) Cortical maps of frequency of disagreement between parcellations across independent rfMRI sessions of same subject (left) with tNLM filtering (h=0.72) and (right) with LB filtering (t=4).

Chapter 7

Exploration of microstructural parcellation of the cortex using multi-contrast MRI

Chapter 3 reviews several historical and recent *in vivo* approaches for parcellation of the cortex based on function and structure. These techniques clearly show sensitivity, albeit limited in several ways, to the microstructural architectonics of the cortex. In this chapter, we explore the idea of *in vivo* microstructural parcellation using multi-contrast MRI. Different *in vivo* MRI contrasts probe different aspects of the microarchitectonic structure of the brain, as reviewed in section 3.2. Motivated by these observations, we propose to fuse information derived from several multi-contrast MRI images to characterize and delineate microarchitectonic properties in the cortex for *in vivo* parcellation of the entire cortex. For this purpose, we developed a multi-contrast image processing and normalization framework, which is described in this chapter along with some preliminary results (some of which were also presented elsewhere [Leahy, 2014]).

7.1 Multi-contrast data processing

We use several T_1-, T_2-, and diffusion-weighted MRI images acquired on a 3 T Siemens Tim Trio full-body clinical scanner, and combine them using our novel framework as illustrated in Fig. 7.1. We use a high-resolution T_1-weighted MPRAGE image for macro-anatomic localization (voxel size of $0.5 \times 0.5 \times 0.8$ mm^3, TR=2070 ms, TE=4.33 ms, TI=1100 ms, flip angle 12 degrees, 5 averages). We use quantitative relaxometry parameters as they have been observed to be more effective in capturing microstructural features [Geyer, 2013, Cohen-Adad et al., 2012, Cohen-Adad, 2014]. The quantitative

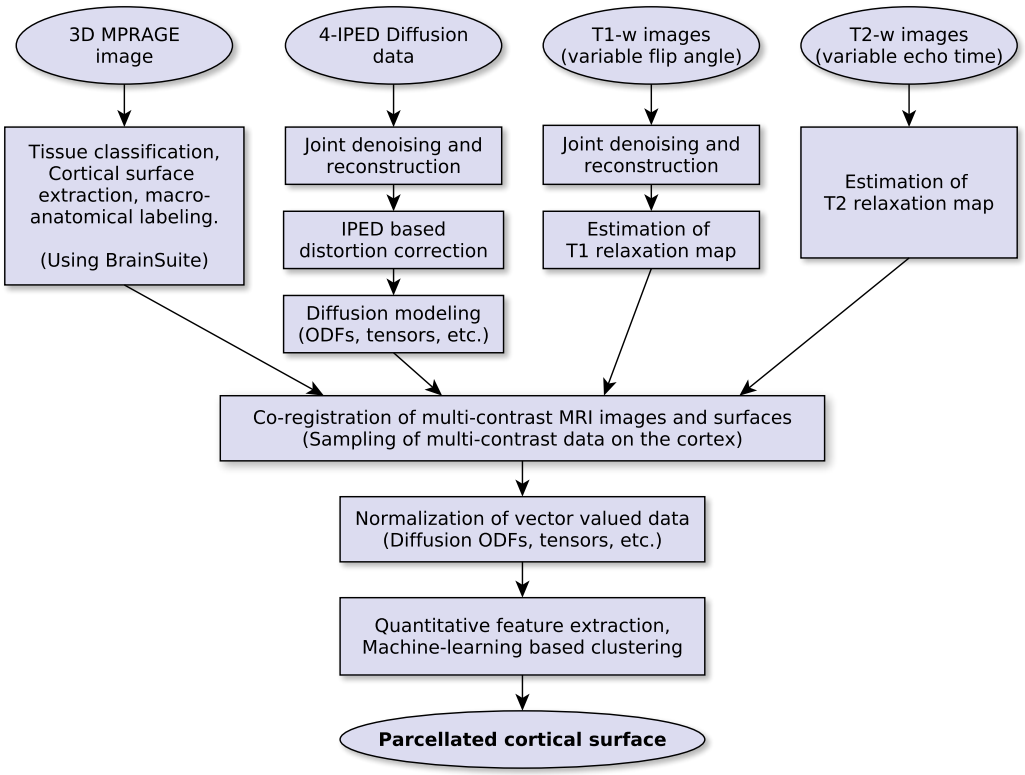

Figure 7.1: Overview of the proposed multi-contrast work-flow for microstructural parcellation.

T_1 maps are found using four high-resolution T_1-weighted images with different flip angles (voxel size of $0.7 \times 0.7 \times 1.0$ mm^3, TI=800 ms, TE=3.3 ms, TR=2500 ms, filp angles of 3, 7, 10, and 15 degrees). Quantitative T_2 maps are obtained by acquiring eight T_2 weighed images with variable echo times using the Carr-Purcell-Meiboom-Gill (CPMG) sequence (voxel size of $2.0 \times 2.0 \times 2.0$ mm^3, TR=8130 ms, TE=15, 30, 45, 60, 75, 90, 105, and 120 ms). In addition we also used a diffusion dataset acquired with two different b-values (voxel size of $2.0 \times 2.0 \times 2.0$ mm^3, TR=10000 ms, TE=84 ms, 6/8 partial Fourier, Echo-spacing=0.75 ms, 32 volumes at b=1000 s/mm^2, 68 volumes at b=2500 s/mm^2, 3 volumes at b=0 s/mm^2) using our interlaced phase encoding technique [Bhushan et al., 2014b, 2013].

The T_1-weighted and diffusion data were denoised using magnitude-based [Varadarajan and Haldar, 2013] and joint-reconstruction based [Haldar et al., 2013, Lam et al., 2013] denoising techniques respectively before further processing. The multi-shell diffusion data was distortion corrected separately for each b-value using the constrained reconstruction approach as described in chapter 5 [Bhushan et al., 2014b, 2013]. In order to fuse the data across different contrasts, we first estimated a tessellated representation of the cortical surfaces (pial and inner white matter) as well as the tissue fraction maps from high-resolution MPRAGE image using BrainSuite software [Shattuck and Leahy, 2002]. Then we co-registered all images (T_1-, T_2 and diffusion-weighted) to the MPRAGE image in a rigid fashion using a

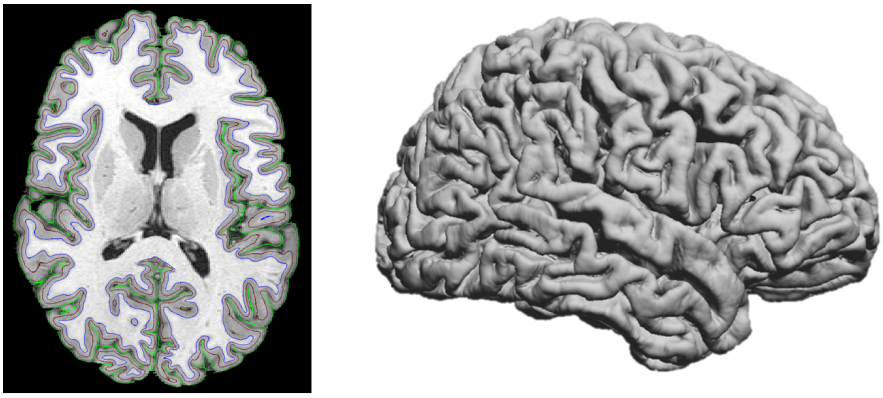

Figure 7.2: The mid-cortical surface was extracted using BrainSuite, whose location is shown by the brown line in (a). Blue and green lines represent the location of the inner and pial surface, respectively. (b) 3D rendering of the extracted mid-cortical surface.

custom-tailored approach, in which the transformations from INVERSION-based registration [Bhushan et al., 2015b, 2014a] were refined using mutual information [Bhushan et al., 2012]. All the data were sampled on the mid-cortical surface, which is defined as the surface mid-way between the pial and inner surface and is shown in Fig. 7.2. The cortical surface and the volumetric MPRAGE image were also labeled in BrainSuite using the surface-volume registration (SVReg) function so that the labels on the surface and volume have one-to-one correspondence [Joshi et al., 2012, 2007]. We also estimated the cortical thickness using a novel technique which uses the tissue fraction maps to estimate the accurate thickness in the highly folded cortex [Joshi et al., 2014].

The quantitative T_2 maps were modeled using the two-compartment model, where the first compartment models the contribution from Cerebrospinal fluid (CSF) and the second compartment models non-CSF. As we are sampling all the data on the mid-cortex inside the cortical ribbon, we assume that the second non-CSF component is the contribution from the gray matter. Under this model, the observed signal in each voxel at echo-time t is expressed as

$$S(t) = M_{\text{CSF}}\, \mathrm{e}^{-t/T_{2,\text{CSF}}} + M_{\text{GM}}\, \mathrm{e}^{-t/T_{2,\text{GM}}} \tag{7.1}$$

where, $T_{2,\text{CSF}}$ is the T_2 relaxation constant of the CSF component which we assume to be constant across all the voxels, $T_{2,\text{GM}}$ is the T_2 relaxation constant of the GM component and M_{CSF} and M_{GM} are the scalar constants representing the relative volume of the CSF and GM components. The value of $T_{2,\text{CSF}}$ was estimated by fitting a single exponential model to signals from a few voxels containing only CSF and was found to be roughly 1000 ms. Other parameters were estimated for each voxel separately using the variable projection method [Golub and Pereyra, 2003, 1973], where the non-linear parameter

$T_{2,\text{GM}}$ was assumed to lie between 10-300ms based on values from the literature.

A variable flip FLASH sequence was used for acquiring the T_1-weighted images with variable flip angles. Assuming a single compartment and ignoring T_2^* weighting, the observed T_1-weighted signal at each voxel with flip angle of α can be expressed as:

$$S(\alpha) = M_0 \sin(\alpha) \left(\frac{1 - 2\,\mathrm{e}^{-\frac{TI}{T_1}} + \mathrm{e}^{-\frac{TR}{T_1}}}{1 + \cos(\alpha)\,\mathrm{e}^{-\frac{TR}{T_1}}} \right) \tag{7.2}$$

where, T_1 is the unknown relaxation parameter, TI is the inversion time, and TR is the repetition time. The unknown parameters were estimated by a variable projection approach similar to that described in [Haldar et al., 2007]. We used a single compartment model for T_1 maps because our T_1-weighted images were high resolution with relatively low signal-to-noise ratio. As also noted in [Lutti et al., 2014], we found that the T_1 maps were very sensitive to the inhomogeneities in the transmit and receive B_1 fields and so in the following we also use the T_1-weighted themselves in a similar fashion to Glasser and Van Essen [2011].

The denoised and distortion corrected diffusion images were used to estimate diffusion tensor and diffusion orientation distribution functions (ODFs) separately at two different b-values. Ideally, multi-shell data should be combined to estimated a better representation of the ODFs [Varadarajan and Haldar, 2015] but for this preliminary study we are using the simple model. We estimate the diffusion tensors using a weighted linear least-squares method [Koay et al., 2006] and the ODFs using two approaches: the Funk-Radon transform and the Funk-Radon and cosine transform (FRACT) [Haldar and Leahy, 2013]. FRACT is a newer approach of estimating ODFs that has higher angular resolution, which could be useful in characterizing the complex architecture in the cortex. We represent the diffusion tensor at each voxel by three eigenvalues and eigenvectors. The ODFs are represented using the linear combination of the first 45 spherical harmonic basis functions *i.e.* a total of 45 coefficients are estimated for each voxel in the diffusion data. The diffusion data can also be sampled on the cortical surface in a similar fashion to the T_1 and T_2 maps and intensity images. However, the diffusion data is orientation dependent. Hence, it requires special normalization to align this orientation with that of the cortical surface.

7.2 Normalization of diffusion data for cortical parcellation

Relaxation-based MR contrasts are scalar in nature, so it is straight forward to compare their intensity or quantitative values across different regions on the cortex. However, as seen in the cyto- and myelo-architectonic maps, the cortical layers from 1 to 6 are defined along a direction which is orthogonal to the pial surface (towards the inner surface). With the highly folded geometry of the brain, this means that the cortical layers are oriented along different directions at different points on the cortex as shown in

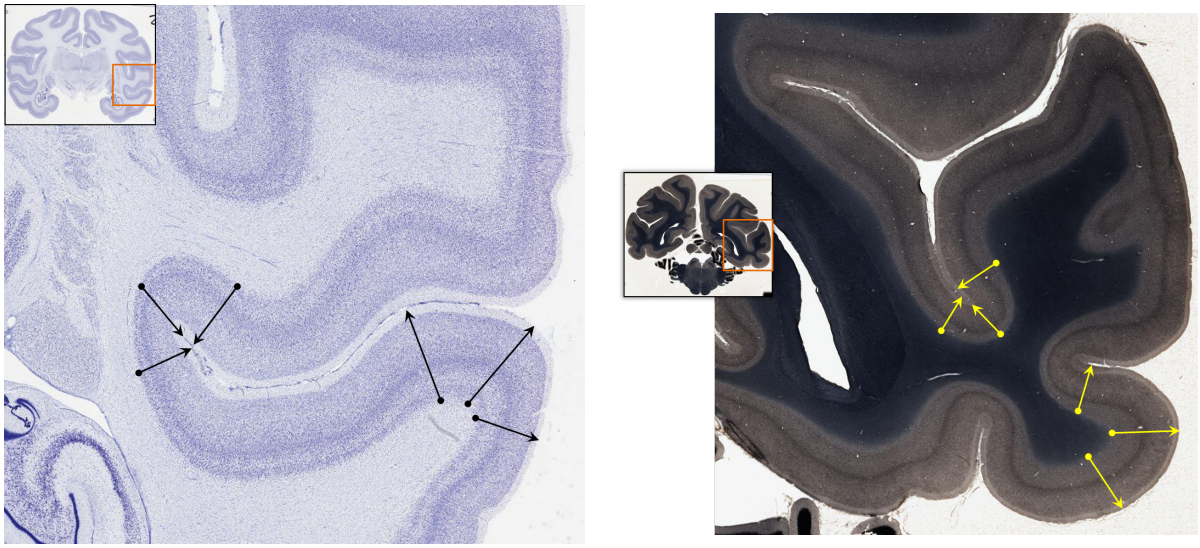

(a) (b)

Figure 7.3: High-resolution histological slices of macaque brains stained with (a) Nissl and (b) Weil stain. The Nissl method stains the cell bodies in the slices to reveal cytoarchitecture, while the Weil method stains myelin sheaths [Weil, 1928] showing myeloarchitecture. Orientation of the arrows indicate the approximately orientation of the cortical layers starting from layer 6 (round end) to layer 1 (pointed end). These histology images were obtained from http://brainmaps.org[1] [Mikula et al., 2007, Web].

Fig. 7.3. As the diffusion signal is sensitive to the microstructural details and is orientation-dependent, it will vary or rotate relative to a fixed coordinate system, even within a single architectonic region, because of the convoluted nature of the cortical ribbon. In most previous studies, some scalar valued or radially symmetric parameters are extracted from the diffusion data for easy comparison [Anwander et al., 2010, Truong et al., 2014, Kleinnijenhuis et al., 2013a, McNab et al., 2013b, Nagy et al., 2013]. For example, the principal direction of the diffusion tensor model [Anwander et al., 2010, Truong et al., 2014, Kleinnijenhuis et al., 2013a, McNab et al., 2013b] or the radially symmetric parameters of the ODFs [Nagy et al., 2013] were used to perform a comparison with other regions of the cortex. While this simplifies the issue with orientation dependent diffusion data, it comes at a loss of a large amount of potentially useful information in the diffusion signal. Note that this not a limitation of the spatial resolution of the diffusion data and even ultra-high resolution diffusion dataset will have same dependence on the underlying microarchitectonic details, as seen in *ex vivo* data. These orientation-dependent information could be specially important because the myeloarchitectonic differences between different cortical areas

[1]Image are obtained under Creative Commons Attribution 3.0 License for academic purposes from: (a) Nissl stain – http://brainmaps.org/ajax-viewer.php?datid=20&sname=n21&vX=1107&vY=1001.58&vT=4 and (b) Weil stain http://brainmaps.org/ajax-viewer.php?datid=21&sname=m26&vX=742.495&vY=440.09&vT=3.

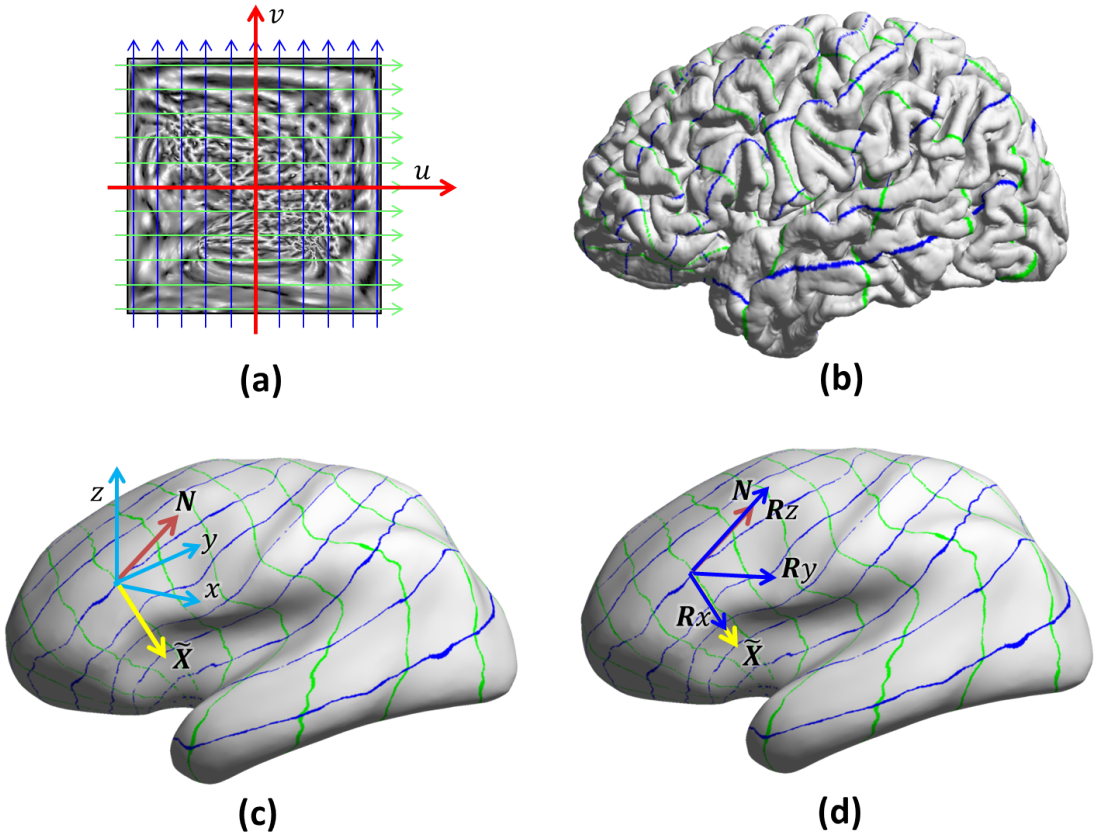

Figure 7.4: Overview of the normalization approach. (a) Mapping of the cortex (one hemisphere) to a unit square using [Joshi et al., 2007]. The 2D points in this unit square are parameterized by coordinates (u, v). (b) The 2D grid of (u, v) coordinates, shown as colored lines, mapped back to the original mid-cortical surface of the subject using the mapping found in (a). (c) Local representation of different coordinate systems on one particular face. The 2D grid of colored lines is same as that in (b) but shown on smoothed surface. $\mathbf{N}$ is the direction of the normal to the surface at that face and $\widetilde{\mathbf{X}}$ is the (systematic) x-direction mapped from the flat map at that face. $[x, y, z]$ represents the 3D coordinate system in which the surface coordinates are defined. (d) The modified local coordinate system at that face after applying the reorientation with rotation matrix $\mathbf{R}$ to $[x, y, z]$. Note that $\mathbf{N}, \widetilde{\mathbf{X}}$ and $\mathbf{R}$ can be different at each face on the surface depending on the local surface geometry.

are known to be subtle and extra information along different directions could be helpful to potentially identify underlying microstructure with currently feasible *in vivo* spatial resolution.

We propose a novel automated orientation normalization technique which can normalize the diffusion information such that the orientation-dependent information is retained and the vector valued diffusion properties can be directly compared without any loss of information. The intuition behind our techniques lies in the fact that it is known from several histological staining studies that cortical layers run parallel to the pial surface, and layers change along the direction which is orthogonal to the surface. This directly

implies that an orientation-dependent function should be re-oriented to a new 'normalized' coordinate system in which the direction along the normal to the pial surfaces should coincide for all the points on the cortex. While this first step of normalization is intuitive and forms the idea behind comparing anisotropy along and normal to the cortical surface [Anwander et al., 2010, McNab et al., 2013b], it is not complete by itself for 3D functions. Another reorientation step is required to rotate the information that is oriented in the plane of the cortex to be appropriately normalized. This is required because the first rotation step to match the normal to pial surface does not use information along the cortical surface (*i.e.* vertex/face connectivity pattern with neighbors), which make the orientation along the plane of cortex ambiguous after the first rotation step.

In our approach, we use the idea of mapping of the cortex to a 2D manifold to define a coordinate system, which is used to define a second reorientation step to properly normalize the orientation-dependent information in the plane of the cortex. In other words, we use a 'normalized' coordinate system in which the z-axis points outward towards the normal to the pial surface and the x, y-axes point towards local 2D axes defined by the mapping to the 2D square. This is illustrated in Fig. 7.4 and is described mathematically in the text below. Our mesh representation of the cortex is made up of a set of connected triangles defined by their ordered vertices. Let us assume that the 3D coordinates of the three vertices of the i^{th} triangle are given by $\mathbf{X}_1^i, \mathbf{X}_2^i$ and $\mathbf{X}_3^i$, such that $\mathbf{X}_1^i = [x_1^i, y_1^i, z_1^i]^\top$ and likewise for $\mathbf{X}_2^i$ and $\mathbf{X}_3^i$. We define the direction of the normal to the surface at this triangle to be the normal to the plane of the triangle which is expressed as $\mathbf{N}^i = \frac{(\mathbf{X}_2^i - \mathbf{X}_1^i) \times (\mathbf{X}_3^i - \mathbf{X}_1^i)}{|(\mathbf{X}_2^i - \mathbf{X}_1^i) \times (\mathbf{X}_3^i - \mathbf{X}_1^i)|}$, where $\times$ represents the cross product of the vectors. $\mathbf{N}^i$ always points away from the cortical surface for all triangle faces because the vertices are ordered in counter-clockwise fashion. Let $\mathbf{Z} = [0, 0, 1]^\top$, then the first rotation operation, to align the normal to surfaces at each point on the cortical surface, is achieved by rotating the data by an angle $\theta_1^i = \arccos(\langle \mathbf{Z}, \mathbf{N}^i \rangle)$ with rotation axis $\mathbf{r}_1^i = \frac{\mathbf{N}^i \times \mathbf{Z}}{|\mathbf{N}^i \times \mathbf{Z}|}$, where $\langle \cdot \rangle$ represents the dot product. In terms of axis-angle representation, the first rotation operation is expressed as the rotation matrix $\mathbf{R}_1^i = (\mathbf{r}_1^i, \theta_1^i)$.

For the second reorientation step, we use the flattening technique described in [Joshi et al., 2004, 2007] to obtain a mapping from the cortical surfaces to a flat unit square, which minimizes the p-harmonic energy of the mapped vertices with the constraint that the curve circumscribing the corpus callosum lies on the border of the unit square. The purpose of this flattening is to systematically define a 2D coordinate system on the cortical surface as shown in Fig. 7.4. We use $p = 4$ because it produced the best trade-off between distortion of the triangle faces and retention of overall shape. With this flat mapping, each vertex of the i^{th} triangle face is assigned a 2D coordinate (from the unit square) such that $\mathbf{X}_1^i \mapsto (u_1^i, v_1^i)$, $\mathbf{X}_2^i \mapsto (u_2^i, v_2^i)$ and $\mathbf{X}_3^i \mapsto (u_3^i, v_3^i)$. This can also be expressed as two functions $\varphi_u^i : \mathbf{X} \mapsto u$ and $\varphi_v^i : \mathbf{X} \mapsto v$ which map the 3D coordinates of the points, including vertices, in the i^{th} triangle to 2D coordinates (u, v) on the unit square. We can then constrain the axes of the systematic local 2D coordinates on the triangle to lie along the direction of the gradients of φ_u^i and φ_v^i on the triangle

face. Assuming that the flat mapping functions φ_u^i and φ_v^i are piece-wise linear for each triangle, then we can express the directions of the axes of the systematic local 2D coordinate system as

$$\widetilde{\mathbf{X}}^i = \mathbf{T}_x^i \frac{\partial \varphi_u^i}{\partial t_x^i} + \mathbf{T}_y^i \frac{\partial \varphi_u^i}{\partial t_y^i} \tag{7.3}$$

$$\widetilde{\mathbf{Y}}^i = \mathbf{T}_x^i \frac{\partial \varphi_v^i}{\partial t_x^i} + \mathbf{T}_y^i \frac{\partial \varphi_v^i}{\partial t_y^i} \tag{7.4}$$

where, $\mathbf{T}_x^i$ and $\mathbf{T}_y^i$ represent the 3D direction of the axes of the triangle's coordinate system, (t_x^i, t_y^i) represents the coordinates in the triangle's coordinate system and the gradient terms $\frac{\partial \varphi^i}{\partial t^i}$ are described in [Joshi et al., 2004, 2007]. The main difference between the triangle's coordinate axis $\mathbf{T}_x^i$ and systematic local axis $\widetilde{\mathbf{X}}^i$ is that the former is defined arbitrarily for each triangle using the triangle's sides where as the later is defined using the flat mapping function. Given these systematic 2D coordinate systems and assuming $\widetilde{\mathbf{X}}^i$ to be unit length, we can define the second rotation matrix as $\mathbf{R}_2^i = (\mathbf{r}_2^i, \theta_2^i)$ in axis-angle representation, where $\theta_2^i = \arccos(\langle [1,0,0], \widetilde{\mathbf{X}}^i \rangle)$ and $\mathbf{r}_2^i = [0,0,1]$. The rotation matrix $\mathbf{R}_2^i$ rotates the vector function along the z-axis such that the x-axes align.

Combining both the set of rotations we get the final rotation matrix $\mathbf{R}^i = \mathbf{R}_2^i \mathbf{R}_1^i$. This rotation based normalization can be used either to rotate the fitted diffusion model or to re-define the diffusion encoding gradient directions in the normalized coordinate system. In our preliminary results, we use this normalization for both tensor and ODF models, which allows use to use all the spherical harmonic coefficients (SHCs) of the ODFs for direct comparison. This could be useful as ODFs are non-parametric in nature and can capture subtle details. Note that in the above description we have assumed that the data is defined on the faces of the cortical mesh, primarily because it is more intuitive and straightforward to define the gradient operator in the plane of the faces. However, similar expressions can also be derived to operate entirely on the vertices following similar logic as above.

7.3 Feature extraction and parcellation

The data processing and normalization technique described above allows us to fuse the information from multi-contrast MRI images on the cortex. Next, we extract a number of features from these multi-contrast images and make use of machine learning techniques to parcellate the cortex. We use quantitative relaxation parameters (T_1 and T_2), intensity maps (T_1-weighted and T_2-weighted) and diffusion parameters as features. Diffusion parameters include the SHCs of ODFs computed with reorientation normalization (45 SHCs for each b-value) and parameters derived from the diffusion tensor models, which include fractional anisotropy (FA), mean diffusivity (MD), axial diffusivity and radial diffusivity. In addition, inspired by the previous studies reviewed in Sec. 3.2, we also constructed and added additional features: quantitative T_1/T_2 ratio, T1w/T2w similar to that in [Glasser and Van Essen, 2011],

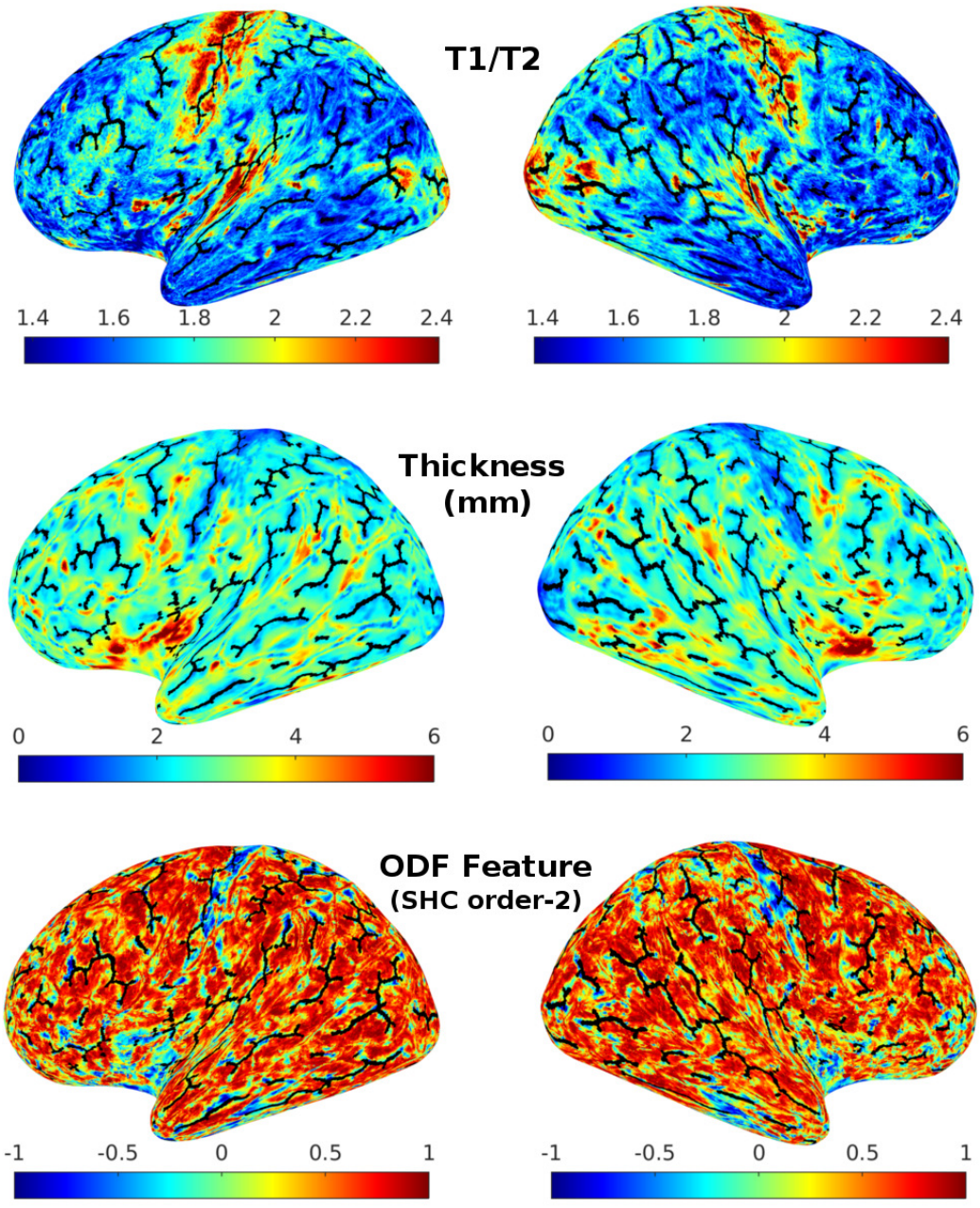

Figure 7.5: Examples of the features extracted from the dataset for one subject, shown on the smooth surface. The sulcal curves for individual subjects are marked in black.

ratio of T1w images with different flip-angles, M_{GM} from eq. (7.1), anisotropic Laplace equation based cortical thickness [Joshi et al., 2014] and order-wise norm of ODF SHCs (4 orders for diffusion data with each b-value). With all these constructed features, we obtain more than 100 features at each point on the cortex, which are then fed to a classification/segmentation algorithm. Figure 7.5 displays three representative examples of cortical features we obtained on a single subject.

Classification of the data using multiple features is the primary aim of the clustering techniques in the broader field of data analysis and mining [Estivill-Castro, 2002, Berkhin, 2006]. In our application, the data is the set of features extracted for each vertex on the cortical surface. We use a probabilistic approach to parcellate or cluster the cortical vertices based on the observed features. We assume that the manifestation of the features from each cluster or parcel follows a Gaussian distribution and that the data points are generated from a randomly selected mixture of these parcels. The assumption of the Gaussian distribution is somewhat arbitrary but has been successfully used in several image segmentation applications, and the statistical properties of the Gaussian mixtures are widely studied. We use an expectation-maximization (EM) approach to estimate the parameters of the Gaussian mixture model (GMM). As the solution to EM approach can depend on the initialization, we use the GMM parameters which yielded maximum likelihood across four different initializations. For each initialization, the mean of different Gaussian components were selected using the kmeans++ algorithm [Arthur and Vassilvitskii, 2007], which is an efficient method for choosing the initial centroids for clustering algorithms. The covariance matrix of the Gaussian mixture was initialized to be a diagonal matrix with diagonals representing the variance of each kmeans++ centroid and the mixing proportions were initialized to be uniformly distributed.

We constructed a $V \times F$ feature matrix which was used for GMM classification. Each row of this matrix represents a vertex on the surface. The elements of the row are the set of F features as described above. Each column represents one particular feature. In other words, each row represents a point in the F-dimensional feature space, and there are a total of V points to be clustered into K clusters/parcels. In our dataset, the total number of points on the cortical surface, including both hemispheres, was about $V \approx 150,000$. To ease the computational cost for our preliminary results, we sub-divided the cortex into four lobes, such that each subdivision had corresponding lobes defined on both hemispheres. This results in four separate feature matrices which were used independently for the GMM clustering. As the unit of the different features are different, we normalized columns of the matrices to be zero mean and unit variance.

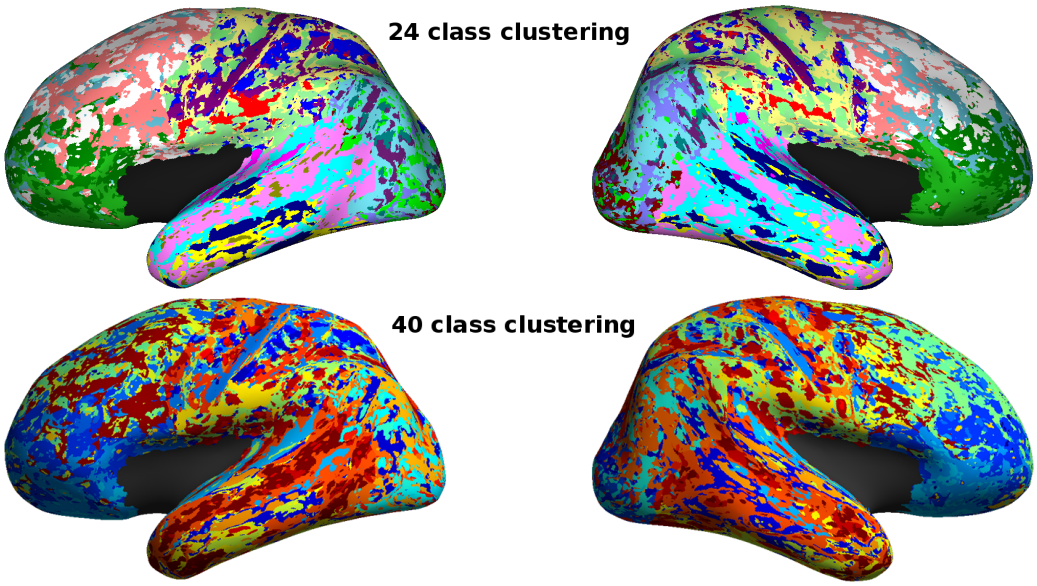

Figure 7.6: Preliminary segmentation results using (a) 24 class clustering and (b) 40 class clustering method.

7.4 Preliminary results

Fig. 7.6 shows the results of this clustering approach with GMM clustering with $K = 24$ (each of the four lobes was clustered with $K = 6$) and $K = 40$ (each of the four lobes was clustered with $K = 10$). Each cluster is shown with a unique color on the inflated cortical surface. There are a number of interesting features in both of the results. The clusters show very strong consistency across left and right hemisphere, *i.e.* homologous regions on left and right hemisphere are clustered together. Note that the above feature matrix formulation does not contain any spatial information, which means that the clustering algorithm does not have information about which set of points are spatially neighbors or which set of points are contralateral to each other. The presence of such strong contralateral consistency is very encouraging and has been observed in previous histological as well as *in vivo* studies [Brodmann, 1909, von Economo and Koskinas, 1925, Geyer and Turner, 2013]. Next, we also notice the presence of 3-4 clusters running parallel to the central sulcus, which is also consistent with the clusters in the Brodmann's microarchitectonic parcellation. Several other clusters also show similarity with Brodmann areas, albeit noisily, for example, the clusters in the temporal lobe and visual cortex. We also notice that larger clusters get sub-divided when the number of clusters is increased from $K = 24$ to $K = 40$. This is also consistent with a number of architectonic maps, for example, von Economo's maps have a substantially larger number of regions compared to Brodmann maps, but the increase is largely due to a subdivision of the regions found by Brodmann.

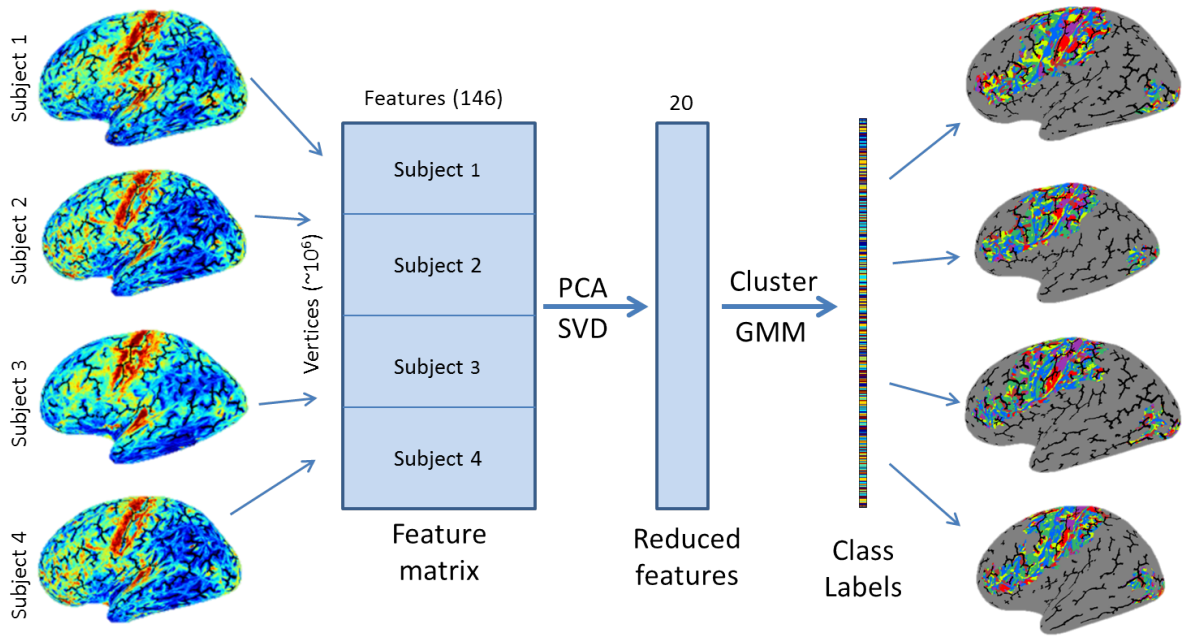

Figure 7.7: Overview of multi-subject clustering.

Multi-subject evaluation

Next we investigate our approach using a multi-subject parcellation. Here we study whether the set of features used in our approach contain meaningful information that are consistent across different subjects as described pictorially in Fig. 7.7. To study this, we pooled data across four different subjects from the dataset provided by the Human connectome project (HCP). The HCP provides high-resolution T_1- and T_2-weighted images and diffusion weighted images (b-values of 1000, 2000, and 3000), however, the quantitative relaxometry data is not available. We used the cortical surfaces provided with the minimally processed HCP dataset and sampled all the data on the cortical surfaces. The diffusion dataset was normalization as described above and the normalized diffusion models (diffusion tensors and ODFs) were fitted separately for each b-value. We used the following set of features for each face on the cortex: 44 order-8 SHCs to describe the normalized ODFs and the 4 order-wise norms of the SHCs for each of three different b-values (total of $3 \times (44 + 4) = 144$ diffusion ODF features), T_1 and T_2 intensity, ratio of T_1- and T_2-weighted intensity images and cortical thickness calculated by the anisotropic Laplace equation. This gives us a total of $F = 146$ features for each vertex on the cortex. These were used to create a feature matrix for each subject as described previously. This feature matrix had no knowledge of spatial location of the vertices and, similar to the previous section, we selected only a small subset of vertices to lower the computational cost (homologous subsets based on macro-anatomical labels provided by HCP). The feature matrices for the four subjects were then concatenated to create the final feature

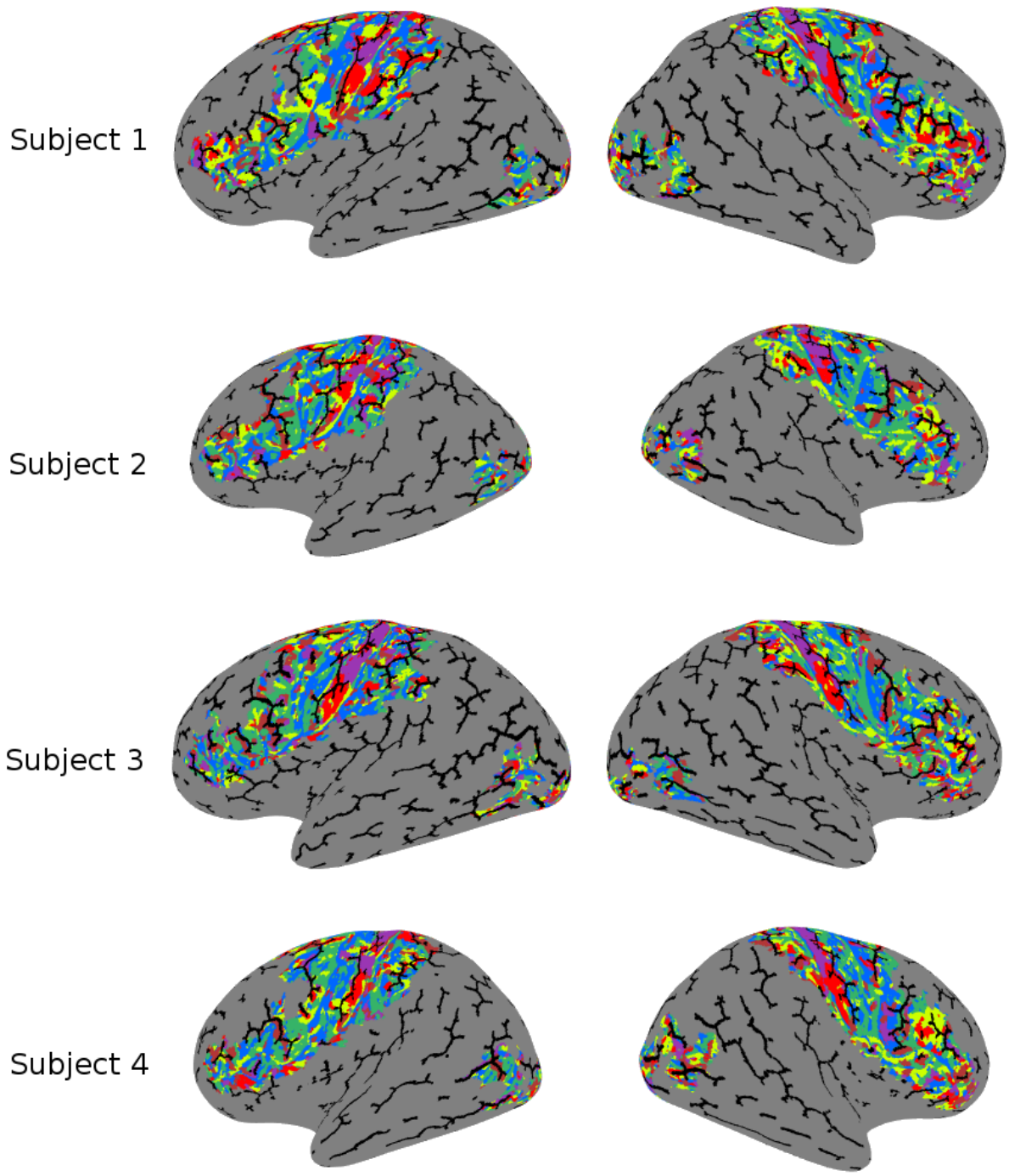

Figure 7.8: Cortical classification results on four subjects with 6-classes, shown on an inflated smooth surface. Sulcal curves for individual subjects are marked in black. Each unique colors represents a unique cluster. Only vertices corresponding to the colored areas were used in the clustering.

matrix of size $4V \times F$, which was normalized column-wise to be zero mean and unit variance. We also used the principle component analysis (PCA) to reduce the dimensionality of this feature matrix. PCA was performed by singular value decomposition (SVD) using left-singular vectors corresponding to the top 20 singular values. We used GMM clustering with this reduced set of features in similar fashion as described earlier.

The motivation behind using a concatenated feature matrix is to study whether the set of features convey meaningful information across a population. If so, then a clustering algorithm that is 'blind' to where the data points are located should cluster similar regions/structures across subjects. The GMM clustering algorithm has no spatial or population knowledge which allows us to evaluate the consistency of the set of features across different subjects and cortical regions. Figure 7.8 shows the results of this clustering (or cortical parcellation) for the selected cortical regions with $K = 6$ classes for four subjects. These results are displayed on the inflated cortical surfaces with major sulci overlaid in black for the anatomical reference. Each cluster is assigned a unique color on the smooth cortex. Similar to our previous results, we see some correspondence in clusters across contralateral regions, which is again encouraging since the spatial information was not used in the clustering. Further, it seems to be successful in segmenting several regions consistent with existing architectonic mappings. Thin regions are seen running parallel to the central-sulcus which are difficult to identify without knowledge of the microstructural properties of the cortex. This classification also identifies similar regions across subjects into the same class. For example, the post-central gyrus is sub-classified into two parts consistently across subjects. The classification in other areas were noisier yet shows some consistency across subjects.

7.5 Conclusions

In this chapter, we explored the idea of microarchitectonic *in vivo* parcellation of the cerebral cortex using multi-contrast MRI. These results are clearly preliminary but do indicate that multi-contrast methods can identify good contralateral and inter-subject consistency of the parcellation in several areas of the cortex, even without any spatial knowledge. Microstructural parcellation of the entire cortex in an ambitious goal. Although several investigators have already explored this goal in several ways (see Sec. 3.2) considerable further exploration, study and development is required before these approaches can be used for routine microarchitectonic parcellation.

There are several avenues for improvements in our proposed approach using machine learning techniques. We have used a simple set of feature derived from quantitative relaxometry and diffusion models. However, there are several feature construction approaches, such as Gabor-filtering [Kamarainen et al., 2006], which are commonly used in other related field of computer vision and pattern analysis [Saeys et al., 2007, Lillywhite et al., 2013]. These approaches can be adopted to work on the folded cortical

surface to enhance the set of accessible features. Further, a semi-supervised approach can also be used where a known set of homogeneous areas, derived from either *ex vivo* or independent task-based functional studies, can be used for feature selection, as also proposed by Geyer [2013]. Several advanced techniques such as subspace-, dictionary- and spectral-based classification approaches can also be employed for obtaining the parcels from large a number of features [Bengio et al., 2013, Luo et al., 2016, Wu et al., 2016, Chen and Feng, 2012].

Lack of ground truth is another challenge with *in vivo* microstructural parcellation of the cortex, which limits the quantitative evaluation of the resulting clusters. In our approach, we used visual comparison and multi-subject clustering to gain some insight into the quality of the features we were using. However, as the underlying architectonic structure can be variable across populations, it is difficult to assess the quality of the parcels. Data from different trials of the same subject can be used to study the reproducibility of the parcellation. Validation from animal studies could also be very helpful in this context, where initially *in vivo* data is collected followed by histology to obtain a gold reference parcellation.

Chapter 8

Conclusions

In this dissertation, we presented several new methods and approaches which are geared toward improving the accuracy of multi-contrast MRI image analysis. We presented two approaches for correction of susceptibility-induced geometric distortion artifacts in diffusion MRI: (1) an interlaced phase-encoding (IPED) sampling scheme with constrained joint reconstruction approach in chapter 5, and (2) a non-rigid registration-based approach which can perform correction in the absence of magnetic field inhomogeneity maps in chapter 4. In both of these approaches, we exploited prior knowledge about the physical properties of the images to simplify the problem. In IPED sampling, we used the prior that the diffusion processes are smoothly varying across neighboring directions, which allowed us to lower the data-acquisition requirement to half, thus reducing the scan time by a factor of two (as compared to the reversed-gradient method) and at the same time achieve distortion correction accuracy which is comparable to the state-of-the-art method in our experiments with simulated and *in vivo* data. For the registration-based approach, we used the known inverted contrast relationship to transform the problem of an *inter*-modal image registration problem to an *intra*-modal problem. This allowed us to exploit well-behaved properties of *intra*-modal cost functions which can be minimized easily and thus achieve robust performance and improved accuracy as compared to other method and software tools in our experiments.

We presented a novel filtering technique for resting functional MRI in chapter 6 that enables direct visualization of the dynamic brain activity on the cortical surface without artifactual spatial blurring. The proposed filtering approach is an adaptation of the non-local means filtering [Buades et al., 2005] for functional MRI, which we call 'temporal non-local means', where we use the temporal information to adaptively change the weights of the smoothing kernel at each point on the cortex. This helps to suppress the unwanted signal and noise by averaging across points that have similar time course but at the same time respect the functional boundaries and avoid any spatial blurring across boundaries. Temporal non-local means filtering allows direct visualization of spatio-temporal brain activity on the brain surface which could facilitate the study of complex dynamic activity across different regions of the brain. We

also demonstrated its utility in functional parcellation of the cortex, where the parcellation obtained with use of temporal non-local means showed higher consistency with regions identified independently using task-based experiments and probabilistic Brodmann areas.

In chapter 7, we proposed an approach for parcellating the cortex based on microstructural information using *in vivo* MRI images. While obtaining microstructural information in the whole brain with *in vivo* imaging is a tough challenge, there has been a considerable effort in this direction (see review in Sec. 3.2). Our proposed approach is motivated by several prior observations and fuses information from multi-contrast MRI images to generate a set of features that are indicative of the microstructural information. We used T_1-, T_2- and diffusion-weighted images to obtain several features with both intensity maps and quantitative maps obtained by fitting an appropriate model. In the context of fusing information, we also described an approach to systematically normalize the orientation-dependent diffusion data so that we can make use of all information and not be limited by orientation invariant features as used in prior approaches. The preliminary results with two *in vivo* datasets suggest that the extracted set of features show meaningful information and obtain a parcellation, even in the absence of any spatial information, which is similar in nature to that observed with the histological parcellation (Brodmann's and von Economo's) as well as showing substantial consistency across subjects and contralateral cortical regions.

In addition to developing novel computational methods, we also made available the implementation of several of our proposed methods under the GNU General Public License, version 2.0. These methods were implemented in using a combination of MATLAB (The MathWorks, Inc., USA) and C programming language, whose source code are available from http://neuroimage.usc.edu/. The distortion correction methods are also a part of the BrainSuite software and are available as pre-compiled executables for Windows, Linux and Mac platforms from http://brainsuite.org/. We hope that these implementations help translate the recent advances to regular practice in the field of neuroimaging.

The new methods in this thesis are a small step toward improving the accuracy and utility of multi-contrast MRI images. There are several possible improvements to the proposed approaches, which we have discussed in the individual chapters. Our approaches make use of problem-specific prior knowledge about diffusion properties, contrast, and dynamic temporal information to improve the quality of images and the accuracy of the fused multi-contrast information. There are several other forms of problem-specific prior knowledge which could be employed to further improve the accuracy and/or improve acquisition such as consistency of edges across images with different contrasts [Haldar et al., 2013], use of appropriate likelihood noise models [Varadarajan and Haldar, 2013], use of shape and size priors [Schmid et al., 2011, Ashburner et al., 1997]. Further, owing to recent advances in machine learning, non-intuitive prior information can also be learned directly from the data itself using advanced learning techniques [Bhatia and Lombaert, 2015, Rueckert et al., 2013], which could complement our current

understanding and knowledge.

MRI provides a unique sensitivity to a wide range of physical properties of soft tissue in a non-invasive fashion which has been exploited to obtain multiple application-specific MR contrasts useful for research and clinical neuroimaging. The fusion of information across such multi-contrast images could provide more information and allow deeper insight into underlying tissue, connectivity and functional characteristics. The use of such information fusion is still limited in regular clinical and research settings because of the presence of sequence specific artifacts in multi-contrast images. The use and development of analysis and acquisition techniques that exploit prior knowledge to reduce artifacts and improve fusion of information under practical constraints of scan time and feasible computational complexity could be very beneficial for diagnosis, prognosis, and exploration purposes.

This page intentionally left blank.

Bibliography

Brainmaps: An interactive multiresolution brain atlas. URL http://brainmaps.org. Last accessed on 27 December 2015. (Cited on pages 43 and 148.)

Rare intermittent EPI artifacts: Spiking, sparking and arcing, May 2012. URL http://practicalfmri.blogspot.com/2012/05/rare-intermittent-epi-artifacts-spiking.html. Last accessed on 27 December 2015. (Cited on page 7.)

J. J. H. Ackerman and J. J. Neil. Biophysics of diffusion in cells. In D. K. Jones, editor, *Diffusion MRI: Theory, Methods, and Applications*, 2014. doi:10.1093/med/9780195369779.003.0008. (Cited on page 42.)

M. Aggarwal, D. W. Nauen, J. C. Troncoso, and S. Mori. Probing region-specific microstructure of human cortical areas using high angular and spatial resolution diffusion MRI. *NeuroImage*, 105:198 – 207, 2015. doi:10.1016/j.neuroimage.2014.10.053. (Cited on page 45.)

D. C. Alexander. Multiple-fiber reconstruction algorithms for diffusion MRI. *Annals of the New York Academy of Sciences*, 1064(1):113–133, 2005. ISSN 1749-6632. doi:10.1196/annals.1340.018. (Cited on page 46.)

D. C. Alexander. A general framework for experiment design in diffusion MRI and its application in measuring direct tissue-microstructure features. *Magnetic Resonance in Medicine*, 60(2):439–448, 2008. ISSN 1522-2594. doi:10.1002/mrm.21646. (Cited on page 46.)

E. Alonso-Ortiz, I. R. Levesque, and G. B. Pike. MRI-based myelin water imaging: A technical review. *Magnetic Resonance in Medicine*, 73(1):70–81, 2015. ISSN 1522-2594. doi:10.1002/mrm.25198. (Cited on pages 39, 41, and 42.)

K. Amunts and M. Catani. Cytoarchitectonics, receptorarchitectonics, and network topology of language. In A. W. Toga, editor, *Brain Mapping*, pages 177 – 185. Academic Press, 2015. ISBN 978-0-12-397316-0. doi:10.1016/B978-0-12-397025-1.00211-6. (Cited on page 33.)

K. Amunts and K. Zilles. Architectonic mapping of the human brain beyond Brodmann. *Neuron*, 88(6):1086 – 1107, 2015. ISSN 0896-6273. doi:10.1016/j.neuron.2015.12.001. (Cited on pages 31, 33, 37, 38, and 41.)

K. Amunts, A. Schleicher, U. Bürgel, H. Mohlberg, H. B. M. Uylings, and K. Zilles. Broca's region revisited: Cytoarchitecture and intersubject variability. *The Journal of Comparative Neurology*, 412(2):319–341, 1999. doi:10.1002/(SICI)1096-9861(19990920)412:2<319::AID-CNE10>3.0.CO;2-7. (Cited on page 37.)

K. Amunts, A. Malikovic, H. Mohlberg, T. Schormann, and K. Zilles. Brodmann's areas 17 and 18 brought into stereotaxic space – where and how variable? *NeuroImage*, 11(1):66 – 84, 2000. ISSN 1053-8119. doi:10.1006/nimg.1999.0516. (Cited on page 37.)

K. Amunts, A. Schleicher, and K. Zilles. Cytoarchitecture of the cerebral cortex – more than localization. *NeuroImage*, 37(4):1061 – 1065, 2007. ISSN 1053-8119. doi:10.1016/j.neuroimage.2007.02.037. (Cited on page 37.)

K. Amunts, C. Lepage, L. Borgeat, H. Mohlberg, T. Dickscheid, M.-É. Rousseau, S. Bludau, P.-L. Bazin, L. B. Lewis, A.-M. Oros-Peusquens, N. J. Shah, T. Lippert, K. Zilles, and A. C. Evans. BigBrain: An ultrahigh-resolution 3D human brain model. *Science*, 340(6139):1472–1475, 2013. ISSN 0036-8075. doi:10.1126/science.1235381. (Cited on pages 34 and 38.)

K. Amunts, M. J. Hawrylycz, D. C. V. Essen, J. D. V. Horn, N. Harel, J.-B. Poline, F. D. Martino, J. G. Bjaalie, G. Dehaene-Lambertz, S. Dehaene, P. Valdes-Sosa, B. Thirion, K. Zilles, S. L. Hill, M. B. Abrams, P. A. Tass, W. Vanduffel, A. C. Evans, and S. B. Eickhoff. Interoperable atlases of the human brain. *NeuroImage*, 99:525 – 532, 2014. ISSN 1053-8119. doi:10.1016/j.neuroimage.2014.06.010. (Cited on page 38.)

M. Andellini, V. Cannatà, S. Gazzellini, B. Bernardi, and A. Napolitano. Test-retest reliability of graph metrics of resting state MRI functional brain networks: A review. *Journal of Neuroscience Methods*, 253:183 – 192, 2015. doi:10.1016/j.jneumeth.2015.05.020. (Cited on page 47.)

A. W. Anderson. Measurement of fiber orientation distributions using high angular resolution diffusion imaging. *Magnetic Resonance in Medicine*, 54(5):1194–1206, 2005. ISSN 1522-2594. doi:10.1002/mrm.20667. (Cited on pages 76 and 78.)

J. L. R. Andersson. Geometric distortions in diffusion MRI. In H. Johansen-Berg and T. E. Behrens, editors, *Diffusion MRI: from Quantitative Measurement to in-vivo Neuroanatomy*, pages 63 – 85. Academic Press, San Diego, 2nd edition, 2014. ISBN 978-0-12-396460-1. doi:10.1016/B978-0-12-396460-1.00004-4. (Cited on pages 14, 16, 20, and 23.)

J. L. R. Andersson and S. Skare. Image distortion and its correction in diffusion MRI. In D. K. Jones, editor, *Diffusion MRI: Theory, Methods, and Applications*, pages 285–302. Oxford University Press, USA, 2011. doi:10.1093/med/9780195369779.003.0017. (Cited on pages 6, 14, 16, 19, 20, 23, 25, 26, 28, 51, 52, 56, 71, and 92.)

J. L. R. Andersson, S. Skare, and J. Ashburner. How to correct susceptibility distortions in spin-echo echo-planar images: application to diffusion tensor imaging. *NeuroImage*, 20(2):870–888, 2003. ISSN 1053-8119. doi:10.1016/S1053-8119(03)00336-7. (Cited on pages 16, 18, 20, 21, 22, 52, 58, 71, 74, 76, 77, 81, and 92.)

S. Angenent, S. Haker, A. Tannenbaum, and R. Kikinis. On the Laplace-Beltrami operator and brain surface flattening. *IEEE Transactions on Medical Imaging*, 18(8):700–711, Aug 1999. ISSN 0278-0062. doi:10.1109/42.796283. (Cited on pages 98 and 123.)

A. Anticevic, D. L. Dierker, S. K. Gillespie, G. Repovs, J. G. Csernansky, D. C. V. Essen, and D. M. Barch. Comparing surface-based and volume-based analyses of functional neuroimaging data in patients with schizophre-

nia. *NeuroImage*, 41(3):835 – 848, 2008. ISSN 1053-8119. doi:10.1016/j.neuroimage.2008.02.052. (Cited on page 36.)

J. S. Antrobus, J. L. Singer, S. Goldstein, and M. Fortgang. Mind-wandering and cognitive structure. *Transactions of the New York Academy of Sciences*, 32(2):242–252, 1970. ISSN 2164-0947. doi:10.1111/j.2164-0947.1970.tb02056.x. (Cited on pages 107 and 120.)

A. Anwander, A. Pampel, and T. R. Knösche. In vivo measurement of cortical anisotropy by diffusion-weighted imaging correlates with cortex type. In *18th Scientific Meeting of International Society for Magnetic Resonance in Medicine (ISMRM), Stockholm, Sweden*, 2010. (Cited on pages 43, 148, and 150.)

M. A. Arbib, editor. *The Handbook of Brain Theory and Neural Networks*. MIT press, 2nd edition, November 2002. ISBN 9780262011976. URL https://mitpress.mit.edu/books/handbook-brain-theory-and-neural-networks. (Cited on page 31.)

S. Ardekani and U. Sinha. Geometric distortion correction of high-resolution 3 T diffusion tensor brain images. *Magnetic Resonance in Medicine*, 54(5):1163–1171, 2005. ISSN 1522-2594. doi:10.1002/mrm.20651. (Cited on pages 23, 52, 53, and 54.)

V. Arsigny, P. Fillard, X. Pennec, and N. Ayache. Log-Euclidean metrics for fast and simple calculus on diffusion tensors. *Magnetic Resonance in Medicine*, 56(2):411–421, 2006. ISSN 1522-2594. doi:10.1002/mrm.20965. (Cited on pages 81 and 95.)

D. Arthur and S. Vassilvitskii. k-means++: The advantages of careful seeding. In *Proceedings of the eighteenth annual ACM-SIAM symposium on Discrete algorithms*, pages 1027–1035, 2007. (Cited on page 153.)

J. Ashburner and K. J. Friston. Spatial normalization. In A. Toga, editor, *Brain Warping*, pages 27–44. Academic Press, 1999. (Cited on page 36.)

J. Ashburner, P. Neelin, D. L. Collins, A. Evans, and K. Friston. Incorporating prior knowledge into image registration. *NeuroImage*, 6(4):344 – 352, 1997. ISSN 1053-8119. doi:10.1006/nimg.1997.0299. (Cited on page 160.)

J. C. Augustinack, K. Helmer, K. E. Huber, S. Kakunoori, L. Zöllei, and B. Fischl. Direct visualization of the perforant pathway in the human brain with *ex vivo* diffusion tensor imaging. *Frontiers in Human Neuroscience*, 4(42), 2010. doi:10.3389/fnhum.2010.00042. (Cited on pages 41 and 44.)

J. C. Augustinack, K. E. Huber, A. A. Stevens, M. Roy, M. P. Frosch, A. J. W. van der Kouwe, L. L. Wald, K. Van Leemput, A. C. McKee, and B. Fischl. Predicting the location of human perirhinal cortex, Brodmann's area 35, from MRI. *NeuroImage*, 64:32 – 42, 2013a. ISSN 1053-8119. doi:10.1016/j.neuroimage.2012.08.071. (Cited on page 41.)

J. C. Augustinack, A. J. W. van der Kouwe, and B. Fischl. Medial temporal cortices in ex vivo magnetic resonance imaging. *Journal of Comparative Neurology*, 521(18):4177–4188, 2013b. doi:10.1002/cne.23432. (Cited on page 41.)

J. C. Augustinack, C. Magnain, M. Reuter, A. J. W. van der Kouwe, D. Boas, and B. Fischl. MRI parcellation of ex vivo medial temporal lobe. *NeuroImage*, 93, Part 2:252 – 259, 2014. ISSN 1053-8119. doi:10.1016/j.neuroimage.2013.05.053. (Cited on page 41.)

R. Bammer, S. J. Holdsworth, M. Aksoy, and S. T. Skare. Phase errors in diffusion-weighted imaging. In D. K. Jones, editor, *Diffusion MRI: Theory, Methods, and Applications*, pages 218–249. Oxford University Press, USA, 2011. doi:10.1093/med/9780195369779.003.0014. (Cited on page 28.)

D. Barazany and Y. Assaf. Visualization of cortical lamination patterns with magnetic resonance imaging. *Cerebral Cortex*, 22(9):2016–2023, 2012. doi:10.1093/cercor/bhr277. (Cited on page 40.)

E. L. Barbier, S. Marrett, A. Danek, A. Vortmeyer, P. van Gelderen, J. Duyn, P. Bandettini, J. Grafman, and A. P. Koretsky. Imaging cortical anatomy by high-resolution MR at 3.0T: Detection of the stripe of gennari in visual area 17. *Magnetic Resonance in Medicine*, 48(4):735–738, 2002. ISSN 1522-2594. doi:10.1002/mrm.10255. (Cited on page 39.)

D. M. Barch, G. C. Burgess, M. P. Harms, S. E. Petersen, B. L. Schlaggar, M. Corbetta, M. F. Glasser, S. Curtiss, S. Dixit, C. Feldt, D. Nolan, E. Bryant, T. Hartley, O. Footer, J. M. Bjork, R. Poldrack, S. Smith, H. Johansen-Berg, A. Z. Snyder, and D. C. Van Essen. Function in the human connectome: Task-fMRI and individual differences in behavior. *NeuroImage*, 80:169 – 189, 2013. ISSN 1053-8119. doi:10.1016/j.neuroimage.2013.05.033. (Cited on page 103.)

A. J. Barkovich. Concepts of myelin and myelination in neuroradiology. *American Journal of Neuroradiology*, 21 (6):1099–1109, 2000. URL http://www.ajnr.org/content/21/6/1099.short. (Cited on pages 38 and 39.)

R. H. Bartels, J. C. Beatty, and B. A. Barsky. *An Introduction to Splines for Use in Computer Graphics and Geometric Modeling*. Morgan Kaufmann Publishers Inc., San Francisco, CA, USA, 1987. ISBN 0-934613-27-3. (Cited on page 60.)

P. J. Basser and D. K. Jones. Diffusion-tensor MRI: theory, experimental design and data analysis–a technical review. *NMR in Biomedicine*, 15(7-8):456–467, 2002. ISSN 1099-1492. doi:10.1002/nbm.783. (Cited on page 42.)

P.-L. Bazin, M. Weiss, J. Dinse, A. Schäfer, R. Trampel, and R. Turner. A computational framework for ultra-high resolution cortical segmentation at 7 Tesla. *NeuroImage*, 93, Part 2:201 – 209, 2014. ISSN 1053-8119. doi:10.1016/j.neuroimage.2013.03.077. (Cited on page 40.)

M. F. Bear, B. W. Conners, and M. A. Paradiso. *Neuroscience: Exploring the Brain*. Lippincott Williams & Wilkins, Baltimore, MD, USA, 2007. ISBN 978-0-7817-6003-4. (Cited on page 31.)

C. Beaulieu. The basis of anisotropic water diffusion in the nervous system – a technical review. *NMR in Biomedicine*, 15(7-8):435–455, 2002. ISSN 1099-1492. doi:10.1002/nbm.782. (Cited on page 42.)

C. Beaulieu. The biological basis of diffusion anisotropy. In H. Johansen-Berg and T. E. Behrens, editors, *Diffusion MRI*, pages 105 – 126. Academic Press, San Diego, 2009. ISBN 978-0-12-374709-9. doi:10.1016/B978-0-12-374709-9.00006-7. (Cited on page 42.)

C. Beaulieu. What makes diffusion anisotropic in the nervous system? In D. K. Jones, editor, *Diffusion MRI: Theory, Methods, and Applications*, pages 92–109. Oxford University Press, 2011. doi:10.1093/med/9780195369779.003.0007. (Cited on page 42.)

C. Beaulieu. The biological basis of diffusion anisotropy. In H. Johansen-Berg and T. E. Behrens, editors, *Diffusion MRI*, pages 155 – 183. Academic Press,, second edition edition, 2014. doi:10.1016/B978-0-12-396460-1.00008-1. (Cited on page 42.)

C. F. Beckmann, C. E. Mackay, N. Filippini, and S. M. Smith. Group comparison of resting-state fMRI data using multi-subject ICA and dual regression. *Neuroimage*, 47(Suppl 1):S148, 2009a. (Cited on page 49.)

M. Beckmann, H. Johansen-Berg, and M. F. S. Rushworth. Connectivity-based parcellation of human cingulate cortex and its relation to functional specialization. *The Journal of Neuroscience*, 29(4):1175–1190, 2009b. doi:10.1523/JNEUROSCI.3328-08.2009. (Cited on page 47.)

T. Behrens, J. C. Klein, S. Jbabdi, and H. Johansen-Berg. Connectivity-based parcellation of gray matter. In *Diffusion MRI: Theory, Methods, and Applications*. Oxford University Press, 2010. doi:10.1093/med/9780195369779.001.0001. (Cited on pages 47, 48, and 49.)

T. E. J. Behrens and H. Johansen-Berg. Relating connectional architecture to grey matter function using diffusion imaging. *Philosophical Transactions of the Royal Society of London B: Biological Sciences*, 360(1457):903–911, 2005. doi:10.1098/rstb.2005.1640. (Cited on pages 47 and 49.)

T. E. J. Behrens, H. Johansen-Berg, M. W. Woolrich, S. M. Smith, C. A. M. Wheeler-Kingshott, P. A. Boulby, G. J. Barker, E. L. Sillery, K. Sheehan, O. Ciccarelli, A. J. Thompson, J. M. Brady, and P. M. Matthews. Non-invasive mapping of connections between human thalamus and cortex using diffusion imaging. *Nature neuroscience*, 6 (7):750–757, 2003. doi:10.1038/nn1075. (Cited on page 47.)

Y. Bengio, A. Courville, and P. Vincent. Representation learning: A review and new perspectives. *IEEE Transactions on Pattern Analysis and Machine Intelligence*, 35(8):1798–1828, Aug 2013. ISSN 0162-8828. doi:10.1109/TPAMI.2013.50. (Cited on page 158.)

P. Berkhin. A survey of clustering data mining techniques. In J. Kogan, C. Nicholas, and M. Teboulle, editors, *Grouping Multidimensional Data: Recent Advances in Clustering*, pages 25–71, Berlin, Heidelberg, 2006. Springer Berlin Heidelberg. ISBN 978-3-540-28349-2. doi:10.1007/3-540-28349-8_2. (Cited on page 153.)

M. Bernier, M. Chamberland, J.-C. Houde, M. Descoteaux, and K. Whittingstall. Using fMRI non-local means denoising to uncover activation in sub-cortical structures at 1.5 T for guided HARDI tractography. *Frontiers in Human Neuroscience*, 8(715), 2014. doi:10.3389/fnhum.2014.00715. (Cited on page 99.)

M. A. Bernstein, K. F. King, and X. J. Zhou. *Handbook of MRI Pulse Sequences*. Elsevier Academic Press, San Diego, CA, 2004. ISBN 9780120928613. (Cited on pages 4, 5, 6, 8, 9, 10, 12, 22, 23, and 59.)

K. K. Bhatia and H. Lombaert, editors. *Machine Learning Meets Medical Imaging*, Image Processing, Computer Vision, Pattern Recognition, and Graphics, 2015. Springer International Publishing, Switzerland. ISBN 978-3-319-27928-2. doi:10.1007/978-3-319-27929-9. Proceedings of the first international workshop on Medical Learning Meets Medical Imaging (MLMMI) held on July 11, 2015, in Lille, France, in conjunction with the 32nd International Conference on Machine Learning (ICML). (Cited on page 160.)

C. Bhushan, J. P. Haldar, A. A. Joshi, and R. M. Leahy. Correcting susceptibility-induced distortion in diffusion-weighted MRI using constrained nonrigid registration. In *Asia-Pacific Signal Information Processing Association Annual Summit and Conference (APSIPA ASC), Hollywood, CA*, pages 1–9, 2012. URL http://ieeexplore.ieee.org/xpls/abs_all.jsp?arnumber=6412009. (Cited on pages 2, 3, 16, 20, 23, 52, 53, 67, and 146.)

C. Bhushan, A. A. Joshi, R. M. Leahy, and J. P. Haldar. Accelerating data acquisition for reversed-gradient distortion correction in diffusion MRI: A constrained reconstruction approach. In *21st Scientific Meeting of International Society for Magnetic Resonance in Medicine (ISMRM), Salt Lake City, Utah*, page 55, 2013. (Cited on pages 2, 18, 21, 22, 52, 58, 71, and 145.)

C. Bhushan, J. P. Haldar, A. A. Joshi, D. W. Shattuck, and R. M. Leahy. INVERSION: A robust method for co-registration of MPRAGE and diffusion MRI images. In *Joint Annual Meeting ISMRM-ESMRMB, Milan, Italy*, page 2583, 2014a. (Cited on pages 2, 25, and 146.)

C. Bhushan, A. A. Joshi, R. M. Leahy, and J. P. Haldar. Improved B_0-distortion correction in diffusion MRI using interlaced q-space sampling and constrained reconstruction. *Magnetic Resonance in Medicine*, 72(5): 1218–1232, 2014b. ISSN 1522-2594. doi:10.1002/mrm.25026. (Cited on pages 2, 16, 18, 21, 22, 52, 58, 62, 71, and 145.)

C. Bhushan, M. Chong, S. Choi, A. A. Joshi, J. P. Haldar, H. Damasio, and R. M. Leahy. Non-local means filtering reveals real-time whole-brain cortical interactions in resting fMRI. *USC-SIPI Technical Report*, page 423, 2015a. URL http://sipi.usc.edu/reports/abstracts.php?rid=sipi-423. (Cited on page 2.)

C. Bhushan, J. P. Haldar, S. Choi, A. A. Joshi, D. W. Shattuck, and R. M. Leahy. Co-registration and distortion correction of diffusion and anatomical images based on inverse contrast normalization. *NeuroImage*, 115:269 – 280, 2015b. ISSN 1053-8119. doi:10.1016/j.neuroimage.2015.03.050. (Cited on pages 2, 16, 20, 23, 25, and 146.)

C. Bhushan, M. Chong, S. Choi, A. A. Joshi, J. P. Haldar, H. Damasio, and R. M. Leahy. Non-local means filtering for cortical parcellation of resting fMRI. In *22nd Annual Meeting of the Organization for Human Brain Mapping (OHBM), Geneva, Switzerland*, page 2294, 2016. (Cited on page 2.)

B. Biswal. Resting-state functional connectivity. In A. W. Toga, editor, *Brain Mapping*, pages 581 – 585. Academic Press, 2015. ISBN 978-0-12-397316-0. doi:10.1016/B978-0-12-397025-1.00335-3. (Cited on pages 47, 48, and 49.)

B. Biswal, F. Zerrin Yetkin, V. M. Haughton, and J. S. Hyde. Functional connectivity in the motor cortex of resting human brain using echo-planar MRI. *Magnetic Resonance in Medicine*, 34(4):537–541, 1995. ISSN 1522-2594. doi:10.1002/mrm.1910340409. (Cited on pages 49 and 97.)

S. Bludau, S. B. Eickhoff, H. Mohlberg, S. Caspers, A. R. Laird, P. T. Fox, A. Schleicher, K. Zilles, and K. Amunts. Cytoarchitecture, probability maps and functions of the human frontal pole. *NeuroImage*, 93, Part 2:260 – 275, 2014. ISSN 1053-8119. doi:10.1016/j.neuroimage.2013.05.052. (Cited on page 38.)

T. Blumensath, S. Jbabdi, M. F. Glasser, D. C. Van Essen, K. Ugurbil, T. E. Behrens, and S. M. Smith. Spatially constrained hierarchical parcellation of the brain with resting-state fMRI. *NeuroImage*, 76(0):313 – 324, 2013. ISSN 1053-8119. doi:10.1016/j.neuroimage.2013.03.024. (Cited on pages 49, 97, 100, 102, 121, and 122.)

R. Bowtell, D. McIntyre, M. Commandre, P. Glover, and P. Mansfield. Correction of geometric distortion in echo planar images. In *Proceedings of the Society of Magnetic Resonance, San Francisco*, page 411, 1994. (Cited on pages 16, 21, 22, and 58.)

M. Brant-Zawadzki, G. D. Gillan, and W. R. Nitz. Mp rage: A three-dimensional, T1-weighted, gradient-echo sequence–initial experience in the brain. *Radiology*, 182(3):769–775, 1992. doi:10.1148/radiology.182.3.1535892. URL http://dx.doi.org/10.1148/radiology.182.3.1535892. (Cited on page 35.)

M. Brett, I. S. Johnsrude, and A. M. Owen. The problem of functional localization in the human brain. *Nature Reviews Neuroscience*, 3(3):243–249, Mar 2002. ISSN 1471-003X. doi:10.1038/nrn756. (Cited on pages 35 and 37.)

H. Bridge, S. Clare, M. Jenkinson, P. Jezzard, A. J. Parker, and P. M. Matthews. Independent anatomical and functional measures of the V1/V2 boundary in human visual cortex. *Journal of Vision*, 5(2):1, 2005. doi:10.1167/5.2.1. (Cited on page 39.)

K. Brodmann. *Vergleichende Lokalisationslehre der Großhirnrinde in ihren Prinzipien dargestellt auf Grund des Zellenbaues*. Johann Ambrosius Barth, Leipzig, 1909. (Cited on pages 32, 33, 46, and 154.)

K. Brodmann. *Brodmann's Localisation in the Cerebral Cortex*. Springer US, 2006. ISBN 978-0-387-26917-7. doi:10.1007/b138298. Translated by Laurence J. Garey. (Cited on pages 32 and 33.)

R. W. Brown, Y.-C. N. Cheng, E. M. Haacke, M. R. Thompson, and R. Venkatesan. Segmented k-space and Echo Planar Imaging. In *Magnetic Resonance Imaging: Physical Principles and Sequence Design*, pages 511–567. John Wiley & Sons, Inc., Hoboken, New Jersey, 2014a. ISBN 9781118633953. doi:10.1002/9781118633953.ch19. (Cited on pages 6, 9, and 12.)

R. W. Brown, Y.-C. N. Cheng, E. M. Haacke, M. R. Thompson, and R. Venkatesan. Magnetic field inhomogeneity effects and T_2^* dephasing. In *Magnetic Resonance Imaging: Physical Principles and Sequence Design*, pages 569–617. John Wiley & Sons, Inc., Hoboken, New Jersey, 2014b. ISBN 9781118633953. doi:10.1002/9781118633953.ch20. (Cited on pages 13, 14, 22, 23, and 59.)

R. W. Brown, Y.-C. N. Cheng, E. M. Haacke, M. R. Thompson, and R. Venkatesan. *Magnetic Resonance Imaging: Physical Principles and Sequence Design*. John Wiley & Sons, Inc., Hoboken, New Jersey, second edition, 2014c. ISBN 978-0-471-72085-0. doi:10.1002/9781118633953. (Cited on pages 4, 9, 11, and 13.)

A. Buades, B. Coll, and J.-M. Morel. A non-local algorithm for image denoising. In *IEEE Computer Society Conference on Computer Vision and Pattern Recognition*, volume 2, pages 60–65, June 2005. doi:10.1109/CVPR.2005.38. (Cited on pages 99, 100, and 159.)

R. L. Buckner and J. L. Vincent. Unrest at rest: Default activity and spontaneous network correlations. *NeuroImage*, 37:1091–1096, 2007. doi:10.1016/j.neuroimage.2007.01.010. (Cited on pages 107 and 120.)

R. L. Buckner, J. R. Andrews-Hanna, and D. L. Schacter. The brain's default network. *Annals of the New York Academy of Sciences*, 1124(1):1–38, 2008. ISSN 1749-6632. doi:10.1196/annals.1440.011. (Cited on pages 98, 101, and 111.)

M. H. Buonocore and L. Gao. Ghost artifact reduction for echo planar imaging using image phase correction. *Magnetic Resonance in Medicine*, 38(1):89–100, 1997. ISSN 1522-2594. doi:10.1002/mrm.1910380114. (Cited on page 9.)

M. H. Buonocore and D. C. Zhu. Image-based ghost correction for interleaved EPI. *Magnetic Resonance in Medicine*, 45(1):96–108, 2001. ISSN 1522-2594. doi:10.1002/1522-2594(200101)45:1<96::AID-MRM1014>3.0.CO;2-J. (Cited on page 9.)

D. Bzdok, A. R. Laird, K. Zilles, P. T. Fox, and S. B. Eickhoff. An investigation of the structural, connectional, and functional subspecialization in the human amygdala. *Human brain mapping*, 34(12):3247–3266, 2013. (Cited on pages 48 and 49.)

V. D. Calhoun, J. Liu, and T. Adali. A review of group ICA for fmri data and ICA for joint inference of imaging, genetic, and ERP data. *NeuroImage*, 45(1):S163 – S172, 2009. ISSN 1053-8119. doi:10.1016/j.neuroimage.2008.10.057. (Cited on page 49.)

E. Caruyer, C. Lenglet, G. Sapiro, and R. Deriche. Design of multishell sampling schemes with uniform coverage in diffusion MRI. *Magnetic Resonance in Medicine*, 69(6):1534–1540, 2013. ISSN 1522-2594. doi:10.1002/mrm.24736. (Cited on pages 80 and 91.)

S. Caspers, S. B. Eickhoff, K. Zilles, and K. Amunts. Microstructural grey matter parcellation and its relevance for connectome analyses. *NeuroImage*, 80:18 – 26, 2013. ISSN 1053-8119. doi:10.1016/j.neuroimage.2013.04.003. (Cited on pages 37 and 38.)

M. C. Chambers, C. Bhushan, J. P. Haldar, R. M. Leahy, and D. W. Shattuck. Correcting inhomogeneity-induced distortion in fMRI using non-rigid registration. In *IEEE International Symposium on Biomedical Imaging, New York City, USA*, pages 1364–1367, April 2015. doi:10.1109/ISBI.2015.7164129. (Cited on page 97.)

H. Chang and J. M. Fitzpatrick. A technique for accurate magnetic resonance imaging in the presence of field inhomogeneities. *IEEE Transactions on Medical Imaging*, 11(3):319–329, sep 1992. ISSN 0278-0062. doi:10.1109/42.158935. (Cited on pages 14, 16, 20, 21, 58, 74, and 76.)

W. Chen and G. Feng. Spectral clustering: A semi-supervised approach. *Neurocomputing*, 77(1):229 – 242, 2012. ISSN 0925-2312. doi:10.1016/j.neucom.2011.09.002. (Cited on page 158.)

K. Choi, A. R. Franco, P. E. Holtzheimer, H. S. Mayberg, and X. P. Hu. Diffusion tensor imaging distortion correction with T1. In *International Society for Magnetic Resonance in Medicine (ISMRM), Montréal, Québec, Canada*, page 1946, 2011. (Cited on page 56.)

M. Chong, A. A. Joshi, J. P. Haldar, E. DuPre, W.-M. Luh, D. W. Shattuck, R. N. Spreng, and R. M. Leahy. A group approach to functional cortical parcellation from resting-state fMRI. In *21st Annual Meeting of the Organization for Human Brain Mapping (OHBM), Honolulu, Hawaii*, page 3778, 2015. (Cited on pages 48 and 49.)

M. Chong, C. Bhushan, A. A. Joshi, J. P. Haldar, R. N. Spreng, and R. M. Leahy. Individual performance of resting fMRI parcellation with group connectivity priors. In *22nd Annual Meeting of the Organization for Human Brain Mapping (OHBM), Geneva, Switzerland*, page 4440, 2016. (Cited on pages 48 and 49.)

G. E. Christensen, S. C. Joshi, and M. I. Miller. Volumetric transformation of brain anatomy. *IEEE Transactions on Medical Imaging*, 16(6):864–877, Dec 1997. ISSN 0278-0062. doi:10.1109/42.650882. (Cited on page 35.)

S. Y. Chun and J. A. Fessler. A simple regularizer for B-spline nonrigid image registration that encourages local invertibility. *IEEE Journal of Selected Topics in Signal Processing*, 3(1):159–169, 2009. ISSN 1932-4553. doi:10.1109/JSTSP.2008.2011116. (Cited on page 60.)

J.-Y. Chung, M.-H. In, S.-H. Oh, M. Zaitsev, O. Speck, and Z.-H. Cho. An improved PSF mapping method for EPI distortion correction in human brain at ultra high field (7T). *Magnetic Resonance Materials in Physics, Biology and Medicine*, 24(3):179–190, 2011. ISSN 0968-5243. doi:10.1007/s10334-011-0251-1. (Cited on page 25.)

S. Clare and H. Bridge. Methodological issues relating to in vivo cortical myelography using MRI. *Human Brain Mapping*, 26(4):240–250, 2005. doi:10.1002/hbm.20162. (Cited on page 39.)

V. P. Clark, E. Courchesne, and M. Grafe. In vivo myeloarchitectonic analysis of human striate and extrastriate cortex using magnetic resonance imaging. *Cerebral Cortex*, 2(5):417–424, 1992. doi:10.1093/cercor/2.5.417. (Cited on page 39.)

E. Clarke and K. Dewhurst. The genesis of cortical localization. In *An Illustrated History of Brain Function: Imaging the Brain from Antiquity to the Present*, Norman Neurosciences Series, pages 115–127. Jeremy Norman Co., second edition, 1995. (Cited on page 33.)

M. J. Clarkson, I. Malone, M. Modat, K. Leung, N. Ryan, D. Alexander, N. C. Fox, and S. Ourselin. A framework for using diffusion weighted imaging to improve cortical parcellation. In T. Jiang, N. Navab, J. Pluim, and M. Viergever, editors, *Medical Image Computing and Computer-Assisted Intervention (MICCAI)*, volume 6361

of *Lecture Notes in Computer Science*, pages 534–541. Springer Berlin Heidelberg, 2010. ISBN 978-3-642-15704-2. doi:10.1007/978-3-642-15705-9_65. (Cited on page 35.)

L. L. Cloutman and M. A. Lambon Ralph. Connectivity-based structural and functional parcellation of the human cortex using diffusion imaging and tractography. *Frontiers in Neuroanatomy*, 6(34), 2012. ISSN 1662-5129. doi:10.3389/fnana.2012.00034. (Cited on pages 47, 48, and 49.)

C. A. Cocosco, V. Kollokian, R. K.-S. Kwan, G. B. Pike, and A. C. Evans. BrainWeb: Online interface to a 3D MRI simulated brain database. In *NeuroImage, Proceedings of 3rd International Conference on Functional Mapping of the Human Brain, Copenhagen*, volume 5, page S425, 1997. (Cited on page 61.)

A. L. Cohen, D. A. Fair, N. U. F. Dosenbach, F. M. Miezin, D. Dierker, D. C. Van Essen, B. L. Schlaggar, and S. E. Petersen. Defining functional areas in individual human brains using resting functional connectivity MRI. *NeuroImage*, 41(1):45 – 57, 2008. ISSN 1053-8119. doi:10.1016/j.neuroimage.2008.01.066. (Cited on pages 47 and 48.)

M. S. Cohen and F. Schmitt. Echo planar imaging before and after fMRI: A personal history. *NeuroImage*, 62(2): 652 – 659, 2012. ISSN 1053-8119. doi:10.1016/j.neuroimage.2012.01.038. (Cited on page 6.)

J. Cohen-Adad. What can we learn from T_2* maps of the cortex? *NeuroImage*, 93, Part 2:189 – 200, 2014. ISSN 1053-8119. doi:10.1016/j.neuroimage.2013.01.023. (Cited on pages 39, 40, and 144.)

J. Cohen-Adad, J. Polimeni, K. Helmer, T. Benner, J. McNab, L. Wald, B. Rosen, and C. Mainero. T2* mapping and B_0 orientation-dependence at 7 T reveal cyto- and myeloarchitecture organization of the human cortex. *NeuroImage*, 60(2):1006 – 1014, 2012. ISSN 1053-8119. doi:10.1016/j.neuroimage.2012.01.053. (Cited on pages 39, 40, and 144.)

D. L. Collins. *3D Model-based segmentation of individual brain structures from magnetic resonance imaging data*. PhD thesis, Department of Biomedical Engineering, McGill University, Montreal, 1994. (Cited on page 35.)

D. L. Collins, C. J. Holmes, T. M. Peters, and A. C. Evans. Automatic 3-D model-based neuroanatomical segmentation. *Human Brain Mapping*, 3(3):190–208, 1995. ISSN 1097-0193. doi:10.1002/hbm.460030304. (Cited on page 35.)

P. Coupé, P. Yger, S. Prima, P. Hellier, C. Kervrann, and C. Barillot. An optimized blockwise nonlocal means denoising filter for 3-D magnetic resonance images. *IEEE Transactions on Medical Imaging*, 27(4):425–441, April 2008. ISSN 0278-0062. doi:10.1109/TMI.2007.906087. (Cited on page 99.)

R. C. Craddock, G. A. James, P. E. Holtzheimer, X. P. Hu, and H. S. Mayberg. A whole brain fMRI atlas generated via spatially constrained spectral clustering. *Human Brain Mapping*, 33(8):1914–1928, 2012. ISSN 1097-0193. doi:10.1002/hbm.21333. (Cited on pages 49, 97, 100, 102, and 121.)

R. C. Craddock, S. Jbabdi, C.-G. Yan, J. T. Vogelstein, F. X. Castellanos, A. Di Martino, C. Kelly, K. Heberlein, S. Colcombe, and M. P. Milham. Imaging human connectomes at the macroscale. *Nature Methods*, 10:524–539, 2013. doi:10.1038/nmeth.2482. (Cited on page 49.)

J. Dagher, T. Reese, and A. Bilgin. High-resolution, large dynamic range field map estimation. *Magnetic Resonance in Medicine*, 71(1):105–117, 2014. ISSN 1522-2594. doi:10.1002/mrm.24636. (Cited on page 14.)

A. M. Dale, B. Fischl, and M. I. Sereno. Cortical surface-based analysis: I. segmentation and surface reconstruction. *NeuroImage*, 9(2):179 – 194, 1999. ISSN 1053-8119. doi:10.1006/nimg.1998.0395. (Cited on pages 35 and 36.)

H. Damasio. *Human Brain Anatomy in Computerized Images*. Oxford University Press, second edition, 2005. ISBN 9780195165616. (Cited on page 35.)

H. Damasio and A. R. Damasio. *Lesion analysis in neuropsychology*. Oxford University Press, USA, 1989. ISBN 978-0195039191. (Cited on page 37.)

F. De Martino, J. Xu, M. Glasser, D. Van Essen, P.-F. van de Moortele, R. Goebel, E. Formisano, K. Ugurbil, and E. Yacoub. Enhanced mylein-related contrast across the human brain at 7T using the ratio of high resolution T1 and T2* weighted images. In *Scientific Meeeting of International Society of Magnetic Resonance in Medicine (ISMRM), Melbourne, Australia*, page 1072, 2012. (Cited on page 41.)

F. De Martino, M. Moerel, J. Xu, P.-F. van de Moortele, K. Ugurbil, R. Goebel, E. Yacoub, and E. Formisano. High-resolution mapping of myeloarchitecture in vivo: Localization of auditory areas in the human brain. *Cerebral Cortex*, 25(10):3394–3405, 2015. doi:10.1093/cercor/bhu150. (Cited on page 41.)

M. A. de Reus and M. P. van den Heuvel. The parcellation-based connectome: Limitations and extensions. *NeuroImage*, 80:397 – 404, 2013. ISSN 1053-8119. doi:10.1016/j.neuroimage.2013.03.053. (Cited on pages 47 and 50.)

J. DeFelipe, L. Alonso-Nanclares, and J. I. Arellano. Microstructure of the neocortex: Comparative aspects. *Journal of Neurocytology*, 31(3):299–316, 2002. ISSN 1573-7381. doi:10.1023/A:1024130211265. (Cited on page 41.)

A. R. Deipolyi, P. Mukherjee, K. Gill, R. G. Henry, S. C. Partridge, S. Veeraraghavan, H. Jin, Y. Lu, S. P. Miller, D. M. Ferriero, D. B. Vigneron, and A. J. Barkovich. Comparing microstructural and macrostructural development of the cerebral cortex in premature newborns: Diffusion tensor imaging versus cortical gyration. *NeuroImage*, 27(3):579 – 586, 2005. doi:10.1016/j.neuroimage.2005.04.027. (Cited on page 43.)

A. Deistung, A. Schäfer, F. Schweser, U. Biedermann, R. Turner, and J. R. Reichenbach. Toward in vivo histology: A comparison of quantitative susceptibility mapping (QSM) with magnitude-, phase-, and r_2*-imaging at ultra-high magnetic field strength. *NeuroImage*, 65:299 – 314, 2013. ISSN 1053-8119. doi:10.1016/j.neuroimage.2012.09.055. (Cited on page 39.)

M. H. Derek L. G. Hill, Philipp G. Batchelor and D. J. Hawkes. Medical image registration. *Physics in Medicine and Biology*, 46(3):R1–R45, 2001. doi:10.1088/0031-9155/46/3/201. (Cited on pages 36, 51, 53, 54, 55, 58, 60, and 67.)

M. Descoteaux, E. Angelino, S. Fitzgibbons, and R. Deriche. Regularized, fast, and robust analytical Q-ball imaging. *Magnetic Resonance in Medicine*, 58(3):497–510, 2007. ISSN 1522-2594. doi:10.1002/mrm.21277. (Cited on pages 46, 76, 78, 93, and 94.)

A. Deshmane, V. Gulani, M. A. Griswold, and N. Seiberlich. Parallel MR imaging. *Journal of Magnetic Resonance Imaging*, 36(1):55–72, 2012. ISSN 1522-2586. doi:10.1002/jmri.23639. (Cited on page 25.)

R. S. Desikan, F. Ségonne, B. Fischl, B. T. Quinn, B. C. Dickerson, D. Blacker, R. L. Buckner, A. M. Dale, R. P. Maguire, B. T. Hyman, M. S. Albert, and R. J. Killiany. An automated labeling system for subdividing the human cerebral cortex on MRI scans into gyral based regions of interest. *NeuroImage*, 31(3):968 – 980, 2006. ISSN 1053-8119. doi:10.1016/j.neuroimage.2006.01.021. (Cited on page 35.)

R. O. Duda, P. E. Hart, and D. G. Stork. *Pattern Classification*, volume 10. John Wiley and Sons, Inc., New York, 2001. (Cited on page 54.)

J. Dudink, K. Pieterman, A. Leemans, M. Kleinnijenhuis, A.-M. van Cappellen van Walsum, and F. Hoebeek. Recent advancements in diffusion MRI for investigating cortical development after preterm birth – potential and pitfalls. *Frontiers in Human Neuroscience*, 8(1066), 2015. doi:10.3389/fnhum.2014.01066. (Cited on page 43.)

J. Dutta, R. M. Leahy, and Q. Li. Non-local means denoising of dynamic PET images. *PLoS ONE*, 8(12):e81390, 12 2013. doi:10.1371/journal.pone.0081390. (Cited on page 99.)

T. Duval, J. A. McNab, K. Setsompop, T. Witzel, T. Schneider, S. Y. Huang, B. Keil, E. Klawiter, L. L. Wald, and J. Cohen-Adad. In vivo estimation of axon diameter in the human spinal cord using 300 mT/m gradients. In *Joint Annual Meeting ISMRM-ESMRMB, Milan, Italy*, page 5005, 2014. (Cited on page 46.)

J. H. Duyn, P. van Gelderen, T.-Q. Li, J. A. de Zwart, A. P. Koretsky, and M. Fukunaga. High-field MRI of brain cortical substructure based on signal phase. *Proceedings of the National Academy of Sciences*, 104(28): 11796–11801, 2007. doi:10.1073/pnas.0610821104. (Cited on page 39.)

J. C. Ehrhardt, C.-S. Lin, V. A. Magnotta, D. J. Fisher, and W. T. C. Yuh. Peripheral nerve stimulation in a whole-body echo-planar imaging system. *Journal of Magnetic Resonance Imaging*, 7(2):405–409, 1997. ISSN 1522-2586. doi:10.1002/jmri.1880070226. (Cited on page 90.)

S. Eickhoff, N. B. Walters, A. Schleicher, J. Kril, G. F. Egan, K. Zilles, J. D. Watson, and K. Amunts. High-resolution MRI reflects myeloarchitecture and cytoarchitecture of human cerebral cortex. *Human Brain Mapping*, 24(3):206 – 215, 2005. ISSN 1097-0193. doi:10.1002/hbm.20082. (Cited on pages 38 and 40.)

S. B. Eickhoff and V. I. Müller. Functional connectivity. In A. W. Toga, editor, *Brain Mapping*, pages 187 – 201. Academic Press, 2015. ISBN 978-0-12-397316-0. doi:10.1016/B978-0-12-397025-1.00212-8. (Cited on pages 47, 48, and 49.)

S. B. Eickhoff, D. Bzdok, A. R. Laird, C. Roski, S. Caspers, K. Zilles, and P. T. Fox. Co-activation patterns distinguish cortical modules, their connectivity and functional differentiation. *NeuroImage*, 57(3):938 – 949, 2011. ISSN 1053-8119. doi:10.1016/j.neuroimage.2011.05.021. (Cited on page 49.)

S. B. Eickhoff, B. Thirion, G. Varoquaux, and D. Bzdok. Connectivity-based parcellation: Critique and implications. *Human Brain Mapping*, 36(12):4771–4792, 2015. doi:10.1002/hbm.22933. (Cited on pages 47, 48, 49, and 50.)

G. N. Elston and L. J. Garey. The cytoarchitectonic map of Korbinian Brodmann: Arealisation and circuit specialisation. In S. Geyer and R. Turner, editors, *Microstructural Parcellation of the Human Cerebral Cortex*, pages 3–32. Springer Berlin Heidelberg, 2013. ISBN 978-3-642-37824-9. doi:10.1007/978-3-642-37824-9_1. URL http://link.springer.com/chapter/10.1007/978-3-642-37824-9_1. (Cited on pages 31 and 32.)

K. V. Embleton, H. A. Haroon, D. M. Morris, M. A. L. Ralph, and G. J. Parker. Distortion correction for diffusion-weighted MRI tractography and fMRI in the temporal lobes. *Human Brain Mapping*, 31(10):1570–1587, 2010. ISSN 1097-0193. doi:10.1002/hbm.20959. (Cited on page 21.)

E. B. Erhardt, S. Rachakonda, E. J. Bedrick, E. A. Allen, T. Adali, and V. D. Calhoun. Comparison of multi-subject ICA methods for analysis of fMRI data. *Human Brain Mapping*, 32(12):2075–2095, 2011. ISSN 1097-0193. doi:10.1002/hbm.21170. (Cited on page 49.)

V. Estivill-Castro. Why so many clustering algorithms: A position paper. *ACM SIGKDD explorations newsletter*, 4(1):65–75, 2002. ISSN 1931-0145. doi:10.1145/568574.568575. (Cited on page 153.)

A. C. Evans, D. L. Collins, and B. Milner. An MRI-based stereotactic atlas from 250 young normal subjects. In *Journal of Social Neuroscience*, volume 18, pages 408–492, 1992. (Cited on page 35.)

A. C. Evans, D. L. Collins, S. R. Mills, E. D. Brown, R. L. Kelly, and T. M. Peters. 3D statistical neuroanatomical models from 305 MRI volumes. In *Nuclear Science Symposium and Medical Imaging Conference*, volume 3, pages 1813–1817, Oct 1993. doi:10.1109/NSSMIC.1993.373602. (Cited on page 35.)

J. Fessler, S. Lee, V. Olafsson, H. Shi, and D. Noll. Toeplitz-based iterative image reconstruction for MRI with correction for magnetic field inhomogeneity. *IEEE Transactions on Signal Processing*, 53(9):3393–3402, 2005. ISSN 1053-587X. doi:10.1109/TSP.2005.853152. (Cited on page 79.)

A. G. Filler. The history, development and impact of computed imaging in neurological diagnosis and neurosurgery: CT, MRI, and DTI. *Nature precedings*, 7(1):1–69, 2009. doi:10.1038/npre.2009.3267.5. (Cited on page 34.)

H. Fischer and R. Ladebeck. Echo-planar imaging image artifacts. In *Echo-Planar Imaging - Theory, technique and applications*, pages 179–200. Springer-Verlag Berlin Heidelberg, 1998. ISBN 978-3-642-80445-8. doi:10.1007/978-3-642-80443-4_6. (Cited on pages 6, 7, 9, 10, 11, 12, 13, 14, 16, and 26.)

B. Fischl. FreeSurfer. *NeuroImage*, 62(2):774 – 781, 2012. ISSN 1053-8119. doi:10.1016/j.neuroimage.2012.01.021. (Cited on pages 35, 36, 51, and 52.)

B. Fischl. Estimating the location of Brodmann areas from cortical folding patterns using histology and ex vivo MRI. In S. Geyer and R. Turner, editors, *Microstructural Parcellation of the Human Cerebral Cortex*, pages

129–156. Springer Berlin Heidelberg, 2013. ISBN 978-3-642-37823-2. doi:10.1007/978-3-642-37824-9_4. URL http://link.springer.com/chapter/10.1007/978-3-642-37824-9_4. (Cited on pages 35, 37, 38, and 39.)

B. Fischl, M. I. Sereno, R. B. Tootell, and A. M. Dale. High-resolution intersubject averaging and a coordinate system for the cortical surface. *Human Brain Mapping*, 8(4):272–284, 1999. ISSN 1097-0193. doi:10.1002/(SICI)1097-0193(1999)8:4<272::AID-HBM10>3.0.CO;2-4. (Cited on page 36.)

B. Fischl, D. H. Salat, E. Busa, M. Albert, M. Dieterich, C. Haselgrove, A. van der Kouwe, R. Killiany, D. Kennedy, S. Klaveness, A. Montillo, N. Makris, B. Rosen, and A. M. Dale. Whole brain segmentation: Automated labeling of neuroanatomical structures in the human brain. *Neuron*, 33(3):341 – 355, 2002. ISSN 0896-6273. doi:10.1016/S0896-6273(02)00569-X. (Cited on page 35.)

B. Fischl, A. van der Kouwe, C. Destrieux, E. Halgren, F. Ségonne, D. H. Salat, E. Busa, L. J. Seidman, J. Goldstein, D. Kennedy, V. Caviness, N. Makris, B. Rosen, and A. M. Dale. Automatically parcellating the human cerebral cortex. *Cerebral Cortex*, 14(1):11–22, 2004. doi:10.1093/cercor/bhg087. (Cited on pages 35, 36, 51, and 52.)

B. Fischl, N. Rajendran, E. Busa, J. Augustinack, O. Hinds, B. T. Yeo, H. Mohlberg, K. Amunts, and K. Zilles. Cortical folding patterns and predicting cytoarchitecture. *Cerebral Cortex*, 18(8):1973–1980, 2008. doi:10.1093/cercor/bhm225. (Cited on pages 35, 37, 38, and 106.)

M. D. Fox, A. Z. Snyder, J. L. Vincent, M. Corbetta, D. C. Van Essen, and M. E. Raichle. The human brain is intrinsically organized into dynamic, anticorrelated functional networks. *Proceedings of the National Academy of Sciences of the United States of America*, 102(27):9673–9678, 2005. doi:10.1073/pnas.0504136102. (Cited on pages 98 and 111.)

M. D. Fox, M. Corbetta, A. Z. Snyder, J. L. Vincent, and M. E. Raichle. Spontaneous neuronal activity distinguishes human dorsal and ventral attention systems. *Proceedings of the National Academy of Sciences*, 103(26):10046–10051, 2006. doi:10.1073/pnas.0604187103. (Cited on pages 111 and 121.)

P. Fransson. Spontaneous low-frequency BOLD signal fluctuations: An fMRI investigation of the resting-state default mode of brain function hypothesis. *Human Brain Mapping*, 26(1):15–29, 2005. ISSN 1097-0193. doi:10.1002/hbm.20113. (Cited on pages 98 and 111.)

K. J. Friston, J. Ashburner, C. D. Frith, J.-B. Poline, J. D. Heather, and R. S. J. Frackowiak. Spatial registration and normalization of images. *Human Brain Mapping*, 3(3):165–189, 1995. ISSN 1097-0193. doi:10.1002/hbm.460030303. (Cited on pages 35, 36, and 56.)

A. K. Funai, J. A. Fessler, D. T. B. Yeo, V. T. Olafsson, and D. C. Noll. Regularized field map estimation in MRI. *IEEE Transactions on Medical Imaging*, 27(10):1484–1494, Oct 2008. ISSN 0278-0062. doi:10.1109/TMI.2008.923956. (Cited on page 14.)

J. Gai, N. Obeid, J. L. Holtrop, X.-L. Wu, F. Lam, M. Fu, J. P. Haldar, W. mei W. Hwu, Z.-P. Liang, and B. P. Sutton. More IMPATIENT: A gridding-accelerated Toeplitz-based strategy for non-Cartesian high-resolution

3D MRI on GPUs. *Journal of Parallel and Distributed Computing*, 73(5):686–697, 2013. ISSN 0743-7315. doi:10.1016/j.jpdc.2013.01.001. (Cited on pages 19, 61, and 79.)

D. Gale and L. S. Shapley. College admissions and the stability of marriage. *The American Mathematical Monthly*, 69(1):9–15, Jan 1962. doi:10.2307/2312726. (Cited on pages 105, 124, and 125.)

D. Gallichan, J. L. R. Andersson, M. Jenkinson, M. D. Robson, and K. L. Miller. Reducing distortions in diffusion-weighted echo planar imaging with a dual-echo blip-reversed sequence. *Magnetic Resonance in Medicine*, 64 (2):382–390, 2010. ISSN 1522-2594. doi:10.1002/mrm.22318. (Cited on pages 21, 22, 52, 58, 71, and 92.)

M. Ganzetti, N. Wenderoth, and D. Mantini. Whole brain myelin mapping using T1- and T2-weighted MR imaging data. *Frontiers in Human Neuroscience*, 8(671), 2014. ISSN 1662-5161. doi:10.3389/fnhum.2014.00671. (Cited on pages 39 and 41.)

M. Ganzetti, N. Wenderoth, and D. Mantini. Mapping pathological changes in brain structure by combining T1- and T2-weighted mr imaging data. *Neuroradiology*, 57(9):917–928, 2015. ISSN 1432-1920. doi:10.1007/s00234-015-1550-4. (Cited on page 41.)

S. Geyer. High-field magnetic resonance mapping of the border between primary motor (area 4) and somatosensory (area 3a) cortex in ex-vivo and in-vivo human brains. In S. Geyer and R. Turner, editors, *Microstructural Parcellation of the Human Cerebral Cortex*, pages 239–254. Springer Berlin Heidelberg, 2013. ISBN 978-3-642-37823-2. doi:10.1007/978-3-642-37824-9_9. URL http://link.springer.com/chapter/10.1007/978-3-642-37824-9_9. (Cited on pages 34, 37, 38, 39, 40, 144, and 158.)

S. Geyer and R. Turner, editors. *Microstructural Parcellation of the Human Cerebral Cortex: From Brodmann's Post-Mortem Map to in Vivo Mapping with High-Field Magnetic Resonance Imaging*. Springer Berlin Heidelberg, 2013. ISBN 978-3-642-37824-9. doi:10.1007/978-3-642-37824-9. (Cited on pages 31, 32, 33, 34, 38, and 154.)

S. Geyer, A. Schleicher, and K. Zilles. Areas 3a, 3b, and 1 of human primary somatosensory cortex: 1. microstructural organization and interindividual variability. *NeuroImage*, 10(1):63 – 83, 1999. ISSN 1053-8119. doi:10.1006/nimg.1999.0440. (Cited on page 37.)

S. Geyer, T. Schormann, H. Mohlberg, and K. Zilles. Areas 3a, 3b, and 1 of human primary somatosensory cortex: 2. spatial normalization to standard anatomical space. *NeuroImage*, 11(6):684 – 696, 2000. ISSN 1053-8119. doi:10.1006/nimg.2000.0548. (Cited on page 37.)

S. Geyer, M. Weiss, K. Reimann, G. Lohmann, and R. Turner. Microstructural parcellation of the human cerebral cortex - from Brodmann's post-mortem map to *in vivo* mapping with high-field magnetic resonance imaging. *Frontiers in Human Neuroscience*, 5(19), 2011. doi:10.3389/fnhum.2011.00019. (Cited on pages 32, 33, 37, 38, 39, and 40.)

A. Gholipour, N. Kehtarnavaz, K. Gopinath, R. Briggs, M. Devous, and R. Haley. Distortion correction via non-rigid registration of functional to anatomical magnetic resonance brain images. In *IEEE International*

Conference on Image Processing, pages 1181–1184, 2006. doi:10.1109/ICIP.2006.312768. (Cited on pages 23, 52, 53, and 67.)

J. D. Gibbons and S. Chakraborti. *Nonparametric Statistical Inference*. Statistics: Textbooks and Monographs. Marcel Dekker, Inc. New York, Fourth edition, 2003. ISBN 0-8247-4052-1. (Cited on page 116.)

M. F. Glasser and D. C. Van Essen. Mapping human cortical areas in vivo based on myelin content as revealed by T1- and T2-weighted MRI. *The Journal of Neuroscience*, 31(32):11597 – 11616, 2011. doi:10.1523/JNEUROSCI.2180-11.2011. (Cited on pages 41, 147, and 151.)

M. F. Glasser, S. N. Sotiropoulos, J. A. Wilson, T. S. Coalson, B. Fischl, J. L. Andersson, J. Xu, S. Jbabdi, M. Webster, J. R. Polimeni, D. C. Van Essen, and M. Jenkinson. The minimal preprocessing pipelines for the Human Connectome Project. *NeuroImage*, 80:105–124, 2013. ISSN 1053-8119. doi:10.1016/j.neuroimage.2013.04.127. (Cited on pages 97, 103, and 121.)

M. F. Glasser, M. S. Goyal, T. M. Preuss, M. E. Raichle, and D. C. V. Essen. Trends and properties of human cerebral cortex: Correlations with cortical myelin content. *NeuroImage*, 93, Part 2:165 – 175, 2014. ISSN 1053-8119. doi:10.1016/j.neuroimage.2013.03.060. (Cited on page 41.)

J. Glaunès, M. Vaillant, and M. I. Miller. Landmark matching via large deformation diffeomorphisms on the sphere. *Journal of Mathematical Imaging and Vision*, 20(1):179–200, 2004. ISSN 1573-7683. doi:10.1023/B:JMIV.0000011323.32914.f3. (Cited on page 36.)

R. Goebel, F. Esposito, and E. Formisano. Analysis of functional image analysis contest (FIAC) data with brainvoyager QX: From single-subject to cortically aligned group general linear model analysis and self-organizing group independent component analysis. *Human brain mapping*, 27(5):392–401, 2006. doi:10.1002/hbm.20249. (Cited on page 36.)

G. Golub and V. Pereyra. Separable nonlinear least squares: the variable projection method and its applications. *Inverse Problems*, 19(2):R1, 2003. doi:10.1088/0266-5611/19/2/201. (Cited on page 146.)

G. H. Golub and V. Pereyra. The differentiation of pseudo-inverses and nonlinear least squares problems whose variables separate. *SIAM Journal on Numerical Analysis*, 10(2):413–432, 1973. doi:10.1137/0710036. (Cited on page 146.)

R. C. Gonzalez and R. E. Woods. *Digital Image Processing*. Prentice-Hall Inc., Upper Saddle River, New Jersey, 2002. (Cited on page 56.)

D. N. Greve and B. Fischl. Accurate and robust brain image alignment using boundary-based registration. *NeuroImage*, 48(1):63–72, 2009. ISSN 1053-8119. doi:10.1016/j.neuroimage.2009.06.060. (Cited on page 65.)

A. Guimond, A. Roche, N. Ayache, and J. Meunier. Three-dimensional multimodal brain warping using the demons algorithm and adaptive intensity corrections. *IEEE Transactions on Medical Imaging*, 20(1):58–69, Jan 2001. ISSN 0278-0062. doi:10.1109/42.906425. (Cited on pages 56 and 57.)

S. Guleria and T. G. Kelly. Myelin, myelination, and corresponding magnetic resonance imaging changes. *Radiologic Clinics of North America*, 52(2):227 – 239, 2014. ISSN 0033-8389. doi:10.1016/j.rcl.2013.11.009. Imaging of White Matter Lesions. (Cited on page 41.)

E. M. Haacke, R. W. Brown, M. R. Thompson, and R. Venkatesan. *Magnetic Resonance Imaging: Physical Principles and Sequence Design*. John Wiley & Sons, Inc., New York, first edition, 1999. ISBN 978-0-471-35128-3. (Cited on pages 5, 6, 9, 11, 12, 13, and 17.)

J. P. Haldar. *Constrained Imaging: Denoising and Sparse Sampling*. PhD thesis, University of Illinois at Urbana-Champaign, 2011. URL http://hdl.handle.net/2142/24286. (Cited on page 7.)

J. P. Haldar and R. M. Leahy. New linear transforms for data on a Fourier 2-sphere with application to diffusion MRI. In *IEEE International Symposium on Biomedical Imaging, 2012*, 2012. (Cited on page 46.)

J. P. Haldar and R. M. Leahy. Linear transforms for fourier data on the sphere: Application to high angular resolution diffusion MRI of the brain. *NeuroImage*, 71(0):233 – 247, 2013. ISSN 1053-8119. doi:10.1016/j.neuroimage.2013.01.022. (Cited on pages 46 and 147.)

J. P. Haldar, J. Anderson, and S.-W. Sun. Maximum likelihood estimation of T1 relaxation parameters using VARPRO. In *Scientific Meeeting of International Society of Magnetic Resonance in Medicine (ISMRM)*, 2007. (Cited on page 147.)

J. P. Haldar, V. J. Wedeen, M. Nezamzadeh, G. Dai, M. W. Weiner, N. Schuff, and Z.-P. Liang. Improved diffusion imaging through SNR-enhancing joint reconstruction. *Magnetic Resonance in Medicine*, 69(1):277–289, 2013. ISSN 1522-2594. doi:10.1002/mrm.24229. (Cited on pages 76, 78, 79, 91, 145, and 160.)

J. P. Haldar, Q. Fan, and K. Setsompop. Whole-brain quantitative diffusion MRI at 660 μm resolution in 25 minutes using gSlider-SMS and SNR-enhancing joint reconstruction. In *24th Annual Meeting of International Society for Magnetic Resonance in Medicine (ISMRM), Singapore*, 2016. (Cited on page 46.)

K. D. Harkins, J. Xu, A. N. Dula, K. Li, W. M. Valentine, D. F. Gochberg, J. C. Gore, and M. D. Does. The microstructural correlates of T_1 in white matter. *Magnetic Resonance in Medicine*, 2015. ISSN 1522-2594. doi:10.1002/mrm.25709. (Cited on pages 39 and 41.)

H. Haroon, D. Morris, K. Embleton, D. Alexander, and G. Parker. Using the model-based residual bootstrap to quantify uncertainty in fiber orientations from Q-ball analysis. *IEEE Transactions on Medical Imaging*, 28(4): 535–550, april 2009. ISSN 0278-0062. doi:10.1109/TMI.2008.2006528. (Cited on page 44.)

H. A. Haroon, R. J. Binney, and G. J. Parker. Probabilistic quantification of regional cortical microstructural complexity. In *Proceedings of the International Society for Magnetic Resonance in Medicine 18, 578*, 2010. (Cited on page 44.)

R. M. Heidemann, D. A. Porter, A. Anwander, T. Feiweier, K. Heberlein, T. R. Knösche, and R. Turner. Diffusion imaging in humans at 7T using readout-segmented EPI and GRAPPA. *Magnetic Resonance in Medicine*, 64(1): 9–14, 2010. doi:10.1002/mrm.22480. (Cited on page 45.)

R. M. Heidemann, A. Anwander, T. Feiweier, T. R. Knösche, and R. Turner. k-space and q-space: Combining ultra-high spatial and angular resolution in diffusion imaging using ZOOPPA at 7 T. *NeuroImage*, 60(2):967 – 978, 2012. doi:10.1016/j.neuroimage.2011.12.081. (Cited on page 45.)

D. Hernando, J. P. Haldar, B. P. Sutton, J. Ma, P. Kellman, and Z.-P. Liang. Joint estimation of water/fat images and field inhomogeneity map. *Magnetic Resonance in Medicine*, 59(3):571–580, 2008. ISSN 1522-2594. doi:10.1002/mrm.21522. (Cited on page 14.)

D. Hernando, P. Kellman, J. P. Haldar, and Z.-P. Liang. Robust water/fat separation in the presence of large field inhomogeneities using a graph cut algorithm. *Magnetic Resonance in Medicine*, 63(1):79–90, 2010. ISSN 1522-2594. doi:10.1002/mrm.22177. (Cited on pages 14 and 92.)

C. P. Hess, P. Mukherjee, E. T. Han, D. Xu, and D. B. Vigneron. Q-ball reconstruction of multimodal fiber orientations using the spherical harmonic basis. *Magnetic Resonance in Medicine*, 56(1):104–117, 2006. ISSN 1522-2594. doi:10.1002/mrm.20931. (Cited on pages 76 and 78.)

M. Holden. A review of geometric transformations for nonrigid body registration. *IEEE Transactions on Medical Imaging*, 27(1):111–128, jan. 2008. ISSN 0278-0062. doi:10.1109/TMI.2007.904691. (Cited on page 36.)

D. Holland, J. M. Kuperman, and A. M. Dale. Efficient correction of inhomogeneous static magnetic field-induced distortion in echo planar imaging. *NeuroImage*, 50(1):175–183, 2010. ISSN 1053-8119. doi:10.1016/j.neuroimage.2009.11.044. (Cited on pages 21, 58, and 92.)

H. Huang, C. Ceritoglu, X. Li, A. Qiu, M. I. Miller, P. C. van Zijl, and S. Mori. Correction of B0 susceptibility induced distortion in diffusion-weighted images using large-deformation diffeomorphic metric mapping. *Magnetic Resonance Imaging*, 26(9):1294–1302, 2008. ISSN 0730-725X. doi:10.1016/j.mri.2008.03.005. (Cited on pages 23, 52, and 54.)

P. Hüppi. Diffusion tensor imaging in brain development. In D. K. Jones, editor, *Diffusion MRI: Theory, Methods, and Applications*, pages 500–518. Oxford University Press, 2011. doi:10.1093/med/9780195369779.003.0030. (Cited on page 43.)

D. Hwang, D.-H. Kim, and Y. P. Du. In vivo multi-slice mapping of myelin water content using $T_2{}^*$ decay. *NeuroImage*, 52(1):198 – 204, 2010. ISSN 1053-8119. doi:10.1016/j.neuroimage.2010.04.023. (Cited on page 39.)

M. Irfanoglu, L. Walker, S. Sammet, C. Pierpaoli, and R. Machiraju. Susceptibility distortion correction for echo planar images with non-uniform B-spline grid sampling: A diffusion tensor image study. In G. Fichtinger, A. Martel, and T. Peters, editors, *Medical Image Computing and Computer-Assisted Intervention 2011*, volume 6892 of *Lecture Notes in Computer Science*, pages 174–181. Springer Berlin / Heidelberg, 2011. ISBN 978-3-642-23628-0. (Cited on pages 23 and 52.)

M. O. Irfanoglu, L. Walker, J. Sarlls, S. Marenco, and C. Pierpaoli. Effects of image distortions originating from susceptibility variations and concomitant fields on diffusion MRI tractography results. *NeuroImage*, 61(1): 275–288, 2012. ISSN 1053-8119. doi:10.1016/j.neuroimage.2012.02.054. (Cited on pages 51 and 73.)

Y. Iwamura, M. Tanaka, M. Sakamoto, and O. Hikosaka. Converging patterns of finger representation and complex response properties of neurons in area 1 of the first somatosensory cortex of the conscious monkey. *Experimental Brain Research*, 51(3):327–337, 1983a. ISSN 1432-1106. doi:10.1007/BF00237869. (Cited on page 34.)

Y. Iwamura, M. Tanaka, M. Sakamoto, and O. Hikosaka. Functional subdivisions representing different finger regions in area 3 of the first somatosensory cortex of the conscious monkey. *Experimental Brain Research*, 51 (3):315–326, 1983b. ISSN 1432-1106. doi:10.1007/BF00237868. (Cited on page 34.)

Y. Iwamura, M. Tanaka, M. Sakamoto, and O. Hikosaka. Diversity in receptive field properties of vertical neuronal arrays in the crown of the postcentral gyrus of the conscious monkey. *Experimental Brain Research*, 58(2): 400–411, 1985. ISSN 1432-1106. doi:10.1007/BF00235321. (Cited on page 34.)

T. Jaermann, N. De Zanche, P. Staempfli, K. P. Pruessmann, A. Valavanis, P. Boesiger, and S. S. Kollias. Preliminary experience with visualization of intracortical fibers by focused high-resolution diffusion tensor imaging. *American Journal of Neuroradiology*, 29(1):146–150, 2008. doi:10.3174/ajnr.A0742. (Cited on page 43.)

M. Jenkinson. Measuring transformation error by RMS deviation. Technical report, Oxford Centre for Functional Magnetic Resonance Imaging of the Brain, Department of Clinical Neurology, Oxford University, Oxford, UK, 2000. (Cited on page 64.)

M. Jenkinson and S. Smith. A global optimisation method for robust affine registration of brain images. *Medical Image Analysis*, 5(2):143–156, 2001. ISSN 1361-8415. doi:10.1016/S1361-8415(01)00036-6. (Cited on pages 36, 51, 53, 54, 55, 58, 64, 65, and 71.)

M. Jenkinson, P. Bannister, M. Brady, and S. Smith. Improved optimization for the robust and accurate linear registration and motion correction of brain images. *NeuroImage*, 17(2):825–841, 2002. ISSN 1053-8119. doi:10.1006/nimg.2002.1132. (Cited on pages 53, 55, 65, and 71.)

M. Jenkinson, C. F. Beckmann, T. E. Behrens, M. W. Woolrich, and S. M. Smith. FSL. *NeuroImage*, 62(2): 782–790, 2012. ISSN 1053-8119. doi:10.1016/j.neuroimage.2011.09.015. (Cited on pages 36, 52, 65, and 71.)

S. N. Jespersen, C. R. Bjarkam, J. R. Nyengaard, M. M. Chakravarty, B. Hansen, T. Vosegaard, L. Østergaard, D. Yablonskiy, N. C. Nielsen, and P. Vestergaard-Poulsen. Neurite density from magnetic resonance diffusion measurements at ultrahigh field: Comparison with light microscopy and electron microscopy. *NeuroImage*, 49 (1):205 – 216, 2010. doi:10.1016/j.neuroimage.2009.08.053. (Cited on page 43.)

S. N. Jespersen, L. A. Leigland, A. Cornea, and C. D. Kroenke. Determination of axonal and dendritic orientation distributions within the developing cerebral cortex by diffusion tensor imaging. *IEEE Transactions on Medical Imaging*, 31(1):16–32, 2012. doi:10.1109/TMI.2011.2162099. (Cited on page 43.)

P. Jezzard. Correction of geometric distortion in fMRI data. *NeuroImage*, 62(2):648–651, 2012. ISSN 1053-8119. doi:10.1016/j.neuroimage.2011.09.010. (Cited on pages 16, 18, 19, 20, 52, and 71.)

P. Jezzard and R. S. Balaban. Correction for geometric distortion in echo planar images from B_0 field variations. *Magnetic Resonance in Medicine*, 34(1):65–73, 1995. ISSN 1522-2594. doi:10.1002/mrm.1910340111. (Cited on pages 13, 14, 16, 18, 19, 20, 52, 71, 73, 74, and 81.)

P. Jezzard and S. Clare. Sources of distortion in functional MRI data. *Human Brain Mapping*, 8(2-3):80–85, 1999. ISSN 1097-0193. doi:10.1002/(SICI)1097-0193(1999)8:2/3<80::AID-HBM2>3.0.CO;2-C. (Cited on page 51.)

S. Jiang, H. Xue, S. Counsell, M. Anjari, J. Allsop, M. Rutherford, D. Rueckert, and J. V. Hajnal. In-utero three dimension high resolution fetal brain diffusion tensor imaging. In N. Ayache, S. Ourselin, and A. Maeder, editors, *Medical Image Computing and Computer-Assisted Intervention (MICCAI) 2007*, volume 4791 of *Lecture Notes in Computer Science*, pages 18–26. Springer Berlin Heidelberg, 2007a. ISBN 978-3-540-75756-6. doi:10.1007/978-3-540-75757-3_3. (Cited on page 30.)

S. Jiang, H. Xue, A. Glover, M. Rutherford, D. Rueckert, and J. V. Hajnal. Mri of moving subjects using multislice snapshot images with volume reconstruction (SVR): Application to fetal, neonatal, and adult brain studies. *IEEE Transactions on Medical Imaging*, 26(7):967–980, July 2007b. ISSN 0278-0062. doi:10.1109/TMI.2007.895456. (Cited on page 30.)

S. Jiang, H. Xue, S. Counsell, M. Anjari, J. Allsop, M. Rutherford, D. Rueckert, and J. V. Hajnal. Diffusion tensor imaging (DTI) of the brain in moving subjects: Application to in-utero fetal and ex-utero studies. *Magnetic Resonance in Medicine*, 62(3):645–655, 2009. ISSN 1522-2594. doi:10.1002/mrm.22032. (Cited on page 30.)

H. Johansen-Berg and T. E. J. Behrens. *Diffusion MRI: from Quantitative Measurement to in-vivo Neuroanatomy*. Academic Press, San Diego, 2009. (Cited on page 51.)

H. Johansen-Berg and T. E. J. Behrens, editors. *Diffusion MRI: from Quantitative Measurement to* In-vivo *Neuroanatomy*. Academic Press, San Diego, second edition, 2014. ISBN 978-0-12-396460-1. doi:10.1016/B978-0-12-396460-1.01001-5. (Cited on pages 47 and 48.)

H. Johansen-Berg, T. E. J. Behrens, M. D. Robson, I. Drobnjak, M. F. S. Rushworth, J. M. Brady, S. M. Smith, D. J. Higham, and P. M. Matthews. Changes in connectivity profiles define functionally distinct regions in human medial frontal cortex. *Proceedings of the National Academy of Sciences*, 101(36):13335–13340, 2004. doi:10.1073/pnas.0403743101. (Cited on page 47.)

H. Johansen-Berg, T. E. Behrens, E. Sillery, O. Ciccarelli, A. J. Thompson, S. M. Smith, and P. M. Matthews. Functional-anatomical validation and individual variation of diffusion tractography-based segmentation of the human thalamus. *Cerebral Cortex*, 15(1):31–39, 2005. doi:10.1093/cercor/bhh105. (Cited on pages 47, 48, and 49.)

H. J. Johnson and G. E. Christensen. Consistent landmark and intensity-based image registration. *IEEE Transactions on Medical Imaging*, 21(5):450–461, 2002. doi:10.1109/TMI.2002.1009381. (Cited on pages 35 and 36.)

D. K. Jones. The effect of gradient sampling schemes on measures derived from diffusion tensor MRI: A monte carlo study. *Magnetic Resonance in Medicine*, 51(4):807–815, 2004. ISSN 1522-2594. doi:10.1002/mrm.20033. (Cited on page 92.)

D. K. Jones. Challenges and limitations of quantifying brain connectivity in vivo with diffusion MRI. *Imaging in Medicine*, 2(3):341–355, 2010. doi:10.2217/iim.10.21. (Cited on page 48.)

D. K. Jones, editor. *Diffusion MRI: Theory, Methods, and Applications*. Oxford University Press, New York, 2011. ISBN 978-0-19-536977-9. doi:10.1093/med/9780195369779.001.0001. (Cited on pages 28, 42, 46, 47, 48, 51, 73, and 76.)

D. K. Jones and M. Cercignani. Twenty-five pitfalls in the analysis of diffusion MRI data. *NMR in Biomedicine*, 23(7):803–820, 2010. ISSN 1099-1492. doi:10.1002/nbm.1543. (Cited on pages 20, 21, 27, 28, 29, 48, 51, 52, 73, and 74.)

D. K. Jones, M. A. Horsfield, and A. Simmons. Optimal strategies for measuring diffusion in anisotropic systems by magnetic resonance imaging. *Magnetic Resonance in Medicine*, 42(3):515–525, 1999. ISSN 1522-2594. doi:10.1002/(SICI)1522-2594(199909)42:3<515::AID-MRM14>3.0.CO;2-Q. (Cited on page 80.)

D. K. Jones, T. R. Knösche, and R. Turner. White matter integrity, fiber count, and other fallacies: The do's and don'ts of diffusion MRI. *NeuroImage*, 73(0):239–254, 2013. ISSN 1053-8119. doi:http://dx.doi.org/10.1016/j.neuroimage.2012.06.081. URL http://www.sciencedirect.com/science/article/pii/S1053811912007306. (Cited on page 48.)

O. Josephs, N. Weiskopf, and R. Deichmann. Detection and correction of spikes in fMRI data. In *Scientific Meeting of International Society for Magnetic Resonance in Medicine (ISMRM), Berlin, Germany*, page 3440, 2007. (Cited on page 7.)

A. A. Joshi, D. W. Shattuck, P. M. Thompson, and R. M. Leahy. Cortical surface parameterization by p-harmonic energy minimization. In *IEEE International Symposium on Biomedical Imaging*, volume 1, pages 428–431, 2004. doi:10.1109/ISBI.2004.1398566. (Cited on pages 36, 150, and 151.)

A. A. Joshi, D. W. Shattuck, P. M. Thompson, and R. M. Leahy. Surface-constrained volumetric brain registration using harmonic mappings. *IEEE Transactions on Medical Imaging*, 26(12):1657–1669, dec. 2007. ISSN 0278-0062. doi:10.1109/TMI.2007.901432. (Cited on pages 35, 36, 51, 52, 146, 149, 150, and 151.)

A. A. Joshi, R. M. Leahy, A. W. Toga, and D. W. Shattuck. A framework for brain registration via simultaneous surface and volume flow. In J. L. Prince, D. L. Pham, and K. J. Myers, editors, *Information Processing in Medical Imaging*, volume 5636 of *Lecture Notes in Computer Science*, pages 576–588. Springer Berlin Heidelberg, 2009a. ISBN 978-3-642-02497-9. doi:10.1007/978-3-642-02498-6_48. (Cited on page 35.)

A. A. Joshi, D. W. Shattuck, P. M. Thompson, and R. M. Leahy. A parameterization-based numerical method for isotropic and anisotropic diffusion smoothing on non-flat surfaces. *IEEE Transactions on Image Processing*, 18 (6):1358–1365, June 2009b. ISSN 1057-7149. doi:10.1109/TIP.2009.2016163. (Cited on page 123.)

A. A. Joshi, D. W. Shattuck, and R. M. Leahy. A method for automated cortical surface registration and labeling. In B. M. Dawant, G. E. Christensen, J. M. Fitzpatrick, and D. Rueckert, editors, *Biomedical Image Registration*, volume 7359 of *Lecture Notes in Computer Science*, pages 180–189. Springer Berlin Heidelberg, 2012. ISBN 978-3-642-31339-4. doi:10.1007/978-3-642-31340-0_19. (Cited on pages 35, 36, 51, 52, and 146.)

A. A. Joshi, C. Bhushan, R. Salloum, D. W. Shattuck, and R. M. Leahy. Estimation of cortical thickness from T1-weighted MRI images using tissue fractions. In *20th Annual Meeting of the Organization for Human Brain Mapping (OHBM), Hamburg*, page 1859, 2014. (Cited on pages 146 and 153.)

S. C. Joshi, M. I. Miller, and U. Grenander. On the geometry and shape of brain sub-manifolds. *International Journal of Pattern Recognition and Artificial Intelligence*, 11(08):1317–1343, 1997. doi:10.1142/S0218001497000615. (Cited on page 36.)

J. Jovicich, S. Czanner, D. Greve, E. Haley, A. van der Kouwe, R. Gollub, D. Kennedy, F. Schmitt, G. Brown, J. MacFall, B. Fischl, and A. Dale. Reliability in multi-site structural MRI studies: Effects of gradient non-linearity correction on phantom and human data. *NeuroImage*, 30(2):436 – 443, 2006. ISSN 1053-8119. doi:10.1016/j.neuroimage.2005.09.046. (Cited on pages 22 and 59.)

Y. M. Kadah and X. Hu. Algebraic reconstruction for magnetic resonance imaging under B_0 inhomogeneity. *IEEE Transactions on Medical Imaging*, 17(3):362–370, 1998. ISSN 0278-0062. doi:10.1109/42.712126. (Cited on pages 14, 18, 52, and 71.)

J.-K. Kamarainen, V. Kyrki, and H. Kälviäinen. Invariance properties of Gabor filter-based features-overview and applications. *IEEE Transactions on Image Processing*, 15(5):1088–1099, May 2006. doi:10.1109/TIP.2005.864174. (Cited on page 157.)

M. E. Kilmer and D. P. O'Leary. Choosing regularization parameters in iterative methods for ill-posed problems. *SIAM Journal on Matrix Analysis and Applications*, 22(4):1204–1221, 2001. (Cited on page 91.)

J.-H. Kim, J.-M. Lee, H. J. Jo, S. H. Kim, J. H. Lee, S. T. Kim, S. W. Seo, R. W. Cox, D. L. Na, S. I. Kim, and Z. S. Saad. Defining functional SMA and pre-SMA subregions in human MFC using resting state fMRI: Functional connectivity-based parcellation method. *NeuroImage*, 49(3):2375 – 2386, 2010. doi:10.1016/j.neuroimage.2009.10.016. (Cited on pages 47 and 48.)

J. C. Klein, T. E. Behrens, M. D. Robson, C. E. Mackay, D. J. Higham, and H. Johansen-Berg. Connectivity-based parcellation of human cortex using diffusion MRI: Establishing reproducibility, validity and observer independence in BA 44/45 and SMA/pre-SMA. *NeuroImage*, 34(1):204–211, 2007. ISSN 1053-8119. doi:10.1016/j.neuroimage.2006.08.022. (Cited on page 48.)

J. C. Klein, T. E. J. Behrens, and H. Johansen-Berg. Connectivity fingerprinting of gray matter. In H. Johansen-Berg and T. E. Behrens, editors, *Diffusion MRI*, pages 481 – 509. Academic Press, second edition, 2014. doi:10.1016/B978-0-12-396460-1.00021-4. (Cited on pages 47, 48, and 49.)

M. Kleinnijenhuis, M. Barth, V. Zerbi, K.-J. Sikma, B. Küsters, K. Slump, D. Norris, D. Ruiter, and A.-M. van Cappellen van Walsum. In vitro layer-specific diffusion weighted imaging in human primary visual cortex. In *Annual meeting of the Organization for Human Brain Mapping (OHBM), Quebec City, Canada*, page 2509, 2011a. (Cited on page 45.)

M. Kleinnijenhuis, K. J. Sikma, M. Barth, P. Dederen, V. Zerbi, B. Küsters, D. Ruiter, C. H. Slump, and A.-M. van Cappellen van Walsum. Validation of diffusion weighted imaging of cortical anisotropy by means of a histological stain for myelin. In *International Society for Magnetic Resonance in Medicine (ISMRM), Montréal, Québec, Canada*, page 2240, 2011b. (Cited on page 45.)

M. Kleinnijenhuis, V. Zerbi, B. Küsters, C. H. Slump, M. Barth, and A.-M. van Cappellen van Walsum. Layer-specific diffusion weighted imaging in human primary visual cortex in vitro. *Cortex*, 49(9):2569 – 2582, 2013a. ISSN 0010-9452. doi:10.1016/j.cortex.2012.11.015. (Cited on pages 45 and 148.)

M. Kleinnijenhuis, H. Zhang, D. Wiedermann, B. Küsters, D. G. Norris, and A.-M. van Cappellen van Walsum. Detailed laminar characteristics of the human neocortex revealed by noddi and histology. In *19th Annual Meeting of the Organization for Human Brain Mapping (OHBM), Seattle*, page 1685, 2013b. (Cited on page 45.)

M. Kleinnijenhuis, H. Zhang, D. Wiedermann, B. Küsters, A.-M. van Cappellen van Walsum, and D. G. Norris. Detailed laminar characteristics of the human neocortex revealed by NODDI. In *21st Scientific Meeting of International Society for Magnetic Resonance in Medicine (ISMRM), Salt Lake City, Utah*, page 5100, 2013c. (Cited on page 45.)

M. Kleinnijenhuis, T. van Mourik, D. G. Norris, D. J. Ruiter, A.-M. van Cappellen van Walsum, and M. Barth. Diffusion tensor characteristics of gyrencephaly using high resolution diffusion MRI in vivo at 7T. *NeuroImage*, 109:378 – 387, 2015. doi:10.1016/j.neuroimage.2015.01.001. (Cited on page 46.)

T. R. Knösche and M. Tittgemeyer. The role of long-range connectivity for the characterization of the functional-anatomical organization of the cortex. *Frontiers in Systems Neuroscience*, 5(58), 2011. doi:10.3389/fnsys.2011.00058. (Cited on pages 47, 48, and 49.)

C. G. Koay, L.-C. Chang, J. D. Carew, C. Pierpaoli, and P. J. Basser. A unifying theoretical and algorithmic framework for least squares methods of estimation in diffusion tensor imaging. *Journal of Magnetic Resonance*, 182(1):115 – 125, 2006. ISSN 1090-7807. doi:10.1016/j.jmr.2006.06.020. (Cited on page 147.)

C. D. Kroenke, E. N. Taber, L. A. Leigland, A. K. Knutsen, and P. V. Bayly. Regional patterns of cerebral cortical differentiation determined by diffusion tensor MRI. *Cerebral Cortex*, 19(12):2916–2929, 2009. doi:10.1093/cercor/bhp061. (Cited on page 43.)

D.-J. Kroon and C. H. Slump. MRI modality transformation in demon registration. In *IEEE International Symposium on Biomedical Imaging: From Nano to Macro*, pages 963–966, 2009. doi:10.1109/ISBI.2009.5193214. (Cited on pages 56 and 57.)

P. Kundu, N. D. Brenowitz, V. Voon, Y. Worbe, P. E. Vértes, S. J. Inati, Z. S. Saad, P. A. Bandettini, and E. T. Bullmore. Integrated strategy for improving functional connectivity mapping using multiecho fMRI. *Proceedings of the National Academy of Sciences*, 110(40):16187–16192, 2013. doi:10.1073/pnas.1301725110. (Cited on page 121.)

K. Kwong. Functional magnetic resonance imaging with echo planar imaging. In P. Pavone and P. Rossi, editors, *Functional MRI*, Syllabus, pages 73–90. Springer Milan, 1996. ISBN 978-3-540-75025-3. doi:10.1007/978-88-470-2194-5_16. (Cited on pages 6 and 11.)

K. K. Kwong, J. W. Belliveau, D. A. Chesler, I. E. Goldberg, R. M. Weisskoff, B. P. Poncelet, D. N. Kennedy, B. E. Hoppel, M. S. Cohen, and R. Turner. Dynamic magnetic resonance imaging of human brain activity during primary sensory stimulation. *Proceedings of the National Academy of Sciences*, 89(12):5675–5679, 1992. doi:10.1073/pnas.89.12.5675. (Cited on page 6.)

J. Kybic, P. Thévenaz, A. Nirkko, and M. Unser. Unwarping of unidirectionally distorted EPI images. *IEEE Transactions on Medical Imaging*, 19(2):80–93, feb. 2000. ISSN 0278-0062. doi:10.1109/42.836368. (Cited on pages 23, 52, and 54.)

A. R. Laird, S. B. Eickhoff, C. Rottschy, D. Bzdok, K. L. Ray, and P. T. Fox. Networks of task co-activations. *NeuroImage*, 80:505 – 514, 2013. ISSN 1053-8119. doi:10.1016/j.neuroimage.2013.04.073. (Cited on page 49.)

F. Lam, S. D. Babacan, J. P. Haldar, M. W. Weiner, N. Schuff, and Z.-P. Liang. Denoising diffusion-weighted magnitude MR images using rank and edge constraints. *Magnetic Resonance in Medicine*, 2013. ISSN 1522-2594. doi:10.1002/mrm.24728. (Cited on pages 76, 89, 91, and 145.)

J. M. Lane and R. F. Riesenfeld. A theoretical development for the computer generation and display of piecewise polynomial surfaces. *IEEE Transactions on Pattern Analysis and Machine Intelligence*, PAMI-2(1):35–46, jan. 1980. ISSN 0162-8828. doi:10.1109/TPAMI.1980.4766968. (Cited on page 60.)

R. Langner, C. Rottschy, A. R. Laird, P. T. Fox, and S. B. Eickhoff. Meta-analytic connectivity modeling revisited: Controlling for activation base rates. *NeuroImage*, 99:559 – 570, 2014. ISSN 1053-8119. doi:10.1016/j.neuroimage.2014.06.007. (Cited on page 49.)

C. Laule, I. M. Vavasour, S. H. Kolind, D. K. B. Li, T. L. Traboulsee, G. R. W. Moore, and A. L. MacKay. Magnetic resonance imaging of myelin. *Neurotherapeutics*, 4(3):460–484, 2007. ISSN 1878-7479. doi:10.1016/j.nurt.2007.05.004. (Cited on pages 39, 41, and 42.)

D. Le Bihan and H. Johansen-Berg. Diffusion MRI at 25: Exploring brain tissue structure and function. *NeuroImage*, 61(2):324–341, 2012. ISSN 1053-8119. doi:10.1016/j.neuroimage.2011.11.006. (Cited on pages 51, 73, and 76.)

R. M. Leahy. Integration of multimodal brain imaging data. In *Gordon Research Conference: Frontiers of Science*, volume 343, pages 902–926, June 2014. doi:10.1126/science.343.6173.902. Talk presented in session "Imaging in Four or More Dimensions" at Image Science: Accelerating the Pace of System Design and Task-Based Evaluation. (Cited on page 144.)

J. Lee, K. H. Jin, and J. C. Ye. Reference-free single-pass EPI Nyquist ghost correction using annihilating filter-based low rank hankel matrix (ALOHA). *Magnetic Resonance in Medicine*, 2016. ISSN 1522-2594. doi:10.1002/mrm.26077. (Cited on page 9.)

M. H. Lee, C. D. Smyser, and J. S. Shimony. Resting-state fMRI: A review of methods and clinical applications. *American Journal of Neuroradiology*, 34(10):1866–1872, 2013. doi:10.3174/ajnr.A3263. (Cited on page 101.)

S. Lefranc, P. Roca, M. Perrot, C. Poupon, D. L. Bihan, J.-F. Mangin, and D. Rivière. Groupwise connectivity-based parcellation of the whole human cortical surface using watershed-driven dimension reduction. *Medical Image Analysis*, 30:11 – 29, 2016. ISSN 1361-8415. doi:10.1016/j.media.2016.01.003. (Cited on page 48.)

C. W. Leuze, B. Dhital, A. Anwander, A. Pampel, R. Heidemann, S. Geyer, M. Gratz, and R. Turner. Visualization of the orientational structure of the human stria of gennari with high-resolution DWI. In *International Society for Magnetic Resonance in Medicine (ISMRM), Montréal, Québec, Canada*, page 2371, 2011. (Cited on page 44.)

C. W. Leuze, A. Anwander, P.-L. Bazin, B. Dhital, C. Stüber, K. Reimann, S. Geyer, and R. Turner. Layer-specific intracortical connectivity revealed with diffusion MRI. *Cerebral Cortex*, 24(2):328–339, 2014. doi:10.1093/cercor/bhs311. (Cited on page 45.)

Z.-P. Liang and P. Lauterbur. *Principles of Magnetic Resonance Imaging*. IEEE Press, New York, 2000. (Cited on pages 4, 5, 13, and 17.)

K. Lillywhite, D.-J. Lee, B. Tippetts, and J. Archibald. A feature construction method for general object recognition. *Pattern Recognition*, 46(12):3300 – 3314, 2013. ISSN 0031-3203. doi:http://dx.doi.org/10.1016/j.patcog.2013.06.002. URL http://www.sciencedirect.com/science/article/pii/S0031320313002549. (Cited on page 157.)

C. Luo, B. Ni, S. Yan, and M. Wang. Image classification by selective regularized subspace learning. *IEEE Transactions on Multimedia*, 18(1):40–50, Jan 2016. ISSN 1520-9210. doi:10.1109/TMM.2015.2495248. (Cited on page 158.)

G. Luppino, M. Matelli, R. M. Camarda, V. Gallese, and G. Rizzolatti. Multiple representations of body movements in mesial area 6 and the adjacent cingulate cortex: An intracortical microstimulation study in the macaque monkey. *The Journal of Comparative Neurology*, 311(4):463–482, 1991. ISSN 1096-9861. doi:10.1002/cne.903110403. (Cited on page 34.)

A. Lutti, F. Dick, M. I. Sereno, and N. Weiskopf. Using high-resolution quantitative mapping of R1 as an index of cortical myelination. *NeuroImage*, 93, Part 2:176 – 188, 2014. ISSN 1053-8119. doi:10.1016/j.neuroimage.2013.06.005. (Cited on pages 39, 40, and 147.)

L. C. Maas, P. Mukherjee, J. Carballido-Gamio, S. Veeraraghavan, S. P. Miller, S. C. Partridge, R. G. Henry, A. J. Barkovich, and D. B. Vigneron. Early laminar organization of the human cerebrum demonstrated with diffusion tensor imaging in extremely premature infants. *NeuroImage*, 22(3):1134 – 1140, 2004. doi:10.1016/j.neuroimage.2004.02.035. (Cited on page 43.)

A. Macovski. Noise in MRI. *Magnetic Resonance in Medicine*, 36(3):494–497, 1996. ISSN 1522-2594. doi:10.1002/mrm.1910360327. (Cited on page 7.)

F. Maes, A. Collignon, D. Vandermeulen, G. Marchal, and P. Suetens. Multimodality image registration by maximization of mutual information. *Medical Imaging, IEEE Transactions on*, 16(2):187–198, april 1997. ISSN 0278-0062. doi:10.1109/42.563664. (Cited on pages 53 and 54.)

G. Mangeat, S. T. Govindarajan, C. Mainero, and J. Cohen-Adad. Multivariate combination of magnetization transfer, T_2* and B0 orientation to study the myelo-architecture of the in vivo human cortex. *NeuroImage*, 119: 89 – 102, 2015. ISSN 1053-8119. doi:10.1016/j.neuroimage.2015.06.033. (Cited on page 41.)

J.-F. Mangin, G. Auzias, O. Coulon, Z. Sun, D. Rivière, and J. Régis. Sulci as landmarks. In A. W. Toga, editor, *Brain Mapping*, pages 45 – 52. Academic Press, 2015. ISBN 978-0-12-397316-0. doi:10.1016/B978-0-12-397025-1.00198-6. (Cited on page 35.)

J. V. Manjón, J. Carbonell-Caballero, J. J. Lull, G. García-Martí, L. Martí-Bonmatí, and M. Robles. MRI denoising using non-local means. *Medical Image Analysis*, 12(4):514 – 523, 2008. ISSN 1361-8415. doi:10.1016/j.media.2008.02.004. (Cited on page 99.)

J. V. Manjón, N. A. Thacker, J. J. Lull, G. Garcia-Martí, L. Martí-Bonmatí, and M. Robles. Multicomponent MR image denoising. *International Journal of Biomedical Imaging*, 2009:1–10, 2009. doi:10.1155/2009/756897. (Cited on page 99.)

P. Mansfield. Multi-planar image formation using NMR spin echoes. *Journal of Physics C: Solid State Physics*, 10(3):L55, 1977. (Cited on pages 6 and 7.)

P. Mansfield. Snap-shot MRI. Nobel Lecture, December 2003. URL http://nobelprize.org/nobel_prizes/medicine/laureates/2003/mansfield-lecture.pdf. (Cited on pages 6 and 7.)

D. S. Margulies, J. Böttger, X. Long, Y. Lv, C. Kelly, A. Schäfer, D. Goldhahn, A. Abbushi, M. P. Milham, G. Lohmann, and A. Villringer. Resting developments: a review of fMRI post-processing methodologies for spontaneous brain activity. *Magnetic Resonance Materials in Physics, Biology and Medicine*, 23(5):289–307, 2010. ISSN 1352-8661. doi:10.1007/s10334-010-0228-5. (Cited on pages 47, 48, and 49.)

R. B. Mars, L. Verhagen, T. E. Gladwin, F.-X. Neubert, J. Sallet, and M. F. S. Rushworth. Comparing brains by matching connectivity profiles. *Neuroscience & Biobehavioral Reviews*, 60:90 – 97, 2016. ISSN 0149-7634. doi:10.1016/j.neubiorev.2015.10.008. (Cited on page 47.)

M. Matelli, G. Luppino, and G. Rizzolatti. Architecture of superior and mesial area 6 and the adjacent cingulate cortex in the macaque monkey. *The Journal of Comparative Neurology*, 311(4):445–462, 1991. ISSN 1096-9861. doi:10.1002/cne.903110402. (Cited on page 34.)

B. Mazoyer. Jean Talairach (1911-2007): A life in stereotaxy. *Human Brain Mapping*, 29(2):250–252, 2008. doi:10.1002/hbm.20473. (Cited on page 35.)

R. C. McKinstry, A. Mathur, J. H. Miller, A. Ozcan, A. Z. Snyder, G. L. Schefft, C. R. Almli, S. I. Shiran, T. E. Conturo, and J. J. Neil. Radial organization of developing preterm human cerebral cortex revealed by non-invasive

water diffusion anisotropy MRI. *Cerebral Cortex*, 12(12):1237–1243, 2002. doi:10.1093/cercor/12.12.1237. (Cited on pages 42 and 43.)

J. A. McNab, S. Jbabdi, S. C. L. Deoni, G. Douaud, T. E. J. Behrens, and K. L. Miller. High resolution diffusion-weighted imaging in fixed human brain using diffusion-weighted steady state free precession. *NeuroImage*, 46 (3):775 – 785, 2009. doi:10.1016/j.neuroimage.2009.01.008. (Cited on page 43.)

J. A. McNab, J. R. Polimeni, and L. L. Wald. Surface based analysis of diffusion orientation for identifying architectonic domains in the in vivo human cortex. In *19th Scientific Meeting of International Society for Magnetic Resonance in Medicine (ISMRM), Montréal, Québec, Canada*, page 412, 2011. (Cited on page 44.)

J. A. McNab, J. R. Polimeni, R. Wang, J. C. Augustinack, K. Fujimoto, A. Player, C. Triantafyllou, T. Janssens, R. Farivar, W. Vanduffel, , and L. L. Wald. Comparison of *In Vivo* human, *In Vivo* macaque and *Ex Vivo* human measurements of diffusion orientation in the cerebral cortex. In *20th Scientific Meeting of International Society for Magnetic Resonance in Medicine (ISMRM), Melbourne, Australia*, page 3593, 2012. (Cited on page 44.)

J. A. McNab, B. L. Edlow, T. Witzel, S. Y. Huang, H. Bhat, K. Heberlein, T. Feiweier, K. Liu, B. Keil, J. Cohen-Adad, M. D. Tisdall, R. D. Folkerth, H. C. Kinney, and L. L. Wald. The human connectome project and beyond: Initial applications of 300 mT/m gradients. *NeuroImage*, 80:234 – 245, 2013a. ISSN 1053-8119. doi:10.1016/j.neuroimage.2013.05.074. (Cited on pages 16 and 46.)

J. A. McNab, J. R. Polimeni, R. Wang, J. C. Augustinack, K. Fujimoto, A. Stevens, T. Janssens, R. Farivar, R. D. Folkerth, W. Vanduffel, and L. L. Wald. Surface based analysis of diffusion orientation for identifying architectonic domains in the in vivo human cortex. *NeuroImage*, 69:87 – 100, 2013b. ISSN 1053-8119. doi:10.1016/j.neuroimage.2012.11.065. (Cited on pages 42, 44, 148, and 150.)

L. Mercier, V. Fonov, C. Haegelen, R. Del Maestro, K. Petrecca, and D. Collins. Comparing two approaches to rigid registration of three-dimensional ultrasound and magnetic resonance images for neurosurgery. *International Journal of Computer Assisted Radiology and Surgery*, 7(1):125–136, 2012. ISSN 1861-6410. doi:10.1007/s11548-011-0620-2. (Cited on page 56.)

J. Meyer. Histogram transformation for inter-modality image registration. In *Proceedings of the 7th IEEE International Conference on Bioinformatics and Bioengineering*, pages 1118–1123, 2007. doi:10.1109/BIBE.2007.4375700. (Cited on page 56.)

S. Mikula, I. Trotts, J. M. Stone, and E. G. Jones. Internet-enabled high-resolution brain mapping and virtual microscopy. *NeuroImage*, 35(1):9 – 15, 2007. doi:10.1016/j.neuroimage.2006.11.053. (Cited on pages 43 and 148.)

K. L. Miller. Diffusion acquisition: Pushing the boundaries. In H. Johansen-Berg and T. E. Behrens, editors, *Diffusion MRI: from Quantitative Measurement to in-vivo Neuroanatomy*, pages 35 – 61. Academic Press, San Diego, 2nd edition, 2014. ISBN 978-0-12-396460-1. doi:10.1016/B978-0-12-396460-1.00003-2. (Cited on pages 7, 27, 45, and 51.)

M. I. Miller, G. E. Christensen, Y. Amit, and U. Grenander. Mathematical textbook of deformable neuroanatomies. *Proceedings of the National Academy of Sciences*, 90(24):11944–11948, 1993. doi:10.1073/pnas.90.24.11944. (Cited on pages 35 and 56.)

H. Mohlberg, S. B. Eickhoff, A. Schleicher, K. Zilles, and K. Amunts. A new processing pipeline and release of cytoarchitectonic probabilistic maps - JuBrain. In *18th Annual Meeting of the Organization for Human Brain Mapping, Beijing, China*, Jun 2012. (Cited on pages 37 and 38.)

D. Moreno-Dominguez, A. Anwander, and T. R. Knösche. A hierarchical method for whole-brain connectivity-based parcellation. *Human Brain Mapping*, 35(10):5000–5025, 2014. ISSN 1097-0193. doi:10.1002/hbm.22528. (Cited on page 48.)

P. S. Morgan, R. W. Bowtell, D. J. McIntyre, and B. S. Worthington. Correction of spatial distortion in EPI due to inhomogeneous static magnetic fields using the reversed gradient method. *Journal of Magnetic Resonance Imaging*, 19(4):499–507, 2004. ISSN 1522-2586. doi:10.1002/jmri.20032. (Cited on pages 21, 58, and 74.)

P. Mukherjee and R. C. McKinstry. Diffusion tensor imaging and tractography of human brain development. *Neuroimaging Clinics of North America*, 16(1):19 – 43, 2006. doi:10.1016/j.nic.2005.11.004. (Cited on page 43.)

P. Munger, G. R. Crelier, T. M. Peters, and G. B. Pike. Conjugate gradient restoration of EPI images. In *International Society for Magnetic Resonance in Medicine (ISMRM), Sydney, Australia*, 1998. (Cited on pages 18 and 20.)

P. Munger, G. R. Crelier, T. M. Peters, and G. B. Pike. An inverse problem approach to the correction of distortion in EPI images. *IEEE Transactions on Medical Imaging*, 19(7):681–689, July 2000. ISSN 0278-0062. doi:10.1109/42.875186. (Cited on pages 16, 17, 18, 20, 52, 71, 74, and 77.)

Z. Nagy, D. Alexander, D. Thomas, N. Weiskopf, and M. Sereno. Discriminating cortical regions using HARDI data. In *18th Annual Meeting of the Organization for Human Brain Mapping (OHBM), Beijing, China*, 2012. (Cited on pages 44 and 46.)

Z. Nagy, D. C. Alexander, D. L. Thomas, N. Weiskopf, and M. I. Sereno. Using high angular resolution diffusion imaging data to discriminate cortical regions. *PLoS ONE*, 8(5):e63842, 05 2013. doi:10.1371/journal.pone.0063842. (Cited on pages 44, 46, and 148.)

L. Nanetti, L. Cerliani, V. Gazzola, R. Renken, and C. Keysers. Group analyses of connectivity-based cortical parcellation using repeated k-means clustering. *Neuroimage*, 47(4):1666–1677, 2009. doi:10.1016/j.neuroimage.2009.06.014. (Cited on page 48.)

K. S. Nayak and D. G. Nishimura. Automatic field map generation and off-resonance correction for projection reconstruction imaging. *Magnetic Resonance in Medicine*, 43(1):151–154, 2000. ISSN 1522-2594. doi:10.1002/(SICI)1522-2594(200001)43:1<151::AID-MRM19>3.0.CO;2-K. (Cited on page 14.)

K. S. Nayak, C.-M. Tsai, C. H. Meyer, and D. G. Nishimura. Efficient off-resonance correction for spiral imaging. *Magnetic Resonance in Medicine*, 45(3):521–524, 2001. ISSN 1522-2594. doi:10.1002/1522-2594(200103)45:3<521::AID-MRM1069>3.0.CO;2-6. (Cited on page 14.)

R. Nieuwenhuys. The myeloarchitectonic studies on the human cerebral cortex of the Vogt-Vogt school, and their significance for the interpretation of functional neuroimaging data. In S. Geyer and R. Turner, editors, *Microstructural Parcellation of the Human Cerebral Cortex*, pages 55–125. Springer Berlin Heidelberg, 2013. ISBN 978-3-642-37823-2. doi:10.1007/978-3-642-37824-9_3. URL http://link.springer.com/chapter/10.1007/978-3-642-37824-9_3. (Cited on pages 31, 32, and 33.)

K. B. Nooner, S. Colcombe, R. Tobe, M. Mennes, M. Benedict, A. Moreno, L. Panek, S. Brown, S. Zavitz, Q. Li, S. Sikka, D. Gutman, S. Bangaru, R. T. Schlachter, S. Kamiel, A. Anwar, C. Hinz, M. Kaplan, A. Rachlin, S. Adelsberg, B. Cheung, R. Khanuja, C. Yan, C. Craddock, V. Calhoun, W. Courtney, M. King, D. Wood, C. Cox, C. Kelly, A. DiMartino, E. Petkova, P. Reiss, N. Duan, D. Thompsen, B. Biswal, B. Coffey, M. Hoptman, D. C. Javitt, N. Pomara, J. Sidtis, H. Koplewicz, F. X. Castellanos, B. Leventhal, and M. Milham. The NKI-Rockland Sample: A model for accelerating the pace of discovery science in psychiatry. *Frontiers in Neuroscience*, 6(152), 2012. ISSN 1662-453X. doi:10.3389/fnins.2012.00152. (Cited on page 62.)

R. J. Ogg and R. G. Steen. Age-related changes in brain T1 are correlated with iron concentration. *Magnetic Resonance in Medicine*, 40(5):749–753, 1998. ISSN 1522-2594. doi:10.1002/mrm.1910400516. (Cited on page 41.)

F. P. M. Oliveira and J. M. R. S. Tavares. Medical image registration: a review. *Computer Methods in Biomechanics and Biomedical Engineering*, 0(0):1–21, 2012. doi:10.1080/10255842.2012.670855. (Cited on pages 36, 51, 53, 54, 55, 58, 60, and 67.)

J. O'Muircheartaigh, C. Vollmar, C. Traynor, G. J. Barker, V. Kumari, M. R. Symms, P. Thompson, J. S. Duncan, M. J. Koepp, and M. P. Richardson. Clustering probabilistic tractograms using independent component analysis applied to the thalamus. *Neuroimage*, 54(3):2020–2032, 2011. doi:10.1016/j.neuroimage.2010.09.054. (Cited on page 48.)

R. Ordidge. The development of echo-planar imaging (EPI): 1977–1982. *Magnetic Resonance Materials in Physics, Biology and Medicine*, 9(3):117–121, 1999. ISSN 0968-5243. doi:10.1007/BF02594607. (Cited on page 6.)

R. Ordidge, P. Mansfield, M. Doyle, and R. Coupland. Real time movie images by NMR. *The British Journal of Radiology*, 55(658):729–733, 1982. ISSN 0730-725X. doi:10.1259/0007-1285-55-658-729. (Cited on page 6.)

R. J. Ordidge, P. Mansfield, and R. E. Coupland. Rapid biomedical imaging by NMR. *The British Journal of Radiology*, 54(646):850–855, 1981. doi:10.1259/0007-1285-54-646-850. (Cited on page 6.)

C. C. Paige and M. A. Saunders. LSQR: An algorithm for sparse linear equations and sparse least squares. *ACM Transactions on Mathematical Software*, 8(1):43–71, 1982. ISSN 0098-3500. doi:10.1145/355984.355989. (Cited on page 78.)

D. Pantazis, A. Joshi, J. Jiang, D. W. Shattuck, L. E. Bernstein, H. Damasio, and R. M. Leahy. Comparison of landmark-based and automatic methods for cortical surface registration. *NeuroImage*, 49(3):2479 – 2493, 2010. ISSN 1053-8119. doi:10.1016/j.neuroimage.2009.09.027. (Cited on page 36.)

R. E. Passingham, K. E. Stephan, and R. Kötter. The anatomical basis of functional localization in the cortex. *Nature Reviews Neuroscience*, 3:606–616, 2002. doi:10.1038/nrn893. (Cited on page 47.)

C. M. Pechura and J. B. Martin, editors. *Mapping the Brain and Its Functions: Integrating Enabling Technologies into Neuroscience Research*, volume 91. National Academies Press, Washington, D.C., 1991. ISBN 0-309-04497-9. URL http://www.nap.edu/read/1816/. (Cited on page 31.)

W. Penfield and E. Boldrey. Somatic motor and sensory representation in the cerebral cortex of man as studied by electrical stimulation. *Brain*, 60(4):389–443, 1937. ISSN 0006-8950. doi:10.1093/brain/60.4.389. (Cited on pages 33 and 37.)

C. Pierpaoli. Artifacts in diffusion MRI. In D. K. Jones, editor, *Diffusion MRI: Theory, Methods, and Applications*, pages 303 – 317, 2010. (Cited on pages 7, 27, 28, 29, 30, and 51.)

C. Pierpaoli, L. Walker, M. O. Irfanoglu, A. Barnett, P. Basser, L.-C. Chang, C. Koay, S. Pajevic, G. Rohde, J. Sarlls, and M. Wu. TORTOISE: an integrated software package for processing of diffusion MRI data. In *International Society for Magnetic Resonance in Medicine, Stockholm, Sweden*, page 1597, 2010. (Cited on pages 20, 23, 52, 54, and 67.)

J. Pipe. Pulse sequences for diffusion-weighted MRI. In H. Johansen-Berg and T. E. Behrens, editors, *Diffusion MRI: from Quantitative Measurement to in-vivo Neuroanatomy*, pages 11 – 34. Academic Press, San Diego, San Diego, 2nd edition, 2014. ISBN 978-0-12-396460-1. doi:10.1016/B978-0-12-396460-1.00002-0. (Cited on pages 6, 7, 25, 26, 27, 28, 29, 45, and 51.)

J. P. Pluim, J. A. Maintz, and M. A. Viergever. Mutual-information-based registration of medical images: A survey. *IEEE Transactions on Medical Imaging*, 22(8):986–1004, aug. 2003. ISSN 0278-0062. doi:10.1109/TMI.2003.815867. (Cited on pages 53 and 55.)

J. P. Pluim, J. B. A. Maintz, and M. A. Viergever. f-information measures in medical image registration. *Medical Imaging, IEEE Transactions on*, 23(12):1508–1516, 2004. ISSN 0278-0062. doi:10.1109/TMI.2004.836872. (Cited on pages 53 and 55.)

G. Postelnicu, L. Zollei, and B. Fischl. Combined volumetric and surface registration. *IEEE Transactions on Medical Imaging*, 28(4):508–522, april 2009. ISSN 0278-0062. doi:10.1109/TMI.2008.2004426. (Cited on page 36.)

M. Poustchi-Amin, S. A. Mirowitz, J. J. Brown, R. C. McKinstry, and T. Li. Principles and applications of echo-planar imaging: A review for the general radiologist. *RadioGraphics*, 21(3):767–779, 2001. doi:10.1148/radiographics.21.3.g01ma23767. (Cited on page 6.)

S. Qi, S. Meesters, K. Nicolay, B. M. ter Haar Romeny, and P. Ossenblok. The influence of construction methodology on structural brain network measures: A review. *Journal of Neuroscience Methods*, 253:170 – 182, 2015. doi:10.1016/j.jneumeth.2015.06.016. (Cited on page 47.)

T. G. Reese, O. Heid, R. M. Weisskoff, and V. J. Wedeen. Reduction of eddy-current-induced distortion in diffusion MRI using a twice-refocused spin echo. *Magnetic Resonance in Medicine*, 49(1):177–182, 2003. ISSN 1522-2594. doi:10.1002/mrm.10308. (Cited on pages 29 and 92.)

I. L. P. Richard and R. Rzedzian. Instant images of the body by magnetic resonance. *Magnetic Resonance in Medicine*, 5(6):563–571, 1987. ISSN 1522-2594. doi:10.1002/mrm.1910050607. (Cited on page 6.)

M. D. Robson, J. C. Gore, and R. T. Constable. Measurement of the point spread function in MRI using constant time imaging. *Magnetic Resonance in Medicine*, 38(5):733–740, 1997. ISSN 1522-2594. doi:10.1002/mrm.1910380509. (Cited on page 25.)

A. Roche, G. Malandain, X. Pennec, and N. Ayache. The correlation ratio as a new similarity measure for multimodal image registration. In W. Wells, A. Colchester, and S. Delp, editors, *Medical Image Computing and Computer-Assisted Interventation (MICCAI)*, volume 1496 of *Lecture Notes in Computer Science*, pages 1115–1124. Springer Berlin Heidelberg, 1998. ISBN 978-3-540-65136-9. doi:10.1007/BFb0056301. (Cited on pages 53, 54, and 63.)

P. E. Roland and K. Zilles. Brain atlases - a new research tool. *Trends in Neurosciences*, 17(11):458 – 467, 1994. ISSN 0166-2236. doi:10.1016/0166-2236(94)90131-7. (Cited on page 37.)

P. E. Roland and K. Zilles. Structural divisions and functional fields in the human cerebral cortex. *Brain Research Reviews*, 26(2-3):87 – 105, 1998. ISSN 0165-0173. doi:10.1016/S0165-0173(97)00058-1. (Cited on page 37.)

P. E. Roland, S. Geyer, K. Amunts, T. Schormann, A. Schleicher, A. Malikovic, and K. Zilles. Cytoarchitectural maps of the human brain in standard anatomical space. *Human brain mapping*, 5(4):222–227, 1997. (Cited on page 37.)

C. Rorden and H.-O. Karnath. Using human brain lesions to infer function: a relic from a past era in the fMRI age? *Nature Reviews Neuroscience*, 5(10):812–819, 2004. doi:10.1038/nrn1521. (Cited on page 34.)

S. Rosenberg. *The Laplacian on a Riemannian manifold: An introduction to analysis on manifolds*. London Mathematical Society Student Texts(No. 31). Cambridge University Press, New York, January 1997. ISBN 9780521468312. doi:10.1017/CBO9780511623783. (Cited on page 123.)

B. J. Roth, S. Puwal, and P. J. Basser. Local magnetic field perturbations caused by magnetic susceptibility heterogeneity in myelin-water layers within an axon. *Journal of Coupled Systems and Multiscale Dynamics*, 3 (3):228–232, 2015. doi:10.1166/jcsmd.2015.1081. (Cited on pages 39 and 41.)

S. Roy, A. Carass, and J. L. Prince. Magnetic resonance image example-based contrast synthesis. *IEEE Transactions on Medical Imaging*, 32(12):2348–2363, 2013. ISSN 0278-0062. doi:10.1109/TMI.2013.2282126. (Cited on page 56.)

M. Rubinov and O. Sporns. Complex network measures of brain connectivity: Uses and interpretations. *NeuroImage*, 52(3):1059 – 1069, 2010. ISSN 1053-8119. doi:10.1016/j.neuroimage.2009.10.003. (Cited on page 47.)

D. Rueckert, L. Sonoda, C. Hayes, D. Hill, M. Leach, and D. Hawkes. Nonrigid registration using free-form deformations: application to breast MR images. *IEEE Transactions on Medical Imaging*, 18(8):712–721, aug. 1999. ISSN 0278-0062. doi:10.1109/42.796284. (Cited on page 60.)

D. Rueckert, R. Wolz, and P. Aljabar. Machine learning meets medical imaging: Learning and discovery of clinically useful information from images. In *Computational Vision and Medical Image Processing IV*, pages 3–8. CRC Press, Leiden, The Netherlands, 2013. (Cited on page 160.)

L. Ruthotto, H. Kugel, J. Olesch, B. Fischer, J. Modersitzki, M. Burger, and C. H. Wolters. Diffeomorphic susceptibility artifact correction of diffusion-weighted magnetic resonance images. *Physics in Medicine and Biology*, 57(18):5715–5731, 2012. doi:10.1088/0031-9155/57/18/5715. (Cited on page 21.)

R. Rzedzian, P. Mansfield, M. Doyle, D. Guilfoyle, B. Chapman, R. E. Coupland, A. Chrispin, and P. Small. Real-time nuclear magnetic resonance clinical imaging in paediatrics. *The Lancet*, 322(8362):1281 – 1282, 1983. ISSN 0140-6736. doi:10.1016/S0140-6736(83)91153-4. Originally published as Volume 2, Issue 8362. (Cited on page 6.)

Y. Saeys, I. Inza, and P. Larrañaga. A review of feature selection techniques in bioinformatics. *Bioinformatics*, 23 (19):2507–2517, 2007. doi:10.1093/bioinformatics/btm344. (Cited on page 157.)

R.-M. Sánchez-Panchuelo, S. T. Francis, D. Schluppeck, and R. W. Bowtell. Correspondence of human visual areas identified using functional and anatomical MRI in vivo at 7 T. *Journal of Magnetic Resonance Imaging*, 35(2):287–299, 2012. doi:10.1002/jmri.22822. (Cited on page 40.)

R.-M. Sánchez-Panchuelo, J. Besle, O. Mougin, P. Gowland, R. Bowtell, D. Schluppeck, and S. Francis. Regional structural differences across functionally parcellated brodmann areas of human primary somatosensory cortex. *NeuroImage*, 93, Part 2:221–230, 2014. ISSN 1053-8119. doi:10.1016/j.neuroimage.2013.03.044. (Cited on page 40.)

S. Sandor and R. Leahy. Towards automated labelling of cerebral cortex using a deformable atlas. In *Information Processing in Medical Imaging (IPMI)*, pages 127–138, 1995. (Cited on page 36.)

S. Sandor and R. Leahy. Surface-based labeling of cortical anatomy using a deformable atlas. *IEEE Transactions on Medical Imaging*, 16(1):41–54, Feb 1997. ISSN 0278-0062. doi:10.1109/42.552054. (Cited on page 36.)

S. Sandrone, M. T. de Schotten, K. Reimann, D. Murphy, S. Geyer, M. Catani, and F. Dell'Acqua. T1-weighted/T2-weighted MRI myelin mapping does not map myelin in the human corpus callosum. In *Annual meeting of the Organization for Human Brain Mapping (OHBM), Honolulu, Hawaii*, page 4085, 2015. (Cited on page 42.)

D. Sarrut, J. Vandemeulebroucke, and S. Rit. Intensity-based deformable registration: Introduction and overview. In J. Ehrhardt and C. Lorenz, editors, *4D Modeling and Estimation of Respiratory Motion for Radiation Therapy*,

Biological and Medical Physics, Biomedical Engineering, pages 103–124. Springer Berlin Heidelberg, 2013. ISBN 978-3-642-36440-2. doi:10.1007/978-3-642-36441-9_6. (Cited on page 55.)

J. Schmid, J. Kim, and N. Magnenat-Thalmann. Robust statistical shape models for MRI bone segmentation in presence of small field of view. *Medical Image Analysis*, 15(1):155 – 168, 2011. ISSN 1361-8415. doi:10.1016/j.media.2010.09.001. (Cited on page 160.)

F. Schmitt. Echo-planar imaging. In A. W. Toga, editor, *Brain Mapping*, pages 53 – 74. Academic Press, San Diego, 2015. ISBN 978-0-12-397316-0. doi:10.1016/B978-0-12-397025-1.00006-3. (Cited on pages 6, 7, and 11.)

F. Schmitt and P. A. Wielopolski. Echo-planar image reconstruction. In *Echo-Planar Imaging - Theory, technique and applications*, pages 141–178. Springer-Verlag Berlin Heidelberg, 1998. ISBN 978-3-642-80445-8. doi:10.1007/978-3-642-80443-4_5. (Cited on pages 6, 9, 10, and 26.)

F. Schmitt, M. K. Stehling, and R. Turner. *Echo-Planar Imaging - Theory, technique and applications*. Springer-Verlag Berlin Heidelberg, 1st edition, 1998. ISBN 978-3-642-80445-8. doi:10.1007/978-3-642-80443-4. (Cited on pages 6, 8, and 13.)

P. Schönknecht, A. Anwander, F. Petzold, S. Schindler, T. R. Knösche, H. E. Möller, U. Hegerl, R. Turner, and S. Geyer. Diffusion imaging-based subdivision of the human hypothalamus: a magnetic resonance study with clinical implications. *European Archives of Psychiatry and Clinical Neuroscience*, 263(6):497–508, 2013. ISSN 1433-8491. doi:10.1007/s00406-012-0389-5. (Cited on page 48.)

S. Seo and M. K. Chung. Laplace-Beltrami eigenfunction expansion of cortical manifolds. In *IEEE International Symposium on Biomedical Imaging: From Nano to Macro*, pages 372–375, March 2011. doi:10.1109/ISBI.2011.5872426. (Cited on page 123.)

S. Seo, M. K. Chung, and H. K. Vorperian. Heat kernel smoothing using Laplace-Beltrami eigenfunctions. In T. Jiang, N. Navab, J. Pluim, and M. Viergever, editors, *Medical Image Computing and Computer-Assisted Intervention (MICCAI)*, volume 6363 of *Lecture Notes in Computer Science*, pages 505–512. Springer Berlin Heidelberg, 2010. ISBN 978-3-642-15710-3. doi:10.1007/978-3-642-15711-0_63. (Cited on page 123.)

M. I. Sereno, A. Lutti, N. Weiskopf, and F. Dick. Mapping the human cortical surface by combining quantitative T1 with retinotopy. *Cerebral Cortex*, 2012. doi:10.1093/cercor/bhs213. (Cited on pages 39 and 40.)

K. Setsompop, B. Bilgic, A. Nummenmaa, Q. Fan, S. F. Cauley, S. Huang, I. Chatnuntawech, Y. Rathi, T. Witzel, and L. L. Wald. SLIce Dithered Enhanced Resolution Simultaneous MultiSlice (SLIDER-SMS) for high resolution (700 um) diffusion imaging of the human brain. In *23rd Annual Meeting of International Society for Magnetic Resonance in Medicine (ISMRM), Toronto, Canada*, page 339, 2015. (Cited on page 46.)

K. Setsompop, J. Stockmann, Q. Fan, T. Witzel, and L. L. Wald. Generalized SLIce Dithered Enhanced Resolution Simultaneous MultiSlice (gSlider-SMS) to increase volume encoding, SNR and partition profile fidelity in high-resolution diffusion imaging. In *24th Annual Meeting International Society for Magnetic Resonance in Medicine, Singapore*, 2016. (Cited on page 46.)

R. Shafee, R. L. Buckner, and B. Fischl. Gray matter myelination of 1555 human brains using partial volume corrected MRI images. *NeuroImage*, 105:473 – 485, 2015. ISSN 1053-8119. doi:10.1016/j.neuroimage.2014.10.054. (Cited on page 41.)

D. W. Shattuck and R. M. Leahy. BrainSuite: An automated cortical surface identification tool. *Medical Image Analysis*, 6(2):129–142, 2002. ISSN 1361-8415. doi:10.1016/S1361-8415(02)00054-3. (Cited on pages 35, 36, 51, 52, and 145.)

D. W. Shattuck, S. R. Sandor-Leahy, K. A. Schaper, D. A. Rottenberg, and R. M. Leahy. Magnetic resonance image tissue classification using a partial volume model. *NeuroImage*, 13(5):856–876, 2001. ISSN 1053-8119. doi:10.1006/nimg.2000.0730. (Cited on pages 35, 51, 52, 56, and 72.)

D. W. Shattuck, A. A. Joshi, J. P. Haldar, C. Bhushan, S. Choi, A. Krause, J. L. Wisnowski, H. Damasio, A. W. Toga, and R. M. Leahy. New BrainSuite13 tools for image segmentation, registration, connectivity analysis and visualization. In *19th Annual Meeting of the Organization for Human Brain Mapping (OHBM), Seattle*, 2013a. (Cited on pages 3 and 35.)

D. W. Shattuck, A. A. Joshi, J. P. Haldar, C. Bhushan, S. Choi, A. C. Krause, J. L. Wisnowski, A. W. Toga, and R. M. Leahy. Software tools for anatomical ROI-based connectivity analysis. In *21st Scientific Meeting of International Society for Magnetic Resonance in Medicine (ISMRM), Salt Lake City, Utah*, page 2691, 2013b. (Cited on pages 3 and 35.)

D. Shen and C. Davatzikos. Very high-resolution morphometry using mass-preserving deformations and HAMMER elastic registration. *NeuroImage*, 18(1):28 – 41, 2003. ISSN 1053-8119. doi:10.1006/nimg.2002.1301. (Cited on page 36.)

X. Shen, X. Papademetris, and R. T. Constable. Graph-theory based parcellation of functional subunits in the brain from resting-state fMRI data. *NeuroImage*, 50(3):1027 – 1035, 2010. ISSN 1053-8119. doi:10.1016/j.neuroimage.2009.12.119. (Cited on page 49.)

J. Shi and J. Malik. Normalized cuts and image segmentation. *IEEE Transactions on Pattern Analysis and Machine Intelligence*, 22(8):888–905, Aug 2000. ISSN 0162-8828. doi:10.1109/34.868688. (Cited on pages 100 and 102.)

H. Shou, A. Eloyan, M. B. Nebel, A. Mejia, J. J. Pekar, S. Mostofsky, B. Caffo, M. A. Lindquist, and C. M. Crainiceanu. Shrinkage prediction of seed-voxel brain connectivity using resting state fMRI. *NeuroImage*, 102 (2):938 – 944, 2014. doi:10.1016/j.neuroimage.2014.05.043. (Cited on page 49.)

I. S. Sigalovsky, B. Fischl, and J. R. Melcher. Mapping an intrinsic MR property of gray matter in auditory cortex of living humans: A possible marker for primary cortex and hemispheric differences. *NeuroImage*, 32(4):1524 – 1537, 2006. ISSN 1053-8119. doi:10.1016/j.neuroimage.2006.05.023. (Cited on page 40.)

A. Simmons, P. S. Tofts, G. J. Barker, and S. R. Arridge. Sources of intensity nonuniformity in spin echo images at 1.5 T. *Magnetic Resonance in Medicine*, 32(1):121–128, 1994. ISSN 1522-2594. doi:10.1002/mrm.1910320117. (Cited on page 71.)

S. T. Skare and R. Bammer. EPI-based pulse sequences for diffusion tensor MRI. In D. K. Jones, editor, *Diffusion MRI: Theory, Methods, and Applications*. Oxford University Press, New York, first edition, 2010. doi:10.1093/med/9780195369779.003.0012. (Cited on pages 6, 7, 9, 12, 25, 26, 27, 28, 29, and 51.)

J. G. Sled and G. B. Pike. Standing-wave and RF penetration artifacts caused by elliptic geometry: an electrodynamic analysis of MRI. *IEEE Transactions on Medical Imaging*, 17(4):653–662, Aug 1998. ISSN 0278-0062. doi:10.1109/42.730409. (Cited on page 71.)

J. G. Sled, A. P. Zijdenbos, and A. C. Evans. A nonparametric method for automatic correction of intensity nonuniformity in MRI data. *IEEE Transactions on Medical Imaging*, 17(1):87–97, Feb 1998. ISSN 0278-0062. doi:10.1109/42.668698. (Cited on page 72.)

S. M. Smith, P. T. Fox, K. L. Miller, D. C. Glahn, P. M. Fox, C. E. Mackay, N. Filippini, K. E. Watkins, R. Toro, A. R. Laird, and C. F. Beckmann. Correspondence of the brain's functional architecture during activation and rest. *Proceedings of the National Academy of Sciences*, 106(31):13040–13045, 2009. doi:10.1073/pnas.0905267106. (Cited on pages 97 and 101.)

S. M. Smith, C. F. Beckmann, J. Andersson, E. J. Auerbach, J. Bijsterbosch, G. Douaud, E. Duff, D. A. Feinberg, L. Griffanti, M. P. Harms, M. Kelly, T. Laumann, K. L. Miller, S. Moeller, S. Petersen, J. Power, G. Salimi-Khorshidi, A. Z. Snyder, A. T. Vu, M. W. Woolrich, J. Xu, E. Yacoub, K. Uğurbil, D. C. Van Essen, and M. F. Glasser. Resting-state fMRI in the Human Connectome Project. *NeuroImage*, 80(0):144 – 168, 2013a. ISSN 1053-8119. doi:10.1016/j.neuroimage.2013.05.039. (Cited on pages 97, 103, and 122.)

S. M. Smith, D. Vidaurre, C. F. Beckmann, M. F. Glasser, M. Jenkinson, K. L. Miller, T. E. Nichols, E. C. Robinson, G. Salimi-Khorshidi, M. W. Woolrich, D. M. Barch, K. Uğurbil, and D. C. Van Essen. Functional connectomics from resting-state fMRI. *Trends in Cognitive Sciences*, 17(12):666 – 682, 2013b. ISSN 1364-6613. doi:10.1016/j.tics.2013.09.016. (Cited on pages 47, 48, 49, 97, 100, and 102.)

T. B. Smith and K. S. Nayak. MRI artifacts and correction strategies. *Imaging in Medicine*, 2(4):445–457, 2010. doi:10.2217/iim.10.33. (Cited on page 7.)

S.-K. Song, S.-W. Sun, M. J. Ramsbottom, C. Chang, J. Russell, and A. H. Cross. Dysmyelination revealed through MRI as increased radial (but unchanged axial) diffusion of water. *NeuroImage*, 17(3):1429 – 1436, 2002. doi:10.1006/nimg.2002.1267. (Cited on page 42.)

O. Sporns. The human connectome: Origins and challenges. *NeuroImage*, 80:53 – 61, 2013. ISSN 1053-8119. doi:10.1016/j.neuroimage.2013.03.023. (Cited on page 47.)

O. Sporns. Contributions and challenges for network models in cognitive neuroscience. *Nature neuroscience*, 17 (5):652–660, 2014. doi:10.1038/nn.3690. (Cited on pages 47 and 49.)

S. St-Jean, P. Coupé, and M. Descoteaux. Non local spatial and angular matching: a new denoising technique for diffusion MRI. In *Joint Annual Meeting ISMRM-ESMRMB 2014*, page 758, 2014. (Cited on page 99.)

C. J. Stam. Modern network science of neurological disorders. *Nature Reviews Neuroscience*, 15:683–695, 2014. doi:10.1038/nrn3801. (Cited on page 47.)

M. Stehling, R. Turner, and P. Mansfield. Echo-planar imaging: magnetic resonance imaging in a fraction of a second. *Science*, 254(5028):43–50, 1991. (Cited on pages 6, 7, and 11.)

C. Studholme, D. Hill, and D. J. Hawkes. An overlap invariant entropy measure of 3D medical image alignment. *Pattern Recognition*, 32(1):71–86, 1999. ISSN 0031-3203. doi:10.1016/S0031-3203(98)00091-0. (Cited on pages 24, 53, 54, and 67.)

C. Studholme, R. T. Constable, and J. S. Duncan. Accurate alignment of functional EPI data to anatomical MRI using a physics-based distortion model. *IEEE Transactions on Medical Imaging*, 19(11):1115–1127, nov. 2000. ISSN 0278-0062. doi:10.1109/42.896788. (Cited on pages 16, 20, 23, 52, 56, and 67.)

B. P. Sutton, D. C. Noll, and J. A. Fessler. Fast, iterative image reconstruction for MRI in the presence of field inhomogeneities. *IEEE Transactions on Medical Imaging*, 22(2):178–188, 2003. ISSN 0278-0062. doi:10.1109/TMI.2002.808360. (Cited on pages 18, 19, 61, and 79.)

L. Swanson. *Brain Architecture: Understanding the Basic Plan*. Oxford University Press, New York, 2nd edition, 2012. ISBN 9780195378580. doi:10.1093/med/9780195378580.001.0001. (Cited on page 31.)

L. W. Swanson and M. Bota. Foundational model of structural connectivity in the nervous system with a schema for wiring diagrams, connectome, and basic plan architecture. *Proceedings of the National Academy of Sciences*, 107(48):20610–20617, 2010. doi:10.1073/pnas.1015128107. (Cited on page 31.)

J. Talairach and P. Tournoux. *Co-planar stereotaxic atlas of the human brain. 3-Dimensional Proportional System: An Approach to Cerebral Imaging*. Thieme Medical, New York, 1988. (Cited on pages 35 and 37.)

R. Tao, P. Fletcher, S. Gerber, and R. Whitaker. A variational image-based approach to the correction of susceptibility artifacts in the alignment of diffusion weighted and structural MRI. In J. Prince, D. Pham, and K. Myers, editors, *Information Processing in Medical Imaging*, volume 5636 of *Lecture Notes in Computer Science*, pages 664–675. Springer Berlin / Heidelberg, 2009. ISBN 978-3-642-02497-9. (Cited on pages 23 and 52.)

M. Tariq, M. Kleinnijenhuis, A.-M. van Cappellen van Walsum, and H. Zhang. Validation of NODDI estimation of dispersion anisotropy in V1 of the human neocortex. In *23rd Annual Meeting of International Society for Magnetic Resonance in Medicine (ISMRM), Toronto, Canada*, page 3928, 2015. (Cited on page 45.)

P. N. Taylor, M. Kaiser, and J. Dauwels. Structural connectivity based whole brain modelling in epilepsy. *Journal of Neuroscience Methods*, 236:51 – 57, 2014. doi:10.1016/j.jneumeth.2014.08.010. (Cited on page 47.)

B. Thirion, G. Flandin, P. Pinel, A. Roche, P. Ciuciu, and J.-B. Poline. Dealing with the shortcomings of spatial normalization: Multi-subject parcellation of fMRI datasets. *Human Brain Mapping*, 27(8):678–693, 2006. ISSN 1097-0193. doi:10.1002/hbm.20210. (Cited on pages 47, 48, and 49.)

B. Thirion, G. Varoquaux, E. Dohmatob, and J.-B. Poline. Which fMRI clustering gives good brain parcellations? *Frontiers in Neuroscience*, 8(167), 2014. ISSN 1662-453X. doi:10.3389/fnins.2014.00167. (Cited on pages 47, 48, 49, and 100.)

P. Thompson and A. W. Toga. A surface-based technique for warping three-dimensional images of the brain. *IEEE Transactions on Medical Imaging*, 15(4):402–417, Aug 1996. ISSN 0278-0062. doi:10.1109/42.511745. (Cited on pages 35 and 36.)

P. M. Thompson and A. W. Toga. A framework for computational anatomy. *Computing and Visualization in Science*, 5(1):13–34, 2002. doi:10.1007/s00791-002-0084-6. (Cited on page 36.)

P. M. Thompson, R. P. Woods, M. S. Mega, and A. W. Toga. Mathematical/computational challenges in creating deformable and probabilistic atlases of the human brain. *Human brain mapping*, 9(2):81–92, 2000. doi:10.1002/(SICI)1097-0193(200002)9:2<81::AID-HBM3>3.0.CO;2-8. (Cited on page 36.)

A. W. Toga, editor. *Brain Mapping: An Encyclopedic Reference*. Academic Press, San Diego, 2015. ISBN 978-0-12-397316-0. URL http://www.sciencedirect.com/science/referenceworks/9780123973160. (Cited on pages 35 and 51.)

A. W. Toga and J. C. Mazziotta, editors. *Brain Mapping: The Systems*. Academic Press, San Diego, 2000. ISBN 0-12-692545-3. (Cited on page 51.)

A. W. Toga and J. C. Mazziotta, editors. *Brain Mapping: The Methods*. Academic Press, San Diego, 2002. ISBN 0-12-693019-8. (Cited on pages 33, 35, and 51.)

A. W. Toga and P. M. Thompson. The role of image registration in brain mapping. *Image and Vision Computing*, 19(1–2):3–24, 2001. ISSN 0262-8856. doi:10.1016/S0262-8856(00)00055-X. (Cited on page 35.)

A. W. Toga, P. M. Thompson, S. Mori, K. Amunts, and K. Zilles. Towards multimodal atlases of the human brain. *Nature Reviews Neuroscience*, 7(12):952–966, 2006. ISSN 1471-003X. doi:10.1038/nrn2012. (Cited on page 37.)

D. Tosun, M. E. Rettmann, and J. L. Prince. Mapping techniques for aligning sulci across multiple brains. *Medical Image Analysis*, 8(3):295 – 309, 2004. ISSN 1361-8415. doi:10.1016/j.media.2004.06.020. (Cited on page 36.)

J.-D. Tournier, S. Mori, and A. Leemans. Diffusion tensor imaging and beyond. *Magnetic Resonance in Medicine*, 65(6):1532–1556, 2011. ISSN 1522-2594. doi:10.1002/mrm.22924. (Cited on pages 73 and 76.)

R. Trampel, D. V. M. Ott, and R. Turner. Do the congenitally blind have a stria of Gennari? first intracortical insights in vivo. *Cerebral Cortex*, 21(9):2075–2081, 2011. doi:10.1093/cercor/bhq282. (Cited on page 40.)

L. C. Triarhou. The cytoarchitectonic map of Constantin von Economo and Georg N. Koskinas. In S. Geyer and R. Turner, editors, *Microstructural Parcellation of the Human Cerebral Cortex*, pages 33–53. Springer Berlin Heidelberg, 2013. ISBN 978-3-642-37823-2. doi:10.1007/978-3-642-37824-9_2. URL http://link.springer.com/chapter/10.1007/978-3-642-37824-9_2. (Cited on pages 32, 33, 34, and 37.)

T.-K. Truong, A. Guidon, and A. W. Song. Cortical depth dependence of the diffusion anisotropy in the human cortical gray matter *In Vivo*. *PLoS ONE*, 9(3):e91424, 03 2014. doi:10.1371/journal.pone.0091424. (Cited on pages 44 and 148.)

J. Tsao. Interpolation artifacts in multimodality image registration based on maximization of mutual information. *IEEE Transactions on Medical Imaging*, 22(7):854–864, 2003. (Cited on pages 53 and 55.)

D. S. Tuch. Q-ball imaging. *Magnetic Resonance in Medicine*, 52(6):1358–1372, 2004. ISSN 1522-2594. doi:10.1002/mrm.20279. (Cited on page 46.)

R. Turner. Diffusion imaging with echo-planar imaging. In *Echo-Planar Imaging - Theory, technique and applications*, pages 311–324. Springer-Verlag Berlin Heidelberg, 1998. ISBN 978-3-642-80445-8. doi:10.1007/978-3-642-80443-4_9. (Cited on page 28.)

R. Turner. MRI methods for in-vivo cortical parcellation. In S. Geyer and R. Turner, editors, *Microstructural Parcellation of the Human Cerebral Cortex*, pages 197–220. Springer Berlin Heidelberg, 2013. ISBN 978-3-642-37823-2. doi:10.1007/978-3-642-37824-9_7. URL http://link.springer.com/chapter/10.1007/978-3-642-37824-9_7. (Cited on pages 38 and 39.)

R. Turner and S. Geyer. Introduction to the neuroimage special issue: In vivo Brodmann mapping of the human brain. *NeuroImage*, 93, Part 2:155 – 156, 2014. ISSN 1053-8119. doi:10.1016/j.neuroimage.2014.01.018. (Cited on pages 34, 37, 38, and 39.)

R. Turner, D. Le Bihan, and A. Scott Chesnicks. Echo-planar imaging of diffusion and perfusion. *Magnetic Resonance in Medicine*, 19(2):247–253, 1991. ISSN 1522-2594. doi:10.1002/mrm.1910190210. (Cited on pages 6 and 28.)

R. Turner, A.-M. Oros-Peusquens, S. Romanzetti, K. Zilles, and N. J. Shah. Optimised in vivo visualisation of cortical structures in the human brain at 3 T using IR-TSE. *Magnetic Resonance Imaging*, 26(7):935 – 942, 2008. ISSN 0730-725X. doi:10.1016/j.mri.2008.01.043. (Cited on page 40.)

J. M. Tyszka, C. Readhead, E. L. Bearer, R. G. Pautler, and R. E. Jacobs. Statistical diffusion tensor histology reveals regional dysmyelination effects in the shiverer mouse mutant. *NeuroImage*, 29(4):1058 – 1065, 2006. doi:10.1016/j.neuroimage.2005.08.037. (Cited on page 42.)

N. Tzourio-Mazoyer, B. Landeau, D. Papathanassiou, F. Crivello, O. Etard, N. Delcroix, B. Mazoyer, and M. Joliot. Automated anatomical labeling of activations in SPM using a macroscopic anatomical parcellation of the MNI MRI single-subject brain. *NeuroImage*, 15(1):273 – 289, 2002. ISSN 1053-8119. doi:10.1006/nimg.2001.0978. (Cited on pages 35 and 36.)

M. P. van den Heuvel and H. E. Hulshoff Pol. Exploring the brain network: A review on resting-state fMRI functional connectivity. *European Neuropsychopharmacology*, 20(8):519 – 534, 2010. ISSN 0924-977X. doi:10.1016/j.euroneuro.2010.03.008. (Cited on pages 47, 48, and 49.)

D. C. Van Essen. Surface-based approaches to spatial localization and registration in primate cerebral cortex. *Neuroimage*, 23(Suppl. 1):S97–S107, 2004. doi:10.1016/j.neuroimage.2004.07.024. (Cited on page 36.)

D. C. Van Essen. A population-average, landmark-and surface-based (PALS) atlas of human cerebral cortex. *Neuroimage*, 28(3):635–662, 2005. doi:10.1016/j.neuroimage.2005.06.058. (Cited on page 36.)

D. C. Van Essen and M. F. Glasser. In vivo architectonics: A cortico-centric perspective. *NeuroImage*, 93, Part 2: 157 – 164, 2014. ISSN 1053-8119. doi:10.1016/j.neuroimage.2013.04.095. (Cited on page 41.)

D. C. Van Essen, H. A. Drury, S. Joshi, and M. I. Miller. Functional and structural mapping of human cerebral cortex: Solutions are in the surfaces. *Proceedings of the National Academy of Sciences*, 95(3):788–795, 1998. doi:10.1073/pnas.95.3.788. (Cited on page 36.)

D. C. Van Essen, M. F. Glasser, D. L. Dierker, J. Harwell, and T. Coalson. Parcellations and hemispheric asymmetries of human cerebral cortex analyzed on surface-based atlases. *Cerebral Cortex*, 22(10):2241–2262, 2012. doi:10.1093/cercor/bhr291. (Cited on pages 35, 103, and 106.)

D. C. Van Essen, S. M. Smith, D. M. Barch, T. E. Behrens, E. Yacoub, and K. Ugurbil. The WU-Minn Human Connectome Project: An overview. *NeuroImage*, 80(0):62 – 79, 2013. ISSN 1053-8119. doi:10.1016/j.neuroimage.2013.05.041. (Cited on page 103.)

D. Varadarajan and J. P. Haldar. A quadratic majorize-minimize framework for statistical estimation with noisy Rician and noncentral Chi-distributed MR images. In *IEEE International Symposium on Biomedical Imaging (ISBI), San Francisco, CA*, pages 712 – 715, 2013. doi:10.1109/ISBI.2013.6556574. (Cited on pages 91, 145, and 160.)

D. Varadarajan and J. P. Haldar. MS-FRACT: Optimized linear transform methods for ODF estimation in multi-shell diffusion MRI. In *IEEE 12th International Symposium on Biomedical Imaging (ISBI), New York*, pages 1172–1175, April 2015. doi:10.1109/ISBI.2015.7164081. (Cited on page 147.)

J. L. Vincent, A. Z. Snyder, M. D. Fox, B. J. Shannon, J. R. Andrews, M. E. Raichle, and R. L. Buckner. Coherent spontaneous activity identifies a hippocampal-parietal memory network. *Journal of Neurophysiology*, 96(6): 3517–3531, 2006. ISSN 0022-3077. doi:10.1152/jn.00048.2006. (Cited on page 121.)

J. L. Vincent, I. Kahn, A. Z. Snyder, M. E. Raichle, and R. L. Buckner. Evidence for a frontoparietal control system revealed by intrinsic functional connectivity. *Journal of Neurophysiology*, 100(6):3328–3342, 2008. ISSN 0022-3077. doi:10.1152/jn.90355.2008. (Cited on pages 98 and 111.)

P. Viola and W. M. Wells III. Alignment by maximization of mutual information. *International Journal of Computer Vision*, 24(2):137–154, 1997. ISSN 0920-5691. doi:10.1023/A:1007958904918. (Cited on pages 53, 54, and 67.)

P. A. Viola. *Alignment by Maximization of Mutual Information*. PhD thesis, Massachusetts Institute of Technology, 1995. (Cited on page 54.)

C. Vogt and O. Vogt. Allgemeinere ergebnisse unserer hirnforschung. *J. Psychol. Neurol.*, 25:279–468, 1919. (Cited on pages 33, 34, and 46.)

C. Vogt and O. Vogt. Die vergleichend-architektonische und die vergleichend-reizphysiologische felderung der großhirnrinde unter besonderer berücksichtigung der menschlichen. *Naturwissenschaften*, 14(50):1190–1194, 1926. ISSN 1432-1904. doi:10.1007/BF01451766. (Cited on pages 33 and 37.)

C. F. von Economo and G. N. Koskinas. *Die Cytoarchitektonik der Hirnrinde des erwachsenen Menschen: Textband und Atlas mit 112 Mikrophotographischen Tafeln*. Springer, Berlin, 1925. (Cited on pages 32, 46, and 154.)

N. B. Walters, G. F. Egan, J. J. Kril, M. Kean, P. Waley, M. Jenkinson, and J. D. G. Watson. In vivo identification of human cortical areas using high-resolution MRI: An approach to cerebral structure-function correlation. *Proceedings of the National Academy of Sciences*, 100(5):2981–2986, 2003. doi:10.1073/pnas.0437896100. (Cited on page 40.)

Q. Wang, R. Chen, J. JaJa, Y. Jin, L. E. Hong, and E. H. Herskovits. Connectivity-based brain parcellation. *Neuroinformatics*, 14(1):83–97, 2015. ISSN 1559-0089. doi:10.1007/s12021-015-9280-7. (Cited on page 48.)

Y. Wang, M.-C. Chiang, and P. M. Thompson. Automated surface matching using mutual information applied to Riemann surface structures. In *Medical Image Computing and Computer-Assisted Intervention (MICCAI)*, pages 666–674. Springer Berlin Heidelberg, 2005. doi:10.1007/11566489_82. (Cited on page 36.)

C. Wasserthal, A. Brechmann, J. Stadler, B. Fischl, and K. Engel. Localizing the human primary auditory cortex in vivo using structural MRI. *NeuroImage*, 93, Part 2(0):237 – 251, 2014. ISSN 1053-8119. doi:10.1016/j.neuroimage.2013.07.046. (Cited on page 41.)

V. J. Wedeen, S. Song, L. Wald, T. G. Reese, T. Benner, and W. Tseng. Diffusion spectrum MRI of cortical architectonics: visualization of cortical layers and segmentation of cortical areas by analysis of planar structure. In *12th Scientific Meeting of International Society for Magnetic Resonance in Medicine (ISMRM), Kyoto, Japan*, page 622, 2004. (Cited on page 43.)

V. J. Wedeen, P. Hagmann, W.-Y. I. Tseng, T. G. Reese, and R. M. Weisskoff. Mapping complex tissue architecture with diffusion spectrum magnetic resonance imaging. *Magnetic Resonance in Medicine*, 54(6):1377–1386, 2005. ISSN 1522-2594. doi:10.1002/mrm.20642. (Cited on page 91.)

A. Weil. A rapid method for staining myelin sheaths. *Archives of Neurology & Psychiatry*, 20(2):392–393, 1928. doi:10.1001/archneurpsyc.1928.02210140160013. (Cited on page 148.)

J. Weis and L. Budinský. Simulation of the influence of magnetic field inhomogeneity and distortion correction in MR imaging. *Magnetic Resonance Imaging*, 8(4):483 – 489, 1990. ISSN 0730-725X. doi:10.1016/0730-725X(90)90056-8. (Cited on pages 18, 20, and 21.)

R. M. Weisskoff and T. L. Davis. Correcting gross distortion on echo planar images. In *Proceedings of the SMRM 11th Annual Meeting Berlin*, page 4515, 1992. (Cited on pages 16, 18, 20, and 21.)

M. R. Wiegell, D. S. Tuch, H. B. W. Larsson, and V. J. Wedeen. Automatic segmentation of thalamic nuclei from diffusion tensor magnetic resonance imaging. *NeuroImage*, 19(2):391 – 401, 2003. ISSN 1053-8119. doi:10.1016/S1053-8119(03)00044-2. (Cited on page 47.)

P. A. Wielopolski, F. Schmitt, and M. K. Stehling. Echo-planar imaging pulse sequences. In *Echo-Planar Imaging - Theory, technique and applications*, pages 65–139. Springer-Verlag Berlin Heidelberg, 1998. ISBN 978-3-642-80445-8. doi:10.1007/978-3-642-80443-4_4. (Cited on pages 6, 10, 11, 25, and 26.)

N. Wiest-Daesslé, S. Prima, P. Coupé, S. Morrissey, and C. Barillot. Rician noise removal by non-local means filtering for low signal-to-noise ratio MRI: Applications to DT-MRI. In D. Metaxas, L. Axel, G. Fichtinger, and G. Székely, editors, *Medical Image Computing and Computer-Assisted Intervention (MICCAI)*, volume 5242 of *Lecture Notes in Computer Science*, pages 171–179. Springer Berlin Heidelberg, 2008. ISBN 978-3-540-85989-5. doi:10.1007/978-3-540-85990-1_21. (Cited on page 99.)

G. S. Wig, B. L. Schlaggar, and S. E. Petersen. Concepts and principles in the analysis of brain networks. *Annals of the New York Academy of Sciences*, 1224(1):126–146, 2011. ISSN 1749-6632. doi:10.1111/j.1749-6632.2010.05947.x. (Cited on page 47.)

G. S. Wig, T. O. Laumann, A. L. Cohen, J. D. Power, S. M. Nelson, M. F. Glasser, F. M. Miezin, A. Z. Snyder, B. L. Schlaggar, and S. E. Petersen. Parcellating an individual subject's cortical and subcortical brain structures using snowball sampling of resting-state correlations. *Cerebral Cortex*, 24(8):2036–2054, 2014a. doi:10.1093/cercor/bht056. (Cited on page 49.)

G. S. Wig, T. O. Laumann, and S. E. Petersen. An approach for parcellating human cortical areas using resting-state correlations. *NeuroImage*, 93, Part 2:276 – 291, 2014b. ISSN 1053-8119. doi:10.1016/j.neuroimage.2013.07.035. (Cited on pages 49, 97, and 100.)

M. J. Wilhelm, H. H. Ong, S. L. Wehrli, C. Li, P.-H. Tsai, D. B. Hackney, and F. W. Wehrli. Direct magnetic resonance detection of myelin and prospects for quantitative imaging of myelin density. *Proceedings of the National Academy of Sciences*, 109(24):9605–9610, 2012. doi:10.1073/pnas.1115107109. (Cited on pages 39 and 42.)

R. P. Woods, S. T. Grafton, C. J. Holmes, S. R. Cherry, and J. C. Mazziotta. Automated image registration: I. general methods and intrasubject, intramodality validation. *Journal of Computer Assisted Tomography*, 22(1): 139–152, 1998. doi:10.1097/00004728-199801000-00027. (Cited on pages 35 and 36.)

M. W. Woolrich, B. D. Ripley, M. Brady, and S. M. Smith. Temporal autocorrelation in univariate linear modeling of FMRI data. *NeuroImage*, 14(6):1370 – 1386, 2001. ISSN 1053-8119. doi:10.1006/nimg.2001.0931. (Cited on page 103.)

F. Wu, X.-Y. Jing, X. You, D. Yue, R. Hu, and J.-Y. Yang. Multi-view low-rank dictionary learning for image classification. *Pattern Recognition*, 50:143 – 154, 2016. doi:10.1016/j.patcog.2015.08.012. (Cited on page 158.)

M. Wu, L.-C. Chang, L. Walker, H. Lemaitre, A. Barnett, S. Marenco, and C. Pierpaoli. Comparison of EPI distortion correction methods in diffusion tensor MRI using a novel framework. In D. Metaxas, L. Axel, G. Fichtinger, and G. Székely, editors, *Medical Image Computing and Computer-Assisted Intervention (MICCAI)*, volume 5242 of *Lecture Notes in Computer Science*, pages 321–329. Springer Berlin / Heidelberg, 2008. ISBN 978-3-540-85989-5. (Cited on pages 23, 52, 54, and 67.)

X.-X. Xing, T. Xu, Z. Yang, and X.-N. Zuo. Non-local means smoothing: A demonstration on multiband R-FMRI. In *19th Annual Meeting of the Organization for Human Brain Mapping (OHBM)*, page 2030, 2013. (Cited on page 99.)

N. N. Yadav, T. Stait-Gardner, , and W. S. Price. Hardware considerations for diffusion MRI. In D. K. Jones, editor, *Diffusion MRI: Theory, Methods, and Applications*, pages 171–181. Oxford University Press, USA, 2011. doi:10.1093/med/9780195369779.003.0011. (Cited on page 28.)

X.-F. Yao and Z.-J. Song. Deformable registration for geometric distortion correction of diffusion tensor imaging. In P. Real, D. Diaz-Pernil, H. Molina-Abril, A. Berciano, and W. Kropatsch, editors, *Computer Analysis of Images and Patterns*, volume 6854 of *Lecture Notes in Computer Science*, pages 545–553. Springer Berlin / Heidelberg, 2011. ISBN 978-3-642-23671-6. (Cited on pages 23, 52, 53, and 67.)

B. T. T. Yeo. Automatic labeling of the human cerebral cortex. In A. W. Toga, editor, *Brain Mapping*, pages 357 – 363. Academic Press, Waltham, 2015. ISBN 978-0-12-397316-0. doi:10.1016/B978-0-12-397025-1.00306-7. (Cited on pages 35, 36, and 49.)

B. T. T. Yeo, F. M. Krienen, J. Sepulcre, M. R. Sabuncu, D. Lashkari, M. Hollinshead, J. L. Roffman, J. W. Smoller, L. Zöllei, J. R. Polimeni, B. Fischl, H. Liu, and R. L. Buckner. The organization of the human cerebral cortex estimated by intrinsic functional connectivity. *Journal of Neurophysiology*, 106(3):1125–1165, 2011. ISSN 0022-3077. doi:10.1152/jn.00338.2011. (Cited on pages 49 and 101.)

S. X. Yu and J. Shi. Multiclass spectral clustering. In *Ninth IEEE International Conference on Computer Vision (ICCV)*, volume 1, pages 313–319, Oct 2003. doi:10.1109/ICCV.2003.1238361. (Cited on pages 100 and 102.)

M. Zaitsev, J. Hennig, and O. Speck. Point spread function mapping with parallel imaging techniques and high acceleration factors: Fast, robust, and flexible method for echo-planar imaging distortion correction. *Magnetic Resonance in Medicine*, 52(5):1156–1166, 2004. ISSN 1522-2594. doi:10.1002/mrm.20261. (Cited on page 25.)

A. Zalesky, A. Fornito, L. Cocchi, L. L. Gollo, and M. Breakspear. Time-resolved resting-state brain networks. *Proceedings of the National Academy of Sciences*, 111(28):10341–10346, 2014. doi:10.1073/pnas.1400181111. (Cited on page 121.)

H. Zeng and R. T. Constable. Image distortion correction in EPI: Comparison of field mapping with point spread function mapping. *Magnetic Resonance in Medicine*, 48(1):137–146, 2002. ISSN 1522-2594. doi:10.1002/mrm.10200. (Cited on page 25.)

H. Zhang, T. Schneider, C. A. Wheeler-Kingshott, and D. C. Alexander. NODDI: Practical *in vivo* neurite orientation dispersion and density imaging of the human brain. *NeuroImage*, 61(4):1000 – 1016, 2012. doi:10.1016/j.neuroimage.2012.03.072. (Cited on pages 45 and 46.)

J. Zhang, H. Huang, M. Aggarwal, and S. Mori. Diffusion tensor microimaging and its applications. In D. K. Jones, editor, *Diffusion MRI: Theory, Methods, and Applications*, pages 425–438. Oxford University Press, 2011. doi:10.1093/med/9780195369779.003.0025. (Cited on page 43.)

K. Zilles and K. Amunts. Centenary of Brodmann's map – conception and fate. *Nature Reviews Neuroscience*, 11: 139–145, February 2010. doi:10.1038/nrn2776. (Cited on pages 31, 32, 33, 37, and 106.)

K. Zilles and K. Amunts. Architecture of the cerebral cortex. In J. K. Mai and G. Paxinos, editors, *The Human Nervous System*, pages 836–895. Academic Press, San Diego, third edition, 2012. ISBN 978-0-12-374236-0. doi:10.1016/B978-0-12-374236-0.10023-9. (Cited on pages 31 and 33.)

K. Zilles and N. Palomero-Gallagher. Cyto-, myelo-, and receptor architectonics of the human parietal cortex. *NeuroImage*, 14(1):S8–S20, 2001. ISSN 1053-8119. doi:10.1006/nimg.2001.0823. (Cited on pages 33, 37, and 38.)

K. Zilles and N. Palomero-Gallagher. Gyrification in the human brain. In A. W. Toga, editor, *Brain Mapping*, pages 37 – 44. Academic Press, 2015. ISBN 978-0-12-397316-0. doi:10.1016/B978-0-12-397025-1.00197-4. (Cited on page 35.)

K. Zilles, E. Armstrong, A. Schleicher, and H.-J. Kretschmann. The human pattern of gyrification in the cerebral cortex. *Anatomy and Embryology*, 179(2):173–179, 1988. ISSN 1432-0568. doi:10.1007/BF00304699. (Cited on page 37.)

K. Zilles, L. Werner, M. Qü, A. Schleicher, and G. Gross. Quantitative auto radiography of 11 different transmitter binding sites in the basal forebrain region of the rat – evidence of heterogeneity in distribution patterns. *Neuroscience*, 42(2):473–481, 1991. ISSN 0306-4522. doi:10.1016/0306-4522(91)90390-A. (Cited on page 33.)

K. Zilles, N. Palomero-Gallagher, C. Grefkes, F. Scheperjans, C. Boy, K. Amunts, and A. Schleicher. Architectonics of the human cerebral cortex and transmitter receptor fingerprints: reconciling functional neuroanatomy and neurochemistry. *European Neuropsychopharmacology*, 12(6):587 – 599, 2002a. ISSN 0924-977X. doi:10.1016/S0924-977X(02)00108-6. (Cited on page 33.)

K. Zilles, A. Schleicher, N. Palomero-Gallagher, and K. Amunts. Quantitative analysis of cyto- and receptor architecture of the human brain. In *Brain Mapping: The Methods*. Academic Press, San Diego, 2002b. (Cited on pages 33 and 34.)

K. Zilles, N. Palomero-Gallagher, and K. Amunts. Cytoarchitecture and maps of the human cerebral cortex. In A. W. Toga, editor, *Brain Mapping*, pages 115 – 135. Academic Press, 2015a. ISBN 978-0-12-397316-0. doi:10.1016/B978-0-12-397025-1.00207-4. (Cited on pages 31, 33, and 34.)

K. Zilles, N. Palomero-Gallagher, and K. Amunts. Myeloarchitecture and maps of the cerebral cortex. In A. W. Toga, editor, *Brain Mapping*, pages 137 – 156. Academic Press, 2015b. ISBN 978-0-12-397316-0. doi:10.1016/B978-0-12-397025-1.00209-8. (Cited on pages 31, 32, and 33.)

X.-N. Zuo and X.-X. Xing. Effects of non-local diffusion on structural MRI preprocessing and default network mapping: Statistical comparisons with isotropic/anisotropic diffusion. *PLoS ONE*, 6(10):e26703, 10 2011. doi:10.1371/journal.pone.0026703. (Cited on page 99.)